FROM FEW-CYCLE FEMTOSECOND PULSE TO SINGLE ATTOSECOND PULSE-CONTROLLING AND TRACKING ELECTRON DYNAMICS WITH ATTOSECOND PRECISION

by

HE WANG

B.A., University of Science and Technology of China, 2005

AN ABSTRACT OF A DISSERTATION

submitted in partial fulfillment of the requirements for the degree

DOCTOR OF PHILOSOPHY

Department of Physics
College of Arts and Sciences

KANSAS STATE UNIVERSITY
Manhattan, Kansas

2010

Abstract

The few-cycle femtosecond laser pulse has proved itself to be a powerful tool for controlling the electron dynamics inside atoms and molecules. By applying such few-cycle pulses as a driving field, single isolated attosecond pulses can be produced through the high-order harmonic generation process, which provide a novel tool for capturing the real time electron motion. The first part of the thesis is devoted to the state of the art few-cycle near infrared (NIR) laser pulse development, which includes absolute phase control (carrier-envelope phase stabilization), amplitude control (power stabilization), and relative phase control (pulse compression and shaping). Then the double optical gating (DOG) method for generating single attosecond pulses and the attosecond streaking experiment for characterizing such pulses are presented. Various experimental limitations in the attosecond streaking measurement are illustrated through simulation. Finally by using the single attosecond pulses generated by DOG, an attosecond transient absorption experiment is performed to study the autoionization process of argon. When the delay between a few-cycle NIR pulse and a single attosecond XUV pulse is scanned, the Fano resonance shapes of the argon autoionizing states are modified by the NIR pulse, which shows the direct observation and control of electron-electron correlation in the temporal domain.

FROM FEW-CYCLE FEMTOSECOND PULSE TO SINGLE ATTOSECOND PULSE-CONTROLLING AND TRACKING ELECTRON DYNAMICS WITH ATTOSECOND PRECISION

by

HE WANG

B.A., University of Science and Technology of China, 2005

A DISSERTATION

submitted in partial fulfillment of the requirements for the degree

DOCTOR OF PHILOSOPHY

Department of Physics
College of Arts and Sciences

KANSAS STATE UNIVERSITY
Manhattan, Kansas

2010

Approved by:

Major Professor
Zenghu Chang

Copyright

Abstract

The few-cycle femtosecond laser pulse has proved itself to be a powerful tool for controlling the electron dynamics inside atoms and molecules. By applying such few-cycle pulses as a driving field, single isolated attosecond pulses can be produced through the high-order harmonic generation process, which provide a novel tool for capturing the real time electron motion. The first part of the thesis is devoted to the state of the art few-cycle near infrared (NIR) laser pulse development, which includes absolute phase control (carrier-envelope phase stabilization), amplitude control (power stabilization), and relative phase control (pulse compression and shaping). Then the double optical gating (DOG) method for generating single attosecond pulses and the attosecond streaking experiment for characterizing such pulses are presented. Various experimental limitations in the attosecond streaking measurement are illustrated through simulation. Finally by using the single attosecond pulses generated by DOG, an attosecond transient absorption experiment is performed to study the autoionization process of argon. When the delay between a few-cycle NIR pulse and a single attosecond XUV pulse is scanned, the Fano resonance shapes of the argon autoionizing states are modified by the NIR pulse, which shows the direct observation and control of electron-electron correlation in the temporal domain.

Table of Contents

List of Figures

List of Tables

Acknowledgements

First I am really grateful to the enormous guidance and encouragement from my supervisor Dr. Zenghu Chang, it is he who brings me to this exciting field of attosecond science and teaches me how to conduct effective research. I still remember every exciting moment we shared when the nice experimental results were obtained. The most difficult time was my final project. At the beginning of this year the newly built experimental setup was partially damaged by accident and I was so frustrated at that time. It was my supervisor again who advised me to quickly change the experimental method as an alternative, which finally led to the nice results presented in the Chapter five. This is the real lesson I have learned on how to conduct good research: even when you have a lot of uncertainties and make some mistakes, you need to try and think but never stop; otherwise you will never discover new things by yourself.

I do thank Dr. Hiroki Mashiko, and Dr. Chengquan Li. They set excellent examples for me when I first joined this group. From them I learned a lot of practical skills of aligning optics and writing Labview programs.

I also want to thank Dr. Shouyuan Chen, Michael Chini, and Chenxia Yun. We have been in a very pleasant team working together on the MARS laser. Without Shouyuan's help on the final project, it would have been impossible for me to handle both the laser and experimental setup. I do enjoy the thought provoking discussions with Michael and thank him for helping me on paper writing. Especially I want to thank him for helping me proofread my thesis and correct the English.

My class fellow Steve Gilbertson is a very diligent researcher, and it is my honor to work with such a productive colleague. I have been working with Yi Wu on the pulse shaper project, and I admire his practical approach to solving problems. A lot of thanks need to be given to my lab mates, Sabih Khan, Dr. Kun Zhao and Qi Zhang. They have been helping a lot on my experiments. I do appreciate the help from Al Rankin. Without his help on design and assembly of experimental setup, many projects cannot be realized.

Finally I would like to thank all of my Ph. D committee members and outside chair: Dr. Brett DePaola, Dr. Brett Esry, Dr. Viktor Chikan and Dr. Margaret Rys for guiding me and serving on my committee.

CHAPTER 1 - Introduction

Since the electron was first discovered by J. J. Thomson as a fundamental particle more than one century ago [1], it has always been a dream for scientists and engineers to observe and control its fast dynamics. As a building block of the atoms, molecules and materials, the electron is fundamentally important since its behaviors, such as correlation, excitation and relaxation, determine the physical and chemical properties of the world around us [2].

Quantum mechanically, since the spacing between energy levels is on the order of several electron volts in atoms and molecules, and sub-electron volts in materials due to their spatial confinement, the time scale of electron dynamics is on the order of tens and hundreds of attoseconds (10^{-18} s). To capture the fast motion of electrons, pulses of attosecond duration are prerequisite. On the other hand, the electron behavior in the atoms and molecules is mainly governed by the electron-electron repulsion and electron-nuclear attraction. Those Coulomb fields are on the order of 10^9 V/cm for the ground state as well as low lying states of atoms and molecules. In order to initiate the dynamics as well as to control the electron motion, the applied field has to be comparable with that of the unperturbed system, which is beyond the reach of static fields. With the recent development of high power femtosecond laser, the dreams of observing and controlling the electron dynamics is within the realm of possibility [3].

1.1 High harmonic generation (HHG)

When the femtosecond pulses are focused to the intensity of 10^{14}W/cm^2 on an atomic or molecular gas target, the electric field from the laser becomes comparable to the Coulomb field. Besides the strong ionization, the odd order high harmonics of the driving laser can be detected experimentally. High harmonic generation (HHG) was first discovered in 1988 by research groups in Chicago and France [4, 5]. Different from perturbative harmonic generation [6], HHG starts with a rapid decrease for the low-order harmonics consistent with perturbation theory, followed by a plateau region where the harmonic intensity drops more slowly and then an abrupt cutoff as shown in Fig.1-1.

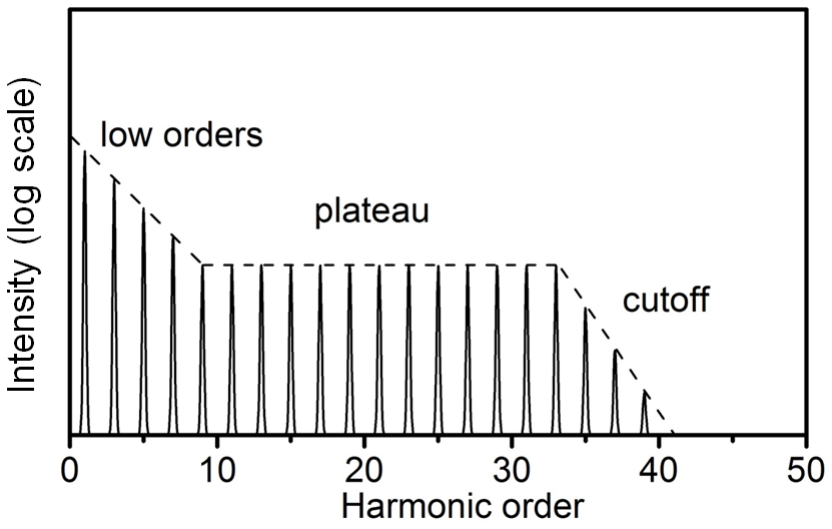

Figure 1-1 Typical high harmonic spectrum. The spectrum consists of three parts: the perturbative regime at low orders, the plateau for intermediate orders, and the cutoff at the highest orders.

1.2 Recollision model of HHG

Instead of applying multi-photon picture in the perturbative regime, a recollision model [7-9] which includes tunneling, acceleration and recombination was proposed to explain the mechanism of HHG as shown in Fig. 1-2. There are two very important aspects derived from this model, and they will serve as the motivation and guideline of the whole thesis.

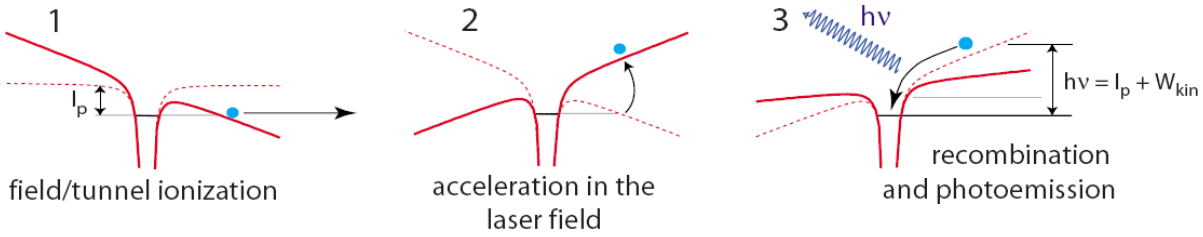

Figure 1-2 Recollision model in HHG.

1.2.1 Electron motion governed by the electric field

The first key point one is that in a strong laser field the electron motion is ultimately governed by the oscillating electric field of the laser pulse. Let us start from the tunneling ionization. At modest laser intensities, the normal multi-photon excitation route for ionization via intermediate states applies as shown in Fig. 1-3(a). If the incident field is strong enough and

frequency is low enough then, within a quasi-static approximation, the field is able to distort the atomic potential to such an extent that a potential barrier is formed through which the electron can tunnel as shown in Fig. 1-3(b).

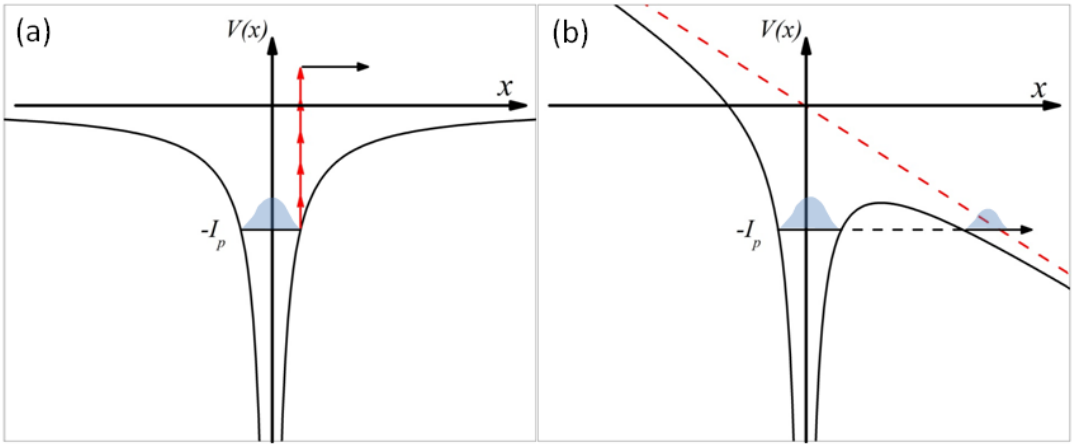

Figure 1-3 Physical pictures of atomic ionization under different laser intensities. (a) Multi-photon regime: at moderate intensity (<10^{14} W/cm2) the Coulomb potential is unperturbed, and electron is ionized by absorbing N photons. (b) Tunneling regime: at sufficiently high intensity (<10^{15} W/cm^2), the Coulomb potential barrier is formed, and the electron tunnels out.

To classify different regimes between multi-photon ionization and tunneling ionization and to give a qualitative physical picture, the Keldysh parameter γ was introduced to describe the ionization behavior [10], which is defined as:

$$\gamma = \sqrt{\frac{I_p}{2U_p}}, \tag{1.1}$$

where I_p is the ionization potential of the target atoms, U_p is called the ponderomotive potential, which is the average quiver energy the electron gains in the laser field and is expressed as:

$$U_p = \frac{e^2 \xi_{laser}^2}{4m\omega^2}, \tag{1.2}$$

where e and m are the electron charge and mass, ξ_{laser} and ω are the amplitude and the angular frequency of the laser field. The multi-photon ionization process dominates for $\gamma >> 1$, but if the laser intensity increases until $\gamma << 1$, the tunneling ionization process takes over. Since the HHG process happens at the intensity of 10^{14}W/cm^2, its Keldysh parameter is smaller than one for

typical Ti:Sapphire laser (800 nm central wavelength) and noble gas target (I_p~10 eV). Therefore, the electron tunnels out when the electric field of the laser suppresses the Coulomb potential in the first step of HHG.

Once the electron tunnels out, the Coulomb field drops dramatically and the electric field from the laser starts to take over and control the electron motion. Based on Newton's law the electron equations of motion can be expressed as:

$$a(t) = \ddot{x}(t) = \frac{e\xi_{laser}}{m}\cos(\omega t), \tag{1.3}$$

$$v(t) = \dot{x}(t) = \frac{e\xi_{laser}}{m\omega}\sin(\omega t) + v_0, \tag{1.4}$$

$$x(t) = -\frac{e\xi_{laser}}{m\omega^2}\cos(\omega t) + v_0 t + x_0. \tag{1.5}$$

If the free electron is born at the time $t = t_0$ within the first quarter of the cycle, assuming the initial conditions $v(t_0) = x(t_0) = 0$, and $\phi_0 = \omega t_0$, the electron is accelerated and driven back to the initial position (See Appendix A for detailed calculation). During the recombination process the net gain of electron kinetic energy is released in the form of XUV radiation, which leads to the HHG process observed experimentally.

As shown in Fig. 1-4 (a), when the electron was born at a phase of 18 degree, the maximum kinetic energy of $3.17U_p$ is accumulated. Including the energy gain during the tunneling process, the cutoff of HHG is predicted as $\hbar\omega_{cutoff} = 3.17U_p + I_p$ [7]. Below the cutoff energy, contributions from the two electron trajectories are possible. According to the time interval between birth and recombination, they are termed as the long and short trajectories respectively, as shown in Fig. 1-4 (a) and (b).

Thus, the electric field again governs the motion of free electrons. In order to control the dynamics of either bound or free electron, the key is to control the electric field of the laser pulse.

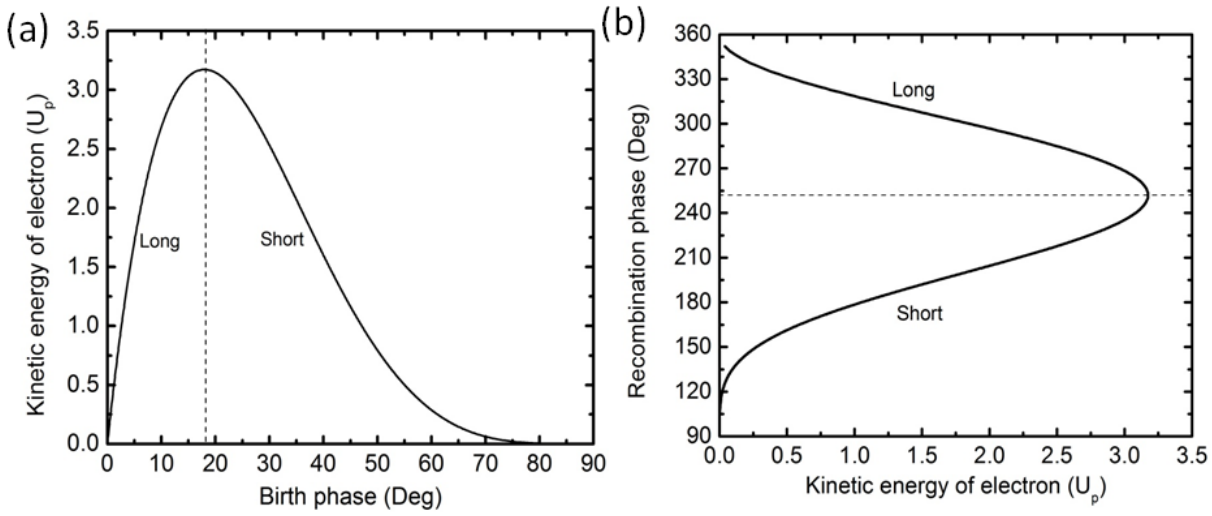

Figure 1-4 (a) Plot of birth time and final kinetic energy. (b) Plot of recombination time and final kinetic energy. When the electron was born at 18 degrees, the kinetic energy of the free electron reaches the cutoff 3.17 U_p. Below the cutoff, two trajectories (long and short) lead to the same final energy.

1.2.2 Emergence of attosecond pulses

In the recollision model the tunneling ionization of the atom plays a central role in attosecond science since substantial ionization occurs within a fraction of an optical cycle (T=2.67 fs for 800 nm central wavelength). Quantitatively, in the tunneling regime the ionization rate was predicted by ADK theory [11] (See Appendix A for details). When the laser pulse with 800 nm central wavelength and peak intensity $2\times10^{14}W/cm^2$ is focused on a hydrogen atom in the ground state ($\gamma=0.73$), the tunneling rate predicted by ADK formula during one laser cycle is plotted as shown in Fig. 1-5(a). It can been seen that tunneling mainly happens around the peak of each laser oscillation and forms the electron wave packet lasting for about 340 as, around the one eighth of the laser period. This is extremely important, as it explains the origin of attosecond pulse. If the laser intensity is reduced to the multi-photon ionization regime, the ADK rate, based on quasi-static picture, is not longer valid. Instead the non-adiabatic formula is more suitable [12], which predicts an electron wave packet of femtosecond duration.

Since HHG happens in the tunneling regime, the attosecond nature is naturally encoded. The tunneling model leads to the formation of an outgoing electron wave packet each time the electric field reaches its peak value. After the acceleration of the electron wavepacket in the laser field and recombination near the zero crossing of the field, a train of attosecond bursts with half-cycle separation is generated in the temporal domain as shown in Fig. 1-5(b). The experimental observation of discrete harmonics in the spectral domain is the interference of attosecond pulses within the train in the temporal domain.

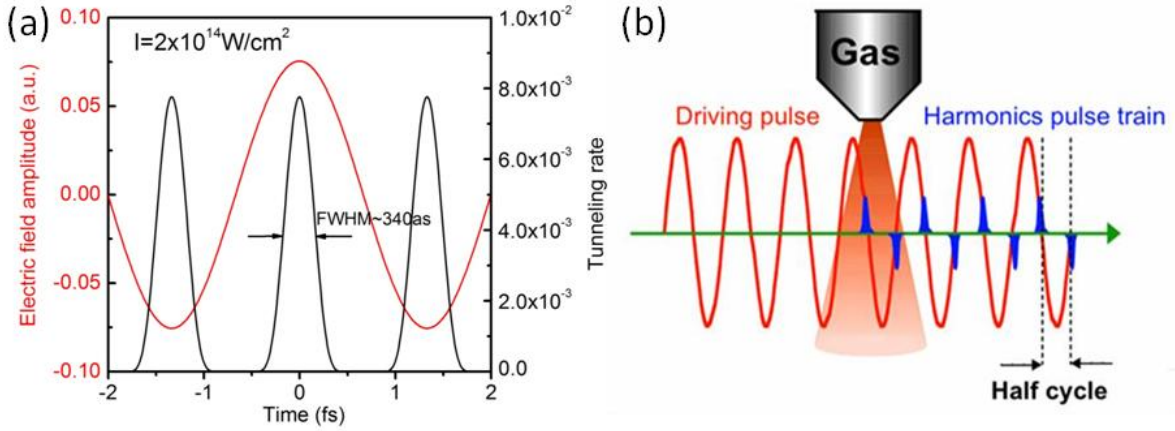

Figure 1-5 (a)Tunneling rate of ground state hydrogen atom during one laser cycle at intensity of $2X10^{14}W/cm^2$ for 800 nm central wavelength. (b) HHG consists of attosecond pulses with half-cycle separation in the temporal domain.

1.3 Generation of single attosecond pulses

The breakthrough happened in 2001, when two groups independently proved that HHG consists of XUV bursts lasting several hundreds of attoseconds in the temporal domain by cross-correlation measurements [13, 14]. Even though the HHG process naturally results in an attosecond pulse train in the temporal domain, when the fast electron dynamics are studied, it is much better to select a single attosecond pulse to do pump-probe experiments since it has a very well defined timing and a broad continuous spectrum to simultaneously access many resonant states. The single attosecond pulses were produced from few-cycle driving pulses [15] by selecting the XUV near the cutoff regime [16] or applying driving field with time-dependent ellipticity as shown in Fig. 1-6(a) and (b) [17]. The method shown in Fig. 1-6 (a) is termed amplitude gating, where the XUV spectrum near the cutoff are only produced by the driving field with highest amplitude. The approach depicted in Fig. 1-6 (b) is called polarization gating. Since

HHG can be efficiently produced when the linearly polarized driving field is used, by combining a left circular pulse and a right circular pulse with proper delay, a half cycle linear portion in the middle naturally generates a single attosecond pulse.

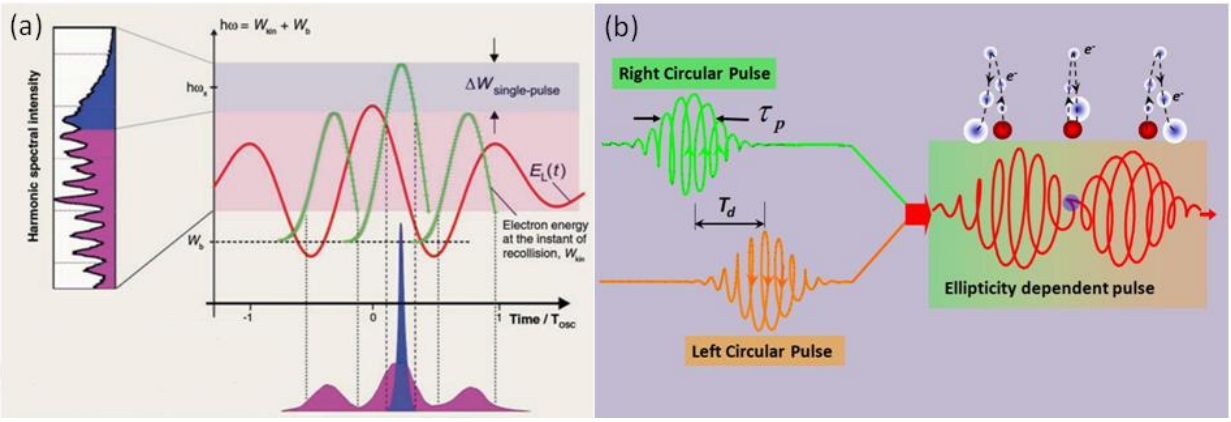

Figure 1-6 Different ways of generating single attosecond pulses: (a) the single attosecond pulses were generated by selecting the cutoff regime of HHG when few-cycle pulses were used as driving field; (b) when the left circular and right circular pulses were delayed and overlapped properly, only the linear portion in the middle produces single attosecond pulses.

Single attosecond pulses can be used to track the electron dynamics directly in the temporal domain, and this opens up a brand new field of attosecond science [3, 18]. In the following years, many experiments have been performed, such as the measurement of the Auger process in the temporal domain [19], mapping of sub-cycle dynamics of tunneling ionization [20], direct control of electron localization during the dissociation process in molecules [21].

1.4 Thesis outline

This thesis is devoted to the control of attosecond electron dynamics, as well as generation and application of single attosecond pulses.

Chapter 2 and Chapter 3 mainly focus on the state of the art few-cycle laser pulse development for studying attosecond electron dynamics, which includes amplitude control (power stabilization), absolute phase control (carrier-envelope phase stabilization) and relative phase control (pulse shaping and compression by adaptive phase modulator). The carrier-envelope (CE) phase stabilized chirped pulse amplifier (CPA) and hollow core fiber setup will be

presented in detail. Several laser pulse characterization and control techniques will also be discussed, such as *f*-to-*2f* interferometry, and Multiphoton Intrapulse Interference Phase Scan (MIIPS).

Chapter 4 mainly discusses our novel approach to generate single isolated attosecond pulses by Double Optical Gating (DOG), and the attosecond streak camera is used to characterize the pulses. When the Principal Component Generalized Projections Algorithm (PCGPA) is applied to reconstruct the attosecond XUV pulse from the streaking spectrogram, several experimental constraints are discussed, which serve to guide the experiment and shed light on how the XUV attosecond pulse is embedded in the streaking spectrogram.

Chapter 5 studies attosecond dynamics of the autoionization process in argon with the single attosecond pulse generated from DOG. In the attosecond transient absorption experiment the near infrared (NIR) pump-XUV probe technique is used. When the delay between the NIR and XUV pulses is scanned, it is found that the NIR laser field causes changes to the resonance peak position and shape, and causes a reduction in the XUV transmission. The features were found to depend strongly on the laser intensity. The shifting, splitting, and broadening of the Fano resonance peak in the laser field are attributed to the coupling, both resonant and non-resonant, of the bound and continuum states by the NIR laser. The measurement demonstrates control of the autoionization process with unprecedented temporal attosecond precision, and allows direct observation and control of electron-electron correlation in the temporal domain.

Finally a short remark is given to summarize the entire thesis.

CHAPTER 2 - Stabilization of the power and carrier-envelope phase of few-cycle pulse laser pulses

When a multi-cycle laser pulse is used to produce HHG, an attosecond pulse train is formed in the temporal domain. To track the real time electron dynamics with pump-probe techniques within the range of several femtoseconds, single attoseond pulses are required. One way of generating single attosecnd pulses is to use few-cycle driving laser fields. This chapter mainly covers the generation of few-cycle laser pulses. To control and optimize such pulses, carrier-envelope (CE) phase stabilization and power locking will be discussed in detail.

2.1 Chirped pulse amplifier laser system

Currently sub-30 fs, milli-joule level Ti:Sapphire chirped pulse amplifier (CPA) laser systems are commercially available and becoming a standard tool in ultrafast laser labs [22]. The CPA laser system consists of an oscillator, stretcher, amplifier and compressor as shown in Fig. 2-1, and it was first time designed by Strickland and Mourou in 1985 to boost the pulse energy from nano-joule to milli-joule level [23]. In CPA the seed pulse from the oscillator is stretched, amplified and compressed to maintain high gain without damaging of the gain medium.

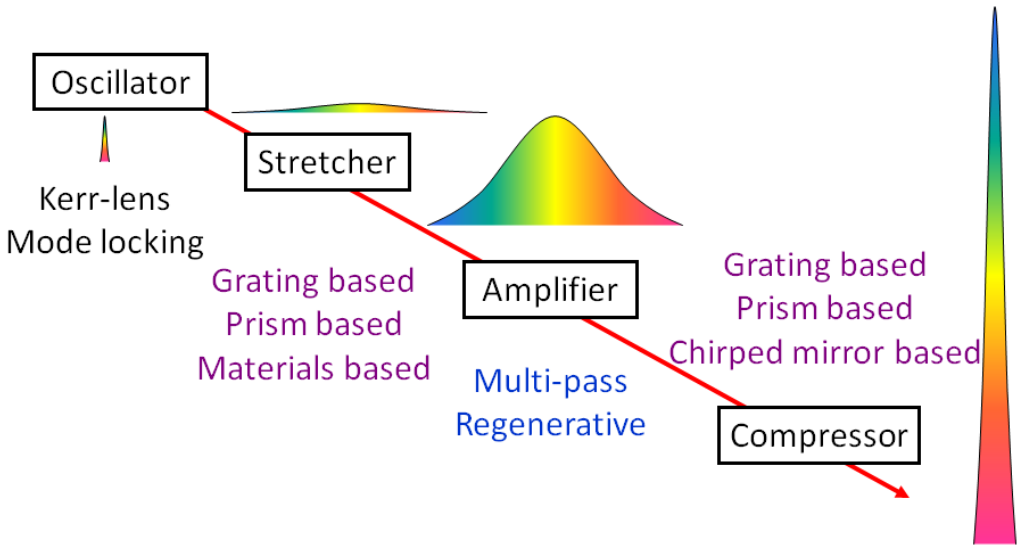

Figure 2-1 The operating principle of CPA laser system. It includes oscillator, stretcher, amplifier and compressor.

The most widely used oscillator is the Kerr-lens mode locking Ti:Sapphire oscillator because of its compactness and robustness [24]. Current Ti:Sapphire oscillators can generate more than one octave-spanning spectra with pulse duration below 5 fs [25]. However, when the seed pulses from the oscillator are amplified from the nano-joule to the milli-joule level with CPA, they are broadened to more than 10 fs due to gain narrowing of the pulse spectrum [23]. The stretcher and compressor can be made of dispersive glasses, chirped mirrors, prism pairs or grating pairs [22]. The grating pairs based stretcher and compressor were originally proposed by Treacy and Martinez [26, 27], and are most commonly used in high-power CPA laser systems because of their large stretching and compressing factor (>10,000 times) and the high damage threshold of reflective optics.

Two types of CPA amplifier are commonly used. One type is the multi-pass amplifier, in which the seed pulse travels different paths during the amplification process. Since there is no uniquely defined cavity, the amplified spontaneous emission (ASE) is suppressed due to the geometry. Also since only the crystal contributes the total material dispersion, the high order dispersion is minimized and the pulse duration can easily be compressed down to less than 30 fs after the amplification [28, 29]. The other type is the regenerative amplifier [30]. In a regenerative amplifier, the seed pulse follows the same optical path and for several round trips within a cavity geometry during the amplification. One or two Pockels cells are used to switch in the seed and switch out the amplified pulse by changing the polarization at a specific time delay. Since the number of round trips inside the cavity can easily be optimized by controlling the timing of the Pockels cells, the overall energy extraction efficiency (~15%) of regenerative amplifiers is better than that of multi-pass amplifiers. Due to the very well-defined cavity, the final output beam profile and pointing stability are also better than multi-pass amplifiers. Regenerative amplifiers are therefore used as pre-amplifiers in high power laser systems. However, the ASE is generally higher for regenerative amplifiers than for multi-pass amplifiers and the pulse contrast is not as good. Furthermore, the high order dispersion introduced by dispersive materials inside cavity add small pre and post pulses to the main pulse and make it difficult to be compressed to the TL pulse duration.

In our lab we have two laser systems. One is our home-designed Kansas Light Source (KLS) [31], which is a single-stage multi-pass amplifier including pre-amplifier and power amplifier. The other one is the Manhattan Attosecond Radiation Source (MARS) purchased from

Coherent Corp. (Legend Elite Duo^{TM}), which is a two stage amplifier including regenerative amplifier as a pre-amplifier and single pass amplifier as a power amplifier.

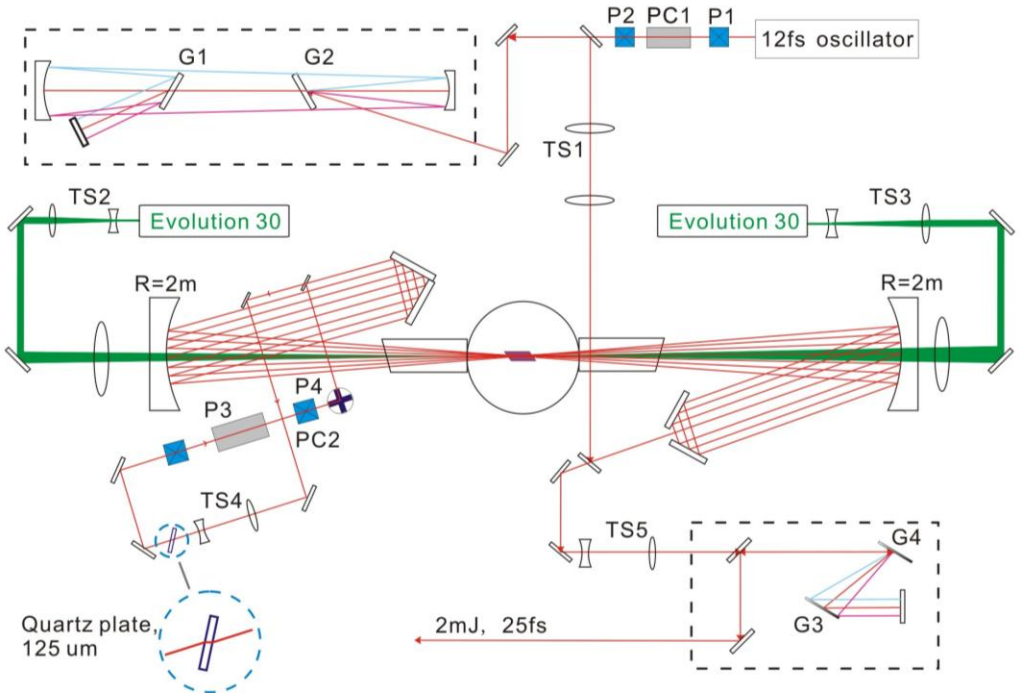

Figure 2-2 KLS multi-pass CPA laser system layout. P1, P2, P3, P4: polarizer; PC1, PC2: Pockels cell; TS1, TS2, TS3: telescope; G1, G2, G3, G4: grating. Figure adapted from Ref [32].

Fig. 2-2 shows the layout of the KLS. The oscillator is a Kerr-lens mode locked Ti:Sapphire oscillator (FemtoSource Pro^{TM} from Femtolasers GmbH), which produces 77 MHz, 6 nJ pulses with pulse duration of around 12 fs. 1 KHz pulses are selected by the Pockels cell (Lasermetrics 5046) and sent to a grating-based Martinez type stretcher. The pulses are stretched to ~ 80 ps to avoid the damage of the Ti:Sapphire crystal. Then, the stretched pulses are amplified to 5 mJ with a 14-pass amplifer, where the Ti:Sapphire crystal is cooled to liquid nitrogen temperature [29] to reduce the thermal lens effect. After the first seven passes, the amplified pulses are extracted from the amplifier and pass through a telescope to shrink the beam size, which expands the focal spot size of the amplified pulse at the crystal and matches the pump laser size for efficient extraction of the pump energy. Another Pockels cell which generates a 10 ns duration window is used to suppress amplified spontaneous emission (ASE) generated during the pre-amplification process. After the amplification, the pulses are compressed by a pair of gratings to 2 mJ, 33 fs with 26 nm FWHM spectrum bandwidth. By

inserting a quartz plate between the first and second seven passes as a spectral filter to compensate the gain narrowing effect and using the mixed gratings, the final pulse duration can be compressed to 25 fs [32].

Fig. 2-3 shows the layout of MARS laser amplifier. The oscillator is a Rainbow^{TM} from Femtolasers GmbH, which produces sub-7 fs pulses at a repetition rate of 78 MHz. The first amplification stage is a 14 round trip regenerative amplifier, which amplifies the pulse energy to 4 mJ. The second stage is a single pass amplifier to boost the laser pulse energy to 8 mJ. The Ti:Sapphire crystal in both amplification stages are thermoelectrically cooled to -12 °C. The regenerative amplifer and single pass amplification stages are pumped by 50% of a 45 W Coherent Evolution HE^{TM} pump laser. After the grating based compressor, the final output pulse energy is 6 mJ with a central wavelength of 800 nm and spectral bandwidth of 37 nm, which supports a transform limited pulse duration of 28 fs.

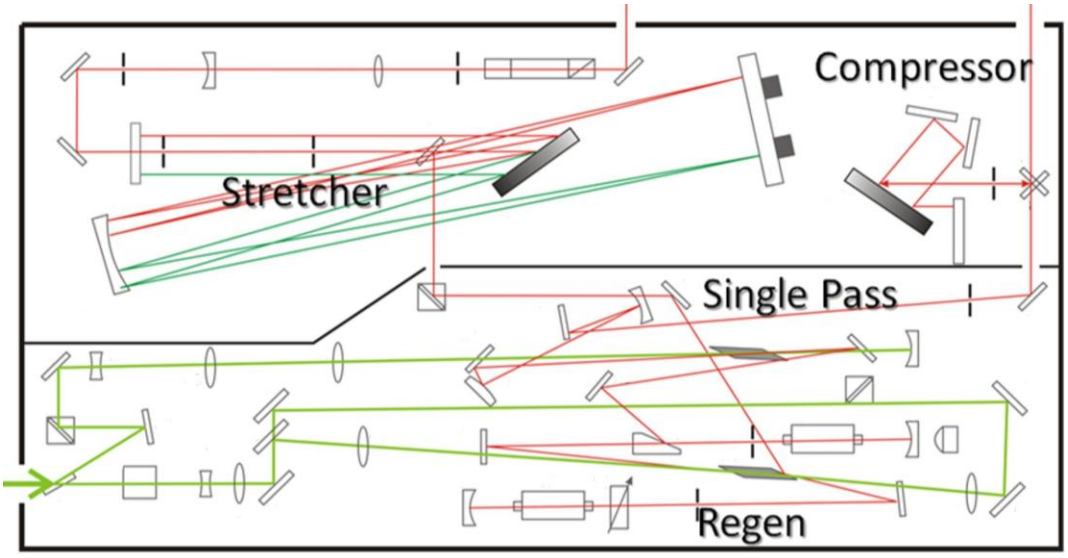

Figure 2-3 MARS regenerative amplifier layout. The seed pulses are first stretched to 180 ps, then 1 KHz pulses are sent into the regenerative amplifier. After 15 round trips, the preamplified pulses pass another single pass amplifier. After the final compression 6 mJ, 30 fs pulses are produced.

2.2 Few cycle pulse generation

Due to the gain narrowing effect, the amplified pulses output from CPA are broadened to ~25 fs, which contains about 10 cycles of oscillation for 800 nm central wavelength. To produce energetic few-cycle pulses, the multi-cycle laser pulses from the CPA lasers are sent to nonlinear optical media such as noble gas-filled hollow-core fibers to broaden the spectral bandwidth so that it covers about one octave in spectral range (typically from 500nm to1000nm) as shown Fig. 2-4 [33, 34]. The positive chirp of the pulses introduced by the nonlinear processes (mainly self phase modulation) and the material dispersion is then removed by pulse compressors such as chirped mirrors, or prism pairs [33, 34]. The chirped mirror is a special type of dielectric mirror with multi-layer coating. It is designed that different optical frequencies has different penetration depths before reflection, which could introduce negative chirp by properly setting the thickness of each layer [35].

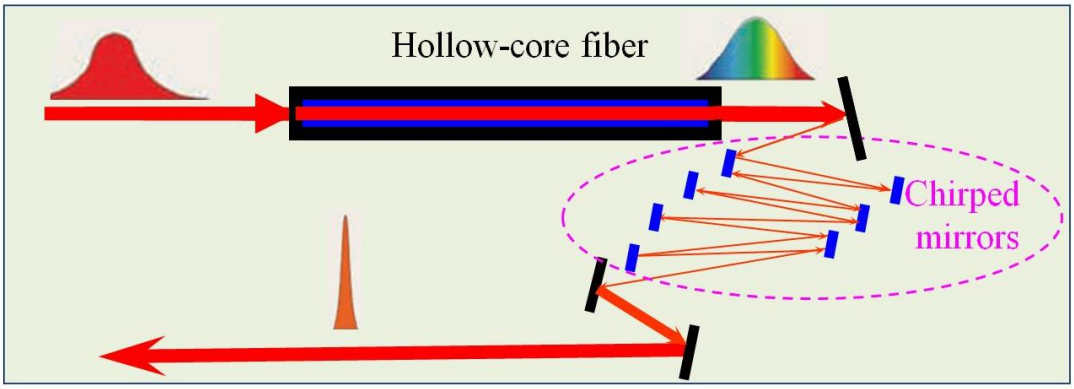

Figure 2-4 Hollow-core fiber compressor.

Previously argon filled hollow-core fiber was used in our lab to broaden the spectrum and produce few-cycle pulses, by using the circularly polarized pulses as input to reduce the ionization at the entrance of the hollow core fiber. 0.6 mJ, 6.2 fs pulses were produced after the hollow core fiber [36]. More recently, with neon filled hollow-core fiber, 1.2 mJ, 5.6 fs linearly polarized pulses have been produced [37]. The 2.5 mJ pulses from the KLS laser were focused into a 0.9 m long hollow-core fiber by f=1.5 m focusing mirror. To minimize the ionization at the entrance of the fiber and maintain high coupling efficiency [38], a large 400 μm core diameter fiber filled with 2 bars of neon gas was used for spectral broadening. The pulses from the fiber were then compressed by chirped mirrors. The frequency-resolved optical gating (FROG) measurement [39] indicated the pulse duration of 5.6 fs as shown in Fig. 2-5 [37].

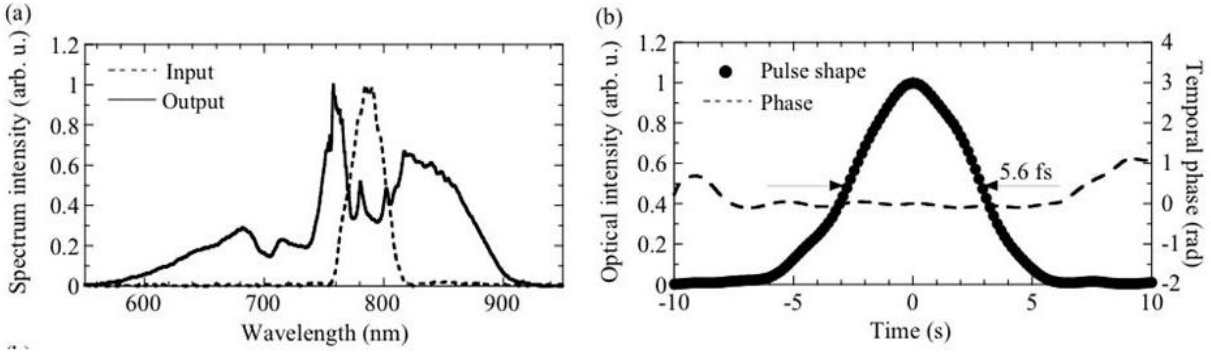

Figure 2-5 (a) Spectra of the input (dashed line) and output (solid line) of the fiber. (b) The pulse shape (filled circle) and temporal phase (dashed line) as reconstructed by FROG. Figure adapted from Ref [37].

2.3 Carrier envelope (CE) phase stabilization of few-cycle pulses

For an ultrafast optical pulse the electric field can be expressed as:

$$E(t) = A(t)\cos[\omega_0 t + \beta(t) + \varphi_{CE}], \tag{2.1}$$

where $A(t)$ is the envelope of the pulse, ω_0 is the carrier frequency, $\beta(t)$ is the high-order phase, which is assumed to be constant after the pulse compression. The carrier-envelope (CE) phase φ_{CE}, denotes the offset between the peak of the pulse envelope and the nearest peak of the carrier-wave electric field. As the width of $A(t)$ approaches few cycle duration, the electric field amplitude changes rapidly within a half cycle, and its distribution is determined by the CE phase as shown in Fig. 2-6. This fast variation of the electric field within the pulse envelope is the origin of carrier-envelope (CE) phase effects in various high field processes such as above threshold ionization (ATI), HHG and electron localization in molecular dissociation [21, 40, 41]. When such few-cycle pulses are used to generate single attosecond pulses [41], the CE phase has to be controlled and stabilized to maintain reproducible isolated attosecond pulses [41]. Instead of directly locking the CE phase of few-cycle pulses, the CE phase of multi-cycle pulses output from the CPA was stabilized. In the discussion of later sections, the CE phase stability of few-cycle pulses and multi-cycle pulses will be measured and compared before and after the hollow-core fiber. Typically CE phase stabilization of a CPA laser consists of a fast loop in the oscillator and a slow loop in the amplifier.

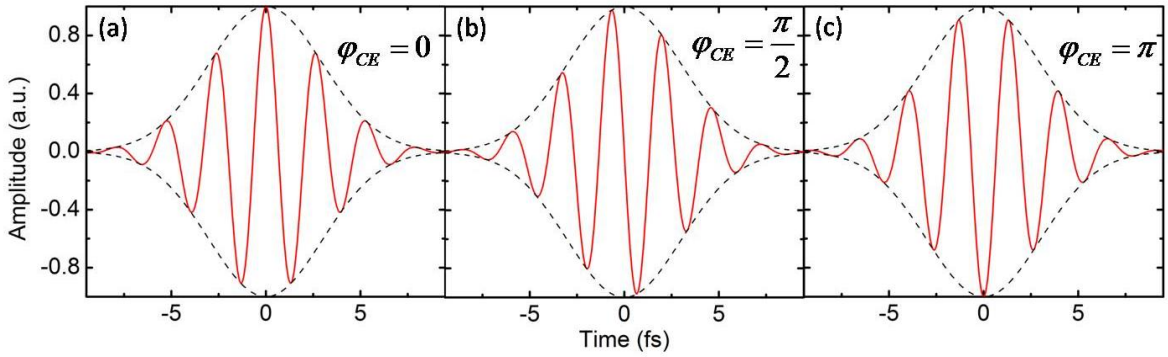

Figure 2-6 5 fs pulses centered at 800 nm with 0, π/2, and π CE phase.

2.3.1 Stabilization of the offset frequency in oscillator

Inside a femtosecond oscillator cavity, a laser pulse circulates through the gain medium, reflects off of the various mirrors, and finally passes through the output coupler. The main dispersive elements in a chirped mirror based Kerr-lens mode-locked (KLM) Ti:Sapphire laser are the laser crystal, the air in the laser path and the mirrors. For a typical Ti:Sapphire oscillator operating at a repetition rate of ~ 80 MHz, the air path is ~2 m and the crystal is ~2 mm thick. Generally when the laser pulse propagates in linear dispersive medium, due to the difference between the phase velocity and group velocity, the CE phase change between consecutive pulses can be express as:

$$\Delta\varphi_{CE}=\Delta\varphi_g-\Delta\varphi_p=\omega_0\left[\frac{L_0}{v_g(\omega_0)}-\frac{L_0}{v_p(\omega_0)}\right]=-2\pi L_0\left.\frac{dn}{d\lambda}\right|_{\omega_0}, \tag{2.2}$$

where $v_g(\omega_0)$ and $v_p(\omega_0)$ are the group velocity and phase velocity at the central frequency ω_0 respectively. L_0 is the effective length of the dispersive medium, and n is the refraction index. For example, $\sim 30\ \mu m$ propagation in fused silica introduces the CE phase shift of π.

Since the phase and group velocities differ inside the oscillator, the CE phase offset will change from one round trip to the next. Because of this, it is technically difficult to lock the CE phase of all the oscillator output pulses to the same value. Instead, in most cases the rate of change of the CE phase is stabilized. The pulses with the same CE phase are then selected by the Pockels cell to seed the amplifier.

The previous discussion described the CE phase offset only in the time domain. However, the CE phase offset can also be understood in the frequency domain. In the temporal domain, a mode-locked laser pulse train is just a steady stream of pulses separated by $T = 1/f_{rep}$, where T is the pulse period and f_{rep} is the laser repetition rate. It is easily shown with Fourier transforms that a shift in time corresponds to a phase shift that is linear with frequency, that is, the phase at angular frequency ω is ωt for a time shift of t. In the spectral domain, successive pulses interfere, but a signal will be observed only at frequencies where they have a phase shift of $2n\pi$ (n is an integer) and add constructively. For a pulse train with time T between pulses, these frequencies are $f_n = n/T = nf_{rep}$. Therefore, the spectrum consists of a comb of frequencies spaced by the repetition rate. Furthermore, if the pulse-to-pulse phase shift $\Delta\phi_{CE}$ is included, in order to still have constructive interference ($f_n T + \Delta\phi_{CE} = 2n\pi$), f_n is given as

$$f_n = f_0 + nf_{rep}, \tag{2.3}$$

where $f_0 = f_{rep}\,\Delta\phi_{CE}/2\pi$ is defined as the carrier-envelope offset frequency.

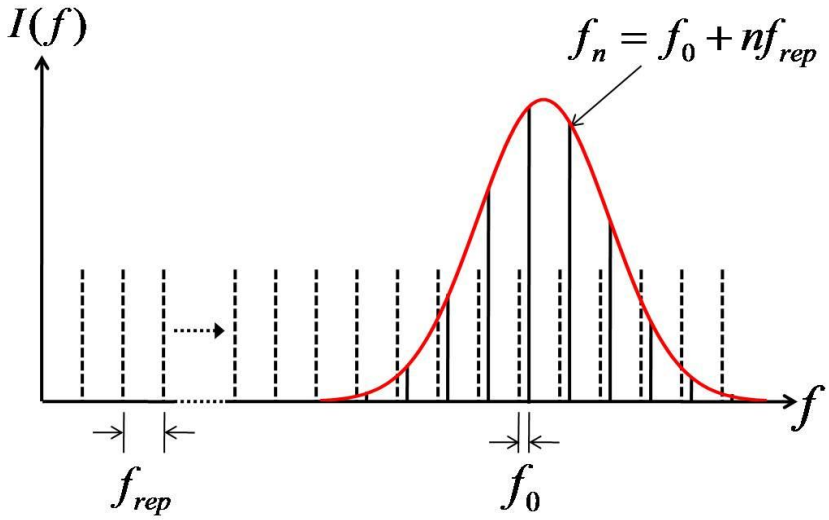

Figure 2-7 Frequency comb of femtosecond oscillator.

The situation is depicted in Fig. 2-7, where the dashed lines represent the equally spaced comb lines and the solid lines underneath the laser spectrum represent the dispersion shifted comb lines. Therefore, the presence of dispersion in a laser cavity results in an offset frequency in the frequency domain that has a simple relationship to the CE phase.

2.3.1.1 CE phase stabilization of KLS oscillator

CE phase stabilization technology has come very far since the first attempt at measuring the CE phase shift between successive pulses from a Ti:Sapphire oscillator using a second-order cross-correlator [42]. Nowadays, CE phase stabilized oscillators are commercially available [43]. Most of the current methods used to stabilize the CE phase were first proposed by Keller's group is 1999 [44], where different nonlinear processes and the respective spectral bandwidth requirements were discussed. Two main methods are the *f*-to-2*f* (SHG) self-referencing method and the *f*-to-zero (DFG) self-referencing method. In the *f*-to-2*f* self-referencing method the frequency doubling of the low comb orders beat with the comb orders in the high frequency spectrum to produce f_0 [45]. Such an octave-span broadband spectrum can be generated either by focusing the beam into a microstructure fiber [46] or directly from the Ti:Sapphire crystal inside the oscillator through self phase modulation [47]. While in *f*-to-zero method [48], the long wavelength signals from DFG are beat with the low comb orders to produce f_0.

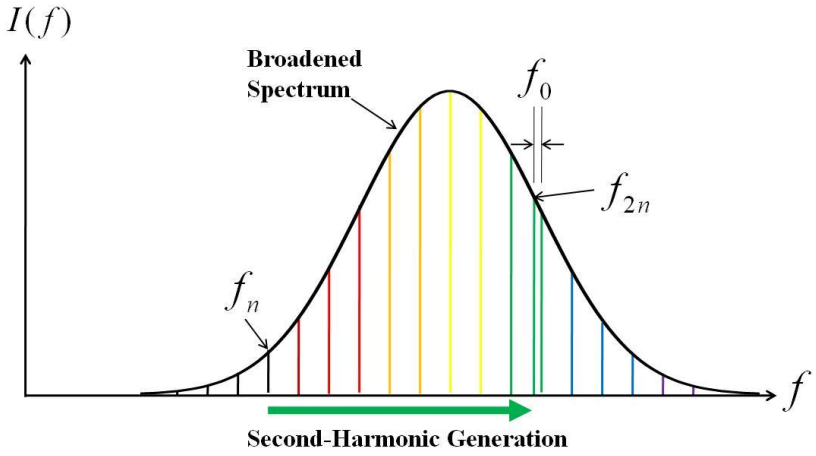

Figure 2-8 Principle of the *f*-to-2*f* self-referencing method.

Fig. 2-8 shows the principle of the *f-to-*2*f* self-referencing method. The original laser spectrum is broadened over an octave in frequency. Then, the low frequency components are frequency doubled and interfered with the high comb orders. Mathematically, the heterodyne beat resulting from the aforementioned process can be represented as:

$$f_0 = 2f_n - f_{2n} = 2(nf_{rep} + f_0) - (2nf_{rep} + f_0) = f_0. \tag{2.4}$$

Thus, the difference between the *f* and 2*f* comb orders is the offset frequency. The next step in the process of locking the CE phase is to track the offset frequency and lock it to an

integer fraction of the laser repetition rate using a servo loop [45] by modulating the pump power with an acousto-optic modulator (AOM). Modulating the pump power changes the nonlinearity in the crystal, which also changes the refractive index and thus the group and phase velocities.

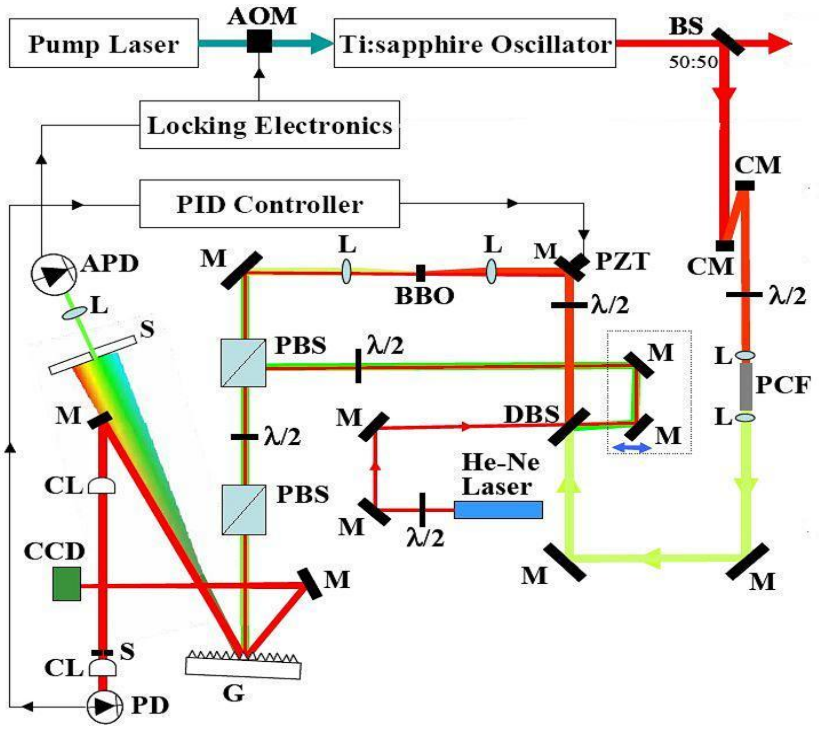

Figure 2-9 Layout of KLS *f*-to-2*f* interferomter for locking the oscillator offset frequency f_0. AOM: acousto-optic modulator, L: Lens, PD: photodiode, APD: avalanche photodiode, G: grating, M: mirror, CM: chirped mirror, S: slit, BS: beam-splitter, PBS: polarizing beam-splitter, CM: chirped mirror, CL: cylindrical Lens, DBS: dichroic beam splitter, PCF: photonics crystal fiber, NDF: neutral density filter. Figure adapted from Ref [49].

In our lab, the KLS oscillator CE phase is stabilized by the *f*-to-2*f* self-referencing method as shown in Fig. 2-9 [49]. The Ti:Sapphire oscillator had a spectral FWHM of 100 nm centered at 790 nm. Half of the output power from the oscillator (200 mW) was focused into a photonic crystal fiber (Menlo Systems). The spectrum of the white light emerging from the fiber extended from 500 nm to ~1130 nm. In the home-built Mach-Zehnder *f*-to-2*f* interferometer, the infrared light was frequency doubled by a Type I BBO crystal. The second harmonic beam interfered with the 532 nm component from the short wavelength arm. The Mach-Zehnder interferometer was stabilized by a He-Ne laser [49]. The beat signal near the offset frequency was filtered from the avalanche photodiode output in the locking electronics (Menlo Systems

XPS 800). The offset frequency was compared to $f_{rep}/4$, the quarter-repetition rate value, yielding a phase error signal that was used to control AOM modulator placed in the beam of the oscillator pump laser. The offset frequency was stabilized by varying the pump power using the AOM.

2.3.1.2 Long term CE phase stabilization of MARS oscillator

The CE phase of the MARS laser oscillator is stabilized by the *f-to*-zero self-referencing method as shown in Fig. 2-10 [48]. The Ti:Sapphire oscillator had a spectral FWHM of 200 nm centered at 750 nm. The carrier-envelope offset frequency f_0 was obtained by detecting the beat signal of difference-frequency generation (DFG) when the output laser beam from output coupler was focused into a highly nonlinear periodically poled lithium niobate (PPLN) crystal. Similarly to the KLS, the offset frequency was compared to $f_{rep}/4$ and locked by modulating the pump power with the AOM.

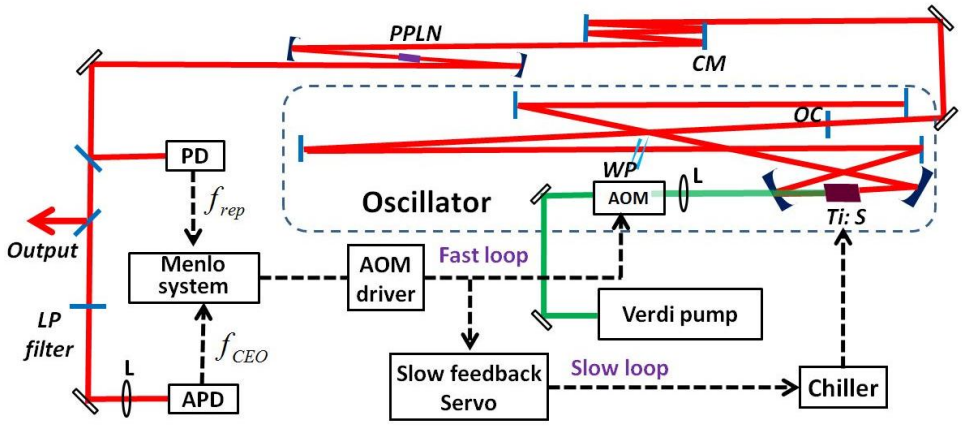

Figure 2-10 MARS laser octave-spanning oscillator layout and double feedback loop. AOM: acousto-optic modulator, L: pump lens, OC: broadband output-coupler on a fused-silica wedge, WP: wedge pair, PD: photodiode, APD: avalanche photodiode, LP filter: low pass filter, CM: chirped mirror. Figure adapted from Ref [52].

There are several advantages for this DFG type CE phase stabilized oscillator. First, a collinear method is used for detecting the beat signal. Thus, temporal jitter noise introduced in interferometric configuration is totally eliminated [49]. Second, there is no strong self phase modulation inside the Ti:Sapphire crystal, which reduces the chance of crystal damage and makes the oscillator easy to align. All the nonlinear processes, such as DFG and self phase

modulation, happen in the PPLN crystal, which is outside the oscillator cavity. Third, since the long wavelength portion (1200 nm) of the output pulse was used to lock the CE phase, the majority of the output power can be used to seed the amplifier. Such high power seeding is important for reducing the ASE and number of round trips in the regenerative amplifier.

Given the particular environment in our Kansas Light Source laboratory, the beat signal f_0 was found to drift within a range of about 8MHz in one day under the free running mode. When the driving voltage of the AOM was scanned across its usable range, it was found that the f_0 can only be controlled over a range of 6MHz, which is not sufficient to compensate the daily slow drift of f_0. This limited the typical oscillator CE phase locking time to about 4 hours when AOM alone was used. Long term CE phase stability is very important for current low count rate attosecond experiments and ion beam laser interaction experiments. To achieve CE phase stabilization for more than one day, an additional stabilization mechanism is necessary to increase the overall control range.

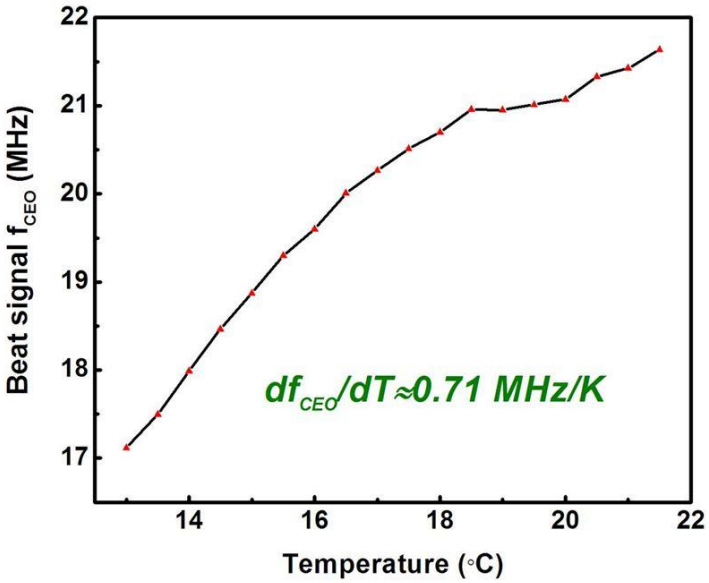

Figure 2-11 The temperature dependence of f_{CEO} (f_0). Figure adapted from Ref [52].

There are several ways to compensate the slow f_0 drift, such as adjusting the insertion of an intracavity prism [50] or a wedge [51]. However, the mode locking of a near-octave-spanning oscillator like the one we used can be disturbed by the mechanical vibration caused by moving these optical components. Instead we chose to use temperature control of the Ti:Sapphire crystal as a slow feedback, which does not introduce any mechanical motion [52]. When the temperature

of the oscillator chiller was scanned from 13° C to 21° C, as shown in Fig. 2-11, the unlocked beat signal f_0 changed nearly linearly and covered a range of 4.52MHz. Adding the temperature control to the AOM control, the whole control range is comparable to the daily drift range of the f_0.

The temperature dependence of f_0 can be understood by examining the effects of temperature on the material dispersion. According to the Eq. (2.2), the offset frequency f_0 can be expressed as:

$$f_0 = f_{rep} L_0 \left. \frac{dn}{d\lambda} \right|_{\omega_0}, \tag{2.5}$$

Since the refraction index is not only a function of optical wavelength λ, but also a function of temperature T, the change of f_0 resulting from temperature control can be expressed as:

$$\begin{aligned} \left. \frac{df_0}{dT} \right|_{\omega_0} &= f_{rep} \frac{\omega_0^2 L}{2\pi c} \frac{d^2 n(\omega,T)}{d\omega dT} + \frac{df_{rep}}{dT} \frac{\omega_0^2 L}{2\pi c} \frac{dn(\omega,T)}{d\omega} \\ &= f_{rep} \frac{\omega_0^2 L}{2\pi c} \frac{d^2 n(\omega,T)}{d\omega dT} + \frac{dn(\omega,T)}{dT} \frac{\omega_0^2 L^2}{\pi c^2} \frac{dn(\omega,T)}{d\omega} \end{aligned}, \tag{2.6}$$

Using the Sellmeier equation for sapphire in Ref. [53], we found the change rate of $df_0/dT = 0.86 MHz/K$, which is close to the measured value of $0.71\, MHz/K$ shown in Fig. 2-11.

To examine whether the temperature change disturbs the mode locking, the oscillator output spectrum and average power were measured with a temperature scan step of 1° C. The oscillator output spectrum and average power were found to remain the same within a temperature range from 12° C to 22° C. When the temperature range was further increased or decreased, a CW peak started to appear in the oscillator output spectrum. To maintain optimized oscillator operation, the temperature control range was set from 13° C to 21° C.

By taking advantage of the temperature dependence of f_0, a double feedback loop was applied for long term stabilization of the CE Phase. The AOM feedback loop is the fast one whereas the temperature control served as the slow loop. Since it took f_0 several minutes to respond to the temperature change, only a binary control, rather than the proportional-integral-derivative control, was necessary to assist the AOM and control the slow CE phase drift. As is

shown in Fig. 2-10, the control signal from the locking electronics (Menlo systems GmbH) to the AOM was measured by a data acquisition card every ten seconds.

The function of the temperature control was to confine the AOM locking point to a narrow range (+/- 10% of the full control range) around the middle of the full control range. When the feedback signal was detected above the upper limit of the AOM locking point range, the chiller's temperature was increased in steps of 0.1° C to compensate the slow drift of the f_0 until the AOM driving voltage returned to within the range. Similarly, the chiller temperature was decreased when the feedback signal was detected below the lower limit of the control point range. The delay time between each step of the temperature change was set to 300 s, which guaranteed that the oscillator reached thermal equilibrium gradually. We chose 0.1° C as the step size because it was the minimum step that the chiller could control, and a small step size minimized the perturbation on the mode locking of the oscillator.

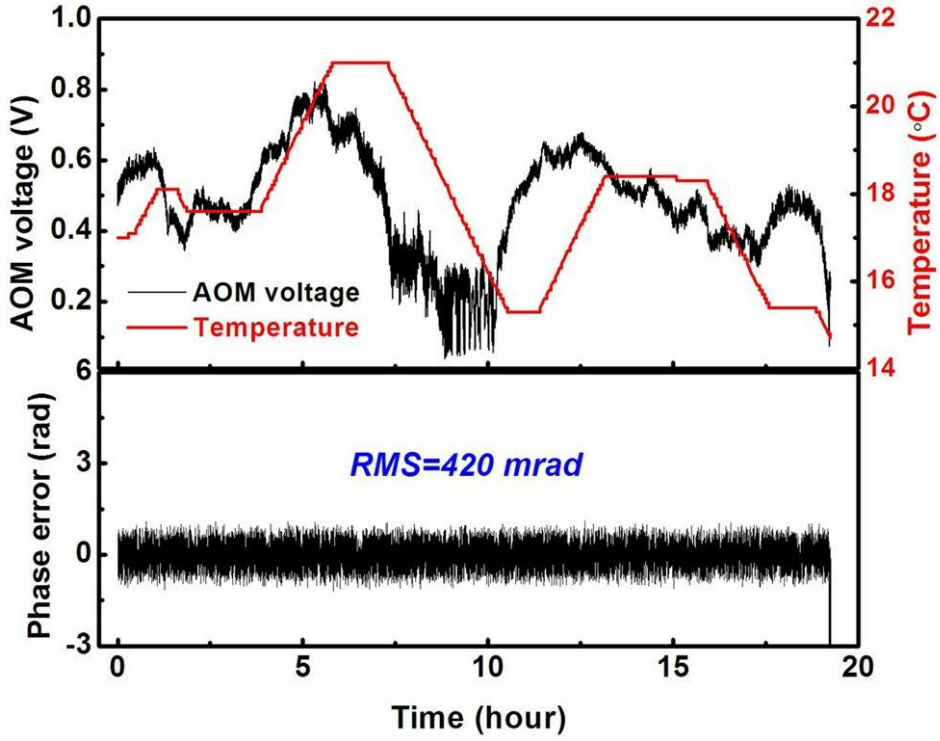

Figure 2-12 (a) 20 h CE phase stabilization achieved by employing the double feedback loop; the black curve shows the AOM driving voltage output; the red curve shows the temperature of the chiller; (b) Phase error during the process of CE phase stabilization. The RMS of the CE phase error is 420 mrad. Figure adapted from Ref [52].

As shown in Fig. 2-12 the wide dynamic range of the double feedback control allowed the long term CE phase stabilization of almost 20 hours. Furthermore, we tested the robustness of this double feedback loop, and found that the CE phase can be stabilized for more than 12 hours on daily basis. 12 hours of CE phase stabilization is three times longer than the typical CE phase stabilization time of ~4 hours under the same conditions but without temperature control, and was sufficient for the data acquisition of current attosecond streaking experiments. In Fig. 2-12(a), when the temperature control reached the preset limit after 20 hours of operation and failed to assist the CE phase stabilization by AOM, the CE phase locking was finally broken. Fig. 2-12(b) shows the in-loop_phase error during the process of CE phase stabilization, and the RMS of the CE phase error is 420 mrad. We also measured the power spectral density (PSD) of the beat signal using a RF spectrum analyzer in the range of 102 kHz to 0.9765 mHz. The integrated phase error was 370 mrad over a 1024 s observation time, as shown in Fig. 2-13.

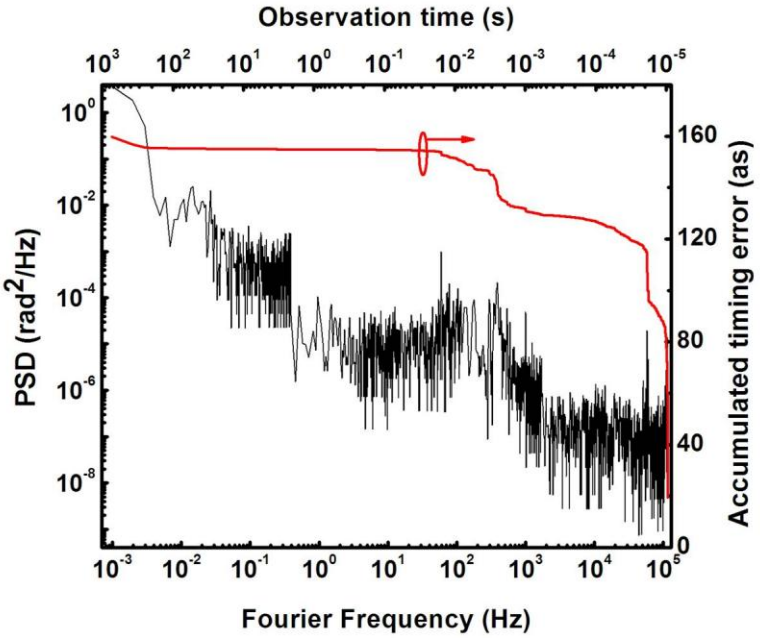

Figure 2-13 Phase-noise power spectral density (PSD) and integrated CE-Phase error calculated from $\Delta\varphi_{RMS}=\left[2\int_{-\infty}^{(-1/\tau_{obs})}S_{\varphi}(\nu)d\nu\right]^{1/2}$**.** $S_{\varphi}(\nu)$**: power spectral density;** $\Delta\varphi_{RMS}$**: root mean square (RMS) fluctuations in the carrier-envelope phase;** τ_{obs}**: observation time. Figure adapted from Ref [52].**

2.3.2 CE phase stabilization of amplified pulses

After the CE phase drifting rate was stabilized in the oscillator, the pulses with the same CE phase were selected by the Pockels cell for amplification. To obtain high energy CE phase stable pulses, any drift introduced during the amplification process must be corrected. The Fourier-transform spectral interferometery (FTSI) measurement technique was used, whereby the amplified pulses were spectrally broadened over an octave in a nonlinear process, typically sapphire crystal, and the second harmonic of the long wavelength components was overlapped and interfere with the short wavelength part of the fundamental by being projected on a common polarization as shown in Fig. 2-14 [54]. The interference pattern was recorded by a spectrometer, and the FTSI method was used to extract the CE phase from the fringes.

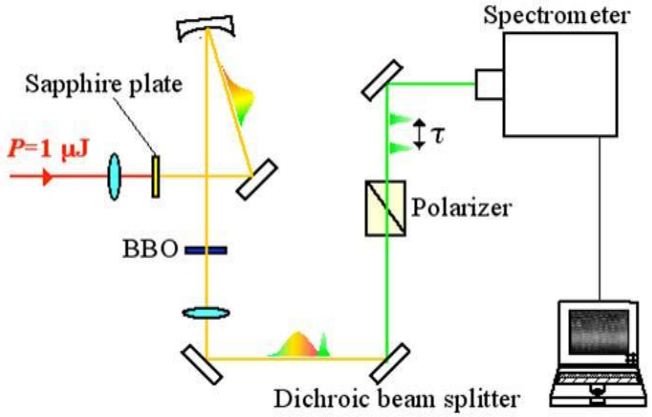

Figure 2-14 *f*-to-2*f* interferometer for measuring and stabilizing the CE phase of the amplified pulse.

It was determined that the CPA process only caused a small, slow drift of the CE phase, which could be pre-compensated using the oscillator CE phase locking servo [41]. However, the early CE phase stable amplifiers used glass blocks in the stretchers and prisms in the compressors. These amplifiers could not reach multi-mJ pulse energy due to the low damage threshold and nonlinear effects of the material in the stretchers and compressors. Therefore, grating-based CPAs were desired as the gratings could handle the higher laser energies. In order to stabilize the CE phase grating-based CPAs, various methods have been used to reduce the vibrational noise, such as floating the table, improving the stability of the optical mounts in the stretcher and compressor, moving the pump laser further away from the amplifier, and padding the laser cover with sound absorption materials. After those improvements, it was soon shown that the grating separation could be manipulated to stabilize the CE phase of amplified laser

pulses for both multi-pass and regenerative amplifier [55-58]. The scheme for phase control by using the grating separation is illustrated in Fig. 2-15.

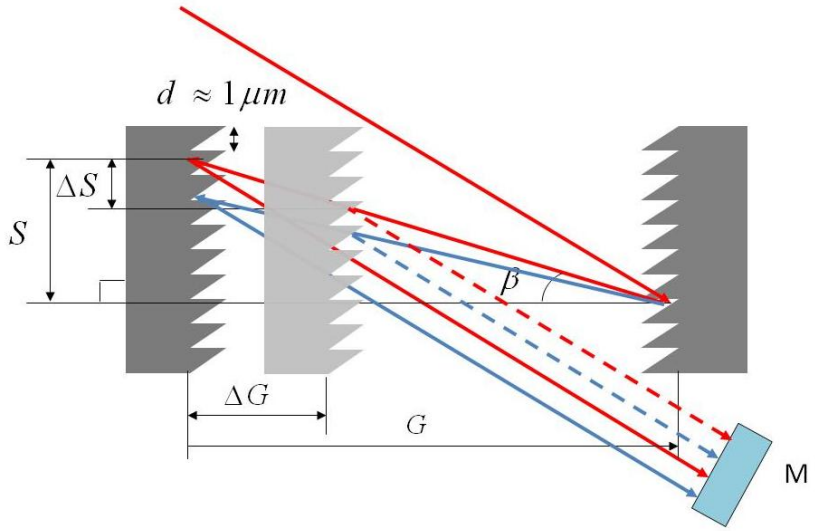

Figure 2-15 CE phase control by shifting the grating separation. Figure adapted from Ref [59].

Using the method of Ref. [55], it was shown that the CE phase shift was given by:

$$\Delta\varphi_{CE} \approx 4\pi(\frac{\Delta G}{d})\tan\beta\,, \tag{2.7}$$

where β is the diffraction angle, ΔG is the small variation of grating separation and $1/d$ is the groove density. For a grating with ~1000 *l*/mm, it was estimated that less than 1 μm of grating movement would cause the CE phase to change by 2π.

As shown in Fig. 2-16, 5% of the final output power from the MARS laser was sent to the *f*-to-2*f* interferometer for detecting the CE phase, and the feedback signal was used to control the grating separation of the compressor with a PZT. The RMS error of the locked CE phase was measured to be 90 mrads over a period of 4.5 h with a 50ms spectrometer integration time as shown in Fig. 2-17.

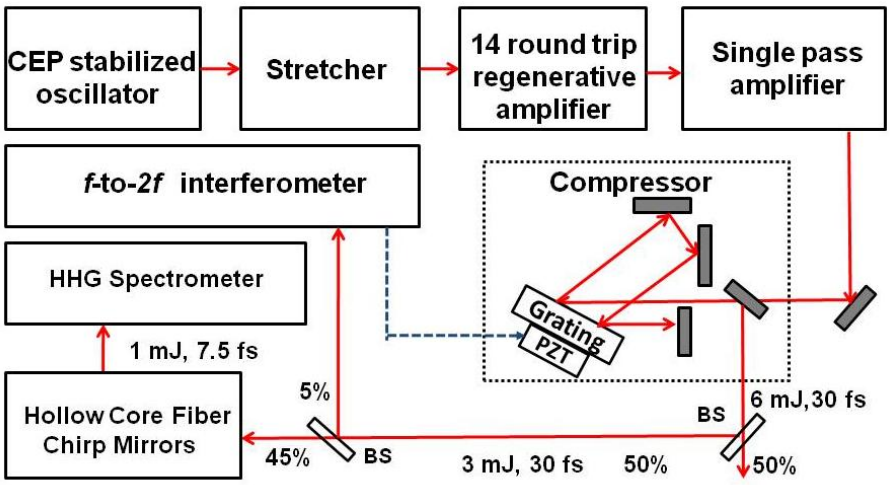

Figure 2-16 Layout of the MARS laser system and CE phase stabilization setup. BS: beam splitter. Figure adapted from Ref [58].

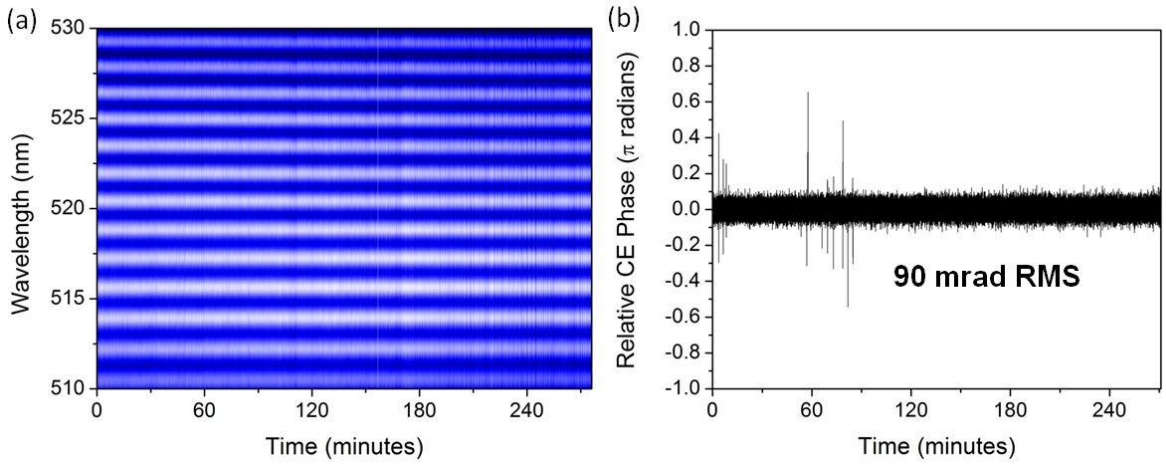

Figure 2-17 Long-term CE phase stabilization: (a) *f* -to-2*f* interference fringes, (b) retrieved CE phase from the fringes, which has a 90 mrad rms averaged over 50 laser shots. Figure adapted from Ref [58].

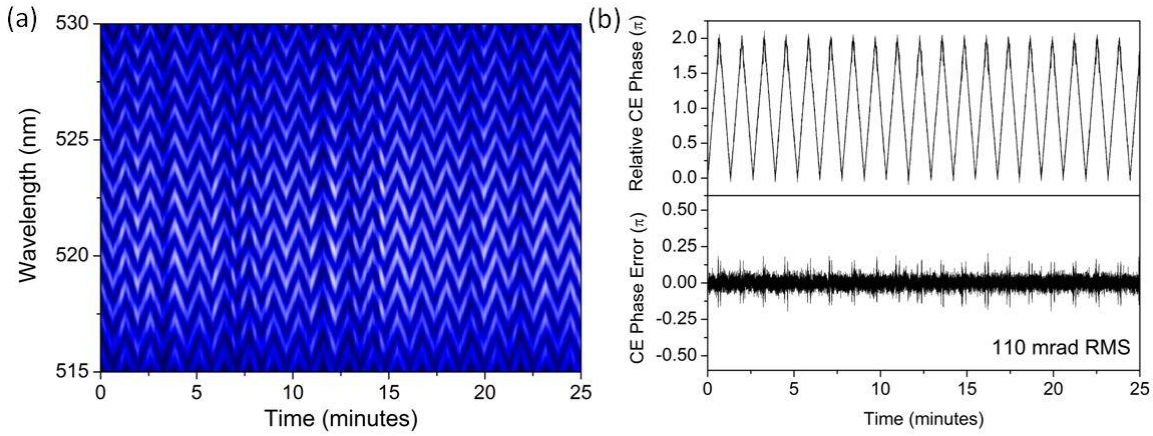

Figure 2-18 Periodic CE phase sweep from $-\pi$ to π: (a) *f*-to-2*f* interferometer fringes, (b) scanning phase value retrieved from the fringes, (c) CE phase error of the retrieved phase relative to the preset scanning phase. The periodic increases in error are due to the PZT response at the turning points of the control voltage. Figure adapted from Ref [58].

To control the CE phase in the experiment, the grating separation of the compressor was stabilized at preset values. As shown in Fig. 2-18, the CE phase was swept from $-\pi$ to π for many cycles that can be used to observe the CE phase effects in high harmonic and attosecond pulse generation experiments [59]. Some regions in Figs. 2-17(a) and 2-18(a) show transient reductions of the fringe visibility, which are likely due to acoustic noise and vibration in the laboratory that could not be avoided over such a long locking period. However, such small disturbances did not affect the quality of the CE phase control.

2.4. Power locking of multi-pass CPA laser system

When the high power few cycle pulses interact with atoms, either in the multi-photon or tunneling regime, the physical outcomes are related with the laser peak intensity in a highly nonlinear fashion. Slow variation of laser power may show up as a fake periodicity in pump-probe experiment by coincidence, and fast fluctuation of the energy between pulses may add statistical error and smear out the real physical information. Therefore, it is important to lock the power of CPA laser system.

Of particular interest, with the advent of few-cycle pulse generation is the effect of power stability on carrier-envelope (CE) phase stabilization [37, 60]. When the *f* -to-2*f* interferometer

was used to measure and stabilize the CE phase, the stability of the CE phase relies on the accuracy of the CE phase measurement, which is sensitive to laser power fluctuations [61]. In the *f* -to-2*f* interferometer, the amplified laser pulses are focused into a sapphire plate to form a single filament, which broadens the pulse spectrum to cover an octave. The CE phase of the laser, φ_{CE}, affects the spectral interference between the component in the pulse with wavelength centered around 500 nm and the frequency doubled component originally centered at 1000 nm of the white light emitted by the filament. The total spectral phase retrieved from the *f*-to-2*f* interferogram can be expressed as

$$\Phi(\omega) = \varphi_{WL}(\omega) - \varphi_{SHG}(\omega) + \omega\tau_0 + (\varphi_{CE} + \delta\varphi_{CE}), \tag{2.8}$$

where $\varphi_{WL}(\omega)$ and $\varphi_{SHG}(\omega)$ are the spectral phase of the fundamental pulse and the frequency doubled pulse, respectively, τ_0 is the time delay between these two components, and $\delta\varphi_{CE}$ is the CE phase change due to self-steepening [62]. In fact, it is the total phase $\Phi(\omega)$ that is obtained from *f*-to-2*f* measurement. All terms in the total phase $\Phi(\omega)$ other than φ_{CE} are influenced by laser intensity fluctuations inside the interferometer [61, 63]. Therefore, it is clear that good laser power stability is required for stabilizing the CE phase.

Under well-controlled environmental conditions (temperature 20° C ±5° C and relative humidity 50±5%), the laser energy fluctuation of typical diode pumped kilohertz femtosecond laser systems is 1.5% RMS [64]. The long term energy drift is also close to this value. Our amplifier is pumped by two Nd:YLF lasers that are diode pumped (Evolution 30 from Coherent Inc). The power fluctuation of this kind of laser is also on the order of 1%. Even when the amplifier is operated near the saturation regime, the output power stability cannot be better than the pump laser power stability. Improving the power stability of the pump laser using a feedback technique or other method may improve the amplifier output stability. On a time scale of minutes to hours, the thermal drift of the seed beam and pump pointing may affect their overlap in the gain medium. This effect can be reduced by improving the stability of the temperature and humidity of the air in the laser room. Previously, a stabilization scheme making use of a photoconductive switch to drive a Pockels cell discharge was introduced [65]. Although the energy fluctuation was suppressed from 7% to 0.64%, 50% of the total energy was lost during the stabilization process. Moreover, since the added Pockels cell was located after the amplifier, the high power pulses could cause nonlinear effects or even damage the device. For regenerative

amplifiers, the laser energy can be stabilized by controlling the gain saturation conditions [66]. However, the pulse duration of the laser systems that demonstrated this technique was 110 fs, which is difficult to use for generating few-cycle pulses. We demonstrate a method to improve the laser power stability of multi-pass amplifiers by using the Pockels cell located between the oscillator and the CPA system [67]. It is easier to produce shorter pulses from multi-pass amplifiers because the dispersion and gain narrowing effect are much less than in regenerative amplifiers.

The new power locking scheme was tested with the KLS laser system as shown in Fig. 2-19. The laser pulses from the oscillator, with a 77 MHz repetition rate were selected by the Pockels cell to be stretched, amplified and compressed. These laser pulses were amplified in a single stage multi-pass amplifier. The first seven passes had high gain, but low efficiency. They pre-amplified the pulses from the few nJ regime to a few μJ. The second seven passes had low gain, but high efficiency, and completed the amplification to the mJ level.

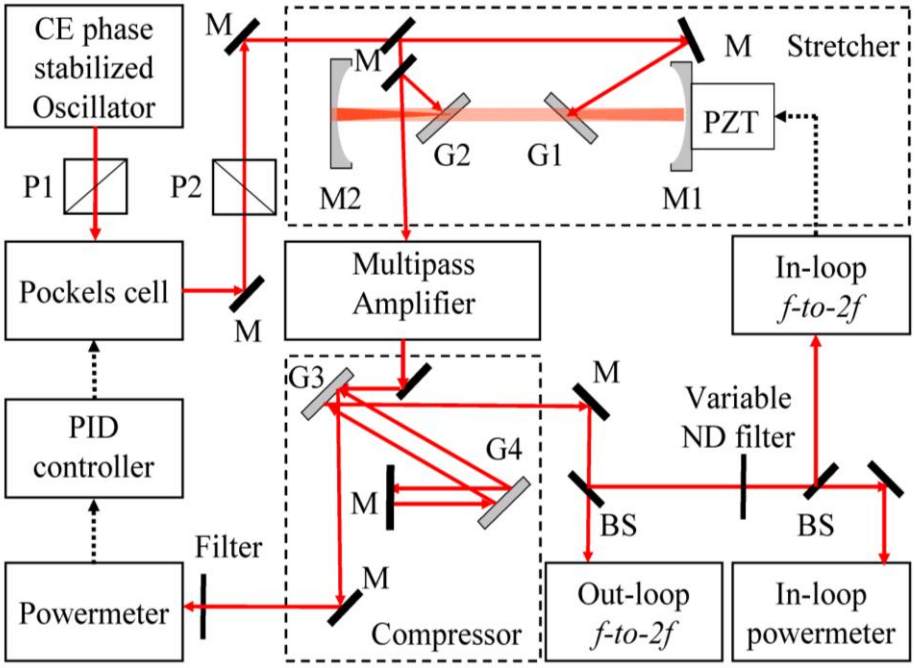

Figure 2-19 The Kansas light source (KLS) laser intensity stabilization system. The in-loop powermeter was put in the path of the zero order diffraction beam and sent the power signal to the PID controller. By using feedback control, the PID varied the voltage applied on the Pockels cell, which in turn changed the polarization of the output from the oscillator and stabilized the laser intensity. *Red arrows* are the laser paths and *dashed arrows* represent electronic circuits. Figure adapted from Ref [67].

The Pockels cell that originally served as a pulse picker was also used as a power modulator in this work. The in-loop powermeter (Newport 1935) with a Si photodiode as the power probe was positioned in the beam path of the zero order diffraction from a compressor grating. The measured average power was proportional to the total output laser power. The analog output of the powermeter was the 1 kHz electronic pulse train from the Si photodiode amplified by the built-in amplifiers of the powermeter. The signal representing the fluctuation of the laser pulse energy was extracted by an external low pass analog filter applied after the powermeter. This signal was then sent to a proportional-integral-derivative (PID) controller (SRS SIM960), which changed the high voltage pulses applied to the Pockels cell to control its transmission. In order to reduce the noise originating from the pump lasers and room light, a 800 nm narrow band pass filter with full width half maximum of 40 nm was placed in front of the powermeter's detector.

The Pockels cell behaves like a voltage controlled wave plate. Without power stabilization, the amplitude of the 1 kHz high voltage pulses applied to the Pockels cells was constant, and usually was set at the half-wave voltage $V_{\lambda/2} \approx 7kV$, which generated a 1 kHz laser pulse train. In order to choose an appropriate working voltage range for the Pockels cell to compensate the laser power fluctuation, the relation between the voltage applied on the Pockels cell and the laser output power after the compressor was measured, as shown in Fig. 2-20. By comparing the transmission curve of the Pockels cell in Fig. 2-20, we concluded that the amplifier worked in the saturation regime. Usually, operating an amplifier close to saturation maximizes the output energy and reduces the susceptibility to fluctuations of the pump and seed pulses. In this scheme, to have enough range for feedback control, the Pockels cell was set to work around 5000 V, which reduced the output power by 10%. Thus, the pulse to amplified spontaneous emission (ASE) energy ratio was changed only by 10%. Pre-pulses and post-pulses due to reflections scaled with the main pulses. The pulse contrast was not affected much by introducing the feedback. At this setting, 10% voltage adjustments could compensate for 3% laser power fluctuation.

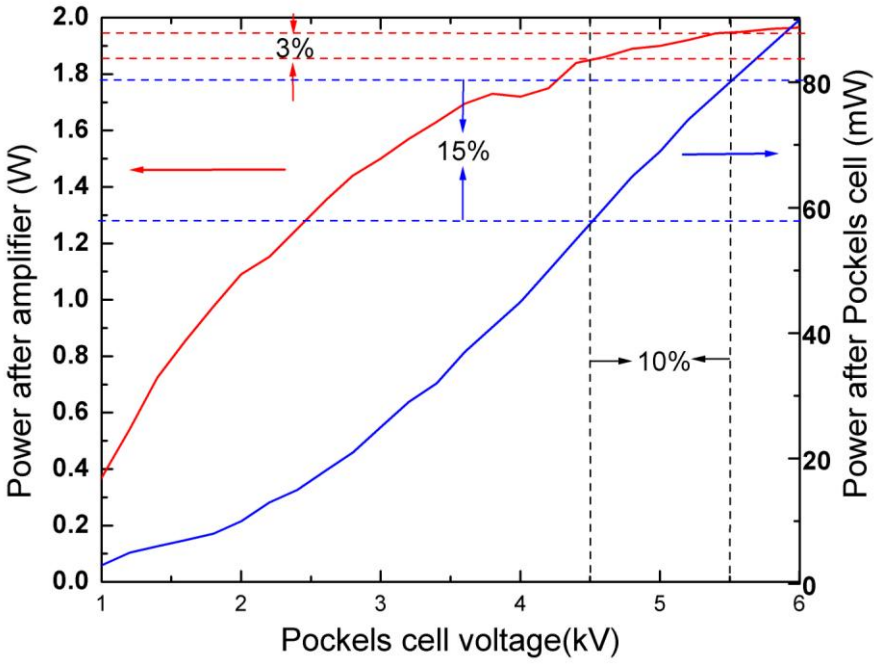

Figure 2-20 The output power vs. Pockels cell voltage. The horizontal axis was the voltage applied on the Pockels cell, and the vertical axis was the power measured after Pockels cell and amplifier respectively. Figure adapted from Ref [67].

Power spectral density measurements showed that the analog signal of the in-loop powermeter contained fast jitter and slow drift without power locking. By optimizing the PID controller parameters and setting 500 Hz as the cutoff frequency of the low pass filter, we suppressed the power noise below 40 Hz as evidenced in Fig. 2-21. In the time domain, the power fluctuation was 1.33% RMS without power locking, like most kilohertz Ti:Sapphire CPA lasers. As shown in Fig. 2-22, the fluctuation of the out-loop power dropped to 0.28% RMS when the feed-back control was turned on, which showed the effectiveness of this scheme. To further prove the success of this method, long term stability data were also measured by using the out-of-loop powermeter as shown in Fig. 2-23, which indicated the RMS power fluctuation 0.3%.

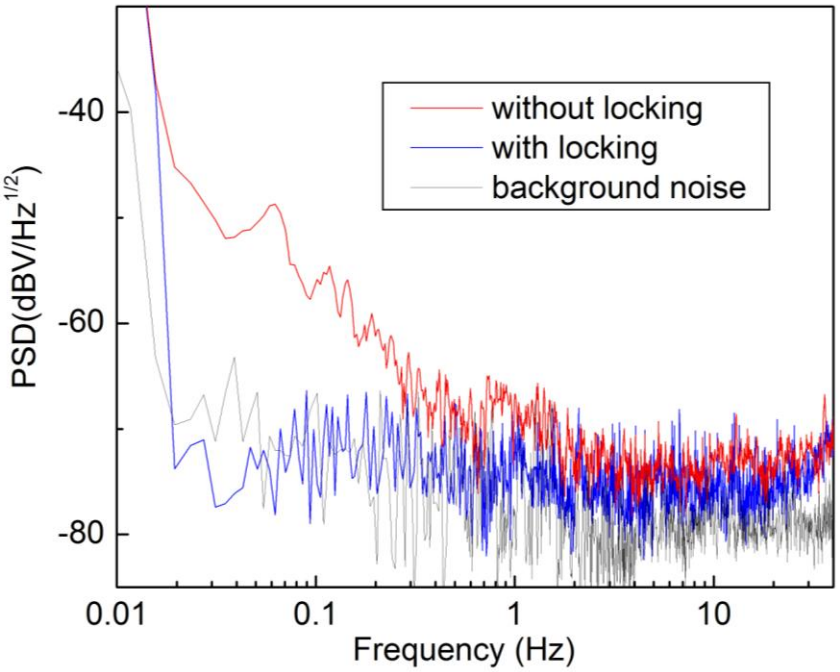

Figure 2-21 The power spectral density of the analog signal from of the powermeter. After locking the power, the low frequency (below 40 Hz) noise was suppressed. Figure adapted from Ref [67].

During the power stabilization process, the voltage on the Pockels cell changed from pulse to pulse. To produce CE phase stabilized pulses, it was important that the voltage change did not introduce significant CE phase variation between pulses. By applying the electric field, the ordinary index of refraction n_0 of the crystal inside the Pockels cell in the *x* and *y* directions was changed to $n_x = n_0 + \Delta n/2$ and $n_y = n_0 - \Delta n/2$ Here, $\Delta n = n_0^3 r_{63} V/L$, $r_{63} \approx 23.3\times10^{-12}\, m/V$ for KD*P crystal, *V* was the voltage applied and *L* was the crystal length. It was assumed that incident laser was polarized 45° from both the x and y directions, which can be described as

$$E_i(t) = \frac{\sqrt{2}}{2} E_{0i}(t)(\hat{i} + \hat{j})e^{i\omega t} \quad , \tag{2.9}$$

where E_{0i} is the amplitude of electric field; $\hat{i}$ and $\hat{j}$ are the unit vectors of x and y direction respectively. At the exit of the crystal, the field was

$$E_e(t)=\frac{\sqrt{2}}{2}[\hat{i}E_{0i}\left(t-\frac{L}{\upsilon_{gx}}\right)e^{i\left(\omega(t-\frac{L}{\upsilon_{px}})\right)}+\hat{j}E_{0i}\left(t-\frac{L}{\upsilon_{gy}}\right)e^{i\left(\omega(t-\frac{L}{\upsilon_{py}})\right)}], \qquad (2.10)$$

where υ_{gx} and υ_{gy} are the group velocities, υ_{px} and υ_{py} are the phase velocities in the x and y directions respectively. To simplify the analysis, it is assumed that $\upsilon_{gx}=\upsilon_{gy}=\upsilon_g$, which can be justified by the fact that the dispersion in the two directions are almost identical. In the moving frame $t'=t-L/\upsilon_g$, the field can be expressed as

$$E_e(t')=\frac{\sqrt{2}}{2}E_{0i}(t')\times[\hat{i}e^{i\frac{\omega}{c}L(n_g-n_x)}+\hat{j}e^{i\frac{\omega}{c}L(n_g-n_y)}]e^{i\omega t'} \quad . \qquad (2.11)$$

The field passing the second polarizer was

$$\begin{aligned}E(t')&=\frac{1}{2}E_{0i}(t')\times[e^{i\frac{\omega}{c}L(n_g-n_x)}+e^{i\frac{\omega}{c}L(n_g-n_y)}]e^{i\omega t'}\\&=\frac{1}{2}E_{0i}(t')\times[e^{-ik_0\Delta nL/2}+e^{ik_0\Delta nL/2}]e^{i\omega t'+k_0(n_g-n_0)}\\&=E_{0i}(t')\cos(k_0\Delta nL/2)e^{i[\omega t'+\Delta\varphi_{CE}]}\end{aligned} \quad . \qquad (2.12)$$

Therefore, when $\upsilon_{gx}=\upsilon_{gy}=\upsilon_g$, then the CE phase change, $\Delta\varphi_{CE}$, was the same in the x and y directions and was independent of the voltage applied on the Pockels cell. When the difference in υ_{gx} and υ_{gy} was taken into account, the CE phase changes in the two directions were:

$$\Delta\varphi_{CE,x}=\omega_c(\frac{1}{v_{gx}}-\frac{1}{v_{px}})L=\Delta\varphi_{CE}-\frac{\partial\Delta n}{2\partial\lambda}2\pi L, \qquad (2.13)$$

$$\Delta\varphi_{CE,y}=\omega_c(\frac{1}{v_{gy}}-\frac{1}{v_{py}})L=\Delta\varphi_{CE}+\frac{\partial\Delta n}{2\partial\lambda}2\pi L, \qquad (2.14)$$

The CE phase difference in the two directions was the following:

$$\begin{aligned}\delta\varphi_{CE} &= \pi L\frac{\partial\Delta n}{\partial\lambda}\\ &= \frac{3}{n_0}(n_0^3 r_{63}\frac{V_{\lambda/2}}{L})\frac{V}{V_{\lambda/2}}(\frac{\partial n_0}{\partial\lambda}2\pi L),\\ &= \frac{3\lambda \mathrm{V}\Delta\varphi_{CE}}{n_0 V_{\lambda/2} L}\end{aligned} \tag{2.15}$$

where $\Delta\varphi_{CE}$ was the CE phase shift without applying the voltage. For KD*P, $\Delta\varphi_{CE}/L = 2\pi/40\mu m$. If $\Delta V/V_{\lambda/2} \le 10\%$, $\Delta\varphi_{CE}$ will change less than 10 mrad, which was much smaller than 150 mrad, the typical RMS fluctuation of the stabilized CE phase.

In order to investigate the effect of power stabilization on the CE phase locking, besides the in-loop *f*-to-2*f* interferometer used to control the grating separation in the stretcher for the slow CE phase drift [56], an out-of-loop *f*-to-2*f* interferometer was used to check the phase stability [60]. The in-loop and out-of-loop CE phase were measured concurrently with and without power locking. As shown in Fig. 2-22, without power locking, the difference of the in-loop and out-of-loop standard deviation was 309 mrad. After locking the power, their difference dropped dramatically to 9 mrad, which proved that the reduction of the power fluctuation could significantly improve the CE phase stability. The correlation between power change and the out-loop CE phase shift can be seen by comparing Figs. 2-22(a) and (e). The result can be understood by using Eq. (2.8). Since the white-light generation and second harmonic generation processes in the two *f*-to-2*f* interferometers were not identical, the CE phase measured by the two interferometers had different power dependencies [61]. Quantitatively, the effect of power fluctuation on the CE phase measurement could be determined by modulating the input power of the in-loop *f*-to-2*f* interferometer and measuring the CE phase from the out-of-loop *f*-to-2*f* interferometer with the power stabilized [60].

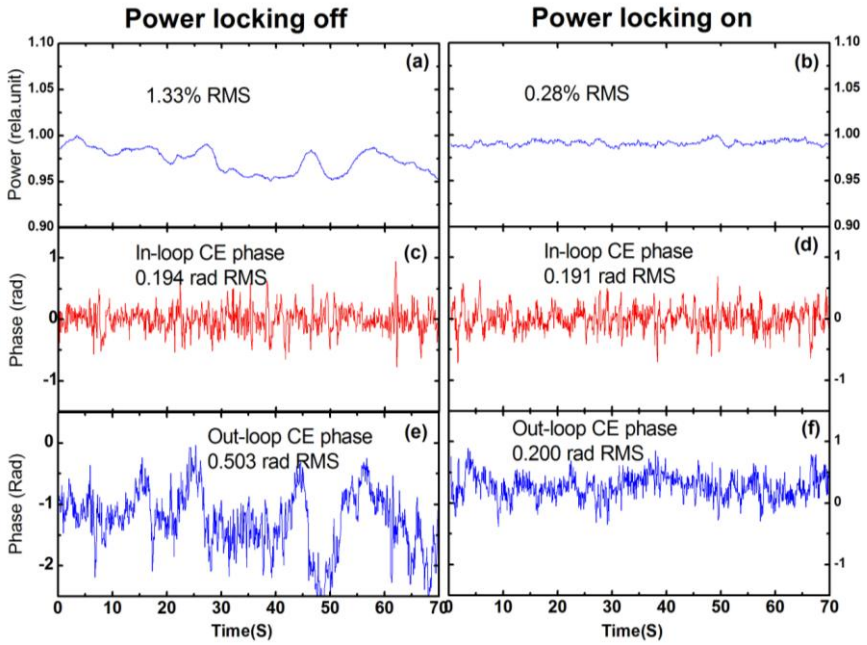

Figure 2-22 The left column and right column were the measurement of laser power and CE phase stability with and without power locking. (a) and (b) show normalized power. After stabilization the power fluctuation had decreased to one fifth of its usual value; (c) and (d) are in-loop CE phase; (e) and (f) are out-loop CE phase. Figure adapted from Ref [67].

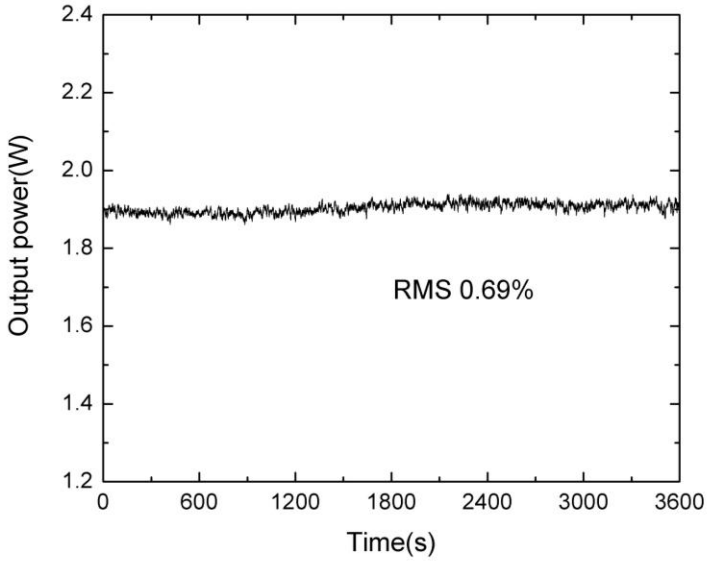

Figure 2-23 The long term stability of the laser output measured by a thermal powermeter. Figure adapted from Ref [67].

In conclusion, it was demonstrated that the laser power fluctuation could be reduced significantly from 1.33% to 0.28% RMS by feedback controlling the voltage applied on the Pockels cell, which reduced the out-of-loop CE phase noise from 500 mrad to 200 mrad RMS. This scheme utilized the Pockels cell that was already in the CPA system, which did not introduce extra optical material dispersion. The power loss was less than 10%, which is much smaller than the previous scheme (50%) [65]. Also the Pockels cell was located before the power amplifier, which introduced a very small nonlinear effect. Since strong laser field-atom interactions are intrinsically nonlinear, even for experiments without CE phase stabilization, the power stabilization demonstrated here is also useful.

3.4 CE phase to power coupling of few cycle pulses

The CE phase of few-cycle high power laser pulses can be determined by measuring the asymmetry of the angular distribution of electrons in ATI [40, 68]. However, it is difficult to apply this technique to multi-cycle pulses. Instead, it is common to lock the CE phase of CPA systems by using *f*-to-2*f* interferometers [54], assuming the phase shift determined from the interferometer fringes is the CE phase shift. Here we follow this tradition. So far, the CE phase stability of CPA systems has been extensively investigated, but very few studies have been conducted to investigate the effects of the hollow-core fiber on the CE phase stability of the compressed pulses.

For CE phase measurement after a hollow-core fiber, the required octave spanning spectrum for the *f*-to-2*f* measurement can be obtained by focusing the output pulses from the hollow-core fiber into a sapphire plate if their bandwidth is narrower than an octave [37]. When the bandwidth of the white-light from the hollow-core fiber covers an octave, it can be used directly to perform *f*-to-2*f* measurements [69]. This approach is more appealing because of the simplicity and the removal of the CE phase noise introduced by the sapphire plate.

Previously, the CE phase error introduced by the nonlinear phase noise in microstructure fiber was studied, and the power dependence of the index of refraction was determined to be the main source of error [70]. In the hollow core fiber, recent experimental studies indicated that the CE phase noise after the fiber could be significantly larger than that of the input pulses [37, 69]. In Ref. 37, when the CE phase was stabilized before a neon-filled hollow-core fiber within 189 mrad RMS, its standard deviation measured by a sapphire plate based *f*-to-2*f* interferometer after

the neon-filled hollow-core fiber was 370 mrad. In another report, when the CE phase was measured to be 490 mrad RMS before the hollow-core fiber, 610 mrad RMS of the CE phase was measured after the fiber using the octave-spanning spectrum of the white-light pulses [69]. The increase of the CE phase noise is likely caused by the laser power fluctuation inside the hollow-core fiber or the sapphire-based interferometers. However, it was not clear which of the two are more susceptible to the power instability. For sapphire-based *f*-to-2*f* interferometers, previous studies showed that 1% energy change can cause 160 mrad of CE phase measurement error [60] and a two step model was proposed to explain the coupling between the energy fluctuation and the CE phase error [71]. Here we study the influence of the laser energy fluctuation on the precision of the *f*-to-2*f* measurements using the octave-spanning white-light from the hollow-core fiber [72].

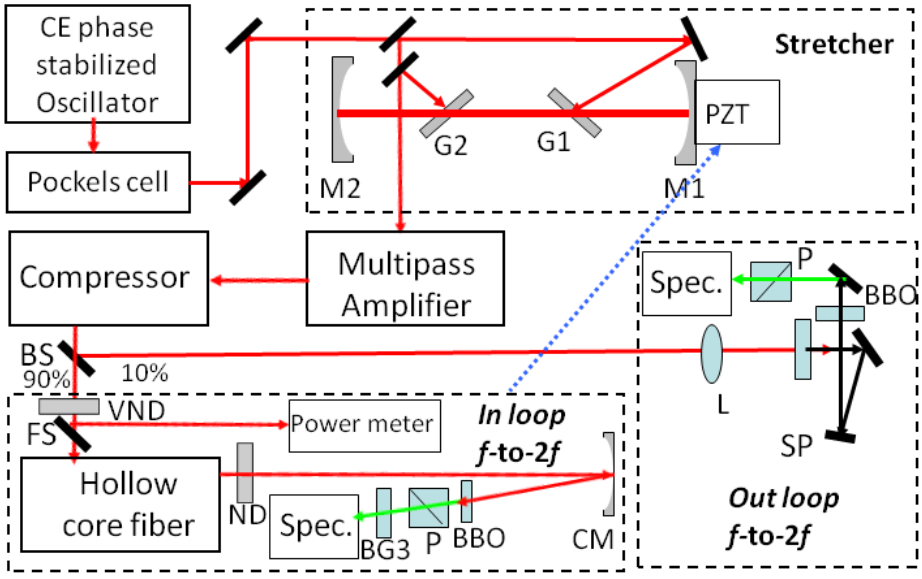

Figure 2-24 Experimental setup for determining the energy to CE phase coupling. VND: variable neutral density filter; L: focusing lens; SP: Sapphire plate; BBO: frequency doubling crystal; P: polarizers; FS: fused silica; Spec.: spectrometer and computer. In stretcher, G1 and G2: gratings; PZT: piezoelectric transducer; M1and M2: mirrors; BS: beam splitter. Figure adapted from Ref [72].

The experiment was carried out with the KLS as shown in Fig. 2-23. The oscillator CE offset frequency f_0 was stabilized. After amplification, more than 2 mJ, 1 kHz, 30 fs pulses with a beam diameter of 1 cm from the laser were focused by a f=1.5 m dielectric mirror and coupled into a 0.9 meter long, 400 μm inner core diameter hollow-core fiber filled with 2 bars of neon

gas. With such high energy seeding pulses, strong self-phase modulation produced white-light pulses with 1.2 mJ energy, whose spectrum covered more than one octave from 400nm to 1000nm as shown in Fig. 2-25. In order to improve the accuracy of CE phase control, the laser power before the hollow-core fiber was stabilized to around 0.5% RMS [67].

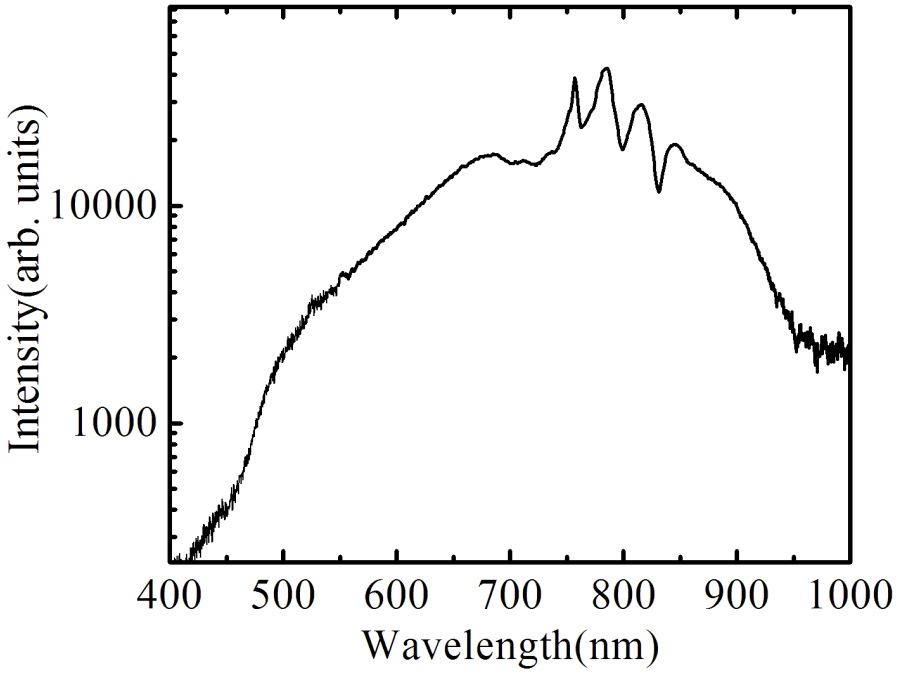

Figure 2-25 The output spectrum of the octave-spanning white-light from the hollow-core fiber with 2 mJ input and 2 bar Ne pressure. Figure adapted from Ref [72].

The effect of the input laser energy stability on the carrier-envelope phase of the pulses from a hollow-core fiber was studied using two *f*-to-2*f* interferometers. The CE phase in the first *f*-to-2*f* interferometer was measured with the octave-spanning white-light spectrum from the hollow-core fiber. The beam from the fiber was collimated by *f*=1.5 m silver mirror and attenuated by a reflective fused silica neutral density (ND) filter. The 1 cm diameter beam was focused into a 100 μm-thick Barium Borate crystal (BBO) with an *f*=50 cm cylindrical mirror for second harmonic generation (SHG). To produce the *f*-to-2*f* interference fringes with the best contrast, the BBO phase matching angle was set to 26 degrees, which corresponds to a maximum Type I SHG efficiency around 900 nm of the fundamental wavelength. A polarizer was used to project the second harmonic and the fundamental field onto the same axis to facilitate interference.

Since the white-light was focused into the BBO without temporal compression by chirped mirrors, the large group delay between the fundamental light centered around 450nm and the second harmonic produced sufficient fringes for extracting the CE phase. A spectrometer (Ocean Optics HR2000+, 380nm-580nm) with a resolution of 0.11 nm was used to record the fringes over a 50 ms exposure time. To avoid the saturation of the spectrometer CCD caused by the strong fundamental light, a BG3 filter was used to block the fundamental wavelength within the above range, but longer than 500nm. The CE phase drift was extracted from the fringes by the standard algorithm of Fourier transform spectral interferometry (FTSI). The second *f*-to-2*f* interferometer was based on a sapphire plate [60].

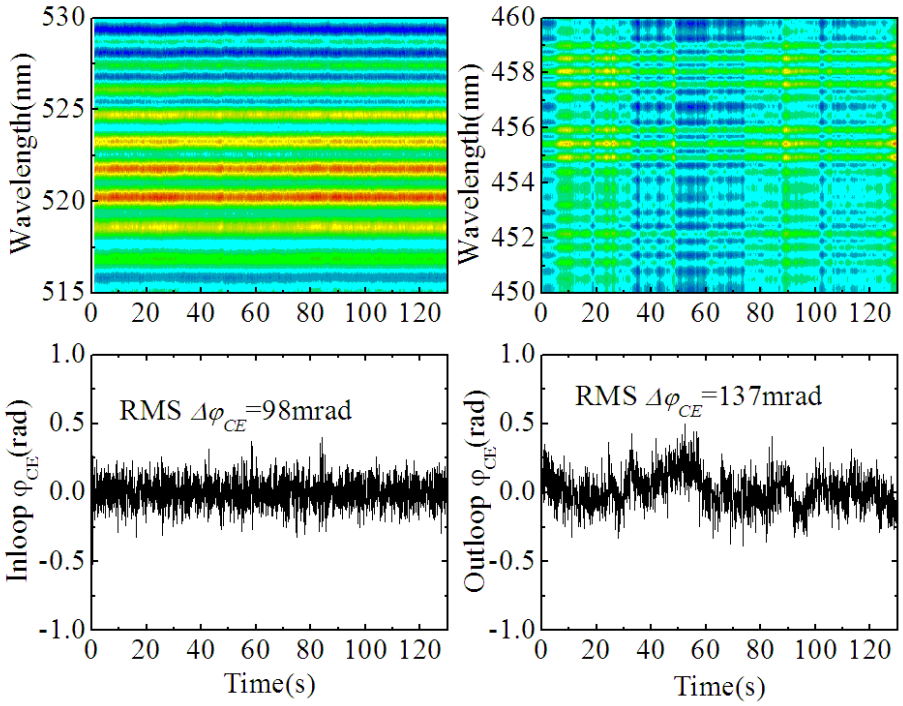

Figure 2-26 In-loop CE phase stabilized by a sapphire plate based *f*-to-2*f* interferometer (left) and out-of-loop CE phase measured by a hollow-core fiber based *f*-to-2*f* interferometer (right). Figure adapted from Ref [72].

First the sapphire plate based *f*-to-2*f* interferometer was used to lock the CE phase before the hollow-core fiber [56], and the hollow-core fiber based *f*-to-2*f* interferometer was used to check the CE phase of the pulses after the fiber. As shown in Fig. 2-26, when the CE phase was locked within an accuracy of 98 mrad before the hollow-core fiber, the CE phase fluctuation after the hollow-core fiber was 137 mrad. Compared with the previous results of 370 mrad after the hollow-core fiber [37], the CE phase stability has been improved by more than a factor of

two. We believe that the main reason is the removal of the sapphire plate in the CE phase measurement after the hollow-core fiber. The power fluctuation after the hollow-core fiber is much larger than that of the input. In this situation, if the sapphire plate was applied after the hollow-core fiber, the white-light generation would increase the error in the CE phase measurement [37].

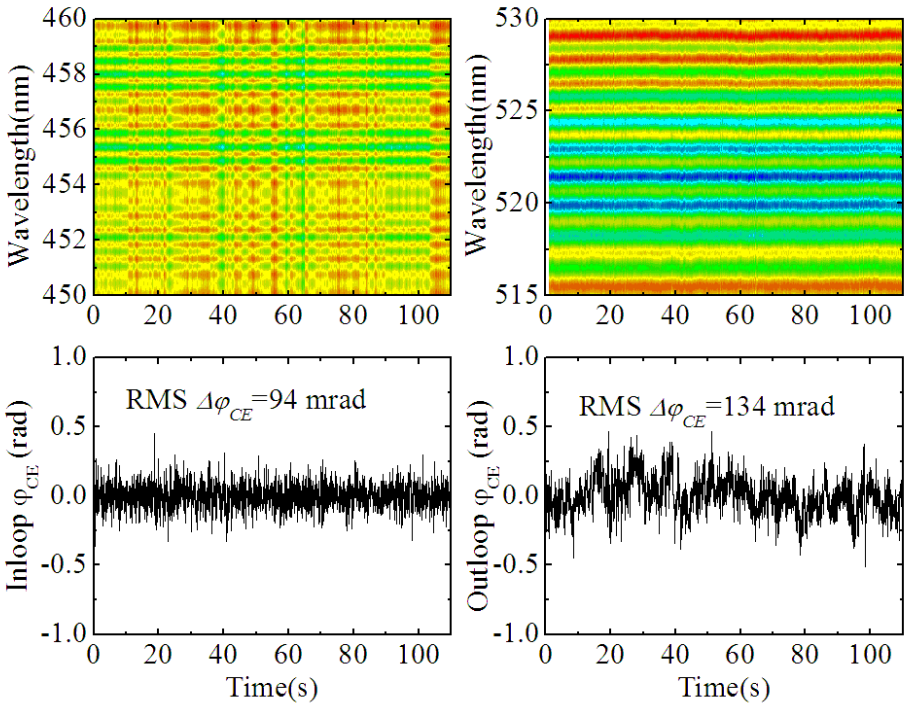

Figure 2-27 In-loop CE phase stabilized by a hollow-core fiber based *f*-to-2*f* interferometer (left) and Out-of-loop CE phase measured by a sapphire plate based *f*-to-2*f* interferometer (right). Figure adapted from Ref [72].

We then locked the CE phase by measuring the phase shift with the white-light from the hollow-core fiber and feedback controlling the grating-based stretcher. As shown in Fig. 2-27, the CE phase was locked within an in-loop accuracy of 94 mrad RMS. At the same time, the out-of-loop sapphire plate based *f*-to-2*f* interferometer measurement showed a CE phase fluctuation of 134 mrad before the fiber. These two experiments indicated that the hollow-core fiber does not introduce significant amounts of CE phase drift when the power of the input pulses is stabilized to 0.5% RMS. They also indicated that the change in grating separation in the CPA stretcher for stabilizing the CE phase did not affect the pulse propagation in the fiber, which was expected because the variation of effective grating separation is less than 1 micrometer [56].

To quantitatively measure the laser energy to CE phase coupling coefficient for the hollow-core fiber based interferometer, a variable reflective fused silica ND filter driven by an electric motor was placed before the focusing mirror of the hollow-core fiber to modulate the input power, as shown in Fig. 2-24. The front surface of the fused silica glass filter is coated with a thin metal film to attenuate the power by reflection. Since the glass does not absorb the 800 nm light, the thermal lensing effect is very small and can be ignored. Previously this method has been used to measure the power to CE phase coupling coefficient for a sapphire plate *f*-to-2*f* interferometer [60]. When the ND filter was driven periodically within the range of 5 degrees, the power was modulated within the range of 10%. 8% of the modulated beam was reflected by a thin fused silica plate to a power meter. In order to keep more than one octave span of the white-light spectrum, the neon pressure inside the hollow core fiber was increased to 2.3 bar to compensate for the power loss caused by the fused silica plate. Under this new pressure of 2.3 bar, we repeated the experiment discussed above to confirm that, regardless of the configuration of the two *f*-to-2*f* interferometers as control loop and measurement loop, the same CE phase stability could be obtained. Finally, the hollow-core fiber *f*-to-2*f* interferometer was used to stabilize the CE phase after the fiber, while the sapphire plate *f*-to-2*f* interferometer was used to measure the out-of-loop CE phase where the laser power was not modulated.

Although the interference fringe intensity was modulated periodically due to the power modulation, the in-loop measurement shows a CE phase fluctuation of 109 mrad in Fig. 2-28(a), which is similar to the case without power modulation. Fig. 2-28(b) shows the anti-correlation between the in-loop power modulations and out-of-loop CE phase measurement. To simplify the analysis, it is assumed that the out-of-loop CE phase drift is only caused by modulation of the in-loop input power. A least-square linear fit in Fig. 2-28(c) shows the 1% power fluctuation introduced a 128 mrad CE phase error. This value is smaller than the 160 mrad for sapphire plate based *f*-to-2*f* interferometers [60], which can be related to the fact that the white-light generation in the hollow-core fiber is produced by the self-phase modulation all the way through the 0.9 m long gas-filled waveguide rather than the strong self-focusing process combined with filamentation in a 2.3 mm sapphire plate [71].

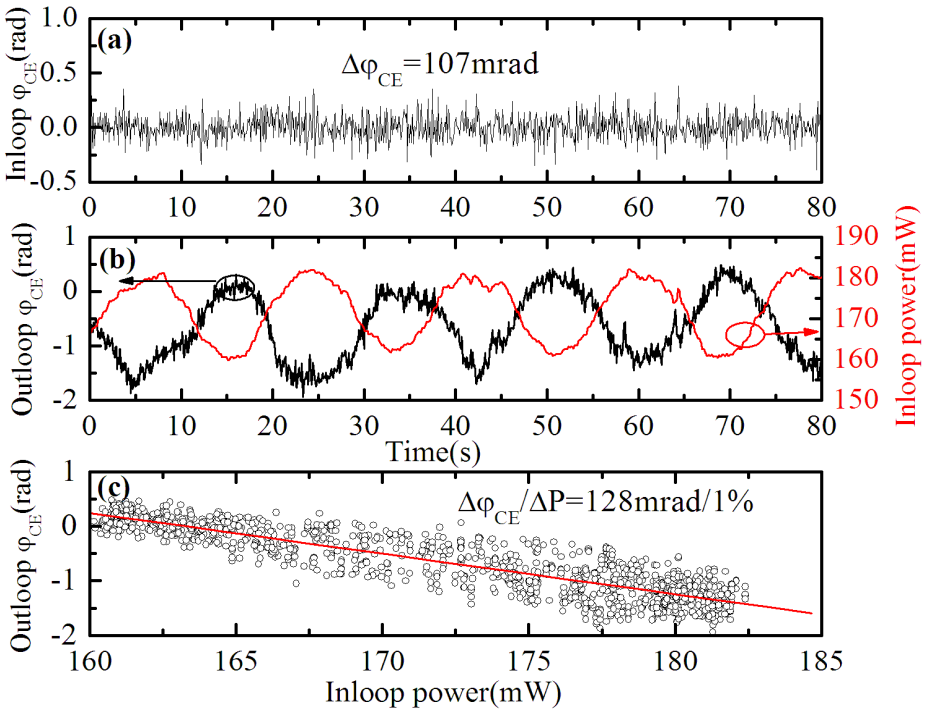

Figure 2-28 (a) In-loop CE phase locked by a hollow-core fiber based *f*-to-2*f* interferometer; (b) Out-of-loop CE phase measured by a sapphire plate based *f*-to-2*f* interferometer and the in-loop power modulation; (c) CE phase change to laser power coupling coefficient by a least-square fitting. Figure adapted from Ref [72].

Due to the dispersion the CE phase changes during the process of propagation, as expressed:

$$\Delta\phi_{CE} = 2\pi L\frac{dn}{d\lambda}, \tag{2.16}$$

where L is the length of the hollow-core fiber and n is the total refractive index. Ignoring the wave guide dispersion, the total refractive index n of the hollow-core fiber can be expressed as:

$$n = n_0 + n_2 I, \tag{2.17}$$

where n_0 is the linear refractive index of the noble gas medium and I is the intensity of the incident wave. Therefore, the total change of CE phase can be expressed as:

$$\Delta\phi_{CE} = 2\pi L(\frac{dn_0}{d\lambda} + \frac{dn_2}{d\lambda} I). \tag{2.18}$$

The nonlinear part can be written as [73]:

$$n_2 = \frac{3}{2n_0^2\varepsilon_0 c}\chi^{(3)}, \tag{2.19}$$

where $\chi^{(3)}$ is the nonlinear susceptibility, ε_0 is the dielectric constant and *c* is the vacuum speed of light.

When the power of the input laser pulse fluctuates, the value of the second term in Eq. (2.18) is influenced and causes the intrinsic CE phase error, which can be expressed:

$$\begin{aligned}\delta\Delta\phi_{CE} &= 2\pi L\frac{dn_2}{d\lambda}\Delta I = 2\pi L\Delta I(-\frac{3\chi^{(3)}}{n_0^3\varepsilon_0 c}\frac{dn_0}{d\lambda}+\frac{3}{2n_0^2\varepsilon_0 c}\frac{d\chi^{(3)}}{d\lambda}) \\ &= 2\pi L\Delta I n_2(-2\frac{dn_0}{n_0 d\lambda}+\frac{d\chi^{(3)}}{\chi^{(3)}d\lambda})\end{aligned} \tag{2.20}$$

For the first term of Eq. (2.20), when the optical frequency ω is much lower than resonance frequency ω_0 of neon gas (21.56 eV), the linear refraction index can be derived from the harmonic oscillator model [74]:

$$n(\omega)=\sqrt{1+\frac{Nq_e^2}{\varepsilon_0 m_e}\left(\frac{1}{\omega_0^2-\omega^2}\right)}. \tag{2.21}$$

Here, q_e and m_e are the charge and mass of the electron, respectively, and *N* is the number density of the ideal gas. For the second term of Eq. (2.20), under the same off-resonant condition, the nonlinear susceptibility can be approximately expressed as [75, 76]:

$$\chi^{(3)}(\omega)\approx\frac{\omega_0-\omega_a}{\omega_0-\omega}\chi^{(3)}(\omega_a), \tag{2.22}$$

where $\chi^{(3)}(\omega_a)$ is the nonlinear susceptibility measured at frequency ω_a. Here we took $\chi^{(3)}(\omega_a)$ for neon gas from Ref. [75], $\chi^{(3)}(1055nm)=6.2\times10^{-28}m^2/V^2$ under 1 atm pressure and at a temperature of 0° C.

Considering the 2 mJ input pulse energy *W*, pulse duration τ of 30 fs, and hollow-core fiber inner core radius *r* of 200 μm, the peak intensity is calculated:

$$I=\frac{W}{\pi r^2\tau}=\frac{2\times10^{-3}J}{\pi\times(200\times10^{-6}m)^2\times30\times10^{-15}s}=5.3\times10^{17}W/m^2. \tag{2.23}$$

When the laser has 1% power fluctuation $\Delta I = I/100 = 5.3\times10^{15}W/m^2$, under the fiber pressure of 2.3 bar and room temperature of 17° C, the intrinsic CE phase error due to intensity fluctuation is calculated from Eq. (2.20) to be $\delta\Delta\phi_{CE}\approx1.2mrad$, which is much smaller than the measured coupling coefficient and can be ignored.

Although the CE phase error due to the fluctuation of nonlinear dispersion is very small in the hollow core fiber, the measured CE phase, which is the phase delay between the blue component centered at $\lambda_1 = 455nm$ and the frequency doubled component originally centered at $\lambda_2 = 910nm$ nm, fluctuates when the input pulse energy changes [60, 71]. To be more specific, the phases of the λ_1 and λ_2 components can be expressed as:

$$\phi_1(L_{pro}) = \phi_{NL}^1 + \phi_L^1(L_{pro}) + \phi_{CE}, \tag{2.24}$$

$$\phi_2(L_{pro}) = \phi_{NL}^2 + \phi_L^2(L_{pro}) + \phi_{CE}. \tag{2.25}$$

Here, ϕ_{NL} is the nonlinear phase shift introduced by the self-phase modulation process and ϕ_L is the linear phase shift introduced by the propagation after self-phase modulation and is a function of the propagation distance L_{pro}. L_{pro} is thus equal to $L - l$, where l is the self phase modulation distance for generating the spectrum with one octave span.

When the 910 *nm* component is frequency doubled in the BBO crystal, its phase becomes:

$$\varphi_2(L_{pro}) = 2\phi_2(L_{pro}) = 2\phi_{NL}^2 + 2\phi_L^2(L_{pro}) + 2\phi_{CE}. \tag{2.26}$$

The measured CE phase is then expressed as:

$$\Phi = \varphi_2(L_{pro}) - \phi_1(L_{pro}) = \left[2\phi_{NL}^2 - \phi_{NL}^1\right] + \left[2\phi_L^2(L_{pro}) - \phi_L^1(L_{pro})\right] + \phi_{CE}. \tag{2.27}$$

When the intensity of the input laser pulse into the hollow-core fiber fluctuates by 1%, the nonlinear phase caused by self phase modulation, given by $\int_0^l 2\pi I/\lambda dz$, also fluctuates. In order to compensate the intensity fluctuation and maintain an octave spanning spectrum, the required self phase modulation distance l also must fluctuate by 1%, which in turn changes the value of the measured CE phase Φ due to the fluctuation of the propagation distance ΔL_{pro}.

Since the octave spanning spectrum is generated at the end of the hollow-core fiber, the self phase modulation distance is close to the total distance of the fiber $l \approx L$. Therefore the fluctuation of the propagation distance is:

$$\Delta L_{pro} = \Delta l = l/100 \approx L/100 = 9mm, \tag{2.28}$$

which gives the CE phase measurement error of:

$$\Delta\Phi = 2\pi\Delta L_{pro}[2\frac{n(\lambda_2)}{\lambda_2} - \frac{n(\lambda_1)}{\lambda_1}] = 2\pi\Delta L[\frac{n(\lambda_2)}{\lambda_1} - \frac{n(\lambda_1)}{\lambda_1}] \approx 120 mrad . \qquad (2.29)$$

In the above discussion if the dispersion of the pulse is also considered, the peak intensity of the pulse drops as it propagates. Therefore, the self phase modulation strength decreases as the pulse becomes longer. To compensate the 1% intensity fluctuation at the entrance of the fiber, the self phase modulation distance *l* changes more than 1% because the pulse duration becomes longer during the propagation process. Considering this factor along with the previous discussion, the prediction our model matches very closely to the measured value of 128 mrad per 1% power fluctuation.

In conclusion, we found that the hollow-core fiber based *f*-to-2*f* interferometer provided a higher accuracy of CE phase measurement than a sapphire plate based interferometer placed after the fiber. The laser energy to CE phase coupling for the hollow-core fiber based *f*-to-2*f* interferometer was measured. It shows that 128 mrad of CE phase measurement error was introduced by a 1% of laser energy change under our experimental conditions. Furthermore, a simple model was proposed to explain the coupling mechanism. Determining the coupling coefficient is important for specifying the power stability of CPA lasers for seeding the hollow-core fibers. Understanding the CE phase properties of such fibers is crucial for attosecond pulse generation, ATI and other experiments at the frontiers of ultrafast science.

Notes: The materials presented in this chapter have mainly been published in: He Wang, Chengquan Li, Jason Tackett, Hiroki Mashiko, Christopher M. Nakamura, Eric Moon and Zenghu Chang, "Power locking of high-repetition-rate chirped pulse amplifiers", *Appl. Phys. B*, **89**, 275 (2007), Chenxia Yun, Shouyuan Chen, He Wang, Michael Chini, and Zenghu Chang, "Temperature feedback control for long-term carrier-envelope phase locking", *Appl. Opt.*, **48**, 5127 (2009) and He Wang, Michael Chini, Eric Moon, Hiroki Mashiko, Chengquan Li and Zenghu Chang, "Coupling between energy and phase in hollow-core fiber based *f*-to-2*f* interferometers", *Opt. Express*, **17**, 12082 (2009).

CHAPTER 3 - Absolute phase control of few cycle pulses by an adaptive phase modulator

In the previous chapter we have discussed how to generate high power few-cycle pulses, and how to control the CE phase of such pulses. There are still two issues unsolved. The first is to push the limit of the shortest achievable few-cycle pulses. Ideally single attosecond pulses could be generated directly from monocycle driving laser field, but such few-cycle pulses usually have spectra that span more than one octave in frequency and their pulse duration and shape are very sensitive to dispersion. For example, a 5 fs Guassian transform limited (TL) pulse becomes 7 fs after passing through 0.25 mm of fused silica plate or 25 cm of air, which gives a stretching factor of nearly 50%. For the same amount of dispersive material, a 30 fs TL pulse is only slightly stretched to 30.4 fs (less than 1.5%). To guarantee the shortest pulse at the target, chirp control of few-cycle pulses is critical. The second issue is to engineer the electric field to a preset shape. This is important since in high field physics electron dynamics are largely governed by the distribution of the electric field inside pulse as discussed in the introductory chapter. To solve the above problems, a liquid crystal based spatial phase modulator was constructed. With adaptive phase correction and control, 5 fs pulses were directly produced at the target, which were nearly transform limited. Combining the absolute CE phase control and spectral phase control, such absolute phase controllable few-cycle pulses allow control over electron dynamics with attosecond precision.

3.1 Comparison of adaptive phase modulator and chirped mirrors

When the pulses from CPA lasers are focused into hollow-core fibers [33, 34], the self phase modulation process broadens the spectrum but also introduces positive chirp into the output pulse. The most frequently used method to compress such white-light broad spectra is the chirped mirror, A chirped mirror consists of multilayer coatings, which allows the different wavelength components of the incident white-light to penetrate and reflect back from different coating depths [35]. By carefully designing the thickness of each layer, the chirped mirror can exhibit negative group delay dispersion (GDD) over the spectral range of the light from the nonlinear medium. Very recently, sub-5 fs pulses with 400 μJ energy measured by second

harmonic (SH) and third harmonic autocorrelators were generated by optimizing the chirped mirror design and by using 23 fs pulses seeding the neon-filled hollow fiber [34]. However, because the negative GDD introduced by a given set of chirped mirrors can only be changed by a discrete amount, it is difficult to accommodate the daily variation of the pulses from the hollow-core fiber. As a result, the compressed pulse duration and shape may change from day to day. Furthermore, owing to the interferometric effects at the air/mirror interface and inside the coating structure, GDD ripples are inevitable [77]. Matched pairs of mirrors have been used to overcome this problem to a certain degree, but not completely. Design and fabrication of chirped mirrors that can compensate high order dispersions is still a challenge. So far, chirped mirrors only compensate GDD and the third order dispersions, while fourth and higher order phase control is important for compressing pulses to a few-cycle field oscillation.

Compared to chirped mirrors, adaptive phase modulators have high flexibility and broad bandwidth of phase control [78, 79]. In principle, they can be adjusted to cope with the day to day phase variations of the white-light pulses and to compensate the high order phase errors. In the past, by using a liquid crystal spatial light modulator (SLM), the white light from two cascaded hollow-core fibers was compressed to 3.8 fs with 15μJ pulse energy [78]. Even shorter pulses, 2.8 fs, were obtained by using a similar phase modulator [79]. Although they are the shortest pulses in the visible and infrared wavelength range, the energy of such extremely short pulses is only 0.5 μJ, which is too low for many high field experiments. For example, attosecond pulse generation has been accomplished by using 5 *f*s laser pulses with more than 300 μJ [80], whose energy is orders of magnitude higher than what the phase modulators have delivered. The low pulse energy is the main obstacle to applying pulses from adaptive phase modulator compressors to strong field physics experiments. In fact, to the best of our knowledge, no such experiments have been done using few-cycle pulses from adaptive compressors. The energy deficiency is the result of the high loss of the phase modulator and the limited input laser energy.

On the other hand, coherent control by shaping the pulse with an adaptive phase modulator has found broad range of applications in physics and chemistry [81, 82]. By adding linear chirp to the pulse directly from a CPA, HHG spectrum shift and broadening have been studied [83, 84]. Optimization of HHG has also been studied by combining the adaptive phase modulator and feedback control [85, 86]. However, none of the control experiment have been directly performed with few cycle high power laser pulses.

We improved the throughput of the adaptive phase modulator and applied it to a hollow-core fiber with high output energy in order to obtain two-cycle pulses with sub-millijoule energy [87].

3.2 Adaptive phase modulator setup

The home-built phase modulator for pulse compression is shown in Fig. 3-1. To test the adaptive phase modulator compressor, we used the KLS, which is a grating-based CPA Ti:sapphire laser system operating at 1 kHz repetition rate. More than 2 mJ, 25 fs pulses from the laser were coupled into a 0.9 meter long, 400 μm inner core diameter hollow fiber filled with 2 bars of neon gas [37]. With such high energy seeding pulses, strong self-phase modulation produced white light whose spectrum covered more than one octave from 500nm to 1000nm, as shown in Fig. 3-2. The energy of the pulse from the fiber was about 1.1 mJ, measured before the collimation mirror. Previously the highest white-light pulse energy used in the phase modulator compression was 0.1 mJ [78]. Thus we gained a factor of more than ten just from the input side. The energetic pulses from the hollow-core fiber were then collimated and sent into a zero-dispersion 4*f* system, which consisted of two gratings with a groove density of 230 lines/mm(Newport 33009BK06-790R), and two cylindrical mirrors with 50 cm focal length (Tower Optical Corp.). A 640-pixel liquid crystal SLM (Jenoptik SLM-S640) was located at the Fourier plane. The broadband laser beam from the hollow-core fiber was angularly dispersed by the first grating. Rather than spherical mirrors, silver-coated cylindrical mirrors were applied to focus each wavelength component to a line on the SLM to avoid damaging the liquid crystal of the SLM by the high energy pulses. The chirp of the pulses was removed by controlling the refractive index on each pixel of the SLM. The second grating recombined the different frequency components into one output beam (See Appendix B, Appendix C for more details of construction and alignment).

Previously, low diffraction efficiency of the gratings was the main limiting factor of the overall throughput of the adaptive phase modulator. We used two gratings with protected silver coatings to achieve high diffraction efficiency (average efficiency is ~80 %) over the bandwidth (500nm-1000nm) of our hollow-core fiber output spectrum. Also, the SLM with broadband anti-reflection coatings on both surfaces provided high transmission of more than 90% in the same wavelength range.

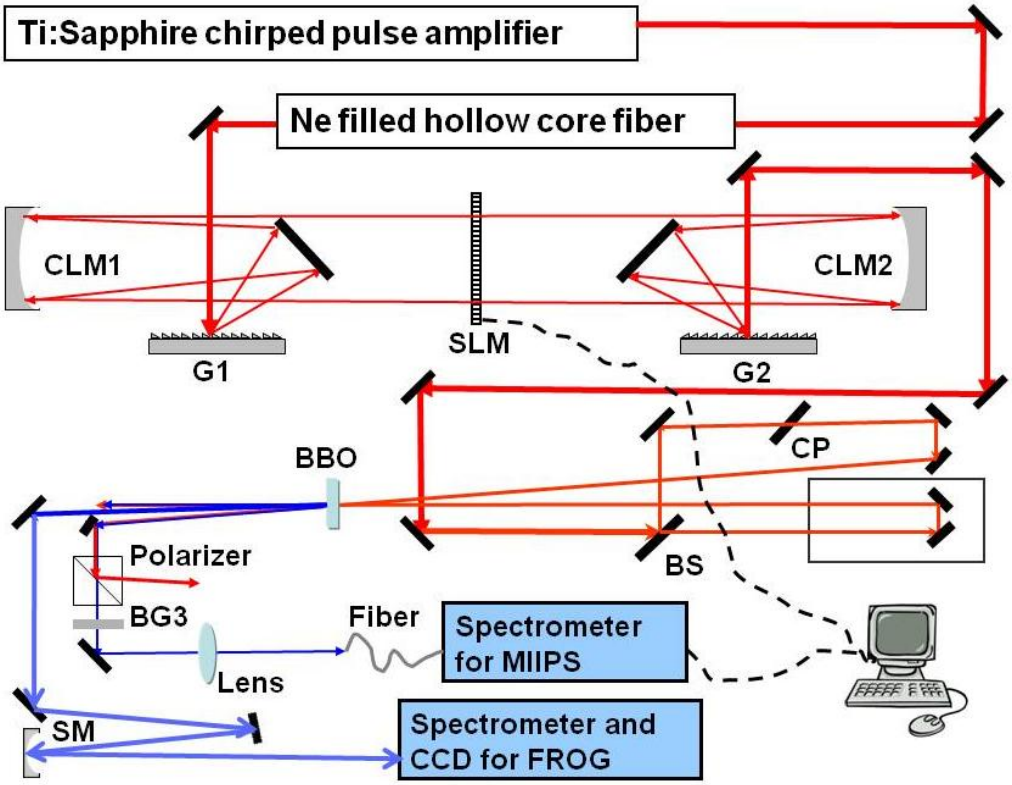

Figure 3-1 The adaptive phase modulator. After hollow-core fiber the chirped white-light pulses were sent to the spatial light modulator through gratings (G1, G2) and cylindrical mirrors (CLM1, CLM2). The output beam was directed to the BBO. The central SH beam was used for FROG measurement, and one side SH beam was used as MIIPS feedback signal. The α-BBO polarizer and the BG3 band-pass filter worked together to eliminate the fundamental beam. The MIIPS retrieved phase was applied on SLM to compress the pulse. BS: beam splitter, CP: compensation plate, SM: spherical mirror. The dashed line represents the feedback loop. Figure adapted from Ref [87].

To determine the frequency response of the 4*f* system, the white-light spectrum was measured before and after the phase modulator, as shown in Fig 3-2. Although the throughput was somewhat lower at the short wavelength side, the transform limited pulse duration supported by the spectrum of the output pulses was sub-5 fs, which was nearly the same as that of the input. With 1.1 mJ per input pulse, the output pulse energy from the system was 0.55 mJ, which was about 37 times higher than what was demonstrated before. The high throughput, 50%, was the major improvement of our adaptive phase modulator.

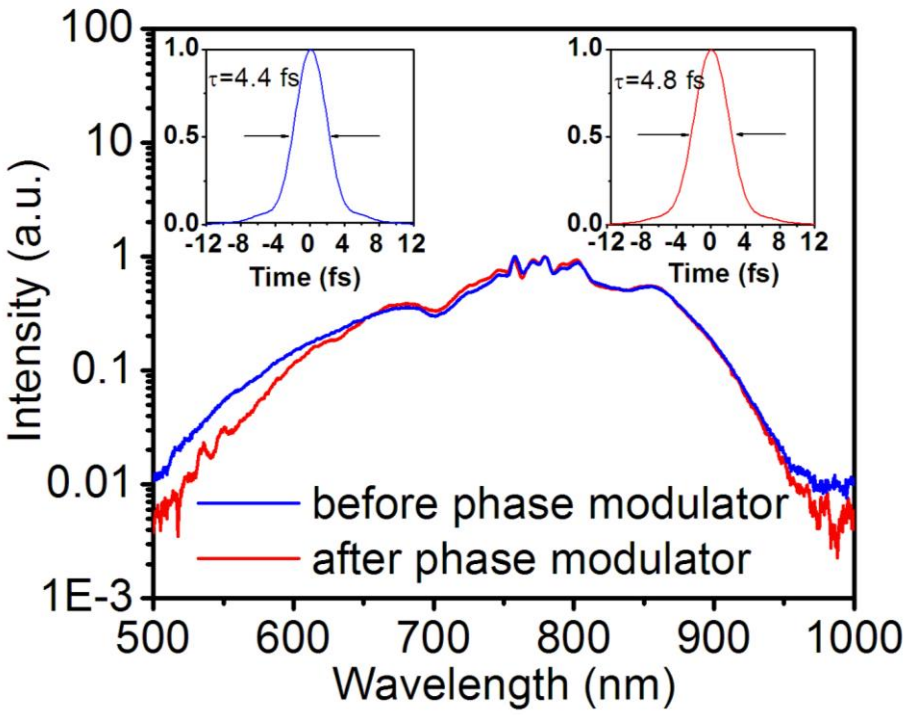

Figure 3-2 The white-light spectrum before the phase modulator (blue) and after the phase modulator (red). The inset shows the transform-limited pulses for both spectra. Figure adapted from Ref [87].

3.3 Pulse compression by MIIPS method

One approach to obtain the shortest pulse is to optimize the second harmonic signal by focusing the compressed white-light pulses to a nonlinear crystal. However, it was found that by optimizing the SH signal, neither genetic algorithm nor evolutionary algorithm can compress the pulse with high accuracy [88, 89]. Another approach is to measure the spectral phase of the white light from the fiber and feed the measured value to the phase modulator for correction. For adaptive pulse compression in the near-octave bandwidth and few-cycle regime, accurate retrieval of the spectral phase of the output pulses from the 4*f* system is crucial.

Our laboratory is equipped with a FROG based on second harmonic generation [39].

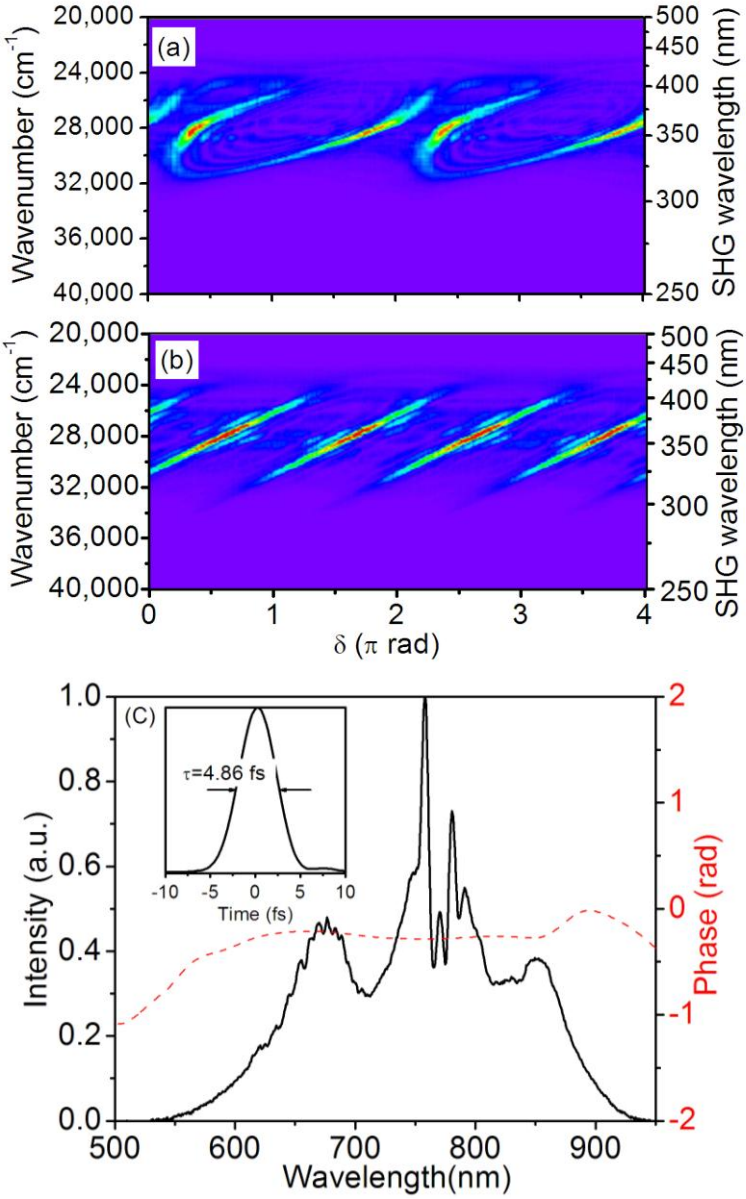

Figure 3-3 The MIIPS traces (α=5, γ=7 fs). (a) from the first iteration; (b) from the last iteration; (c) the phase determined by the last iteration and the corresponding pulse duration. Figure adapted from Ref [87].

We found that it is difficult to measure the phase of the white-light pulses from the fiber before compression with high accuracy because of the poor signal to noise ratios, especially at the two ends of the spectrum (around ~550 nm and around ~950 nm). This is because the SH signal is rather low in those regions when the pulses are strongly chirped. As an alternative, the Multiphoton Intrapulse Interference Phase Scan (MIIPS) method was applied [90, 91].

The MIIPS works by modulating the spectral phase of the pulses with the SLM while simultaneously recording the second harmonic (SH) spectra after the 4*f* system. The applied spectral phase at frequency ω can be expressed as $\Phi(\omega)=\alpha\cos(\gamma\omega-\delta)$, where α and γ are two parameters that need to be chosen properly (In our case α =5, γ=7 fs). By linearly increasing the δ value, one can scan the applied GDD for each frequency ω. When dispersions higher than the second order are ignored, it is found that if the GDD introduced by the phase modulator, $\Phi''(\omega)=\alpha\gamma^2\cos(\gamma\omega-\delta)$, cancels out the GDD of the white light, $\varphi''(\omega)$, at a certain frequency ω then a SH signal peak appears at 2ω. After recording all the SH spectra for δ from 0 to 4π, the two dimensional MIIPS trace was constructed as shown in Fig. 3-3. By searching the peak position δ_p in the MIIPS trace for each SH frequency 2ω, $\varphi_1''(\omega)=-\Phi_1''(\omega)= -\alpha\gamma^2\cos(\gamma\omega-\delta_p)$ is retrieved from the MIIPS pattern for the first iteration. $\varphi_1''(\omega)$ is an approximate value of $\varphi''(\omega)$ since dispersions higher than the second order are ignored. By integrating $\varphi_1''(\omega)$ twice, we obtained the phase $\varphi_1(\omega)$ from the first iteration. To measure the phase more precisely, $-\varphi_1(\omega)$ was wrapped and applied on the SLM for the second iteration, which measured the phase difference $\varphi(\omega)-\varphi_1(\omega)$, the second iteration is done in the same way as the first iteration. After *m* iterations, the phase correction $\varphi_m(\omega)$ becames nearly flat and the retrieved phase $\sum\varphi_m(\omega)$ converges to $\varphi(\omega)$ (More details of MIIPS parameter selection and simulations are presented in Appendix D, Appendix E). In our experiments, *m* = 8. The generation of the SH peak increases the signal to noise ratio. At both ends of the fundamental spectrum (600 nm and 900 nm), the SH peak in MIIPS is much stronger than the SH signal in the FROG before the phase was corrected which is the main reason we chose the MIIPS for measuring the initial phase of the white-light pulses.

In our experiments, since the GDD of white light $\varphi''(\omega)$ is large, $\varphi_0''(\omega)=500\ fs^2$ was added on the SLM to pre-compensate the phase before the first iteration. The linear component of $\varphi_0(\omega)$ was chosen such that the phase load per pixel was minimized [92]. The first iteration of the MIIPS pattern is shown in Fig. 3-3(a). The iterations stopped when the retrieved phase accuracy was higher than 0.01 radians per liquid crystal pixel over the whole fundamental spectrum. The MIIPS pattern after the chirp compensation is shown in Fig. 3-3(b). The evenly spaced parallel SH strip distribution indicates that the residual GDD of the pulses is very small [91]. Since our MIIPS did not resolve the SH peak position clearly below 280nm or above 450nm, there were residual errors on both the short and long wavelength portions of the retrieved

phase. The phase $\varphi_m(\omega)$ retrieved from the last iteration is shown in Fig. 3-3(c). Using this measured phase and the power spectrum at the exit of the 4*f* system shown in Fig. 3-2, Fourier transform gave the pulse duration of 4.86 fs, also shown in Fig. 3-3(c).

The second harmonic signal shown in Fig. 3-3 was generated in a barium borate (BBO) crystal with a type I phase-matching configuration. A 5 μm thickness thin crystal was used for phase-matching over the broad fundamental spectrum range. The phase matching angle of the crystal was set to 40 degrees to enhance the frequency doubling efficiency around 600 nm of the white light. When the SH was measured by a customized Ocean Optics HR2000+ spectrometer that works in the 200nm to 600nm range, the strong fundamental laser light had to be blocked as to not saturate the detector. The configuration we used for detecting the second harmonic signal is shown in Fig. 3-1, which is different from what was used in MIIPS in the past [90]. Taking advantage of the fact that the polarization of the second harmonic beam is orthogonal to the fundamental beam for type I phase matching, an *α*-BBO polarizer was placed after the SH generation BBO crystal to reject most of the fundamental light. A BG3 filter was added to further suppress the fundamental signal. To increase the signal to noise ratio and reduce the integration time of spectrum acquisition, a fused silica UV lens with 5 cm focal length focused the SH signal to an optical fiber that couples the light into the spectrometer. Compared with the prism method that separates SH from the fundamental used in the past with MIIPS, our collinear configuration has higher collection efficiency, which is important for measuring the phase of the weak fundamental at both ends of the spectrum.

After the phase correction by MIIPS, the duration of the compressed pulse was measured by the FROG [93, 94]. Unlike the input pulses, we found that the signal to noise ratio of the FROG pattern obtained with the compressed pulses is good enough for robust phase retrieval. Our MIIPS and FROG shared the same BBO crystal, as shown in Fig.3-1. There are three second harmonic beams exiting the BBO crystal. The center one was used by the FROG, while one of the side beams was sent to the MIIPS. It is well known that few-cycle pulses can be easily distorted by dispersion introduced by propagation in air. In such a configuration, the MIIPS and the FROG measured the pulse at the same location, which is critical for few-cycle pulse characterization. To avoid the chromatic aberration in FROG measurement, a spherical mirror is used in place of a lens to image the SHG into the spectrometer. The measured and reconstructed FROG patterns are shown in Fig. 3-4 (a) and (b) respectively. The retrieved pulse duration is 5.1

fs as shown in Fig. 3-4 (c), which is slightly longer than what was determined by the MIIPS (4.86 fs). The spectral phase in Fig. 3-4(d) shows the chirp was well compensated. Also in Fig. 3-4(d) the retrieved spectrum was compared with the independently measured spectrum. The frequency marginal comparison is shown in Fig. 3-4(e) to confirm the validity of FROG results. Both methods showed that the pulse duration was around 5 fs, which is shorter than what has been produced from the same hollow-core fiber using commercially available chirped mirrors [36, 37]. For pulses with over one octave spectra, it is difficult to get perfect FROG traces due the limited phase-matching bandwidth of the SHG crystal and the spectral response of all the optics in the setup, which explains the difference between the MIIPS results and FROG results.

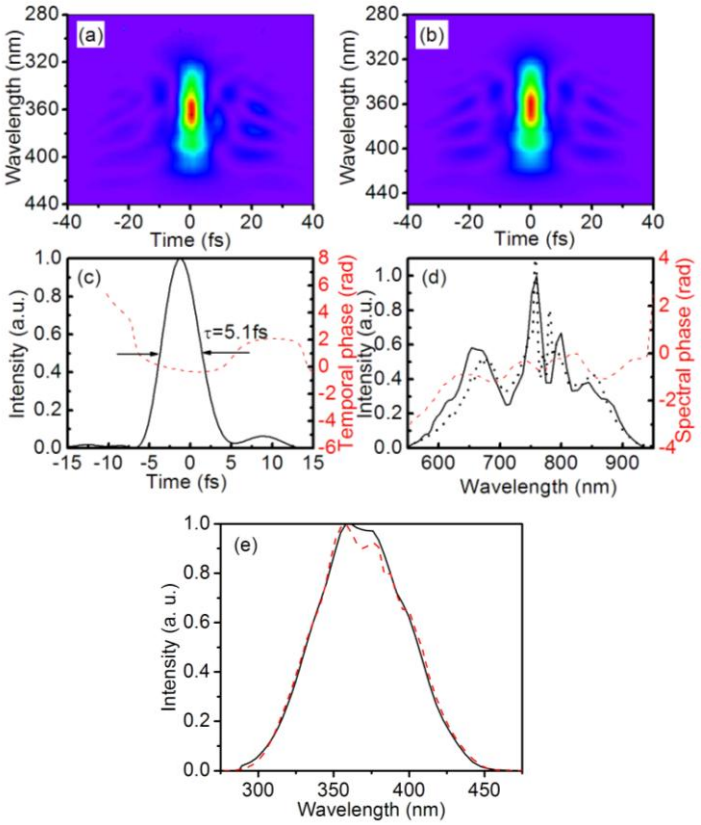

Figure 3-4 Characterization of the laser pulse by the FROG. (a) The measured FROG trace. (b) The reconstructed FROG trace. (c) The retrieved pulse shape and phase (dashed curve). (d) The retrieved power spectrum and phase (dashed curve) and independently measured spectrum (dotted curve). (e) The FROG frequency marginal (dotted red curve) and the autoconvolution (solid black curve) of the measured spectrum from hollow-core fiber. The FROG error is 0.5%, and the trace is at 256×256 grids. Figure adapted from Ref [87].

3.4 HHG from chirped few cycle pulse

The high power of the compressed pulses allowed us to generate high order harmonics. Previously the dependence of high harmonic generation (HHG) spectra on GDD was investigated by using relatively long pulses (30 fs) directly from the CPA system by changing the grating separation [83, 84]. It was found that when the driving laser was positively chirped, the HHG spectra were more discrete and red shifted, whereas for a negatively chirped pump, the HHG spectra became a continuum.

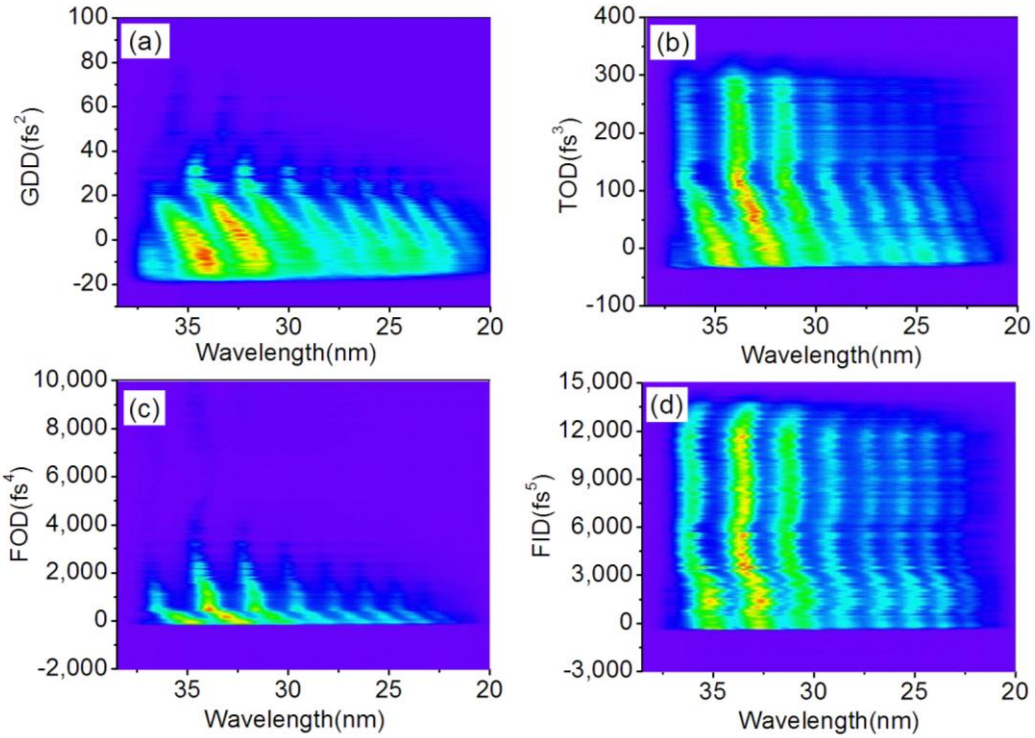

Figure 3-5 Dependence of Ar high order harmonic spectra on the high order phases of the driving laser pulses. Figure adapted from Ref [87].

We performed coherent control of high harmonic generation with the 0.55 mJ, 5.1 fs pulses by independently changing the GDD and high order spectral phases. Our experiment was carried out with both argon and neon gas using a setup described in Ref. 95. The laser beam was focused by a spherical mirror to a gas filled interaction cell with a length of 1.4 mm. The focal length of the mirror was 400 mm. The backing pressure to the gas cell was 30 torr and 60 torr for argon and neon respectively. The gas target was placed approximately 2 mm after the focus to optimize the phase matching for the short trajectory [96]. As seen in Fig. 3-5 (a), when the GDD was scanned, the Ar harmonic peaks shift, like what was discovered with long laser pulses in the

past. The spectra also showed an asymmetric dependence on the positive chirp as compared to the negative chirp. We noticed that asymmetry is even stronger for third order to fifth order phases as shown in Fig. 3-5(b), (c) and (d), a phenomenon that has not been studied before and deserves further investigation. Similar Ne results are shown in Fig. 3-6. To the best of our knowledge, this is the first coherent control of high harmonic generation with few-cycle laser pulses.

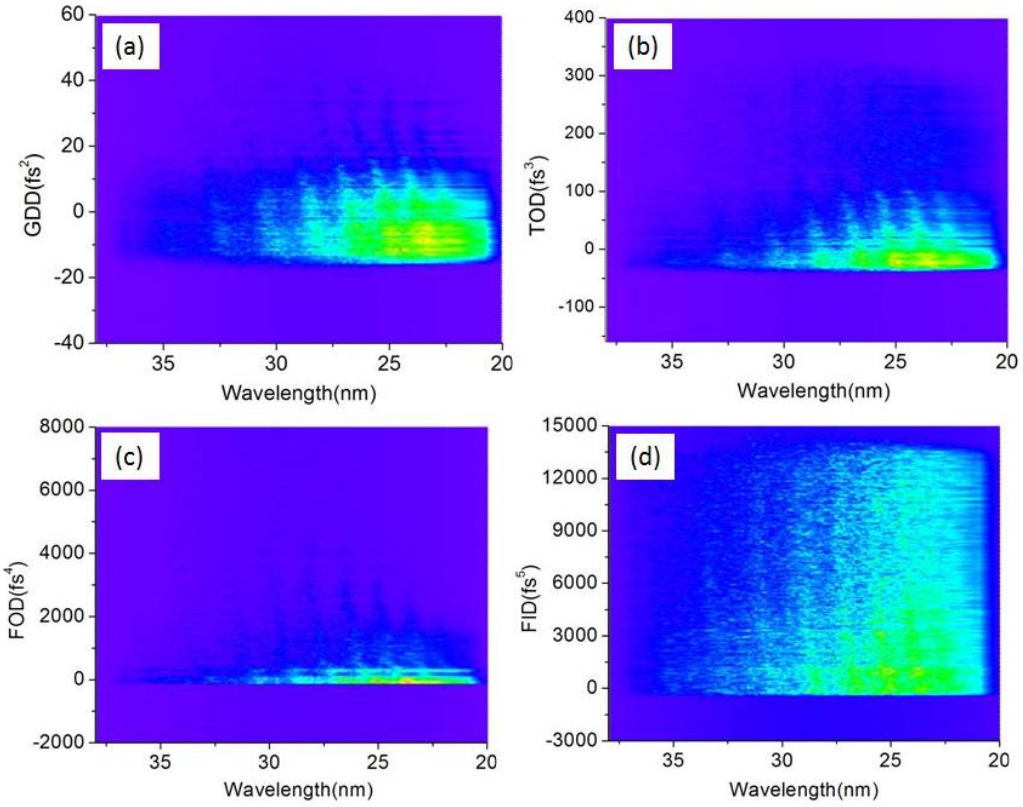

Figure 3-6 Dependence of Ne high order harmonic spectra on the high order phases of the driving laser pulses.

3.5. From relative phase control to absolute phase control of few cycle pulses

Since we have generated of 0.5-mJ, 5-fs pulses by an adaptive phase modulator, in order to make such pulses more usable to the attosecond science community, the CE phase of such pulses has to be locked. This adds an absolute phase control of the few-cycle pulses as shown in Fig. 3-7, which provides a brand new tool for strong field coherent control experiment. Here we stabilize of the carrier-envelope phase of pulses from the phase modulator [97].

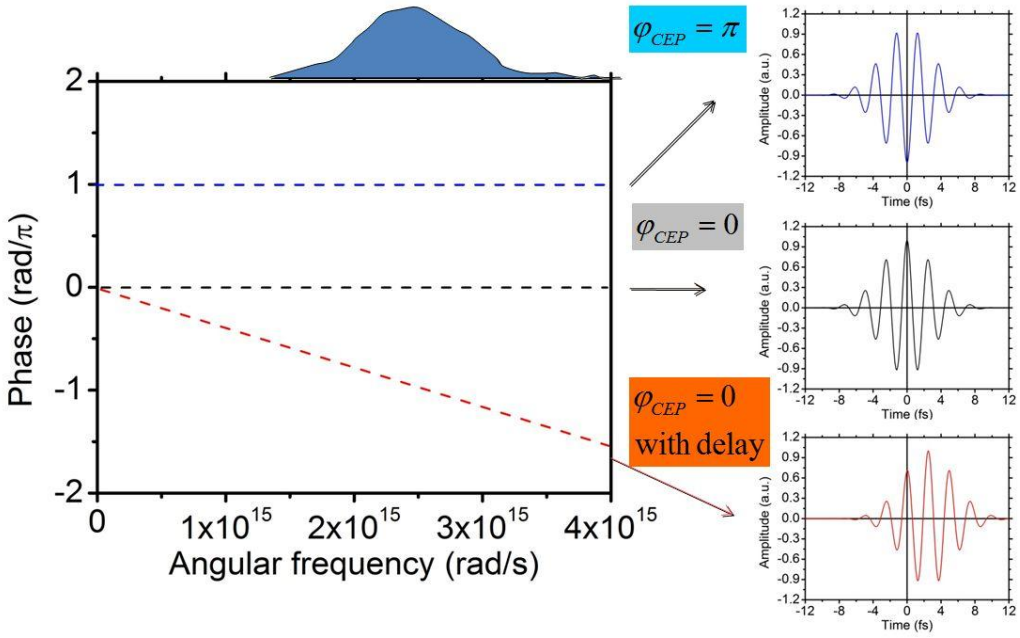

Figure 3-7 Absolute phase control of few cycle pulses.

The experiment was done with the KLS laser system as shown in Fig. 3-8. The CE phase stabilized laser system has already been introduced in previous sections. The in loop *f*-to-2*f* is a sapphire plate based interferometer. The CE phase of the output pulse from the adaptive phase modulator was measured by a simplified *f*-to-*2f* interferometer that took advantage of the 4*f* system of the phase modulator. The modulator was designed to perform spectral phase correction in the range of 500nm to 1000nm. However, the light with wavelength near 460 nm could still go through the 4 *f* system by the second-order diffraction of the grating, which overlapped with the fundamental component near 920nm. A 0.5-mm-thick fused-silica plate was used to reflect about 3% (20 mW) of the whole output beam after the adaptive phase modulator, and an *f* = 30cm spherical mirror was used to focus both the 460-nm and the 920-nm light into a 100 μm BBO crystal. The phase-matching angle of the BBO crystal was tuned to generate the second-

harmonic (SH) of the 920 nm light. A polarizer was used to project the SH and fundamental polarizations onto the same axis to facilitate interference. An Ocean Optics spectrometer (HR2000+, 380-580 nm) with a resolution of 0.11 nm was used to record the fringes at 50-ms exposure time. To avoid the saturation of the CCD in our spectrometer, a BG3 filter was placed in front of it to reduce the strong fundamental wavelength above 500nm. The voltage on the SLM above 910 nm was set to zero to obtain *f*-to-*2f* fringes with good quality. With such an *f*-to-2*f* interferometer, the CE phase after the adaptive phase modulator could be measured.

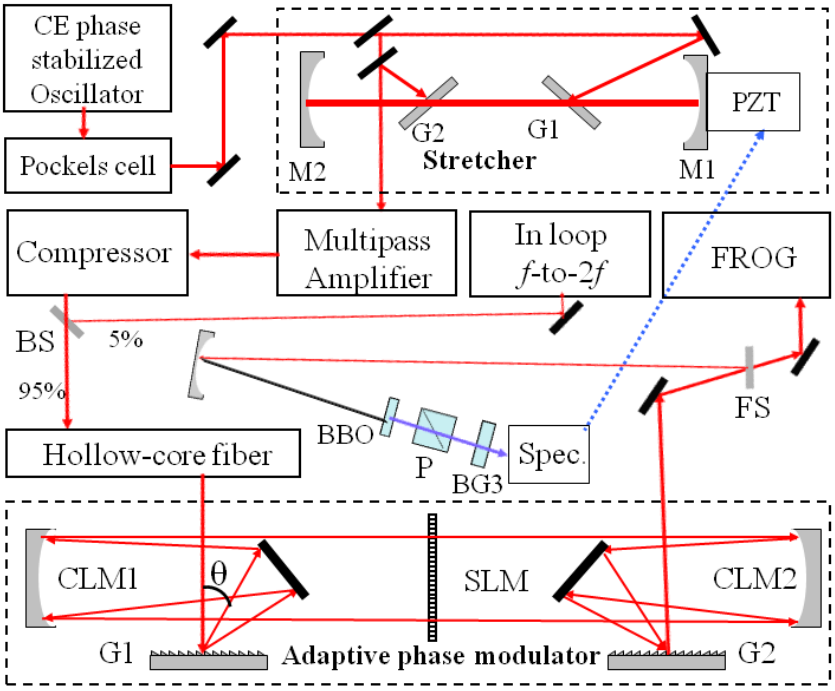

Figure 3-8 Experimental setup for generation of CE phase-controllable 5-fs pulses. G1-G4: gratings; BS: beam splitter; FS: fused-silica plate; CLM1, 2: cylindrical mirrors; SLM: liquid crystal spatial light modulator; SM: spherical mirror; P: Polarizer. Figure adapted from Ref [97].

As shown in Fig. 3-9, when the CE phase was stabilized by a sapphire-plate-based *f*-to-2*f* interferometer before the hollow-core fiber with the accuracy of 172 mrad RMS, the CE phase RMS measured after adaptive phase modulator was 301 mrad (about twice as large as that of input), regardless of whether the SLM was turned on or off. We have previously shown that when CE phase was locked within an accuracy of 98 mrad before the hollow-core fiber, the CE phase fluctuation after the hollow-core fiber was 137 mrad [72]. By comparing the phase error

with and without the phase modulator, we conclude that the extra CE phase drift is caused by the phase modulator. Furthermore, since the phase noise is almost the same when the SLM was on or off, we believe that the possible sources of noise are the mechanical vibration of the 4 *f* system and the pointing fluctuation of the input pulses [98]. Since our adaptive phase modulator is a grating-based zero dispersion 4 *f* system, the effective distance between the two gratings is zero and the role of pointing fluctuation on CE phase can be ignored as shown in Eq. (3.1) [99]

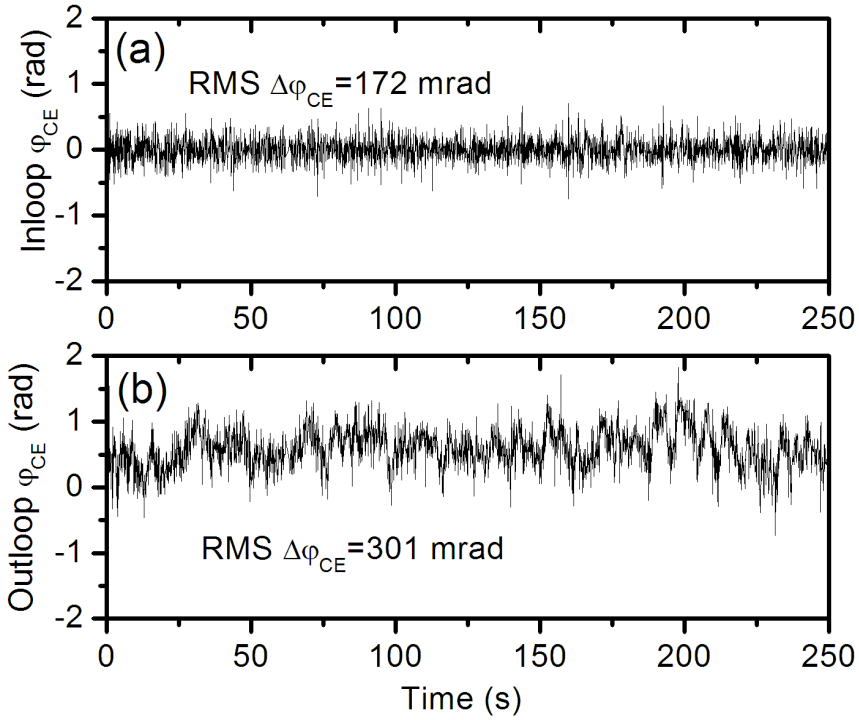

Figure 3-9 CE phase drift introduced by the adaptive phase modulator. (a) CE phase stabilized before the hollow-core fiber using sapphire-based in-loop *f*-to2*f* interferometer; (b) CE phase measured after the adaptive phase modulator by using the hollow-core fiber white-light. Figure adapted from Ref [97].

$$\Delta\varphi_{CE} = 2\pi G / d \sec^2[\gamma - \theta(\omega_0)]\Delta\gamma, \tag{3.1}$$

where G is the effective distance between the two gratings, d is the groove separation of the graing, γ is the angle of incidence, which is zero degrees in our case, ω_0 is the carrier frequency of the pulse, θ is the acute angle between the incident and diffracted rays and $\Delta\gamma$ is the angle of the pointing fluctuation. When G=0, $\Delta\varphi_{CE}$ becomes zero regardless of the pointing fluctuation. However the CE phase drift caused by the small fluctuation of effective distance between two gratings can be expressed as [59]:

$$\Delta\varphi_{CE} = 2\pi\Delta G / d \tan^2[\gamma - \theta(\omega_0)], \tag{3.2}$$

where ΔG is the small change of the effective distance between the two gratings. It is estimated that ΔG of 23 μm introduces 2π CE phase drift for our setup. Thus mechanical vibration of the gratings and cavity mirrors leads to CE phase instability.

There are at least two possible ways to compensate the CE phase shift introduced by the $4f$ system. The CE phase measured after the adaptive phase modulator can be used to feedback control either the liquid crystal spatial light modulator or the grating pairs. In the first approach, a constant phase value equal to the error signal is added to all pixels at the same time in the liquid crystal spatial light modulator [100]. However, the response is slow because the switching time of the modulator is on the order of several milliseconds. Also any voltage on the SLM above 910 nm destroys the fringe quality, preventing us from locking the phase.

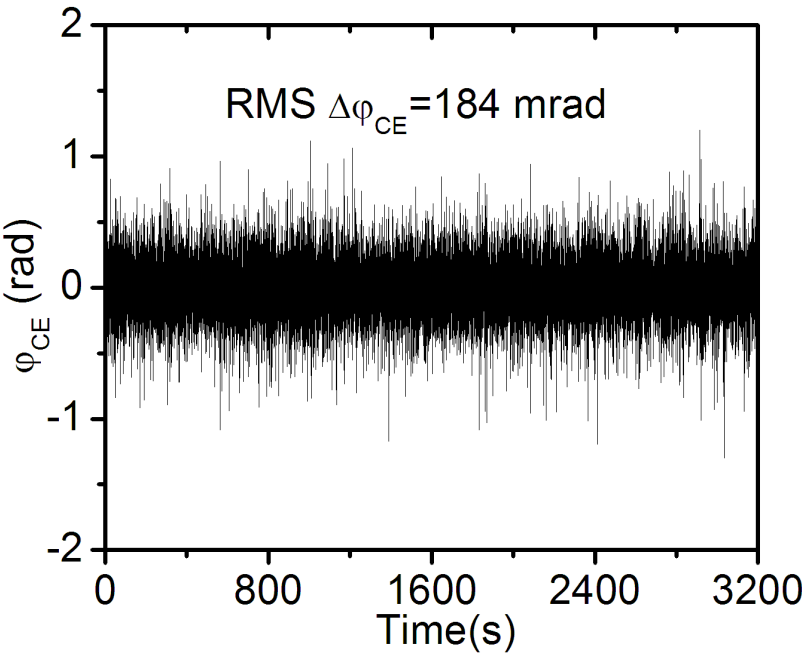

Figure 3-10 Long-term stability of CE phase after the adaptive phase modulator. The CE phase was stabilized by feedback controlling the gratings in the stretcher, using the CE phase measured after the phase modulator to determine the error signal. Figure adapted from Ref [97].

We took the second approach, i.e., the measured CE phase was used to feedback control the grating separation of the CPA stretcher to compensate the total slow CE phase drift that was introduced by the CPA, hollow fiber and phase modulator [72]. As shown in Fig. 3-10, the CE

phase after the phase modulator was locked with accuracy of 184 mrad for nearly one hour. Moreover, by adjusting the grating separation of the stretcher to preset values, the CE phase was swept from $-\pi$ to π as shown in Fig. 3-11, which can be used to observe the CE phase effect of high harmonic generation (HHG) or other high-field processes.

The pulse duration was measured by MIIPS and confirmed by FROG measurement, which gave the same result of 5 fs pulse duration as before.

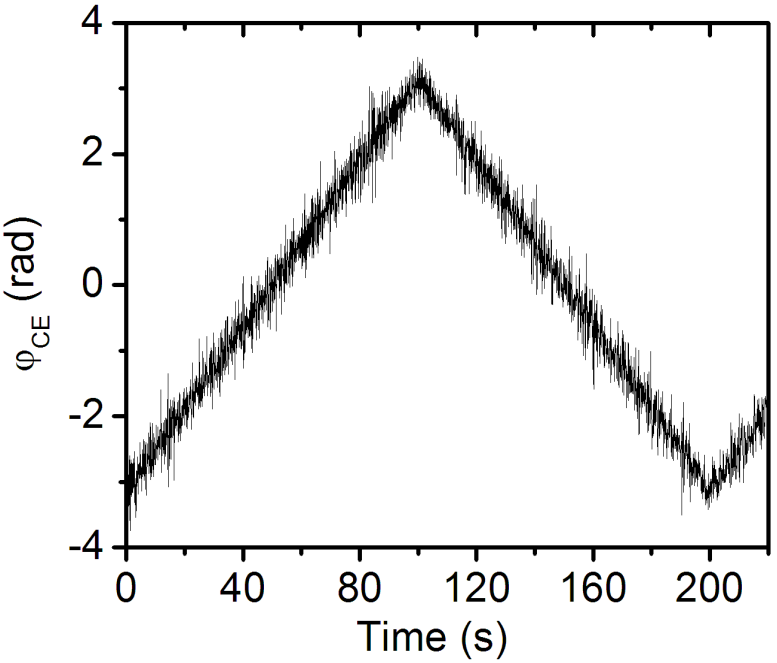

Figure 3-11 CE phase sweep from $-\pi$ to π radian. Figure adapted from Ref [97].

3.6. Short summary and outlook

In conclusion, by improving the throughput of an adaptive phase modulator and by applying it to a high power laser system, we compressed laser pulses to ~5 fs at half-millijoule energy levels. As far as we know, this is the highest energy few-cycle pulse ever achieved by adaptive pulse compressors. By measuring the CE phase after the phase modulator and feeding it back to the stretcher of the CPA, we were able to lock the CE phase for nearly one hour. The MIIPS method was applied to measure the spectral phase of the pulses after the hollow-core fiber for the first time, which serves as the feedback for the phase correction. The high power, two-cycle pulses were used in high harmonic generation. It was found that the harmonic spectra depended strongly on the high order spectral phases. The absolute phase controllable, millijoule

level few-cycle pulses are a new powerful tool for studying single attosecond pulse generation and performing coherent control in new parameter spaces.

Although our adaptive phase modulator has successfully compressed the hollow-core fiber output down to 5 fs pulse duration, still several challenges have to be overcome before the high power few-cycle pulse could be finally realized. Here I list a few issues and possible solutions for future development.

The first issue is the pulse energy. Even our 0.5 mJ pulse energy has already set a new record for such a device. To produce strong and broadband attosecond XUV pulses, higher NIR photon flux would be better. The final output energy can be improved by increasing the input energy of pulse shaper. One possible solution is to use a differentially pumped hollow-core fiber or gas ionization compression. Very recently, 5 mJ, 5 fs pulses have been reported from a pressure gradient fiber with chirped input pulses [101] and 14 mJ, 11 fs pulses have been reported from ionization pre-compression [102]. If such high power few-cycle pulses are used as input, the output pulse energy from the pulse shaper can be scaled up. For improving the efficiency of the pulse shaper itself, the use of transmission gratings is one option which could be taken into consideration since it may have higher diffraction efficiency than the reflective grating. However, self focusing and self phase modulation may happen inside the transmission grating.

Once the energy barrier is overcome, the next issue is to generate as broad spectrum as possible. Yamashita proposed two color seeding of the hollow core fiber [103]. In their experiment, besides the self phase modulation, the induced phase modulation (IPM) was used to enhance the spectrum broadening. By replacing the interferometer with a collinear two color configuration, it is very likely that the temporal jitter between the fundamental field and SHG could be eliminated, which could lead to the generation of over one-octave span coherent spectrum. To control the phase of such a broadband spectrum, again Yamashita has reported a newly developed liquid crystal with a transmittance of more than 85% in the wavelength range from 260 nm to 1100 nm [104, 105], ideally such a two octave spanning spectrum could lead to the generation of monocycle pulses. When more than one-octave spanning spectrum is diffracted by a grating, the second order diffraction of the short wavelength overlaps with the first order diffraction of the long wavelength. By carefully selecting the grazing angle of the

grating, this problem can be minimized to some extent [106]. Still more work needs to be done to achieve this.

The third issue would be the spectral phase measurement and control. The MIIPS method has better signal to noise ratio than FROG and it can start phase correction from quite large phase distortion. Currently the MIIPS method is based on the measurement of the SHG spectrum. Still, the phase matching bandwidth of SHG is not as good as the sum frequency generation in SPIDER [106]. Possibly, a method which combines the good signal to noise ratio of MIIPS and the broadband phase matching of SPIDER could be developed to solve this problem.

Even if all the above prerequisites can be satisfied, several precautions still need to be taken before the successful implementation of adaptive phase modulators in attosecond science. The first is the stability. In order to have accurate control of the absolute phase, the system must be very stable, this could be solved by using heavy mounts and isolating the vibrational noise. Another issue is the pixel nature of the liquid crystal. The pixel diffraction deteriorates the final output beam profile. When the phase correction is applied, the situation could be even worse. Since the phase matching of HHG is quite sensitive to the wave front [86, 96], the spatial-temporal coupling of the pulse shaper [107] needs to be considered carefully if it is used in attosecond science.

Once few cycle or monocycle laser pulses can be engineered in a controllable fashion, the results will be very rewarding. The cutoff extension of HHG [108], as well as suppression and enhancement of certain HHG orders [86], would pave the way for shorter single attosecond pulse generation and coherent control of the XUV pulse.

Notes: The material presented in this chapter has mainly been published in: He Wang, Michael Chini, Yi Wu, Eric Moon, Hiroki Mashiko and Zenghu Chang, "Carrier-envelope phase stabilization of 5 fs, 0.5 mJ pulses from adaptive phase modulators", *Appl. Phys. B*, **98**, 291, (2009) and He Wang, Yi Wu, Chengquan Li, Hiroki Mashiko, Steve Gilbertson, and Zenghu Chang, "Generation of 0.5 mJ, few-cycle pulses by an adaptive phase modulator", *Opt. Express*, **16**, 14448, (2008).

CHAPTER 4 - Single attosecond pulse generation and measurement

To produce single attosecond pulses from HHG, several technologies are available. Since the HHG cutoff is proportional to the laser intensity, one way is to select the XUV spectrum near the cutoff when a few-cycle or even monocycle pulse is used as the driving field [16, 41]. The other way makes use of the ellipticity dependence of the HHG efficiency. By carefully designing the pulse with time dependent ellipticity, the HHG process can only happen within a fraction laser cycle, which leads to the generation of a single attosecond pulse [17, 109-110]. We took the second approach to generate single attosecond pulses. In this chapter we mainly discuss the single attosecond pulse generation by our novel double optical gating (DOG) method and attosecond streaking experiment for characterizing such pulses. Special emphasis will be put on the attosecond reconstruction part. Several experimental limitations and their effects on the accuracy of attosecond pulse reconstruction are discussed in detail.

4.1 Single attosecond pulse generated by double optical gating (DOG)

In 2001 the first single attosecond pulses were generated from 7 fs NIR driving pulses by selected the XUV spectrum near the cutoff range [14]. By using the same technique but with a 3.3 fs NIR driving laser field, 80 as pulses centered around 80 eV were produced and measured most recently [16]. Another approach, which was termed polarization gating (PG) and first proposed by Corkum in 1994 [109], has also been realized experimentally. By converting the 5 fs linearly polarized driving laser field into left circular and right circular pulses and delaying them properly, their small region of temporal overlap (about one half cycle) became a linear field, which produced 130 as attosecond pulses centered around 36 eV [17].

As we have discussed in the previous chapters, few-cycle pulses require more than one octave spanning spectrum and are very sensitive to the dispersion. Few-cycle pulses are therefore difficult to maintain on a daily basis. Such technical barriers hinder the application of attosecond pulses to more broadly in the scientific community. Instead our group developed the double optical gating (DOG) technique, which can be used to generate single attosecond pulses from 8 fs to 12 fs driving laser fields [95, 111, 112]. More recently, with the generalized double optical gating (GDOG) technique, single attosecond pulses were produced directly from the 28 fs pulse after the CPA laser system [113]. DOG is a combination of polarization gating (PG) [17] and

two color gating [114, 115]. By adding a weak second harmonic field, the symmetry of the driving laser field is broken, and the attosecond pulse train is produced at one cycle separation instead of half cycle, which releases the constraint of half cycle width of PG to one cycle gating width of DOG as shown in Fig 4-1.

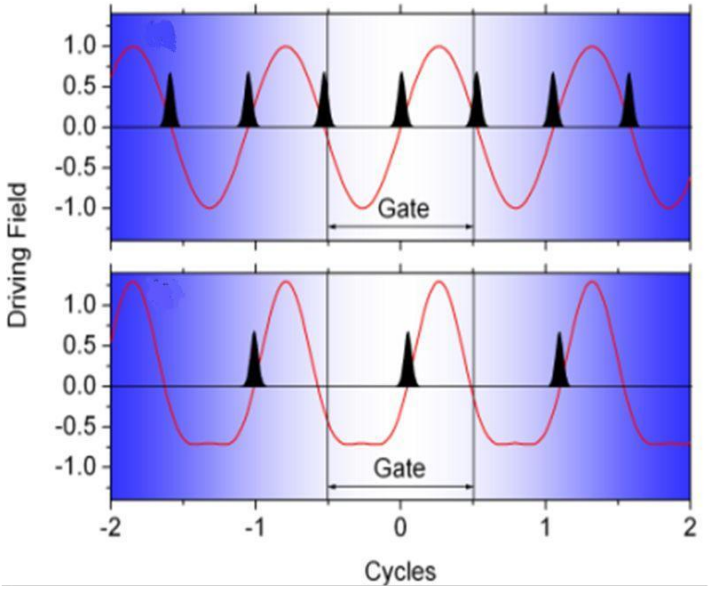

Figure 4-1 By adding SH field and breaking the electric field symmetry, attosecond pulses are produced with one cycle separation instead of half cycle separation. One cycle gate width can isolate the single attosecond pulse. Figure adapted from Ref [95].

Before we discuss the optical implementation of DOG, let's estimate the gate width mathematically. In that way the improvement of DOG over PG can be seen immediately.

For DOG, the laser field can be decomposed into the driving field along the x ($\hat{i}$) axis and the gating field along the y ($\hat{j}$) axis (z is the laser propagation direction)[93],

$$\vec{E}(t) = E_{drive}(t)\hat{i} + E_{gate}(t)\hat{j} \tag{4.1}$$

The driving field is:

$$\begin{aligned} E_{drive}(t) = \frac{1}{2}E_0[(e^{-2\ln 2[(t+T_d/2)^2/\tau_\omega^2]} + e^{-2\ln 2[(t-T_d/2)^2/\tau_\omega^2]})\cos(\omega_0 t + \varphi_{CE}) \\ + ae^{-2\ln 2(t^2/\tau_{2\omega}^2)}\cos(2\omega_0 t + 2\varphi_{CE} + \phi_{\omega,2\omega}) \end{aligned}, \tag{4.2}$$

and the gating field is:

$$E_{gate}(t) = \frac{1}{2}E_0[(e^{-2\ln 2[(t+T_d/2-T_0/4)^2/\tau_\omega^2]} - e^{-2\ln 2[(t-T_d/2-T_0/4)^2/\tau_\omega^2]})\sin(\omega_0 t + \varphi_{CE}), \tag{4.3}$$

where E_0 is the amplitude of the linear fundamental laser field with central frequency ω_0 (period T_0), pulse duration τ_ω, and CE phase φ_{CE}. T_d is the time delay between the two circular pulses. The group delay $T_0/4$ between the gating and the driving field is introduced by the quarter-wave plate. $\phi_{\omega,2\omega}$ is the relative phase between the fundamental and second harmonic pulses. The duration of the second harmonic (SH) pulse is $\tau_{2\omega}$. Finally, a represents the strength of the second harmonic field relative to the fundamental field. Ignoring the small contribution from the SH pulse and $T_0/4$ group delay, the time dependent ellipticity of the laser field can be expressed:

$$\xi(t)=\frac{\left|e^{-2\ln 2[(t-T_d/2)^2/\tau_\omega^2]}-e^{-2\ln 2[(t+T_d/2)^2/\tau_\omega^2]}\right|}{e^{-2\ln 2[(t-T_d/2)^2/\tau_\omega^2]}+e^{-2\ln 2[(t+T_d/2)^2/\tau_\omega^2]}}=\frac{\left|1-e^{-4\ln 2(T_d t/\tau_\omega^2)}\right|}{1+e^{-4\ln 2(T_d t/\tau_\omega^2)}}, \tag{4.4}$$

For the portion where the two circular pulses are fully overlapped ($4\ln 2(T_d t/\tau_\omega^2)<<1$), the ellipticity approximately becomes [116]:

$$\xi(t)\approx\left|2\ln 2\frac{T_d}{\tau_\omega^2}t\right|, \tag{4.5}$$

Typically for HHG photon energy higher than the ionization potential, the harmonic signal drops by more than one order of magnitude when the ellipticity increases from 0 to 0.2 [117, 118]. If the threshold ellipticity is assumed to be ξ_0, the gate width becomes:

$$\delta t=\frac{1}{\ln 2}\xi_0\frac{\tau_\omega^2}{T_d}, \tag{4.6}$$

From the previous discussion it is known that the gate width of DOG can be one cycle of laser oscillation when the SH field is added. For PG to work efficiently, the driving pulse duration has to be around or even less than 5 fs [17, 110, 116]. Since the gate width has been doubled for DOG, either longer pulse duration or shorter delay can be used to produce single attosecond pulse as shown in Fig 4-2.

Experimentally, the DOG was oringinally realized by Mach-Zehnder interferometer method [95]. However, due to the energy loss and the temporal jitter, the interferometer method was replaced by a collinear method as shown in Fig. 4-3[111, 112].

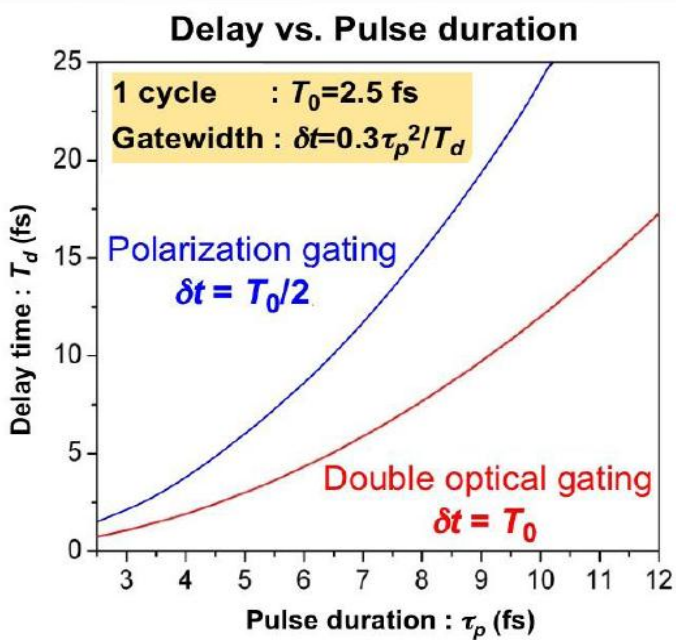

Figure 4-2 Delaly vs. pulse duration for PG and DOG.

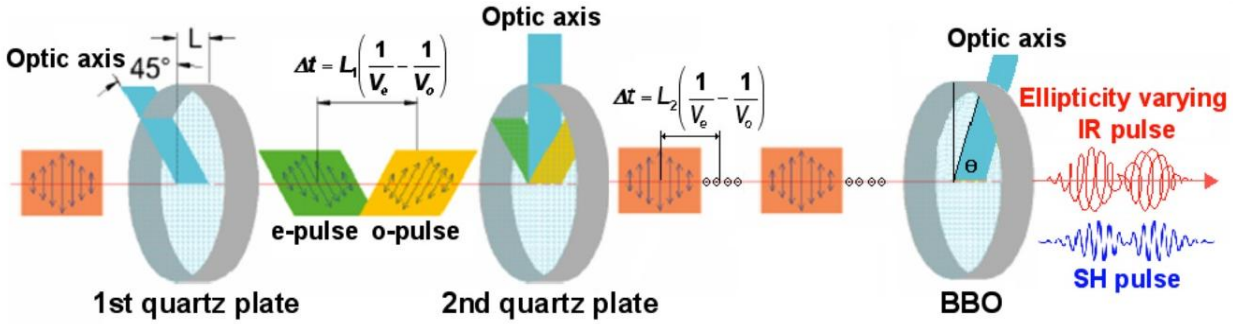

Figure 4-3 Experimental setup of collinear DOG.

This collinear DOG setup is similar to conventional PG except the quarter wave plate is now replaced by the combination of quartz plate and BBO crystal. The laser pulses are sent to an initial quartz plate in order to generate two orthogonally polarized pulses with the required group delay between them that determines the DOG width. The optical axis of the quartz plate is oriented 45° with respect to the polarization direction of the input pulse. For our current experiment, the input pulse duration of NIR is $\tau_\omega = 8\,fs$, and the threshold ellipticity is $\xi = 0.3$. When $\delta t = T = 2.6\,fs$, $T_d = 10.65\,fs$, which is about four cycles of delay. The thickness of the first quartz needs to introduce integer cycles of phase delay in order to keep the electric field correct afterwards.

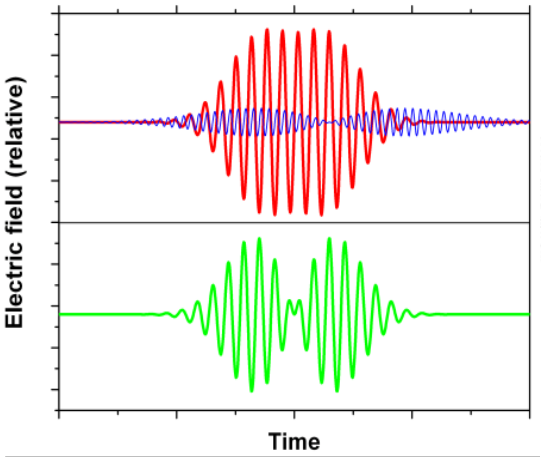

Figure 4-4 Driving field (top) and gating field (bottom) of DOG.

In our case, four cycles of phase delay corresponds to the thickness of 350 μm for the first quartz plate (270 μm thickness for three cycles of phase delay, 430 μm thickness for five cycles of phase delay). The two orthogonally polarized pulses are then sent to a second quartz plate with a thickness of 440 μm. Its optical axis is in the middle of the polarization of these two pulses. Finally, a BBO crystal with thickness of 140 μm generates the SH field. The optic axis of the BBO is aligned in the same plane as the second quartz plate. Since the BBO crystal is negative uniaxial while the quartz is positive uniaxial, the second quartz plate and the BBO combination forms a quarter wave plate for the IR pulses, which transforms the two linearly polarized pulses into two counter-rotating circularly polarized pulse. The electric fields for the driving and gating components are shown and plot in Fig. 4-4.

From Eq. (4.6) above we know that for the same input pulse duration, the DOG only needs half of the delay T_d of PG. Since the driving field at the center of the gate is expressed as [116]:

$$E_{drive}(0) = E_0 e^{-2\ln 2[(T_d/2)^2/\tau_\omega^2]}. \tag{4.7}$$

For the same input laser pulse, the DOG has higher driving field inside the gate than that of PG. In another words, it means that to reach the same intensity of driving field inside the gate, DOG requires less input energy than PG. Based on the ADK calculation (See Appendix A for details of the formula) we can estimate the ionization probability for the DOG and PG assuming the same pulse duration and the same driving field at the center of the gate, from Fig. 4-5 it can be seem that with the peak intensity of $2.8\times10^{14} W/cm^2$, PG doesn't work for the pulse duration

longer than 7 fs because of the ground state depletion of the target. However, DOG can go as long as 12 fs.

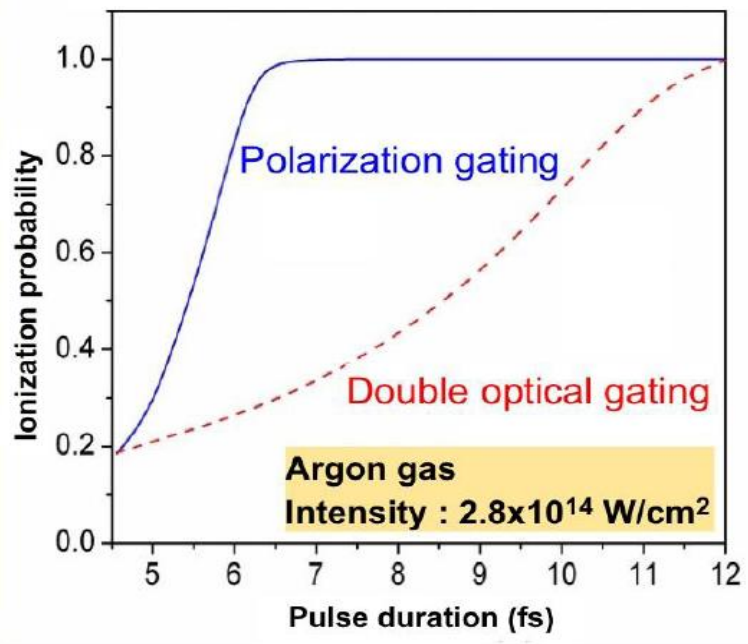

Figure 4-5 Ionization probability calculated by ADK for PG and DOG under different input pulse duration. Figure adapted from Ref [95].

To unambiguously confirm the generation of single attosecond pulses by DOG, the CE phase was scanned. The experiment was done with the CE phase stabilized MARS laser as shown in Chapter 2. The CE phase dependence of the high-order harmonic spectra generated in argon and neon from DOG was measured with an extreme ultraviolet transmission grating spectrometer (more details of XUV spectrometer will be presented in Chapter 5). To generate the short pulse (<10 fs) required by DOG, half of the laser pulse with an energy of 2.5 mJ was sent to a 1m long hollow-core fiber with an inner diameter of 400 μm and filled with neon at a pressure of 2 atm. After self-phase modulation, the 1.2 mJ output laser pulse spectrum cover the region from 600 to 950 nm. The FROG measurement showed that the pulse duration was 7.5 fs after compression by the chirped mirrors as shown in Fig. 4-6, which is short enough to generate a single isolated attosecond pulse [111, 112]. The final output power of the short pulse was 1 mJ after compression of the chirped mirrors. The short pulse was then focused by a 300mm spherical mirror into a 1.5mm gas cell filled with argon at 40 Torr or neon at 60 Torr to generate the HHG. The gas cell was put 1~2 mm after the laser focus to favor the phase matching of the short trajectory [96]. When the CE phase was scanned linearly from 0 to 8π, the continuum

spectrum varied with a 2π periodicity as shown in Fig. 4-7, which is consistent with the 2π periodicity of the electric field generated by DOG [111].

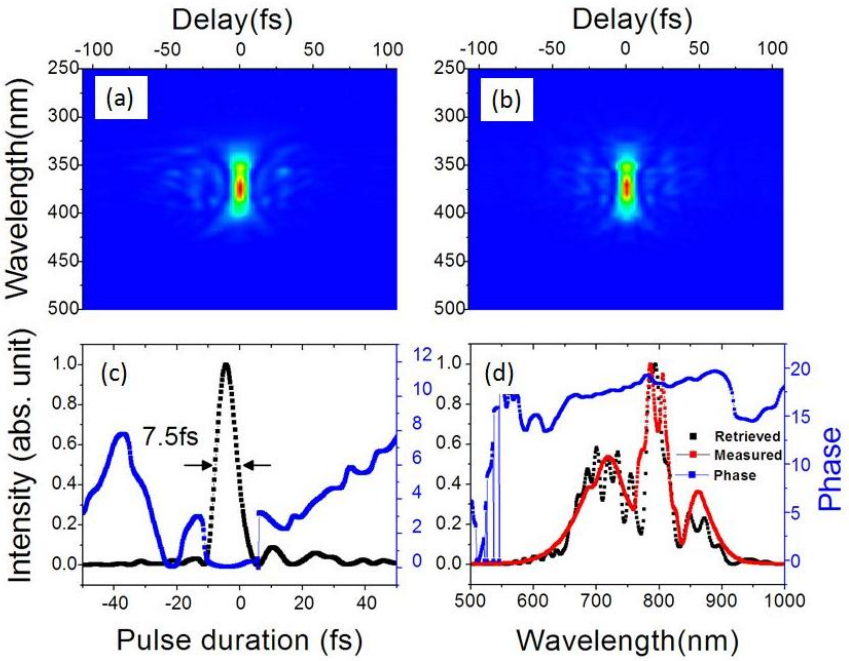

Figure 4-6 FROG measurement of MARS short pulse. (a) The measured FROG trace. (b) The reconstructed FROG trace. (c) The retrieved pulse shape (black dotted curve) and phase (blue dotted curve). (d) The retrieved power spectrum (black dotted curve) and phase (blue dotted line) and independently measured spectrum (red dotted curve).

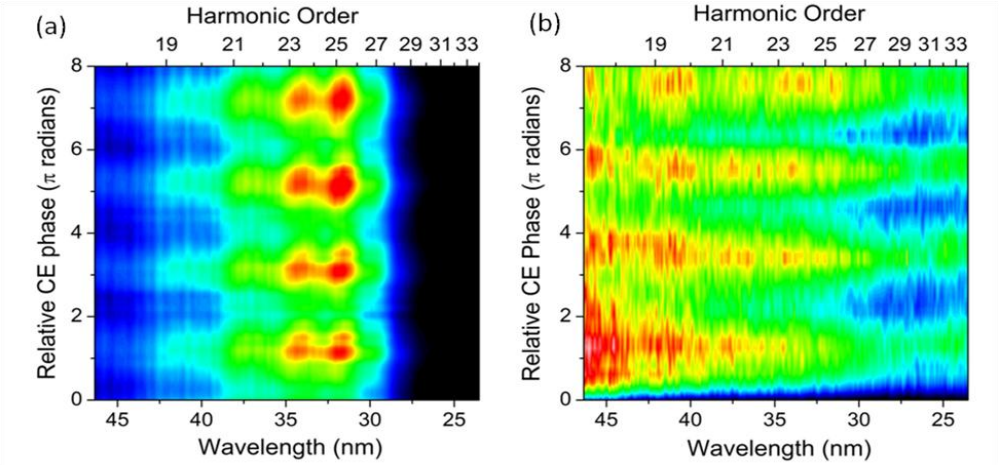

Figure 4-7 DOG harmonic spectra taken with the CE phase scanned from 0 to 8π with (a) argon (b) neon. The 2π periodicity is consistent with the asymmetric electric field of DOG. Figure (a) adapted from Ref [58].

4.2 Practical issues of characterizing the single attosecond pulse

Even though the continuous spectrum from DOG was observed experimentally and the CE phase scan showed 2π periodicity, direct measurement in the temporal domain still needs to be done to ultimately confirm the generation of single attosecond pulses. Like the characterization of femtosecond pulses, for measuring the single attosecond pulse the general rules still hold, but the experiments are more complicated since the XUV wavelength range can easily be absorbed in the air. The energy conversion efficiency of HHG process is low (around 10^{-6}). For a typical milli-joule level CPA laser system, this limits the energy of single attosecond pulse on the order of the nano-joule or even pico-joule level, which makes the nonlinear auto-correlation method difficult to be transferred from visible regime to XUV regime.

Instead the near-infrared (NIR) assisted attosecond streaking technique is used, whereby the momentum of photoelectrons ionized by the XUV pulse in the presence of a NIR streaking field is measured as a function of the time delay between the XUV and NIR pulses [16, 17, 119, 120]. Such measurement yields a two-dimensional spectrogram of delay and electron energy, in which the intensity and phase of both the XUV pulse and NIR streaking field are encoded. Mairesse and Quéré (2005) proposed the use of the Principal Component Generalized Projections Algorithm (PCGPA) [121] for reconstruction of the attosecond pulse from the streaked spectrogram, a technique called FROG-CRAB (Frequency-Resolved Optical Gating for Complete Reconstruction of Attosecond Bursts) [122], which we will refer to only as CRAB. Using this method, a single 130 attosecond XUV pulse generated by polarization gating was successfully retrieved from the streaking spectrogram [17]. Furthermore, 80 as single attosecond XUV pulses generated by amplitude gating were recently retrieved from the streaking spectrogram [16]. However, several practical issues of retrieving attosecond pulses from such two-dimensional spectrograms have hardly been addressed so far. Here we study the effects of five major factors on the pulse retrieval using PCGPA: the count rate, streaking speed, the streaking laser intensity variation, the collection angle of streaked electrons, and the time jitter between the XUV and the streaking field [123].

4.2.1. CRAB Basics

Once the atoms with ionization potential I_p absorb XUV photons, free electrons with momentum $\mathbf{p}$ are produced through dipole transition $d(\mathbf{p})$ from the ground state. Then the strong NIR field introduces a momentum shift to those electrons. The kinetic energy, $W = p^2/2$, of the free electron is measured as a function of the delay τ between the XUV and NIR pulses to construct a spectrogram. In atomic units, the streaked electron spectrogram is expressed as [119, 122]:

$$S(W,\tau) = \left| \int_{-\infty}^{\infty} E_X(t) d[\mathbf{p} + \mathbf{A}_L(t+\tau)] \exp[-i\varphi(\mathbf{p}, t+\tau)] \exp[-i(p^2/2 - \Omega_X + I_p)t] dt \right|^2 , \quad (4.8)$$

$$\varphi(\mathbf{p}, t) = \int_t^{\infty} [\mathbf{p} \cdot \mathbf{A}_L(t') + \frac{1}{2} |\mathbf{A}_L(t')|^2] dt' , \quad (4.9)$$

where $E_X(t)$ is the complex field amplitude of the XUV pulse to be characterized. For simplicity, here we assume the XUV pulse has a Gaussian shape as expressed by

$$E_X(t) \propto \exp[-t^2(1+i\xi)/2\tau_0^2(1+\xi^2)] . \quad (4.10)$$

Here, τ_0 is the transform limited pulse duration of XUV, ξ is the chirp of the XUV pulse, and the XUV pulse duration τ_X is related to the chirp as $\tau_X = \tau_0\sqrt{1+\xi^2}$. Ω_X is the central XUV photon energy. $\mathbf{A}_L(t)$ is the vector potential of the NIR pulse. When the NIR electric field is expressed as $\mathbf{E}_L = \mathbf{E}_0(t)\cos(\omega_L t)$, where ω_L is the carrier frequency and $\mathbf{E}_0(t)$ is the envelope of the NIR pulse assumed as Gaussian shape, the vector potential becomes $\mathbf{A}_L = -\mathbf{E}_0(t)/\omega_L \sin(\omega_L t)$ under the slowly-varying envelope approximation.

In Eq. (4.8), the momentum shift of the classical electron can be understood as a phase modulation of the quantum electron wave packet by the laser field. The phase modulation $\varphi(\mathbf{p}, t)$ is expressed in Eq. (4.9). To understand the physical mechanisms of the phase modulation, we can assume the dipole transition element $|d(\mathbf{p})|^2$ to be constant, since the energy bandwidth of the ionized electrons is narrow compared to the central energy. Under the central momentum approximation we obtain:

$$G(t) = \exp\{-i\int_t^{\infty} [\mathbf{p}_0 \cdot \mathbf{A}_L(t') + \frac{1}{2}|\mathbf{A}_L(t')|^2] dt'\} . \quad (4.11)$$

This measured spectrogram matches the form of CRAB and can be used for reconstruction. Mathematically, the new trace is

$$\hat{S}(W,\tau) \approx \left| \int_{-\infty}^{\infty} E_{\mathrm{X}}(t) G(t+\tau) \exp[-\mathrm{i}(p^2/2 - \Omega_{\mathrm{X}} + I_{\mathrm{p}})t] \mathrm{d}t \right|^2 . \quad (4.12)$$

This expression has the same form as the FROG trace for conventional laser pulse characterization. The phase modulation acts as a temporal phase gate in the FROG language.

Since the gate function is a pure phase modulator $G(t) = e^{-i\varphi(t)}$, the total phase $\varphi(t)$ can be written $\varphi(t) = \varphi_1(t) + \varphi_2(t) + \varphi_3(t)$, with

$$\varphi_1(t) = \int_{t}^{\infty} \mathrm{d}t U_{\mathrm{p}}(t), \quad (4.13)$$

$$\varphi_2(t) = -(\sqrt{8WU_{\mathrm{p}}(t)} / \omega_{\mathrm{L}}) \cos\theta \cos\omega_{\mathrm{L}} t, \quad (4.14)$$

$$\varphi_3(t) = (U_{\mathrm{p}}(t) / 2\omega_{\mathrm{L}}) \sin(2\omega_{\mathrm{L}} t), \quad (4.15)$$

where $U_{\mathrm{p}}(t) = E_0^2(t)/4\omega_{\mathrm{L}}^2$ is the ponderomotive potential, and θ is the observation angle relative to the polarization of NIR pulses [122].

Except where otherwise noted, in the simulation and discussion below the NIR pulse was assumed to be 5 fs in duration with peak intensity of 1×10^{12} W/cm^2 and centred at 800 nm. The XUV spectrum was assumed to support a 90 attosecond transform-limited pulse with a 5000 as^2 linear chirp ($\xi \approx \sqrt{3}$) as the intrinsic chirp of attosecond pulse for the short trajectory electrons, θ is set at zero to maximize the streaking effect, and the delay range was chosen to be 10.67 fs with grid size of 512 by 512 pixels for the CRAB trace.

4.2.2. Shot Noise

Experimentally-obtained CRAB traces, unlike their optical FROG counterparts, are plagued by low count numbers in the spectrogram. A typical setup, such as the one shown in Fig. 4-7 [113], consists of a laser focused to a gas jet for isolated attosecond pulse generation. The number of XUV photons generated in a noble gas is on the order of 10^6 to 10^7 per laser shot [124], very small compared to the photon number of femtosecond NIR lasers. After the XUV photons pass through the residual gas in the chamber from the first jet and the Al filter with a thin layer of Al_2O_3, the number can be reduced to as little as 10%. Further reductions occur from

the low reflectivity of the XUV reflecting optics used in the system as well as small acceptance angles and low quantum efficiency in the detection of the photoelectrons.

The most limiting factor in the count rate is the probability that an XUV photon is absorbed at the second gas jet to generate a photoelectron. The atomic gases used for photoelectron production have photoabsorption cross-sections on the order of 10^{-17} cm^2 at XUV wavelengths [125]. The absorption probability is also a function of the pressure-length product, and the gas pressure is limited by the microchannel plate detector, which requires a vacuum below 10^{-5} torr to avoid damage. Even if the local gas density is maximized by using small gas jets and high backing pressures, the gas density is limited by electron scattering and the probability of photoelectron production is less than 1%. Altogether, attosecond streak cameras with typical XUV coated mirrors, a typical acceptance angle, and typical detectors further reduce the overall efficiency of photoelectron detection to 10^{-6} to 10^{-7}. The low XUV flux from the source and the poor overall detection efficiency limits the number of detected photoelectrons to ~1 per laser shot.

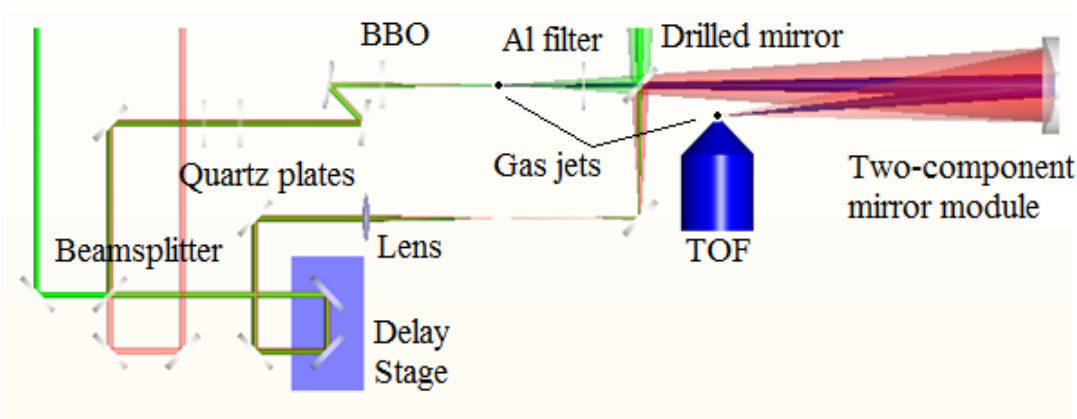

Figure 4-8 Typical setup for the measurement of attosecond pulses consisting of a Mach-Zender configuration. A NIR laser pulse is focused to the first gas jet for attosecond XUV pulse generation. An aluminum filter (Al filter) is used for chirp compensation of the XUV pulse, as well as to block the residual NIR beam. A coated mirror is used to focus the XUV photons to the second gas jet, where the NIR streaking field is superimposed on the XUV focal spot. The momentum spectrum of the streaked electrons falling within the cone of acceptance is measured by a time of flight detector (TOF). The green beam is used for locking the interferometer. Figure adapted from Ref [123].

For such a small number of photoelectrons, statistical counting error or shot noise can

significantly affect the integrity of the streaked spectrogram unless the spectra are recorded for many laser shots. Isolated attosecond pulse generation from all schemes demonstrated so far requires high power, carrier-envelope (CE) phase stabilized laser pulses. Such pulses with uniform pulse energy [67], duration, and CE phase [57] are difficult to maintain over a period of even a few hours, making it a challenge to obtain a sufficiently large statistical sample such that shot noise is negligible. It is thus important to determine how many photoelectron counts are necessary for accurate reconstruction of the attosecond pulse in the presence of shot noise.

4.2.2.1. Simulation of Shot Noise in CRAB Traces

To simulate shot noise in the traces, the spectrogram, shown in Fig. 4-9(a), was resampled to 80 delay steps with step size of ~130 as in order to simulate achievable experimental delay resolution [16, 113]. The energy scale was kept at 512 samples, giving a resolution of ~0.4 eV, which is similar to the energy resolution of previous experiments [16, 113]. In PCGPA, the delay and energy step sizes, $\delta\tau$ and δE respectively, must satisfy the constraint $\delta E \delta\tau = 2\pi / N_{\mathrm{E}}$, where N_{E}, a power of two, is the total number of samples in energy [121, 122]. Experimental CRAB traces must be interpolated in order to satisfy this condition.

The number of counts on each grid point was quantized to integer values with a maximum count of 200, 100, 50, 25, and 10 counts (corresponding to roughly 10000, 5000, 2500, 1250, and 500 total photoelectron counts per delay step), as shown in Fig. 4-9(b) for a maximum pixel count of 50. Shot noise, which follows a Poisson distribution with mean value zero and variance equal to the number of counts at a particular pixel, was simulated using a Monte Carlo method and added to the trace, as shown in Fig. 4-9(c). Finally, bicubic spline interpolation was performed on the trace to return it to a grid size of 512 by 512 pixels suitable for reconstruction with PCGPA, as shown in Fig. 4-9(d). Clearly, the final spectrogram trace with added shot noise in Fig. 4-9(d) is quite dissimilar from the noise-free trace in Fig. 4-9(a). For a more comprehensive study of the effects of shot noise, this process was performed for pulses with spectrum supporting 90 and 180 as transform-limited pulses for several streaking laser intensities and linear chirps.

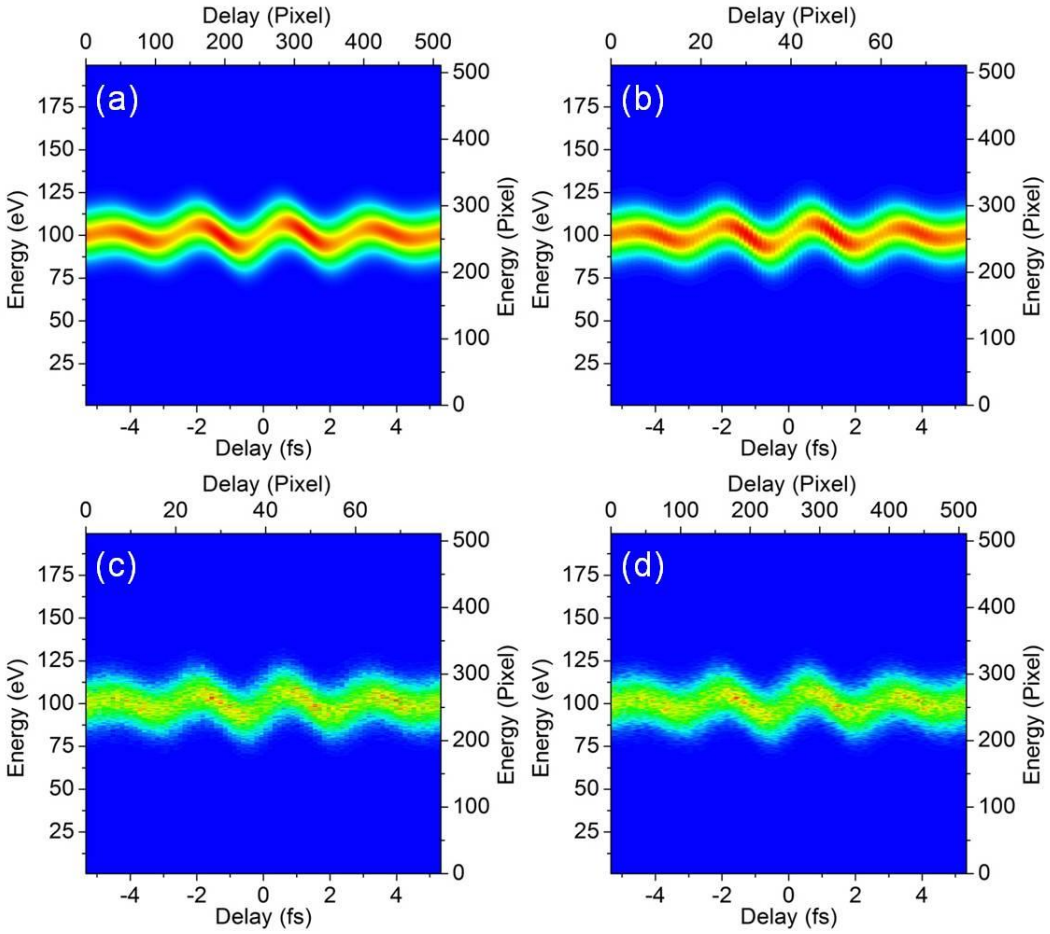

Figure 4-9 Preparation of simulated CRAB traces. All plots are normalized. The XUV spectrum supported a 90 as transform-limited pulse duration and had 5000 as^2 linear chirp. The NIR streaking field had peak intensity of 1×10^{12} W/cm^2. (a) Noise-free trace on a square grid size of 512^2 pixels. (b) The trace was first resampled to 80 delay steps of ~130 as with integer values of counts at each pixel. Here, the maximum pixel count was set to 50. (c) After resampling, shot noise was added as integer values taken from a Poisson distribution centred at zero and with variance equal to the number of counts at each particular pixel. (d) The trace was finally interpolated (using a bicubic spline method) back to a square grid of 512^2 pixels as required for PCGPA. Figure adapted from Ref [123].

4.2.2.2. Effects of Shot Noise on the CRAB Reconstruction

Fig. 4-10 shows the CRAB reconstruction after 1000 iterations for a spectrogram trace with maximum pixel count of 50 and shot noise added. Qualitatively, the reconstructed trace in Fig. 4-10(b) matches more closely to the noise-free trace in Fig. 4-9(a) than it does to the trace with shot noise added shown in Fig. 4-10(a), which is reproduced from Fig. 4-9(d).

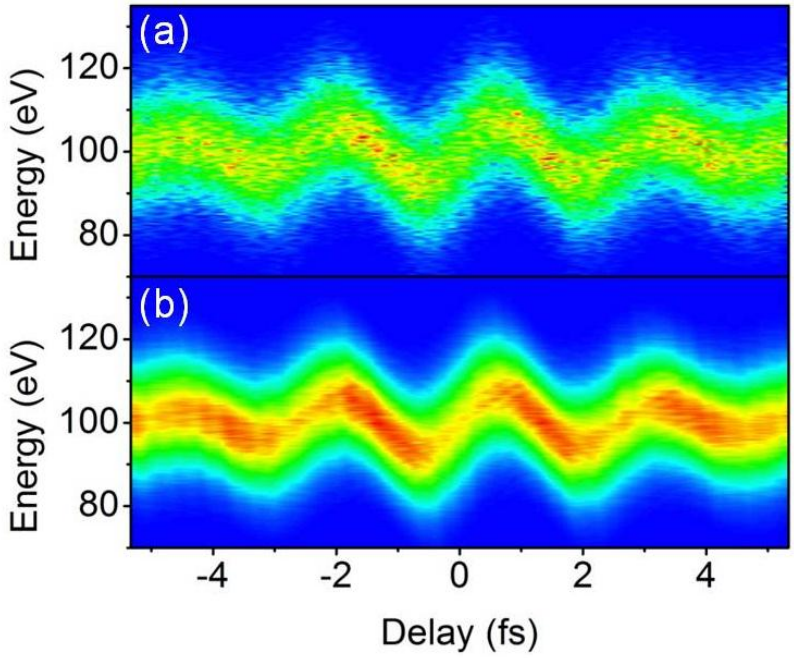

Figure 4-10 (a) Detail of interpolated trace given as input to the PCGPA algorithm, reproduced from figure 2(d). (b) Detail of reconstructed pulse after 1000 iterations of PCGPA. The FROG error was 5.6%. Clearly, the algorithm has retrieved a trace which qualitatively matches the features of the noise-free trace in figure 2(a) more closely than the noisy trace which it was given. Figure adapted from Ref [123].

In order to quantitatively determine the convergence of a FROG algorithm, the FROG error is typically used. The FROG error indicates the degree to which the retrieved and experimental FROG traces match. However, a trace with noise added is fundamentally an incorrect trace and is likely unphysical. It is thus more useful to define a convergence criterion that indicates how well the algorithm has converged to both the noisy trace and the noise-free trace.

We utilize the convergence criterion described by Fittinghoff for optical FROG traces [126], and consider convergence to have occurred in a trace with added noise for

$$R = \varepsilon\left[\tilde{I}^{\mathrm{FROG}}, I^{\mathrm{FROG}}\right] \Big/ \varepsilon\left[I_{\mathrm{n}}^{\mathrm{FROG}}, I^{\mathrm{FROG}}\right] < 2\,, \tag{4.16}$$

where

$$\varepsilon[A,B] = \left[\frac{1}{N^2}\sum_{i=1}^{N}\sum_{j=1}^{N}(A_{ij}-B_{ij})^2\right]^{1/2} \Bigg/ \left[\frac{1}{N^2}\sum_{i=1}^{N}\sum_{j=1}^{N}B_{ij}^2\right]^{1/2}, \tag{4.17}$$

I^{FROG} is the noise-free trace, $I_{\mathrm{n}}^{\mathrm{FROG}}$ is the trace with noise added, and $\tilde{I}^{\mathrm{FROG}}$ is the reconstructed trace. In Eq. (4.17), A_{ij} and B_{ij} represent the pixel located at coordinate (i, j) in each two-dimensional trace and N is the number of pixels in each dimension. In our case, $I_{\mathrm{n}}^{\mathrm{FROG}}$ was interpolated to a grid of 512 by 512 pixels before calculating the convergence criterion. The critical criterion for convergence is set to R less than 2 rather than 1 because the algorithm is given only the noisy trace as input, and we thus cannot expect it to reproduce the noise-free trace.

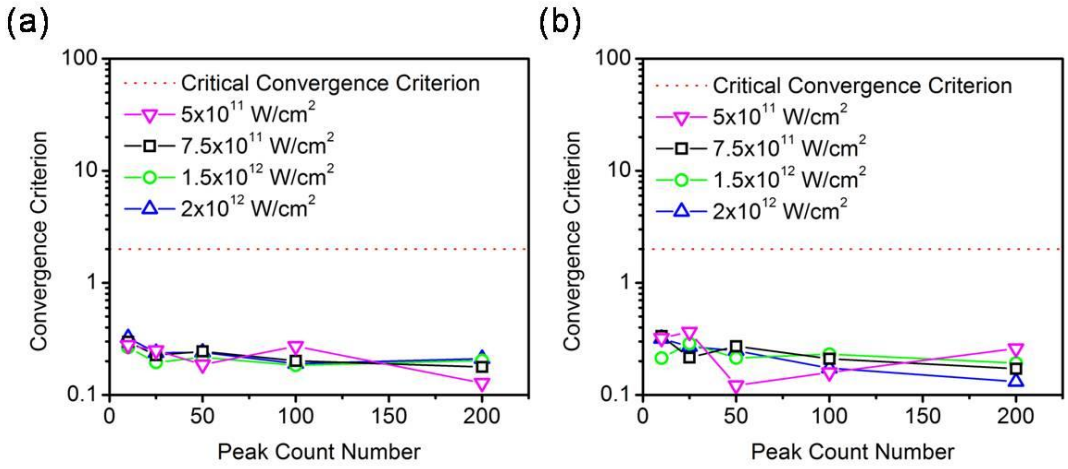

Figure 4-11 Convergence criterion of the retrieved CRAB traces for several streaking intensities from 5×10^{11} to 2×10^{12} W/cm^2. (a) XUV spectrum supporting 90 as transform-limited pulses, with 5000 as^2 linear chirp. (b) XUV spectrum supporting 180 as transform-limited pulses, with 5000 as^2 linear chirp. For all values of peak count number, the convergence criterion is less than 1. Figure adapted from Ref [123].

In fact, as is shown in Fig. 4-11, R is found to be much less than 1 for all values of the maximum pixel count regardless of the XUV bandwidth and NIR streaking intensity (5×10^{11} to 2×10^{12} W/cm^2), indicating that the algorithm converges to a solution much closer to the noise-free CRAB trace than to the noisy trace which it was given. This is similar to the case of optical

FROG in the presence of noise [126], and is likely due to the significant redundancy contained in the CRAB trace. In fact, the attosecond pulse itself contains only $2N_\tau$ degrees of freedom, where N_τ is the number of delay steps after interpolation, whereas the CRAB trace has $N_\tau N_E$ degrees of freedom. Also, the attosecond pulse is completely encoded in a single cycle of the CRAB trace, whereas the results shown here are for 4-cycle traces. Because of this significant redundancy, the algorithm is able to effectively ignore the noise and retrieve something more closely related to the noise-free trace. Moreover, the noisy trace is unlikely to correspond to a physical result, as the noise generally does not satisfy the intensity constraint of PCGPA. In fact, the vast majority of two-dimensional maps do not correspond to CRAB traces of physical pulse and gate combinations. The algorithm, however, can retrieve only a physically allowed trace corresponding to a unique XUV pulse and streaking field combination.

4.2.2.3. The Effects of Shot Noise on XUV Pulse Retrieval

The retrieved attosecond XUV pulse intensity and phase are shown for the cases of 200 and 10 counts in Fig. 4-12(a). Also, as is shown in Fig. 4-12(b), the noise in the wings of the pulse is much larger for fewer counts. The full-width at half-maximum (FWHM) pulse duration and the linear chirp for our retrievals are plotted in Fig. 4-13. For CRAB traces with at least 50 counts for the maximum pixel, we find that we are able to retrieve the pulse duration and linear chirp within 5% of their actual values when the streaking intensity is greater than 5×10^{11} W/cm^2 for XUV pulses with spectrum supporting 90 as transform-limited durations. These values are similar to the experimental error in previous measurement of sub-100 as pulses [16]. Similarly, when the XUV spectrum supports 180 as transform-limited pulses, we are able to retrieve the pulse duration within 3% and the linear chirp within 5% for traces with 50 counts or more. However, as the number of counts is further decreased, the algorithm begins to severely miscalculate the pulse duration, indicating that it has failed to converge to an accurate result. Our simulations indicated that the pulse durations were underestimated for pulses with large values of ξ, whereas they were overestimated for nearly transform-limited pulses.

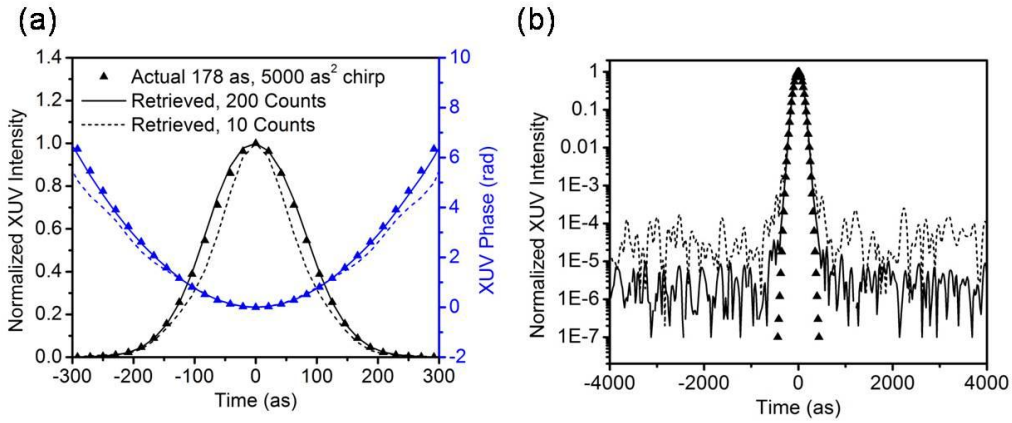

Figure 4-12 (a) Normalized XUV intensity and phase. (b) Normalized XUV intensity on log scale. The streaking intensity was 1×10^{12} W/cm^2. The triangles show the noise-free pulse, whereas the solid line and dashed line show the retrieved pulses with 200 counts and 10 counts at the peak of the energy spectrum, respectively. Figure adapted from Ref [123].

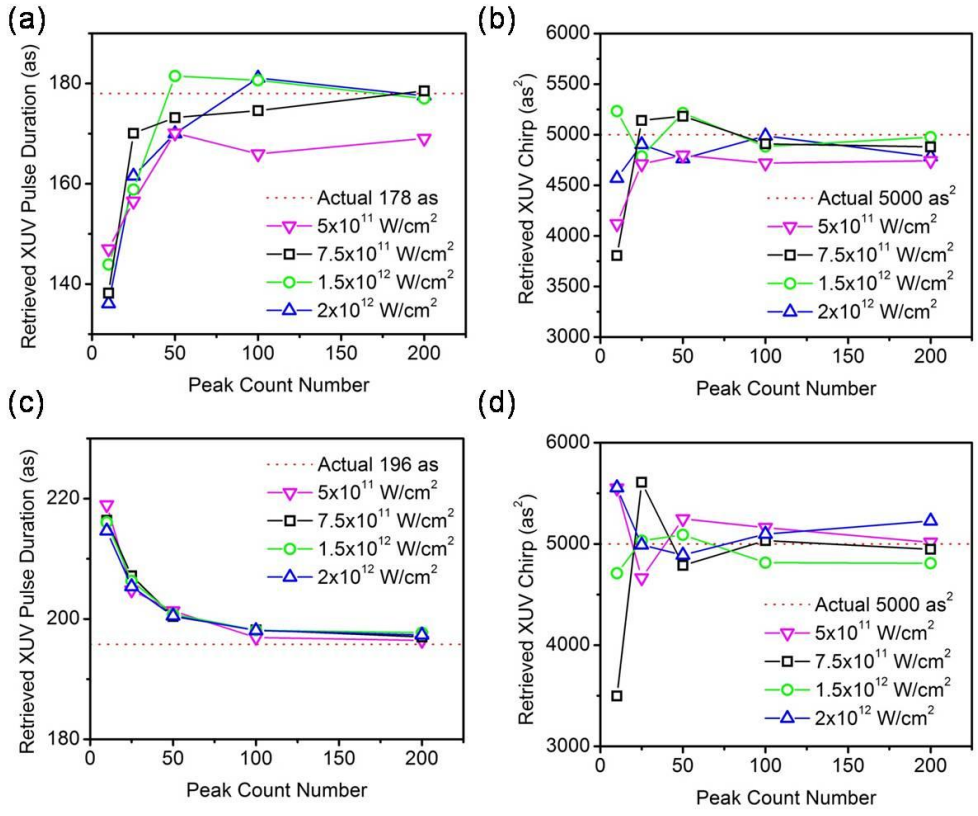

Figure 4-13 (a) Retrieved XUV pulse duration and (b) retrieved linear chirp for pulses with spectrum supporting 90 as transform-limited pulses. For peak count numbers above 50, the

pulse duration and linear chirp are retrieved within 5% of their actual values for streaking intensities greater than 5×10^{11} W/cm^2, indicating convergence of the algorithm. (c) Retrieved XUV pulse duration and (d) retrieved linear chirp for pulses with spectrum supporting 180 as transform-limited pulses. For peak count numbers above 50, the pulse duration is retrieved within 3% and the linear chirp within 5% of their actual values. Figure adapted from Ref [123].

4.2.2.4. Effects of Count Rate on Experimental Data

In order to further test the pulse retrieval with CRAB, experimental attosecond streaking data was used [113]. The isolated attosecond pulses were generated with the DOG. Because our data acquisition system saves the photoelectron energy spectrum recorded for each laser shot, we are easily able to select only a sample of data taken within a given time frame. In the experiment, the photoelectron energy was measured at 32 delay steps with step size of 333 as for 60 seconds, or around 55,000 laser shots, each. The spectral bandwidth supported attosecond pulses with transform-limited pulse durations of 137 as. The detector had 100 energy channels spanning 50 eV, and a resolution of 0.7 eV determined by the precision of our timing electronics and the length of the TOF tube. By analyzing only the data from selected laser shots, we can observe what the resulting CRAB trace would be for accumulation times less than 60 seconds.

Fig. 4-14 shows the reconstructed attosecond temporal profile and phase for effective accumulation times of 60 and 2 seconds (corresponding to total photoelectron counts of roughly 24500 and 800 for each delay step). It is important to note that the measured CRAB traces are corrected for background noise, such as above-threshold ionization electron counts, and the dipole transition matrix element corresponding to the measured photoelectron momentum before reconstruction. However, such a correction is easily made and is independent from the shot noise. As can be seen in Fig. 4-14(a) and (b), a decrease in the accumulation time by more than an order of magnitude yields only small differences in the temporal profile and phase of the reconstructed XUV pulse. Fig. 4-14(c) shows the same temporal profiles as in (a) on a log scale. A substantial increase in the noise in the wings of the pulse is present, just as in the simulated pulses. Such error in the wings of the pulse is to be expected, due to the small number of photoelectron counts corresponding to the low-intensity portions of the pulse. Fig. 4-14(d) shows

the FWHM pulse duration for the different retrievals, as a function of the peak count number. The peak count number here must include the shot noise, as it is taken from experimental data.

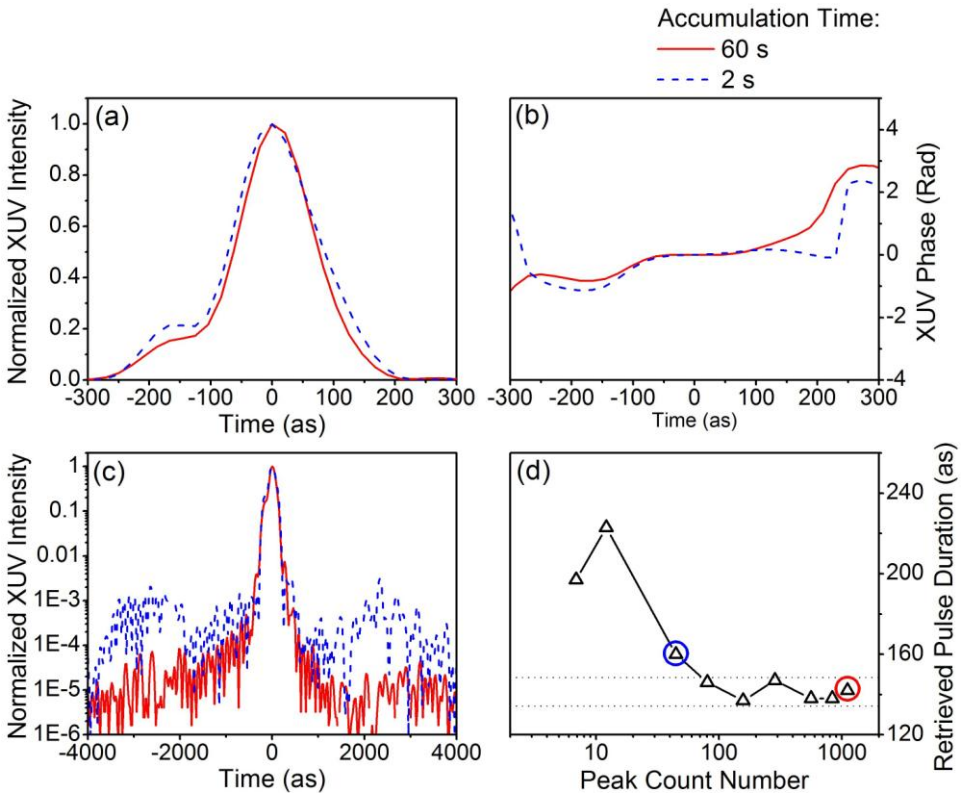

Figure 4-14 (a) Temporal profile of the retrieved attosecond pulse for 60 s (solid red line) and 2 s (dashed blue line) accumulation time. (b) Temporal phase of the retrieved pulse. (c) Log scale plot of the temporal profile. (d) Retrieved XUV pulse duration. The dotted lines indicate a window of ±5% centred at a duration of 141 as, which includes all of the retrieved pulse durations for accumulation times of 4 s and larger. The circles indicate the pulses shown in (a), (b), and (c). The peak counts measured here include the shot noise, and we thus expect that the roughly 80 counts at the peak of the two-dimensional spectrogram corresponding to 4 s accumulation time should relate quite closely to the 50-count simulations due to the statistical nature of the shot noise. Figure adapted from Ref [123].

4.2.3. Streaking Speed

Classically, streaking can be understood as the momentum shift of a free electron by the NIR field as shown in Fig. 4-15, where the momentum shift $\Delta\vec{p}$ equals to the vector potential $A(t_0)$ at electron birth time t_0.

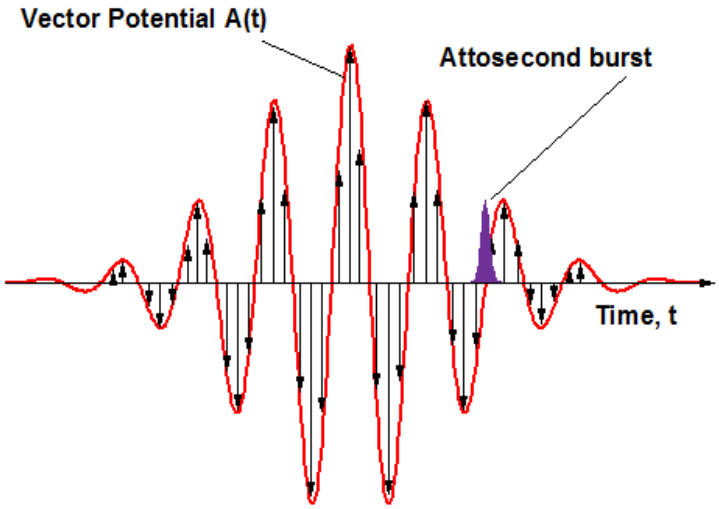

Figure 4-15 Classical picture of attosecond steaking.

According to the Rayleigh criterion, in order to resolve two events separated by Δt in time, they must be shifted with respect to each other by at least as much as their own spectral width [119, 127]. When the quiver energy $U_p(t) = E_0^2(t)/4\omega_L^2$ is much less than central energy $W_0 = p_0^2/2$, the minimum XUV pulse duration that can be measured is determined by [127]:

$$\delta t = \frac{T_L}{2\pi}\sqrt{\frac{\omega_L}{\Delta W}} \quad , \tag{4.18}$$

where T_L is the period of the NIR field, and ΔW is the energy shift caused by the NIR streaking field. Using this criterion for a NIR laser centred at 800 nm, in order to resolve a 90 as XUV pulse centred at 60 eV such as was generated most recently [16], at least 28 eV of ΔW is required, which corresponds to the minimum NIR laser peak intensity of $5.5\times10^{13}\text{W/cm}^2$. Such high intensity of the NIR field can produce free electrons through multi-photon ionization and above-threshold ionization (ATI). Since the cutoff energy of rescattered electrons from ATI can reach $10U_p$ (~33 eV), the ATI electrons overlap with the streaked XUV photoelectrons and add significant background noise to the CRAB trace [120, 128]. To minimize the effect of ATI background, in the early experiments the streaked electrons were collected perpendicular the polarization of the NIR and XUV pulses [14].

When the CRAB trace is used to characterize the XUV pulse, the measurement of the attosecond pulse is converted into a 2-D phase retrieval problem, which is well known in many

other fields [129]. In principle, since the 2-D trace has redundant information and phase retrieval in two or more dimensions essentially always yields a unique solution [129], the high streaking speed required by the Rayleigh criterion above may not be necessary.

4.2.3.1. The dependence of minimum streaking intensity on XUV bandwidth

When the PCGPA algorithm was applied on noisy data with a maximum count of 50 or more, it was found that even with a streaking intensity of $7.5\times10^{11}\mathrm{W/cm^2}$, nearly two orders of magnitude smaller than the value based on the Rayleigh criterion, PCGPA can correctly retrieve the XUV pulse with spectrum supporting a 90 as transform-limited pulse after 1000 iterations as shown in Fig. 4-13(a) and (b). As the maximum count increases, the retrieved pulse duration and chirp become closer to the actual values. Especially for the XUV pulse with spectrum supporting a 180 as transform-limited pulse, the retrieved pulse duration converges in the same way for all the streaking intensities as the maximum count rate increases. Although this minimum streaking intensity is much less than the prediction from the classical streaking camera, our simulations show that it still depends on the bandwidth of the XUV pulse. As shown in Fig. 4-13(a) and (c), when the NIR streaking intensity is $5\times10^{11}\mathrm{W/cm^2}$, the pulse duration is never accurately reconstructed for pulses with spectrum supporting 90 as transform-limited pulses, whereas it is retrieved quite well for pulses with spectrum supporting 180 as transform-limited pulses as the peak count is increased. Therefore, for larger bandwidths, higher streaking intensities are required.

This conclusion is similar to the prediction from classical streaking camera and can be understood from the 2-D pulse retrieval point of view. If the intensity of NIR streaking field is zero, the CRAB trace is only a collection of XUV photoelectron spectra, and no phase information of the XUV pulse is embedded. As the intensity of the NIR streaking field is increased, the ratio between the streaked part and the unstreaked part in the CRAB trace also increases. If the CRAB trace is ideal and an infinite number of iterations of the PCGPA can be run, theoretically there always exists a unique solution to the CRAB trace even when the streaking intensity is low. However, the signal-to-noise ratio of CRAB trace is limited by the maximum count rate in the experiment, and the PCGPA cannot be run for an infinite number of iterations. Therefore, for experimental data the ratio between the streaked part and the unstreaked part in CRAB trace must reach a threshold value for full characterization of the XUV pulses. In

order to reach a similar ratio, spectra with larger bandwidth need to be streaked more, which corresponds to a higher minimum streaking intensity.

4.2.3.2. The dependence of minimum streaking intensity on XUV chirp

Unlike optical FROG, in CRAB the NIR field acts only as a phase modulator in the time domain. When a chirped XUV pulse is streaked by the NIR field, the phase modulation from the NIR field either enhances or cancels the phase of the XUV pulse and generates a streaking trace with asymmetry in each NIR cycle, which contributes to the retrieval of the linear chirp parameters. Therefore, to discuss the minimum streaking intensity requirement in a more comprehensive way, the linear chirp of an XUV pulse with spectrum supporting a 90 as transform-limited pulse was scanned with the above streaking intensities. The peak count was set at 100 to satisfy the convergence discussion above. As shown in Fig. 4-16(a) and (b), even with the linear chirp of 20000 as^2, for which the XUV pulse duration was broadened to one quarter of the NIR cycle, both the pulse duration and the linear chirp of the XUV pulse can be retrieved with high accuracy, which can be attributed to the advantage of 2-D phase retrieval.

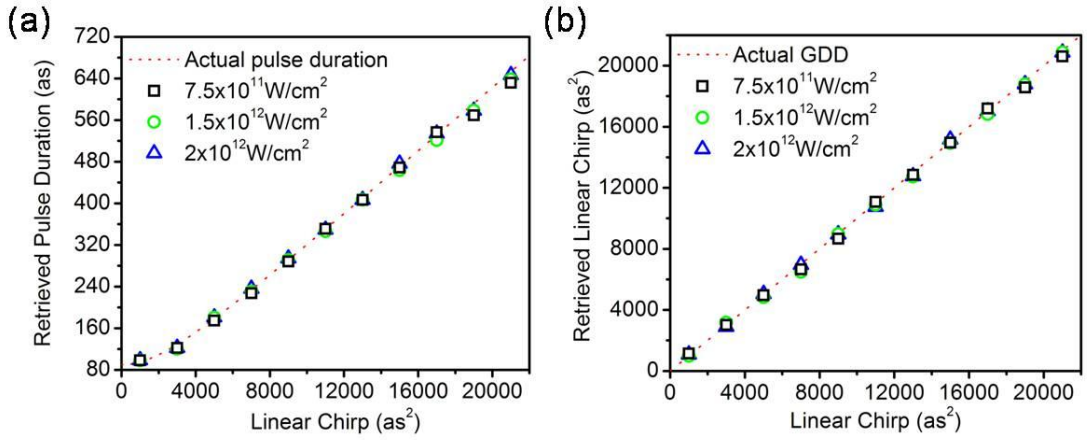

Figure 4-16 (a) Retrieved XUV pulse duration as a function of input linear chirp for different streaking intensities. (b) Retrieved linear chirp as a function of input linear chirp for different streaking intensities. Figure adapted from Ref [123].

Thus the CRAB method requires much lower streaking intensity than the classical streaking camera method to measure the same isolated XUV pulse. This conclusion removes the NIR intensity constraint of measuring attosecond pulses, which is important for characterization of even shorter attosecond pulses.

4.2.4. Laser intensity variation

In the streaking experiments, the electrons are produced within a volume of the target gas determined by the XUV spot size and the length of the interaction region. Within this volume, the streaking laser intensity varies both transversely and longitudinally as shown in Fig. 4-17.

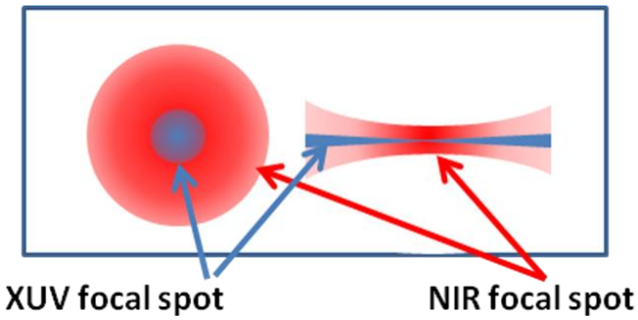

Figure 4-17 Volume effect in streaking experiment.

Specifically, with the drilled mirrors or annular mirrors usually used to reflect and focus the streaking laser beam [16, 17, 113], a Bessel beam is produced at the focal point due to the truncation of the Gaussian beam [130]. The spot size of the central Bessel spot is limited by the inner diameter of the drilled mirror or annular mirror and is smaller than the untruncated case. On the other hand, typical mirrors used to focus the XUV pulses to the target gas have surface accuracy distances many times larger than the XUV wavelength, which can lead to an XUV focal spot similar in size to the NIR focal spot. Photoelectrons born at different locations are thus streaked by different laser intensities, which causes smearing along the energy axis of the CRAB trace.

In order to study this effect, CRAB traces simulated using different NIR streaking intensities were averaged together and sent to the PCGPA for retrieval. We assumed the XUV and NIR focal spots to be Gaussian in shape, and weighted the average by the relative XUV photon number corresponding to each intensity. Fig. 4-18 shows the retrieval results for XUV pulses with a spot size ratio of $w_{XUV}/w_{IR}=0.5$, where w_{XUV} and w_{IR} are the $1/e^2$ radii of the XUV and NIR focal spots. Because of the intensity averaging effect, the CRAB trace becomes blurred along the energy axis as is shown in Fig. 4-18(a). However, as is shown in Fig. 4-18(b), the PCPGA is able to retrieve a trace which matches the averaged trace very closely. In Fig. 4-18(c) the retrieved XUV pulse duration and phase exactly match the original values, and the retrieved gate phase from the averaged CRAB trace is nearly identical to the weighted average of the gate phases corresponding to each streaking intensity, as shown in Fig. 4-18(d).

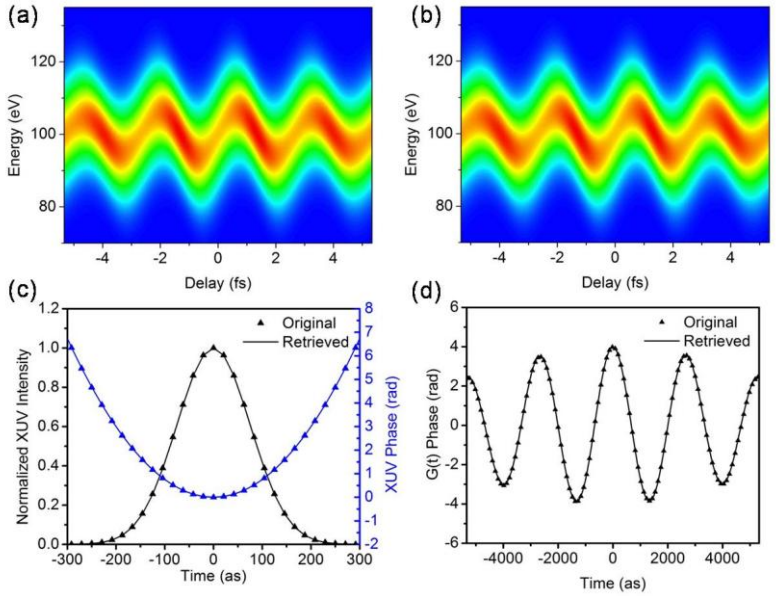

Figure 4-18 (a) Averaged CRAB trace when w_{XUV}/w_{IR}=0.5. (b) Retrieved CRAB trace. (c) Original and retrieved XUV pulse and phase. (c) Original and retrieved gate phase. Figure adapted from Ref [123].

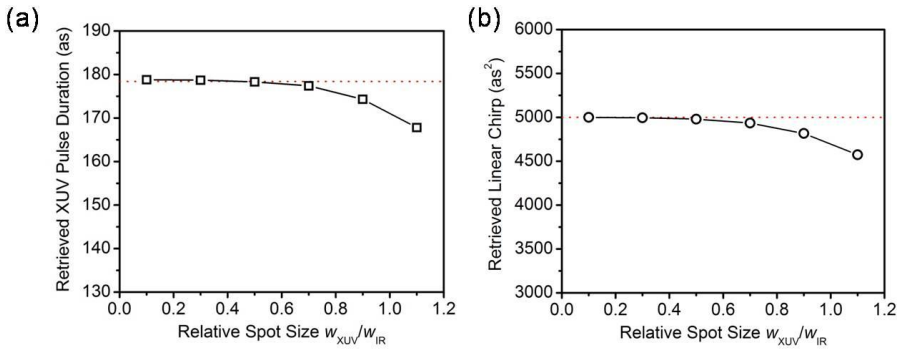

Figure 4-19 Retrieved (a) XUV pulse duration and (b) XUV linear chirp as a function of the spot size ratio w_{XUV}/w_{IR}. The red dashed lines indicate the actual values, whereas the black open shapes represent the retrieved values. Figure adapted from Ref [123].

For a more general test of the CRAB retrieval under intensity fluctuation, averaged CRAB traces with different w_{XUV} to w_{IR} spot size ratio were simulated. As shown in Fig. 4-19 (a) and (b), when the XUV to NIR spot size ratio becomes larger than 0.5, the retrieved XUV pulse duration and phase start to deviate from the actual values. However, even when the XUV spot size is comparable to the NIR spot size at the focus, the XUV pulse duration and linear chirp can

still be retrieved within an accuracy of 5%. This releases the constraint of constant streaking intensity and can easily be realized experimentally.

4.2.5. Collection angle of streaked electrons

Due to the low photon flux and small cross section of the XUV interaction with atoms, the streaked electrons are usually collected within a certain range of solid angle in order to maximize the count and reduce the statistical noise of the CRAB trace [113, 131, 132]. Since the gate phase is a function of the collection angle [122], the smearing effect should be taken into consideration when the CRAB trace is collected within a certain solid angle. In our simulation, we assume the asymmetric parameter to be β=1.4 [133] to resemble the angular distribution of photoelectrons ionized from a Neon gas target centred at 100 eV. The spherical integration and the angular distribution of the photoelectrons are multiplied together in the weighted average of the CRAB trace as shown in Eq. (4.19), where θ_0 is the maximum collection angle, and $\bar{S}(W,\tau,\theta_0)$ is the average CRAB trace.

$$\bar{S}(W,\tau,\theta_0)=\int_0^{2\pi}\int_0^{\theta_0}\hat{S}(W,\tau,\theta)[1+\frac{\beta}{2}(3\cos^2\theta-1)]\sin\theta d\theta d\varphi, \tag{4.19}$$

In Fig. 4-20, when the maximum collection angle was set to 40 degrees, the retrieved the trace looks very similar to the averaged trace, and the XUV pulse duration and phase, as well as the NIR gate phase, are fully recovered.

Since in some experiments, such as those using magnetic bottle detectors or velocity map imaging, the total collection angle of the streaked photoelectrons can reach 2π or 4π solid angle [131, 132], which corresponds to a maximum collection angle θ of 90 or 180 degrees. However, due to the symmetry of the photoelectron emission, the CRAB trace resulting from a maximum collection angle of 180 degrees should be identical to that from 90 degrees. Therefore, we simulated CRAB traces for different maximum collection angles ranging from θ=10 to 90 degrees. As shown in Fig. 4-21(a) and (b), when the maximum collection angle is below 40 degrees, the XUV pulse duration and chirp can be retrieved exactly. Even when the collection angle is further increased to 90 degrees, for which the photoelectrons emitted orthogonally to the streaking laser polarization direction are also collected, the XUV pulse duration and linear chirp can still be retrieved within an error of 5%. This property of the CRAB opens the door for

detection schemes with large collection angles, such as magnetic bottle detectors and velocity map imaging [131, 132].

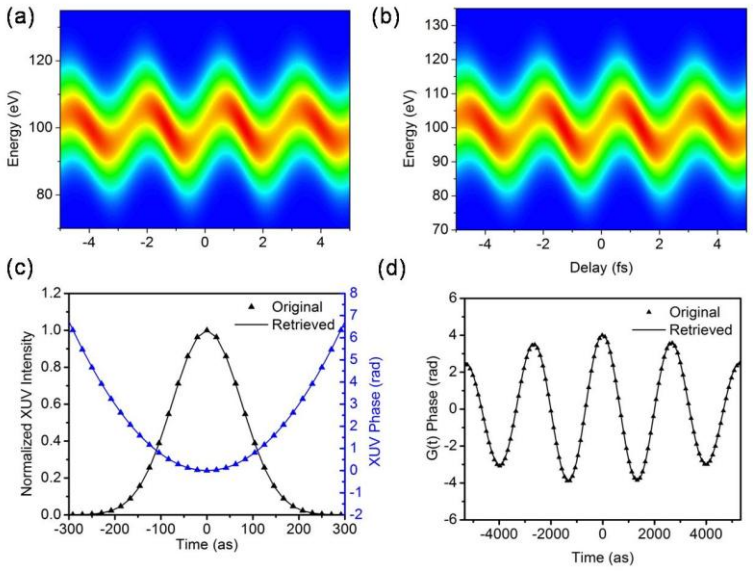

Figure 4-20 (a)Averaged CRAB trace when the maximum collection angle of photoelectrons is 40 degrees. (b) Retrieved CRAB trace. (c) Original and retrieved XUV pulse and phase. (d) Original and retrieved gate phase. Figure adapted from Ref [123].

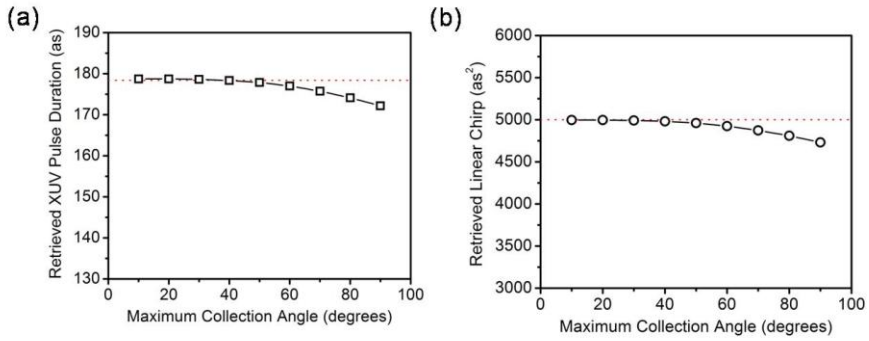

Figure 4-21 Retrieved (a) XUV pulse duration and (b) XUV linear chirp as a function of the maximum collection angle θ_0. The red dashed lines indicate the actual values, whereas the black open shapes represent the retrieved values. Figure adapted from Ref [123].

4.2.6. Time delay jitter

In the streaking experiment, the NIR streaking beam and XUV beam propagate through different optics. Due to mechanical vibration, the time delay between them fluctuates from one

laser shot to the next [113], which broadens the CRAB trace along the delay axis. To study this effect on the final attosecond pulse reconstruction, a CRAB trace was generated by replacing the photoelectron spectrum at each delay step with the average of those from neighbouring delays. More specifically, the averaged CRAB trace is given by:

$$\bar{S}(W,\tau,\Delta\tau_0) = \int_{-\Delta\tau_0/2}^{\Delta\tau_0/2} S(W,\tau+t)dt \tag{4.20}$$

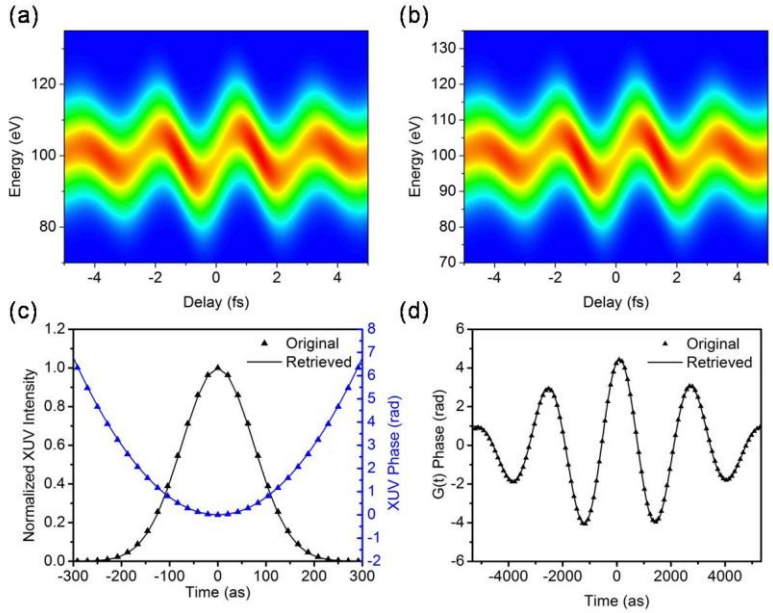

Figure 4-22 (a)Averaged CRAB trace when the time delay jitter is ~200 as. (b) Retrieved CRAB trace. (c) Original and retrieved XUV pulse and phase. (d) Original and retrieved gate phase. Figure adapted from Ref [123].

where $\Delta\tau_0$ is the delay jitter. In Fig. 4-22, when the delay jitter was ~200 as, comparable to the XUV pulse duration, the retrieved the trace looks very similar to the averaged trace, and the XUV pulse duration and phase, as well as the NIR gate phase, are accurately retrieved. As shown in Fig. 4-23(a) and (b), when the delay jitter is ~100 as, the XUV pulse duration and chirp can be retrieved exactly. Even when the delay jitter goes to one quarter of the NIR laser cycle, the XUV pulse duration can still be retrieved within an error of 6% and the linear chirp can be retrieved within an error of 10%. For streaking experiments with many-cycle streaking laser pulses for which the slowly varying envelope approximation holds, this type of timing jitter between the XUV and NIR pulses can also be interpreted as the fluctuation of the CE phase from one laser

shot to the next. Thus, this property of the CRAB relaxes the need for tight CE phase locking and delay stability in streaking experiments.

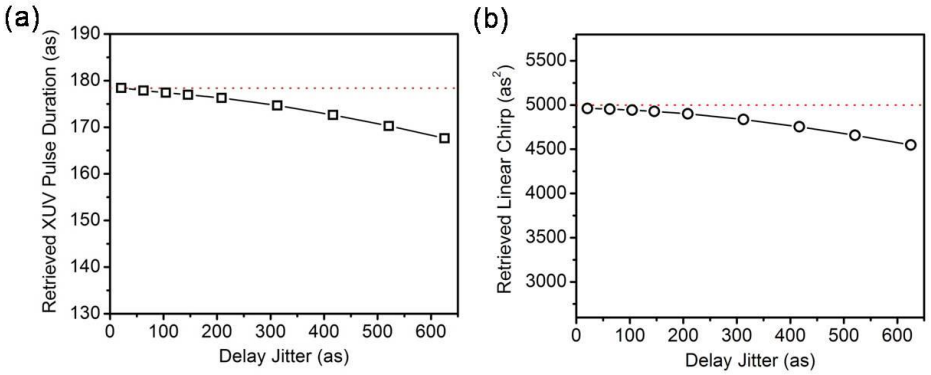

Figure 4-23 Retrieved (a) XUV pulse duration and (b) XUV linear chirp as a function of the time delay jitter. The red dashed lines indicate the actual values, whereas the black open shapes represent the retrieved values. Figure adapted from Ref [123].

4.2.7. Linearity discussion

The simulations of sections 4, 5 and 6 reveal the linear property of CRAB traces, i.e., the summation of two CRAB traces is approximately equal to a third physical CRAB trace. To shed some light on this property, we start from Eq. (4.8) and (4.9) and derive the analytical result of the spectrogram for a sufficiently short XUV pulse using the saddle point approximation [119].

$$S(W,\tau) \propto \frac{|\, d(\mathbf{p}+\mathbf{A}_{\mathrm{L}}(t_0+\tau))E_{\mathrm{X}}(t_0)\,|^2}{\mu} \exp\{-[\frac{(\mathbf{p}+\mathbf{A}_{\mathrm{L}}(t_0+\tau))^2}{2}-W_0]^2\frac{\tau_0^2}{\mu^2}\}, \tag{4.21}$$

where $\mu=\sqrt{(1+\eta\xi)^2+\eta^2}$ and $\eta=\mathbf{E}_{\mathrm{L}}(t_0+\tau)\mathbf{p}(t_0)\tau_0^2$. When $\mathbf{E}_{\mathrm{L}}$ and $\mathbf{A}_{\mathrm{L}}$ are small enough, we can Taylor expand Eq. (5.21) to a first order approximation. The spectrogram can then be written as:

$$\begin{aligned} S(W,\tau) \propto & |\, d(\mathbf{p}+\mathbf{A}_{\mathrm{L}}(t_0+\tau))E_{\mathrm{X}}(t_0)\,|^2 \exp[-(\frac{p^2}{2}-W_0)^2\tau_0^2] \\ & \times[1-2\mathbf{A}_{\mathrm{L}}(t_0+\tau)\mathbf{p}(\frac{p^2}{2}-W_0)\tau_0^2+2\mathbf{E}_{\mathrm{L}}(t_0+\tau)\mathbf{p}(\frac{p^2}{2}-W_0)^2\xi\tau_0^4-\mathbf{E}_{\mathrm{L}}(t_0+\tau)\mathbf{p}\tau_0^2\xi]. \end{aligned} \tag{4.22}$$

From Eq. (4.22), the streaked spectrogram can be decomposed into an unstreaked spectrogram multiplied by terms that have a linear relationship with $\mathbf{A}_{\mathrm{L}}$ and $\mathbf{E}_{\mathrm{L}}$. The averaged

values $\overline{\mathbf{A}}_{\mathrm{L}}$ and $\overline{\mathbf{E}}_{\mathrm{L}}$ for any accumulated spectrogram from different $\mathbf{A}_{\mathrm{i}}$ and $\mathbf{E}_{\mathrm{i}}$ can be expressed as:

$$\overline{\mathbf{A}}_{\mathbf{L}} = \frac{\sum \rho_i \mathbf{A}_i}{\sum \rho_i}, \tag{4.23}$$

$$\overline{\mathbf{E}}_{\mathbf{L}} = \frac{\sum \rho_i \mathbf{E}_i}{\sum \rho_i}, \tag{4.24}$$

where ρ_{i} is the weight of $\mathbf{A}_{\mathrm{i}}$ and $\mathbf{E}_{\mathrm{i}}$. This shows a linear combination of different $\mathbf{A}_{\mathrm{i}}$ and $\mathbf{E}_{\mathrm{i}}$ can still yield a spectrogram as if it is streaked by an average value of $\overline{\mathbf{A}}_{\mathrm{L}}$ and $\overline{\mathbf{E}}_{\mathrm{L}}$ with the same XUV pulse. The error of Eq. (4.22) is introduced by dropping all higher order terms, and is dominated by the second order term $(\mathbf{A}_{\mathrm{L}}\mathbf{p}\tau_0)^2$. This indicates that the linear property of the spectrogram is more prominent when the transform-limited XUV pulse duration is short and the streaking field is weak.

4.2.8. Conclusion and outlook

We have shown that shot noise has little effect on the retrieval of single attosecond pulses with PCGPA for traces with at least 50 photoelectron counts at the peak of the photoelectron spectrum, provided the streaking laser intensity is greater than the minimum streaking intensity. In fact, the algorithm has been shown to always converge to a result closer to the noise-free simulated trace than to that with noise added, and retrieves pulses with duration and linear chirp within 5% of the simulated pulses for maximum pixel counts of at least 50. Such a result is significant, as it suggests a lower limit to the number of counts necessary for accurate attosecond pulse retrieval. Due to the difficulty of maintaining identical CE phase stabilized laser pulses over a long period of time, this makes measurement of single attosecond pulses more accessible to laboratories without state-of-the-art laser systems. Furthermore, we found that the minimum streaking field intensity needed for accurate reconstruction from a noisy CRAB trace can be nearly two orders of magnitude lower than that estimated from the classical streaking model. Such a low streaking field intensity is desirable to suppress the ATI background. However, for larger XUV bandwidths, higher streaking intensities are required, which agrees with the classical prediction qualitatively. Because of the linear property of the CRAB trace, the reconstruction is robust against time jitter between the XUV and streaking fields, intensity variation of the

streaking field, and collection angle of the streaked electrons. These conclusions are important for the characterization of even shorter XUV attosecond pulses because they significantly reduce the constraints on the experiments.

However, the central momentum approximation in the FROG-CRAB reconstruction is still an issue because when the attosecond pulse spectrum becomes broad, the bandwidth could be comparable with the central energy, and the streaking pattern is no longer symmetric with respect to the central energy. Most recently, with the newly developed algorithm, this problem can be solved and one atomic unit pulse in theory can be retrieved [134].

Notes: The material presented in section 4.2 has mainly been published in: He Wang, Michael Chini, Sabih D Khan, Shouyuan Chen, Steve Gilbertson, Ximao Feng, Hiroki Mashiko and Zenghu Chang, "Practical issues of retrieving isolated attosecond pulses", *J. Phys. B: At. Mol. Opt. Phys.*, **42**, 134007, (2009)

CHAPTER 5 - Attosecond time-resolved autoionization of argon

After the generation and characterization of single attosecond pulses, we had two fantastic laser tools in our hand. One is the few-cycle phase controllable femtosecond pulse discussed in Chapter 2 and Chapter 3, which can be used to control the electron dynamics. The other one is the single attosecond pulse presented in previous chapter, which can be used to track the fast the electron motion. In this chapter, we combine those tools together and perform a pump-probe experiment to study the dynamics of autoionzation process in argon with attosecond precision.

5.1 Study of autoionization by transient absorption method

Electron correlation universally exists in multi-electron systems, which affects the physical and chemical properties of atoms, molecules and condensed matter. While nuclear rotation and vibration in molecules can be studied by femtosecond pump-probe techniques [135], observation of the electron-electron interaction requires attosecond time resolution [3]. One of the most interesting processes governed by electron-electron correlation is autoionization [136]. The Fano profile, which is the signature of the autoionization process, has broad significance in many scientific disciplines [137-140]. For decades, spectral-domain measurements with synchrotron radiation have served as a window into the rich dynamics of autoionization [137]. However, the synchrotron pulse duration is too long (100 fs to 100 ps) to probe Fano resonances exposed to a strong field in the time domain since the autoionization lifetimes of noble gases can be as short as a few femtoseconds.

Since the generation of the first isolated attosecond pulses in 2001 [14], it was theoretically proposed [141-145] and experimentally demonstrated [146] that time-resolved Fano profiles can be studied using the attosecond streaking technique. To date, by far most theoretical and experimental investigations of autoionization processes have scrutinized Fano profiles as a function of the photoelectron energy, i.e., after sampling over the entire temporal evolution of the atomic relaxation. However, made possible by significant recent progress in short-pulse laser technology, time-resolved transient XUV photoabsorption measurements have become feasible and give access to complimentary studies of atomic autoionization in the time regime [147, 148]. Photoabsorption measurements typically have higher data collection efficiency and better energy

resolution than what can be obtained by detecting photoelectrons. More importantly, the all-optical photoabsorption measurement can help to separate the electron dynamics of the laser-dressed target from the streaking of the free photoelectrons. Here we demonstrate the first transient absorption experiment using isolated attosecond pulses to probe the $3s3p^6np$ ^{1}P autoionizing states in argon and show that the autoionization process is strongly modified by an intense laser field.

5.2. Fano profile of Ar autoionization state

5.2.1 Fano theory of autoionization

In a multi-electron system, the electron-electron correlation terms make the many body problem difficult to be solved exactly. Instead, theoretically the electronic state of atoms and molecules are classified as belonging to various configurations according to the independent-particle approximation. The actual stationary states can be represented as superpositions of states of different configurations which are "mixed" by the "configuration interaction," i.e. by terms of the Hamiltonian that are disregarded in the independent-particle approximation. The mixing of a configuration belonging to a discrete spectrum with continuous spectrum configurations gives rise to the phenomenon of autoionization. The exact coincidence of the energies of different configuration makes the ordinary perturbation theory inadequate. In Fano's 1961 paper he presented a systematic way of solving such problem, which is very well know and widely accepted [136].

We can follow his treatment and discuss the configuration interaction between one discrete state $|\varphi\rangle$ and continuum state $|\psi_{E'}\rangle$. The total Hamiltonian can be expressed as $H = H_0 + V$, where H_0 is the Hamiltonian under the independent particle picture and V is the interaction between different configurations. Since $|\varphi\rangle$ and $|\psi_{E'}\rangle$ have been diagonalized in their own configurations (sub-space) and V only contributes to the off-diagonal terms, all the matrix elements of H can be written as:

$$\langle\varphi|H|\varphi\rangle = E_\varphi \ , \tag{5.1}$$

$$\langle\psi_{E'}|H|\varphi\rangle = V_{E'} , \tag{5.2}$$

$$\langle \psi_{E''} | H | \psi_{E'} \rangle = E' \delta(E'' - E') . \tag{5.3}$$

When the discrete energy level E_φ lies within the continuous range of values of E', the new eigenfuction $|\Psi_E\rangle$ (autoionizing state) becomes the linear superposition of the discrete state $|\varphi\rangle$ and the continuum state $|\psi_{E'}\rangle$, which can be expressed as:

$$\Psi_E = a\varphi + \int dE' b_{E'} \psi_{E'} , \tag{5.4}$$

where a and $b_{E'}$ are the coefficients, and they can be determined by solving the coupled equations after applying Eq. (5.1-5.3) to Eq. (5.4):

$$E_\varphi a + \int dE' V_{E'}^* b_{E'} = Ea , \tag{5.5}$$

$$V_{E'} a + E' b_{E'} = E b_{E'} . \tag{5.6}$$

By solving the above two equations and normalizing the wavefunction, the coefficients a and $b_{E'}$ are finally expressed as [136]:

$$a = \sin\Delta / \pi V_E , \tag{5.7}$$

$$b_{E'} = \frac{V_{E'}}{\pi V_E} \frac{\sin\Delta}{E - E'} - \cos\Delta \delta(E - E') , \tag{5.8}$$

where Δ is the phase shift due to configuration interaction and is expressed as:

$$\Delta = -\arctan \frac{\pi |V_E|^2}{E - E_\varphi - F(E)} . \tag{5.9}$$

$F(E)$ represents a shift of the resonance position with respect to bound state E_φ and is defined as:

$$F(E) = P \int dE' \frac{|V_{E'}|^2}{E - E'} , \tag{5.10}$$

and *P* here denotes the "principle part of".

When the transition was initiated by some excitation mechanism from initial ground state $|i\rangle$ to final autoionizing state $|\Psi_E\rangle$, the transition amplitude as a function of energy is represented by the matrix element with suitable transition operator T:

$$\begin{aligned}\langle \Psi_E | T | i \rangle &= \frac{1}{\pi V_E^*} \langle \varphi | T | i \rangle \sin\Delta + \frac{1}{\pi V_E^*} P\int dE' \frac{V_E^* \langle \psi_{E'} | T | i \rangle}{E - E'} \sin\Delta - \langle \psi_{E'} | T | i \rangle \cos\Delta \\ &= \frac{1}{\pi V_E^*} \langle \Phi | T | i \rangle \sin\Delta - \langle \psi_{E'} | T | i \rangle \cos\Delta \end{aligned} , \quad (5.11)$$

where $|\Phi\rangle$ is the "modified" discrete state and is expressed as:

$$\Phi = \varphi + P\int dE' \frac{V_{E'} \psi_{E'}}{E - E'} \ . \quad (5.12)$$

The ratio of the transition probability $\left|\langle \Psi_E | T | i \rangle\right|^2$ to the probability $\left|\langle \psi_E | T | i \rangle\right|^2$ of transition to the unperturbed continuum can be expressed as:

$$\frac{\left|\langle \Psi_E | T | i \rangle\right|^2}{\left|\langle \psi_E | T | i \rangle\right|^2} = \frac{(q+\varepsilon)^2}{1+\varepsilon^2} = 1 + \frac{q^2 - 1 + 2q\varepsilon}{1+\varepsilon^2}, \quad (5.13)$$

where $\varepsilon = (E - E_\varphi - F)/(\Gamma/2)$ is the reduced energy defined in terms of the energy of the continuum-embedded excited state E_φ, its energy shift due to the configuration interaction with the autoionization continuum F, and the corresponding width Γ of the autoionization resonance, which equals to $2\pi|V_E|^2$ and is related to the lifetime of the autoionizing state by $\tau = \hbar/\Gamma$. The parameter q represents the ratio of transition amplitudes from the ground state to the modified discrete state and to the continuum state. It determines the shape of the resonance and is represented as:

$$q = \frac{\langle \Phi | T | i \rangle}{\pi V_E^* \langle \psi_{E'} | T | i \rangle} \ . \quad (5.14)$$

To depict this, Fig. 5-1 plots the line shapes for different values of q as a function of reduced energy. When $q \to \pm\infty$, the transition from ground state to discrete state dominates, and the Fano profile becomes narrower and more symmetric. When $q \approx 1$, the transition to discrete state and continuum state become comparable, and the maximum interference happens. When $q \to 0$, the transition to continuum state dominates, and the Fano profile shows a shape called window resonance.

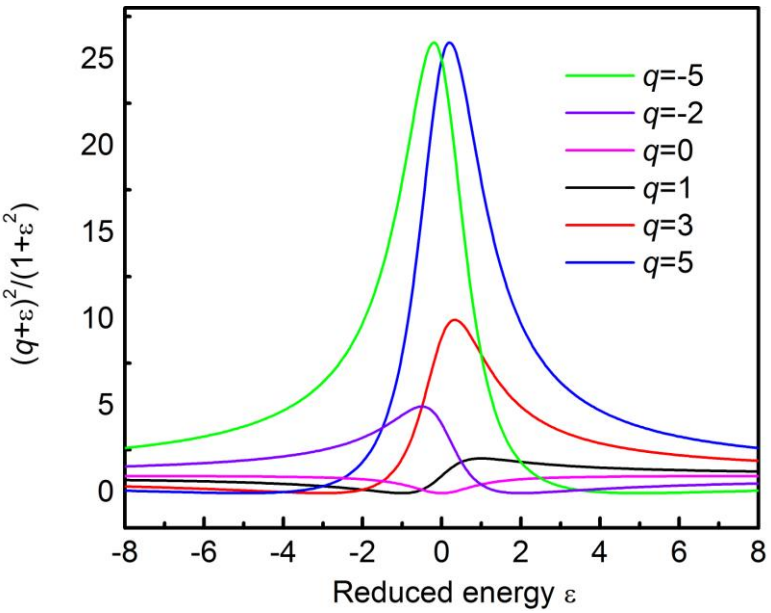

Figure 5-1 Fano line shapes as a function of reduced energy for different *q* parameters.

5.2.2 Ar autoionization state measured by absorption

Fano resonance profiles in the absorption spectrum are the result of interference between the direct ionization to the continuum state with the decay from a bound autoionizing state due to configuration interaction [136]. Based on the model discussed in previous section, the absorption cross-section of an autoionizing state is usually described by the Fano formula as:

$$\sigma = \sigma_a \frac{(q+\varepsilon)^2}{1+\varepsilon^2} + \sigma_b , \tag{5.15}$$

where σ_a and σ_b represent the cross-sections for continuum states that interact and do not interact with the autoionizing state, respectively. The Ar cross section between 25 eV and 30 eV is plotted in Fig. 5-2(a) and the E_r, Γ, τ, and q parameters for the first three peaks of the $3s3p^6np$ ^{1}P autoionizing series are listed in Tab. 1 [137, 149]. A diagram of the argon autoionizing states of interest is depicted in Fig. 5-2(b), where the bound states are not stable and decay to the continuum states by configuration interaction.

As shown in Tab. 1, the line widths of the $3s3p^64p$ and $3s3p^65p$ states are 80 meV and 28 meV respectively [137], which correspond to life times of 8.2 fs and 23.5 fs. To study and control the electron dynamics of such short lived state in real time, attosecond pulse trigger is required.

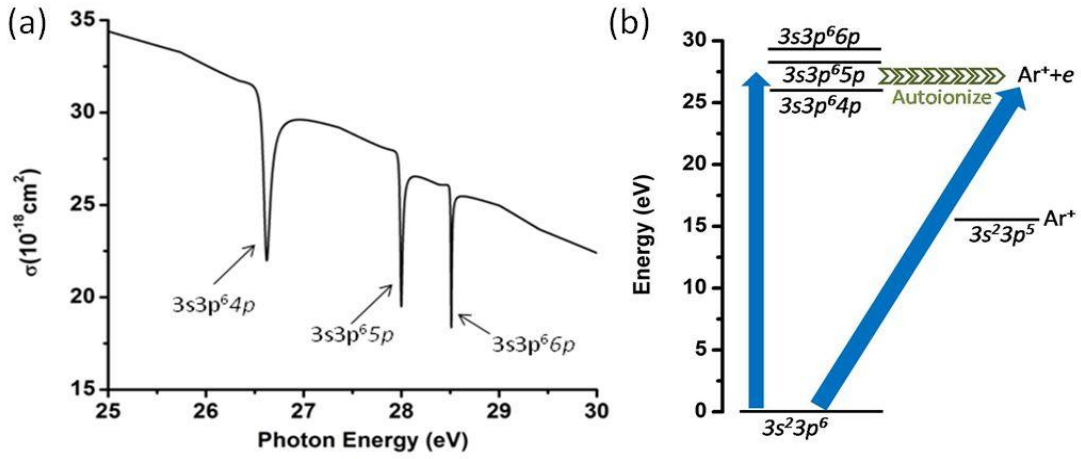

Figure 5-2 (a) Calculated Ar crosssection between 25 eV and 30 eV. (b)Energy diagram of the $3s3p^6np$ ^{1}P autoionizing states in argon.

State	E_r (eV)	Γ (meV)	τ (fs)	q
$3s3p^6 4p$	26.614	80	8.23	-0.22
$3s3p^6 5p$	27.996	28.2	23.34	-0.21
$3s3p^6 6p$	29.509	12.6	52.24	-0.17

Table 1. E_r, Γ, τ, and q parameters for the first three peaks of Ar $3s3p^6np$ ^{1}P autoionizing series.

When the XUV pulse passes through the argon cell, it is partially absorbed. The final transmitted spectrum can be expressed as:

$$T(\omega) = T_0(\omega)\exp[-\rho\sigma(\omega)L], \tag{5.16}$$

where $T_0(\omega)$ is the initial spectrum, $\sigma(\omega)$ is the cross section of target atoms or molecules, ρ is the gas target density, which is a function of gas pressure P and expressed as $\rho = P \times 3.219 \times 10^{16}/(cm^3 \cdot Torr)$ by applying the ideal gas law. In our experiment the 1100 *l/s* turbo (MAG W 1300 from Leybold) was installed in the absorption chamber. Under the background pressure of 10^{-6} Torr, experimentally such pumping speed can support the backing pressure of ~15 Torr inside the gas cell assuming the hole diameter of gas cell is 30 μm. When the 1 mm long gas cell was used, assuming the flat normalized XUV spectrum as input and gas pressure only within the cell, the transmitted XUV spectrum was plotted in Fig. 5-3 for Ar pressure at 10 Torr and 20 Torr respectively, and it can be seen that the transmitted resonance

peak intensity is almost as twice large as the off resonance background even under the backing pressure of 10 Torr, which makes the signal detection feasible.

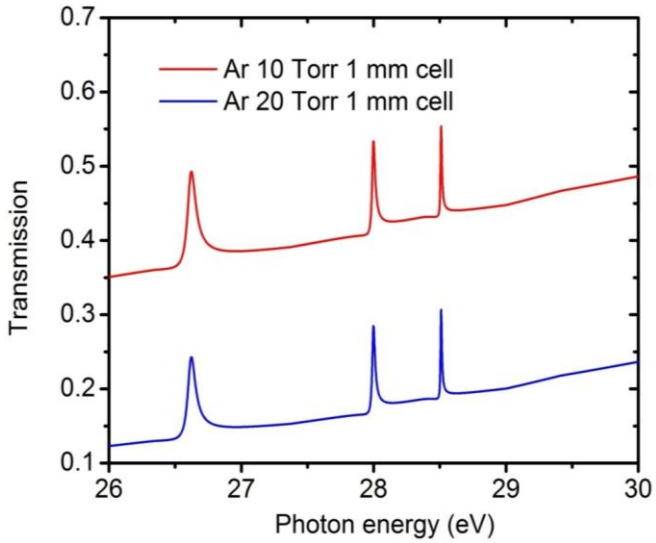

Figure 5-3 Transmitted XUV spectrum through 1 mm long Ar gas cell under different gas pressure.

5.3. Pump-probe experimental setup

To control and measure the autoionizing states of argon atoms, a pump-probe scheme with a Mach-Zehnder configuration was used in the experiment as shown in Fig. 5-4. The laser system was introduced in previous chapters [52, 58]. 1 kHz, 2.5 mJ pulses from a carrier-envelope phase stabilized Ti:sapphire regenerative amplifier (Coherent Legend Elite Duo ^{TM}) were focused into a 400 μm inner diameter hollow-core fiber filled with 1.5 atm of neon gas. After pulse compression by chirped mirrors, the 1 mJ, 8 fs NIR pulses centered at 750 nm were split into two parts. Half of the beam generated the isolated attosecond pulse using the generalized double optical gating (GDOG) [113] from argon gas, and the corresponding XUV supercontinuum spectrum covered the energy range between 20 eV and 40 eV as discussed in the previous chapter. Measurements with an attosecond streak camera and reconstruction by the FROG-CRAB method confirmed the pulse duration to be ~140 as [113]. The attosecond XUV pulse passed through a 300 nm Al foil and was focused by a toroidal mirror (f=250 mm, 9.6 degree grazing incidence angle, R=90.5 mm, r=3230 mm, ARW Optical Corporation) to a second glass gas cell with a 1 mm inner diameter and ~ 30 μm diameter hole on each side filled

with 25 torr of argon gas where more than 80% of the XUV was absorbed. Meanwhile, the other half of the NIR beam was recombined collinearly with the attosecond pulse at the second gas cell by a hole-drilled mirror which reflected a portion of the NIR and allowed the XUV to pass. The diameter of the hole mirror is 3 mm, which reflects 60% of the energy for the NIR beam assuming 8 mm diameter Gaussian beam as an input, and the experimental throughput (50%) is also close to this value. A lens with f=420 mm was used to focus the NIR to the second gas cell. The Rayleigh range of the NIR beam is 3 mm, and the Gouy phase across the 1 mm long gas cell is less than $\pi/10$. Thus the NIR electric field can be assumed to be uniformly applied across the cell. The delay between the NIR and XUV pulses was introduced by a piezo-electric transducer (P-752.1 CD PI). A CW green laser was co-propagated in both arms of the interferometer to stabilize and control the delay between the NIR and XUV pulses [150]. The transmitted XUV pulse through the second cell was refocused by a spherical mirror at 2 degrees grazing incidence angle, and its spectrum was dispersed by a transmission grating (2000 lines/mm) [151] on the MCP/phosphor and CCD image recorder. A second Al filter was installed before the XUV spectrometer to block the scattering NIR light.

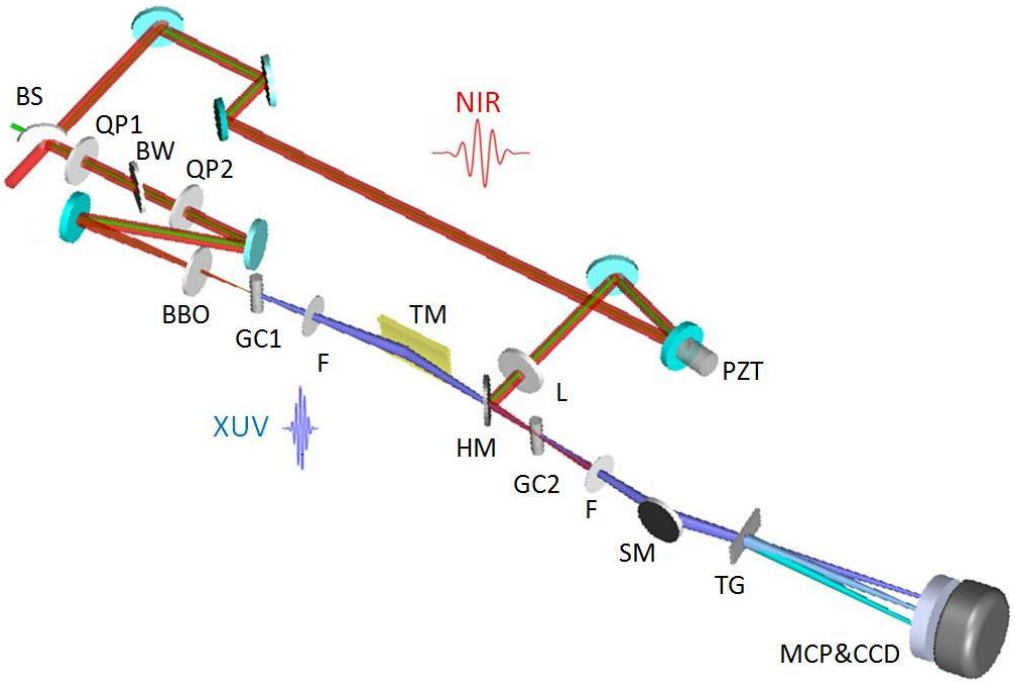

Figure 5-4 Attosecond transient absorption experimental setup. The 7 fs pulse was split into two by a 50/50 beam splitter (BS). Half of the NIR beam propagated through the GDOG optics (QP1, BW, QP2, BBO) and was focused onto the argon gas cell (GC1) to

generate the single attosecond pulses. After the XUV beam passed through the aluminum filter (F), it was focused by a toroidal mirror (TM) into the second gas cell (GC2) filled with argon gas as the absorption target. The other half of the NIR beam was delayed by a PZT mirror and then focused by a lens (L) and recombined with XUV beam by a hole mirror (HM). The transmitted XUV was refocused by a spherical mirror (SM) and dispersed by a transmission grating (TG) onto an MCP/Phosphor and CCD image recorder.

5.4. Spectrometer resolution optimization

The key factor in this experiment is the resolution and calibration of XUV spectrometer. Insufficient spectrometer resolution tends to broaden the Fano profiles of Ar autoionization state and smear out the asymmetric feature of the Fano resonance as shown in Fig. 5-5, where the ideally transmitted XUV spectrum was convolved with a spectrometer resolution of 200 meV. As shown in the figure, all the resonance peaks are broadened and become more symmetric. For the $3s3p^6 4p$ peak, its signal to background contrast drops by a factor of two, and the $3s3p^6 6p$ peak is nearly merged into the background.

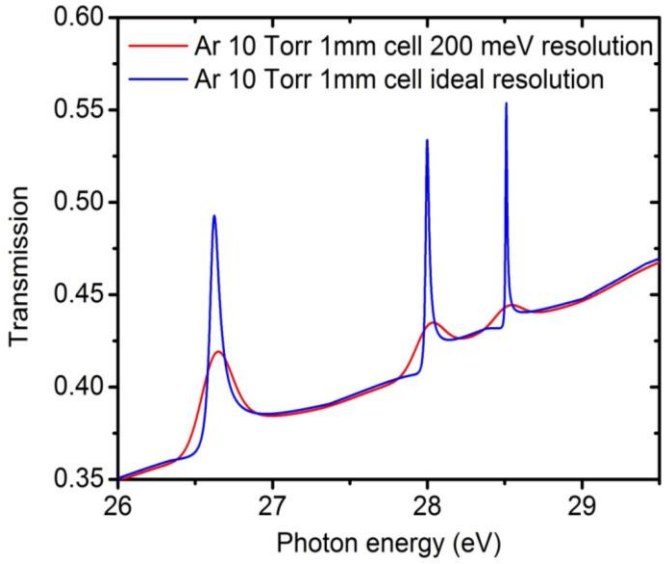

Figure 5-5 Transmitted XUV spectrum under the ideal resolution and 200 meV resolution.

The layout of our XUV spectrometer is displayed in Fig. 5-6 [152]. The XUV source was imaged to MCP/phosphor detector by a spherical mirror under 2 degree grazing incidence angle, and different frequency was dispersed by a transmission grating with 2000 *l/mm*. To optimize the energy resolution of the XUV spectrometer, several factors have to be considered.

First the image distance S_i should be as large as possible since for the same diffraction angle, the spatial separation on the MCP is proportional to the S_i. In our XUV spectrometer, the spherical mirror's radius of curvature R is 29.1 m, and its effective focal length is $f = R/2\sin 2^\circ = 50.8cm$ under 2 degree of grazing incidence angle. The shortest object distance S_o is limited by the chamber configuration and set as 94 cm. From the imaging equation $1/f = 1/S_i + 1/S_o$, thus the image distance S_i is 106 cm. By applying the grating diffraction equation $D\sin\theta = \lambda$, the spatial separation of the XUV spectrum on the MCP screen is expressed as

$$\frac{dE}{dl} = \frac{dE}{S_i d\theta} = \frac{Ed\lambda}{\lambda S_i d\theta} = \frac{E\cos\theta D}{\lambda S_i}, \tag{5.17}$$

where $1/D$ is the groove density of the transmission grating, which is 2000 *l/mm* in current experiment. For the XUV photon energy of 28 eV, the diffraction angle is found to be 5 degree, and dE/dl is calculated to be $0.29eV/mm$. In the experiment, the grazing incidence angle of spectrometer was fine tuned to minimize the aberration of the image on the MCP.

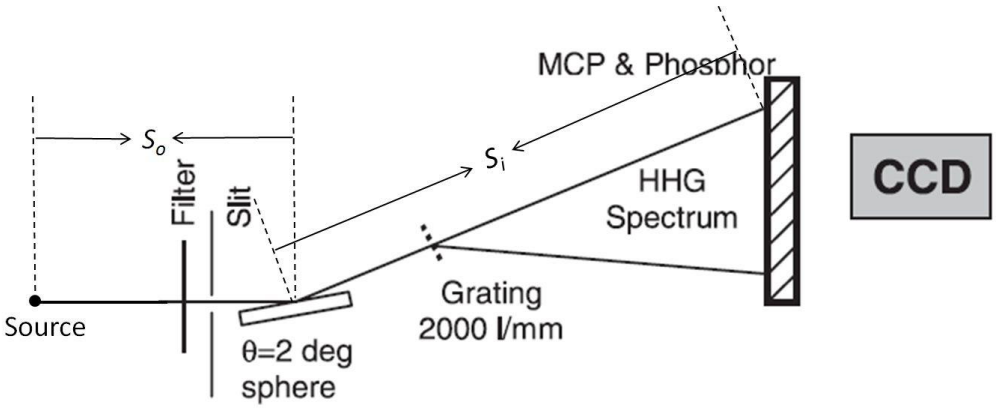

Figure 5-6 Layout of XUV spectrometer. S_o is the object distance, and S_i is the image distance. The XUV source was imaged by a spherical mirror under 2 degree grazing incidence, 2000 *l/mm* transmission grating was used to disperse the spectrum.

Since the dimension of XUV source is around 20~30 μm, its image on the MCP should also be around this size considering 1.12 times of the magnification. On the other hand, the spatial resolution of our MCP phosphor detector is around 100 μm (See Appendix G). The Andor

CCD camera (DV434-FI) has 1024X1024 pixels. When it is used to image the area with 30 mm dimension, each pixel corresponds to ~30 μm. Therefore, in our current design the overall spatial resolution is limited by the MCP/phosphor and is around 100 μm, and it is estimated that the best resolution is 30 meV experimentally.

In Fig. 5-7, the transmitted XUV spectrum was measured experimentally. By comparing the convolution results with the experimental results, the spectrometer resolution was estimated to be 50 meV, and its energy scale was calibrated by the position of the $3s3p^6 4p$ (26.6 eV), $3s3p^6 5p$ (28.0 eV), and $3s3p^6 6p$ (28.5 eV) resonance peaks.

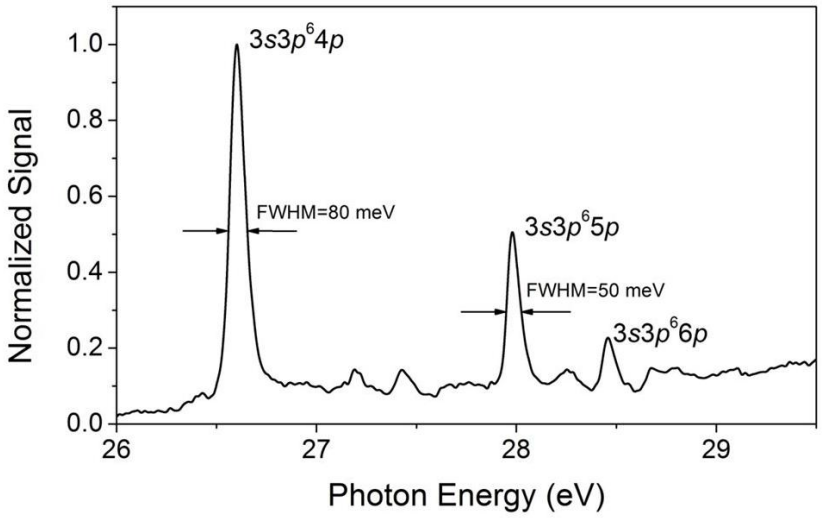

Figure 5-7 Transmitted XUV spectrum indicating argon $3s3p^6np$ ^{1}P autoionizing states. The resolution of the spectrometer was 50 meV.

5.5. Exprimental results

Before the XUV NIR pump-probe experiment was done, the NIR spectrum was measured experimentally as shown in Fig. 5-8. It covers from 550 nm to 1000 nm, which corresponds to the photon energy between 2.1 eV and 1.3 eV. Fourier transform indicates a TL pulse duration of 6.0 fs, and the FROG measurement shows the pulse duration of ~7 fs.

In the experiment, the NIR pulse energy was attenuated to 1 μJ before the hole mirror and the focal spot size measured by the CCD camera was 52 μm and 58 μm on both horizontal and vertical direction, which is very close to the theoretical estimation of 60 μm. For ~7 fs input

pulse duration, its peak intensity is estimated to be about $\sim 2.5\times10^{12}$ W/cm^2 by assuming the Gaussian beam profile and considering the 50% throughput of the hole mirror. Since the NIR beam was truncated in the center when it was reflected by the hole mirror, instead of a Gaussian beam spatial profile, the focal spot is a Bessel beam profile and the inner bright spot occupies 80% of the total pulse energy [130]. Furthermore, since the plano-convex fused silica lens was used in our experiment to focus the NIR pulse, the chromatic aberration and spherical aberration could reduce the peak intensity by another factor of two. The real intensity at the second gas target could be one order of magnitude lower than the estimation ($\sim 8\times10^{11}$ W/cm^2), and more stringent calibration of the peak intensity needs to be done by measuring the momentum shift in the streaking experiment, which is currently not available in our experimental setup.

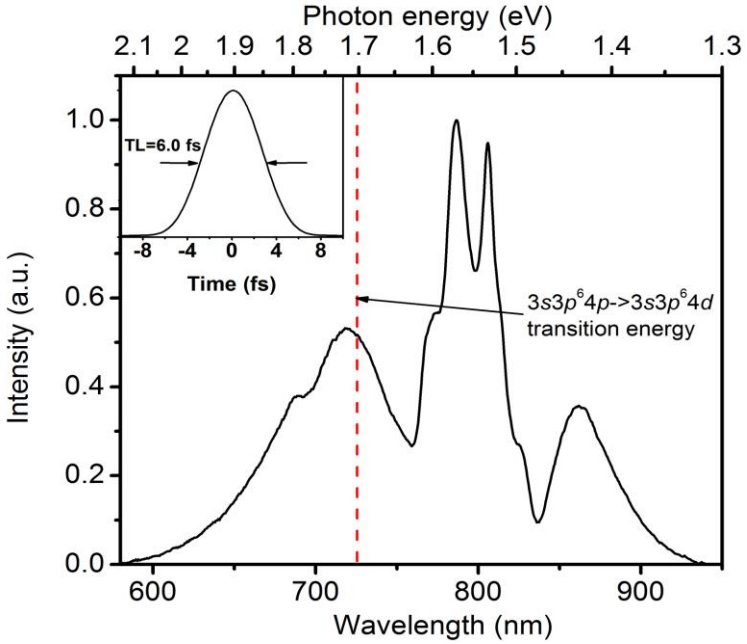

Figure 5-8 The spectrum of NIR pulse. The insert shows its transform limited pulse duration of 6 fs. The red dash line (1.7 eV) indicates to the resonance transition energy between $3s^2 3p^6 4p$ and $3s3p^6 4d$.

Fig. 5-9 shows the transmitted XUV spectrum for different delays between the XUV and NIR pulses. In the plot, negative delays correspond to XUV pulses arriving on the argon target before the NIR pulses. Three resonance peaks $3s3p^6 4p$, $3s3p^6 5p$, and $3s3p^6 6p$ can be identified. As the time delay approaches zero, the NIR pulse gradually shifts the positions of the resonance peaks to higher energy as shown in Fig. 5-9(a). It was observed that the effects of the laser were more apparent on the lower-lying autoionizing states. Fig. 5-9(b) shows the profile of the

resonance peaks at selected delays, and it can be seen that the shifted resonance peaks are also broadened and weakened. In Fig. 5-9(c), the transmitted signal at the energy of the unperturbed $3s3p^6 4p$ and $3s3p^6 5p$ peaks is plotted as a function of the delay. When the XUV and NIR are overlapped, the transmission corresponding to the autoionizing state is minimized. Fig. 5-9(a) also traces the shifting and splitting of the autoionization resonance peaks, indicated with dashed lines.

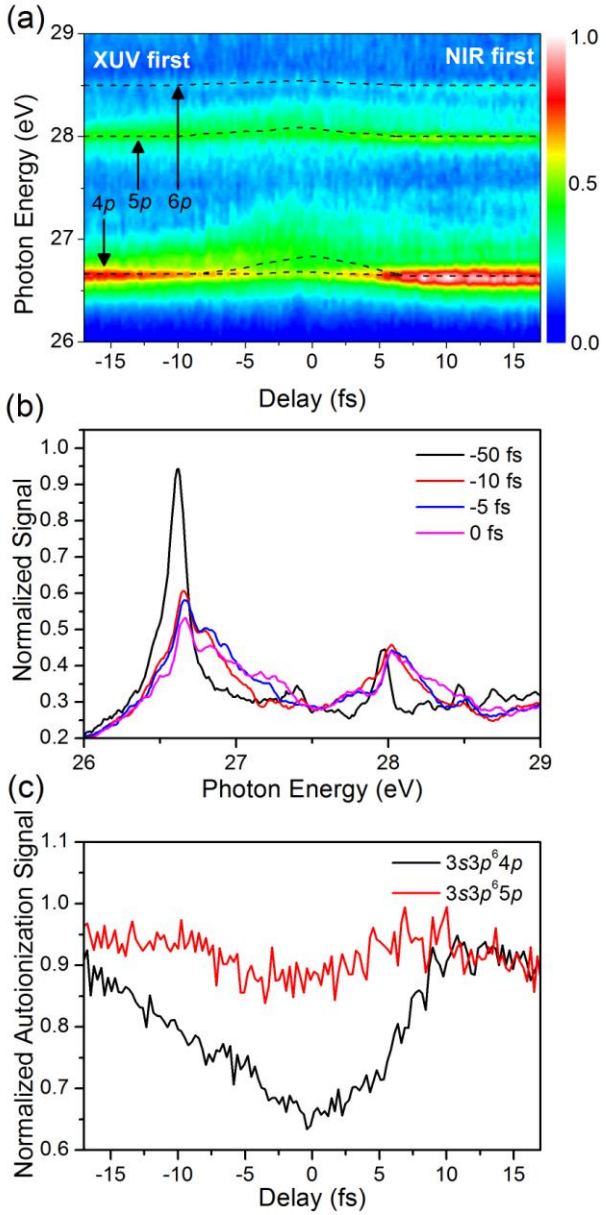

Figure 5-9 (a) Transmitted attosecond XUV spectrum of argon in a strong NIR laser field with a peak intensity of ~10^{11} W/cm^2. Negative delays correspond to the attosecond pulse arriving on the target before the NIR laser pulse. The shifting and splitting of the

resonance peaks are indicated with dashed lines. (b) Transmitted spectrum at selected delays between the XUV and NIR pulses. The resonance peaks are shifted, broadened, and weakened when the two pulses overlap. (c) Dependence of the transmitted signal at the energy of the unperturbed $3s3p^6 4p$ and $3s3p^6 5p$ states on the delay.

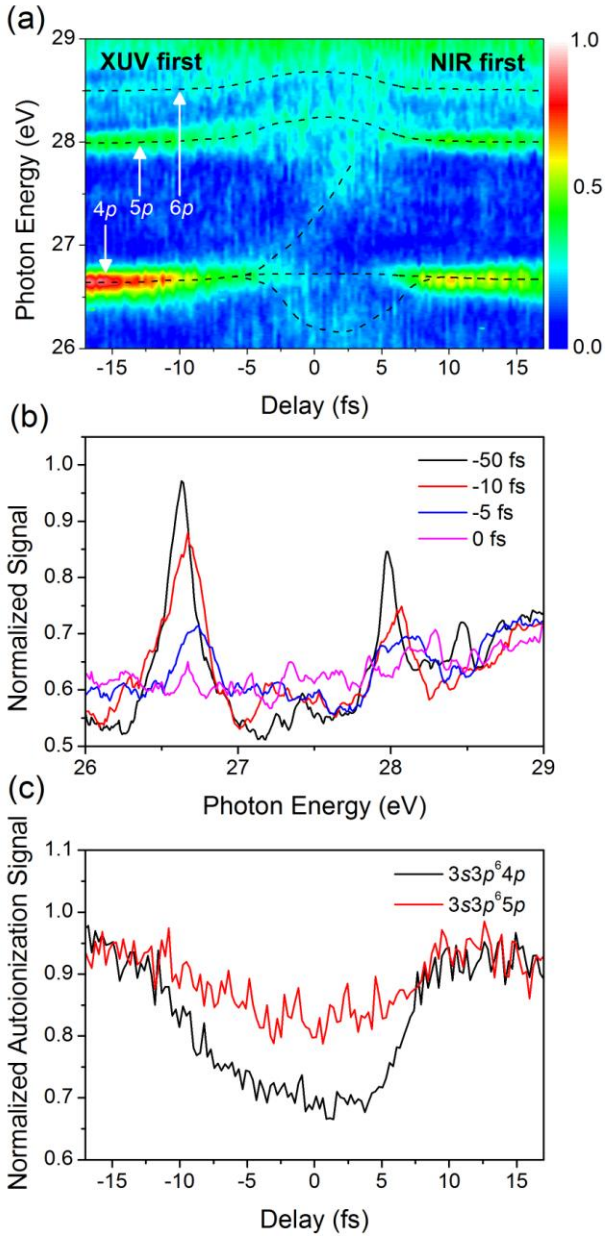

Figure 5-10 (a) Transmitted attosecond XUV spectrum of argon in a strong NIR laser field with a peak intensity of ~10^{12} W/cm^2. Negative delays correspond to the attosecond pulse arriving on the target before the NIR laser pulse. The shifting and splitting of the

resonance peaks are indicated with dashed lines. (b) Transmitted spectrum at selected delays between the XUV and NIR pulses. The resonance peaks are shifted, broadened, and weakened when the two pulses overlap. (c) Dependence of the transmitted signal at the energy of the unperturbed $3s3p^6 4p$ and $3s3p^6 5p$ states on the delay.

To study the effect of the NIR laser intensity on the target, the delay-dependent transmitted XUV spectrum was measured again under the same conditions but with a higher NIR laser pulse energy of 5 μJ, as is shown in Fig. 5-10 (a), where similar phenomena as in Fig. 5-10 were observed. The $3s3p^6 5p$ and $3s3p^6 6p$ states primarily exhibit an energy shift, with the magnitude of the shift decreasing as the resonance energy increases, but the shifting, broadening, and weakening of the autoionization resonance peaks was enhanced compared with our results for the lower intensity in Fig. 5-9. Comparing Fig. 5-9 and Fig. 5-10, we observed that the shift for the $3s3p^6 5p$ and $3s3p^6 6p$ states appears linearly proportional to the laser intensity. Most interestingly, $3s3p^6 4p$ exhibits a dramatic splitting which is asymmetric with respect to zero delay and which extends nearly to the neighboring $3s3p^6 5p$ peak. This is different from the splitting of the $3s3p^6 4p$ state for the lower laser intensity, which was found to be more symmetric with respect to zero delay. In our experiment the strong NIR laser can easily couple the population from the autoionization state to continuum states by single or muli-photon ionization. When the exponential decay process of the autoionization was modified by the ionization of few-cycle NIR pulse, the convolution of their temporal profiles leads to the asymmetric feature observed experimentally, which will be discussed in more details in next section.

5.6. Resonant and Non-resonant coupling effect of strong laser on autoionization state

The observed phenomena indicate a dynamic control over the autoionizing states. Before the discussion of coupling between the autoionizing state and other bound or continuum states by the NIR laser field, let us start from the AC stark shift, which is the coupling between bound states and other bound or continuum states by a moderate laser field [153].

5.6.1 AC stark shift

Non-resonant AC stark shift is usually treated under the theoretical frame work of second-order time-dependent perturbation theory and usually it is expressed as:

$$\Delta E_n = -\frac{E_0^2}{2\hbar}\sum_{m\neq n}\left|\langle n|D_z|m\rangle\right|^2 \frac{\omega_{mn}}{\omega_{mn}^2-\omega^2} = -\frac{E_0^2\alpha_n(\omega)}{4\hbar}, \tag{5.18}$$

where $\langle n|D_z|m\rangle$ is the dipole matrix element, E_0 is the amplitude of the electric field, and $\alpha_n(\omega)$ is known as the dynamic polarizability of the state *n*. There are two extreme cases. One occurs when the laser frequency is much higher than the difference between neighboring energy levels inside the atoms ($\omega >> \omega_{mn}$), which happens when the visible laser is applied on Rydberg atoms. Under this condition, $\alpha_n(\omega) \approx -1/\omega^2$, and the AC stark shift is the same as ponderomotive shift U_p. The other situation is that the laser frequency is much lower than the difference between neighboring energy levels inside the atoms ($\omega << \omega_{mn}$), which corresponds to the situation when the visible laser is applied on the ground state or deeply bound atoms. The AC stark shift can then be expressed as $\Delta E_n = -\frac{E_0^2}{4\hbar\omega_{01}^2}$, where ω_{01} is the energy difference between the ground state and the first excited state [153].

If the laser frequency is close to the atomic transition, the populations of two levels are strongly coupled together under moderate laser intensity. Instead of applying the perturbation theory, the coupled equations need to be solved under the rotating wave approximation, which results in a population oscillation for each of the level with Rabi frequency ω_R and AC stark splitting separated by twice the Rabi frequency for each level [2]:

$$\omega_R = \sqrt{(\Delta\omega)^2 + \frac{\left|D_{ab}E_0\right|^2}{\hbar^2}}\ , \tag{5.19}$$

where $\Delta\omega = \omega - \omega_{ab}$ is the small detuning frequency of laser with respect to the atomic transition frequency ω_{ab}, D_{ab} is the dipole coupling between the two states *a* and *b*.

5.6.2 Autoionization state in strong laser field

The autoionization process itself is already a coupling between the bound state and continuum state by configuration interaction. A laser field can further couple those states to some other bound or continuum states. When the laser induced transition rate becomes comparable to the autoionization rate, the problem is expected to be more complicated because of the interference effects that are an indispensable part of autoionization decays.

5.6.2.1 Qualitative model

Our argon absorption experiment indicates a dynamic control over the autoionizing states, which can be qualitatively understood by considering both non-resonant coupling of the autoionizing states to continuum states and resonant coupling to other autoionizing states induced by the NIR laser as shown in Fig. 5-12 [141, 142, 154].

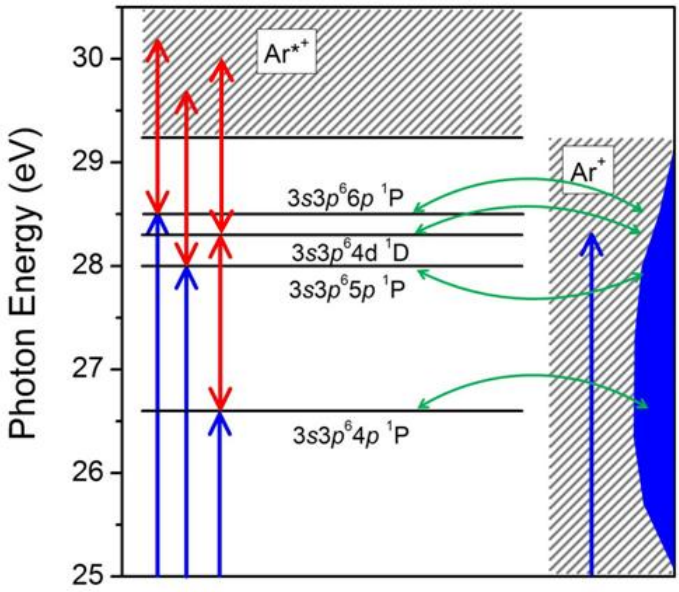

Figure 5-11 Schematic representation of argon autoionizing states exposed to the strong laser field. The blue arrows indicate the attosecond XUV excitation of the ground state to the $3s3p^6np$ ^{1}P states as well as to the Ar^+ ($3s^23p^5\varepsilon l$) continuum. The red arrows indicate the NIR laser coupling between the autoionizing states and the Ar^{*+} ($3s3p^6\varepsilon l$) continuum or to $3s3p^6nl$ quasi-bound states. The configuration interaction indicated (green arrows) couples all autoionizing states to the Ar^+ continuum.

In our experiment, $3s3p^6np$ ^{1}P autoionizing states in argon were first populated by the single attosecond XUV pulse. If there is no NIR field, those states will decay exponentially

because of the coupling to Ar^+ ($3s^2 3p^5 \varepsilon l$) continuum states by the configuration interaction. When those states are further dressed by a strong laser, since there is less than one or two photon energy (1.65 eV for 750 nm central wavelength) separation between the $3s3p^6 4p$ (26.6 eV), $3s3p^6 5p$ (28.0 eV), $3s3p^6 6p$ (28.5 eV) states and the threshold (29.24 eV) of Ar^{*+} ($3s3p^6 \varepsilon l$) continuum states, as shown in Fig.5-12(a) additional couplings between the autoionizing states and Ar^{*+} ($3s3p^6 \varepsilon l$) continuum states by single or multi-photon ionization tend to speed up the decay process and therefore broaden the autoionization peaks.

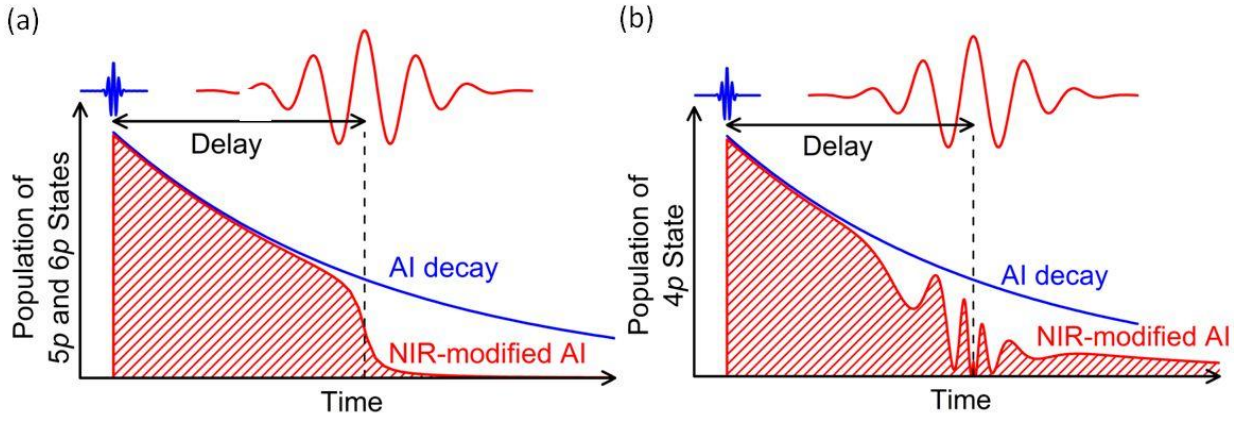

Figure 5-12 (a) Due to the non-resonant NIR coupling (single or multi-photon ionization in our experiment), the autoionization process is speeded up, which causes the broadening and up-shift of the $3s3p^6 5p$ and $3s3p^6 6p$ peaks observed experimentally. (b) Because of the resonant NIR coupling between $3s3p^6 4p$ and $3s3p^6 4d$ states, the population is transferred back and forth between those two states, which introduces extra modulation of autoioization process and leads to the AC stark splitting observed experimentally.

We apply a simple model to demonstrate such effect quantitatively. In our model, when the autoionization process is triggered by a δ function, an electron wave packet is formed in the temporal domain which is expressed as [145]:

$$F_F(t) = \frac{\Gamma}{2}(q-i)e^{-iE_r t-\Gamma t/2} + i\delta(t), \tag{5.20}$$

where $\Gamma/2$ is the ionization rate (Γ is also known as the width of resonance peak), q is the Fano parameter and E_r is the central frequency of the electron wave packet. Fourier transform of such wave packet results in the asymmetric Fano profile in the energy domain. When the single attosecond pulse was applied to trigger the autoionization process in our expriment, the

generated electron wave packet became the convolution of attosecond pulse and the electron wave packet shown in Eq. (5.20).

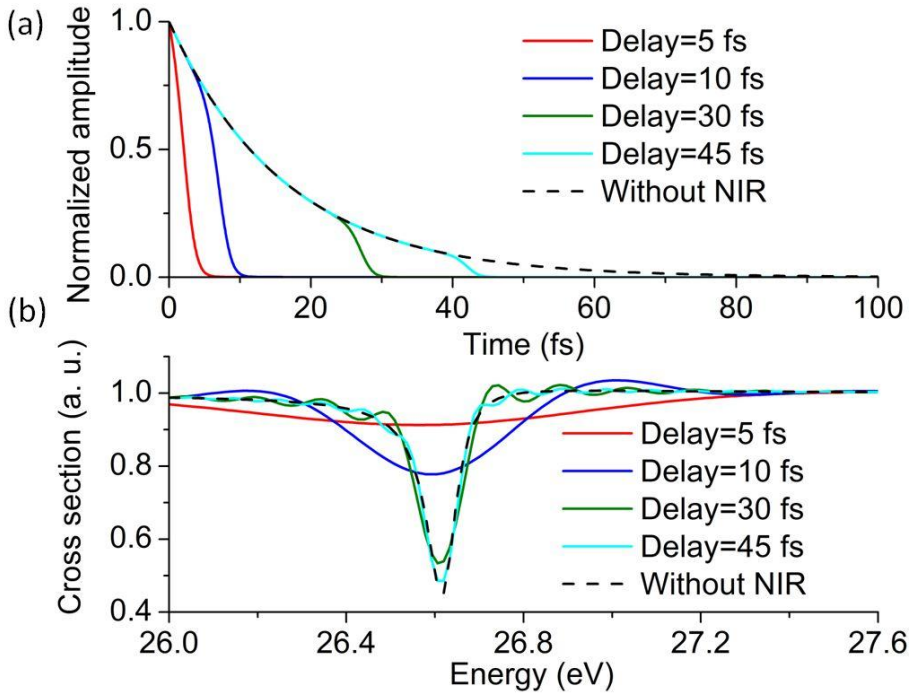

Figure 5-13 The broadening effect of $3s3p^6 4p$ Fano profile caused by NIR ionization at different delays. (a) The exponential decay of autoionization process is truncated by the NIR field ionization. The ionization rate is assumed to be proportional to the NIR intensity in our simulation. (b) The Fano profile at each delay. When the NIR pulse and attosecond XUV pulse become temporally overlapped, the width of autoionization peak is broadened.

Since the attosecond pulse duration (140 as) used in our experiment is much shorter than the life time of the argon autoionization states (> 8fs), in our current model, approximately the attosecond pulse is treated as a sharp δ function. The ionization effect caused by NIR field was incorporated into the unperturbed electron wave packet by adding extra decay which is proportional to the NIR laser intensity.

$$F_F(t,\tau_{delay}) = \frac{\Gamma}{2}(q-i)e^{-iE_r t-\Gamma t/2}e^{-\int_0^t \alpha I(t'-\tau_{delay})dt'} + i\delta(t) \qquad (5.21)$$

where τ_{delay} is the delay between the attosecond pulse and NIR pulse, $I(t)$ is the intensity of the NIR pulse, and α is the coefficient characterizing the ratio between the autoionization decay channel and laser ionization channel. In our simulation, Ar $3s3p^6 4p$ autoionization state is considered, $I(t) = \exp[-4\ln 2t^2/T^2]$ is assumed to have a Gaussian envelope with pulse duration

$T = 5fs$, and α is chosen to be one. As shown in Fig. 5-13 (a) when the exponential decay of autoionization process is truncated by the ionization caused by NIR laser at the different delays, the width of Fano profile is broadened at the same time as shown in Fig. 5-13 (b). Similarly to the AC stark shift in Rydberg atoms, those extra couplings to the continuum states caused by the NIR laser also shift the central energies of the autoionization peaks [153]. Although the shifted peaks are further complicated by the asymmetric Fano profiles and laser-induced broadening, the energy shifts were found to be proportional to the laser intensity and similar in magnitude to the ponderomotive shift (0.16 eV for $3x10^{12}$ W/cm^2).

When resonant coupling to other autoionizing states is also possible, such strong coupling takes over as the dominant mechanism for controlling the autoionization process. Since the $3s3p^6 4p$ (26.6 eV) state is more deeply bound compared to the $3s3p^6 5p$ and $3s3p^6 6p$ states with respect to the Ar^{*+} ($3s3p^6 \varepsilon l$) continuum, coupling only to the Ar^{*+} continuum indicates that the $3s3p^6 4p$ should be less sensitive to the NIR laser. However, the experimental data show an even stronger shift and broadening of the $3s3p^6 4p$ autoionization peak, as well as the asymmetric splitting at high laser intensity, which can be explained by the resonant coupling [141, 142, 154]. Specifically, the $3s3p^6 nd$ states of argon, which lie in the same energy range as the $3s3p^6 np$ ^{1}P manifold of states, cannot be accessed by the absorption of one XUV photon. However, such states can be accessed by two photon (XUV+NIR) processes. In particular, the $3s3p^6 4d$ (28.3 eV) state lies 1.7 eV above the $3s3p^6 4p$ state as shown in Tab. 2 [155], which is approximately equal to the central photon energy of the NIR laser pulse as indicated in Fig. 5-8. When the two states are strongly coupled together in resonance with the NIR photon, as is shown in Fig. 5-11 and Fig. 5-12 (b), Rabi oscillations between the two states can cause AC Stark splitting of each coupled state [154, 156]. Quantitatively such splitting is simulated by adding the Rabi oscillation to the exponential decay of Ar $3s3p^6 4p$ autoionization at different delays:

$$F_F(t, \tau_{delay}) == \frac{\Gamma}{2}(q-i)e^{-iE_r t - \Gamma t/2}\{1+\cos[\beta E(t-\tau_{delay})t]\}/2 + i\delta(t), \qquad (5.22)$$

where $E(t) = \exp[-2\ln 2(t-\tau)^2/T^2]$ is the electric field amplitude, $\beta E(t)$ represents the quasi-static Rabi frequency $\Omega(t)$. Fig. 5-14 (a) shows the modulation of the exponential decay modulated by the Rabi oscillation at different delays and Fig. 5-14 (b) shows its splitting effect on Fano profile. The β is chosen to be 0.3 in our current simulation.

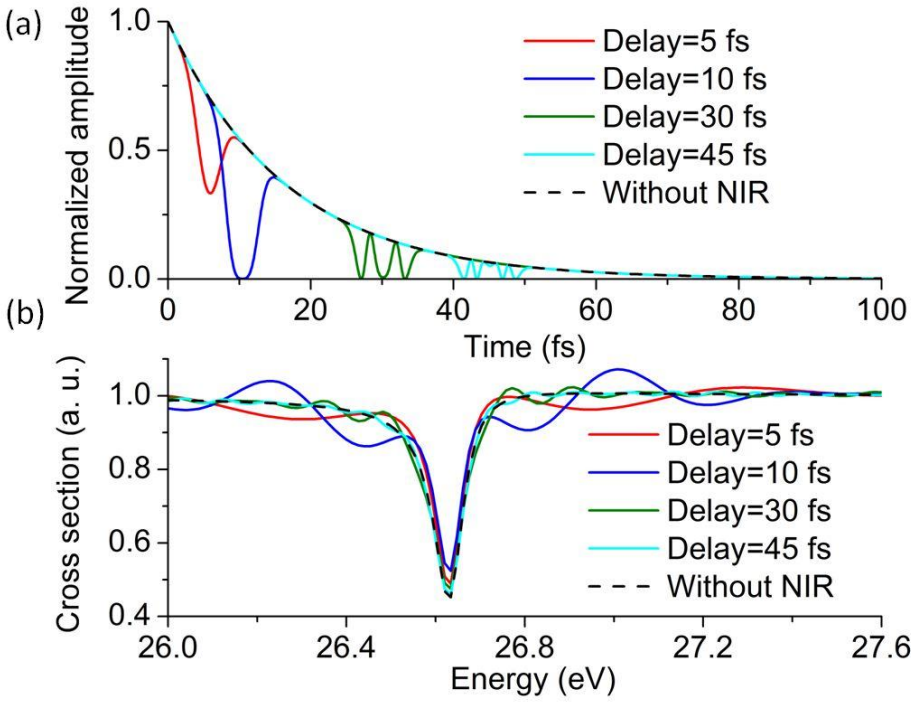

Figure 5-14 The AC splitting effect of argon $3s3p^6 4p$ Fano profile caused by resonance coupling at different delays. (a) The exponential decay of autoionization process is modulated by extra Rabi oscillation induced by NIR field (5 fs). The Rabi frequency is proportional to the amplitude of the electric field. (b) The Fano profile at each delay. When the NIR pulse and attosecond XUV pulse is temporally overlapped, the splitting of autoionization peak is increased.

In the case of pure bound states and resonant coupling, such splitting results in the symmetric Autler-Townes doublet [157]. However, the $3s3p^6 4p$ and $3s3p^6 4d$ states will autoionize by themselves without the participation of NIR laser. The asymmetric Fano lineshapes as well as the slight detuning of the laser central frequency from resonance complicate the inference and lead to the asymmetric splitting observed in this work and in other theoretical treatments [131, 132, 154].

AI state	$3s3p^6 4p\ ^1P$	$3s3p^6 3d\ ^1D$	$3s3p^6 5p\ ^1P$	$3s3p^6 4d\ ^1D$	$3s3p^6 6p\ ^1P$	$3s3p^6 5d\ ^1D$
Energy (eV)	26.63	27.48	28.02	28.29	28.50	28.70

Table 2. Ar $3s3p^6 np\ ^1P$ and $3s3p^6 nd\ ^1D$ autoionization series.

5.6.2.1 Quantum mechanics treatment

Above discussion mainly shows an intuitive physics picture and gives quantitative estimation to some extent. The complete quantum mechanical treatment of our experiment is based on the Ref. 142, and the simulation was mainly done by Dr. Thumm's group at Kansas State University, here I cite some of their results for the completeness of my thesis.

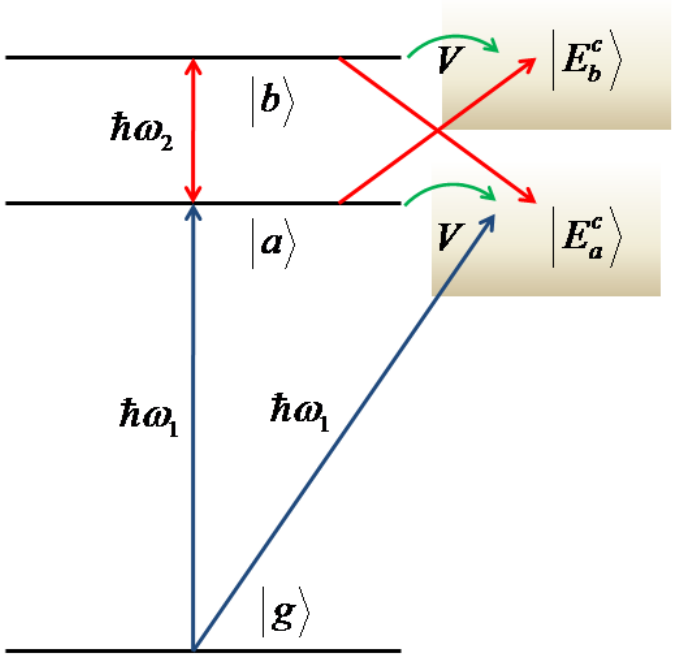

Figure 5-15 Schematic representation of the coupling between the ground, the autoionizing states and the continuum. The blue arrows indicate the weak attosecond XUV excitation of the ground state to the autoionizing state as well as continuum. The red arrows indicate the strong NIR laser coupling between the autoionizing states and the autoionizating states to continuum states. The configuration interaction indicated (green arrows) couples all autoionizing states to continuum.

As shown in Fig. 5-15, $|g\rangle$ is assumed to be the ground state of the atom, $|a\rangle$, $|E_a^c\rangle$ and $|b\rangle$, $|E_b^c\rangle$ are assumed to be the bound and continua parts of autoionization states *a* and *b*. An electric dipole transition induced by a photon energy of $\hbar\omega_1$ causes the excitation $|g\rangle \rightarrow |a\rangle$ and $|g\rangle \rightarrow |E_a\rangle$, while a second photon of energy $\hbar\omega_2$ couples $|a\rangle$ and $|b\rangle$. Each of the bound states $|a\rangle$ and $|b\rangle$ autoionizes to continua $|E_a\rangle$ and $|E_b\rangle$ by configuration interaction. The presence of

the laser photon ω_2, however, can induce additional transitions to these continua as well as to other continua which would not enter the problem under the usual conditions of autoionization. The total Hamiltonian of the problem is written as

$$H = H_0 + V + H_F\,, \tag{5.23}$$

where H_0 is the unperturbed atomic Hamiltonian ($H_0|\mu\rangle = E_\mu|\mu\rangle$, μ =*a*, *b*, *g*), and *V* being the configuration interaction coupling the discrete part of the autoionizing state to the continua. H_F is the free radiation part, which includes the XUV and NIR field in our experiment and can be represented as $H_F = V_X(t)e^{-i\omega_X t} + V_L e^{-i\omega_L t}$. The time dependent wavefunction this model system under the field can be expressed as:

$$|\psi(t)\rangle = C_g(t)|g\rangle + C_a(t)|a\rangle + C_b(t)|b\rangle + \int dE_a^c C_{E_a^c}(t)\left|E_a^c\right\rangle + \int dE_b^c C_{E_b^c}(t)\left|E_b^c\right\rangle \tag{5.24}$$

Substituting this wavefunction into the Schrödinger equation,

$$i\frac{\partial}{\partial t}|\psi(t)\rangle = H(t)|\psi(t)\rangle\,. \tag{5.25}$$

The projection of the individual states in the expansion of leads to a set of coupled differential equations containing amplitudes for the discrete parts as well as for the continua. The introduction of (1) slowly varying amplitudes $C_g(t) = c_g(t)e^{-iE_g t}$, $C_a(t) = c_a(t)e^{-i(E_g+\omega_1)t}$, $C_b(t) = c_b(t)e^{-i(E_g+\omega_1+\omega_2)t}$, $C_{E_a^c}(t) = c_{E_a^c}(t)e^{-i(E_g+\omega_1)t}$, $C_{E_b^c}(t) = c_{E_b^c}(t)e^{-i(E_g+\omega_1+\omega_2)t}$ (2) the rotating wave approximation (RWA) (keep only the time-dependent exponential which are resonant with the photon frequencies). and (3) the adiabatic elimination of the continua by setting the time derivative of the slowly varying continuum amplitudes equal to zero (which basically means they are treated as sinks) lead to the following set of equations for the discrete-state amplitudes:

$$i\hbar\frac{\partial}{\partial t}\begin{pmatrix} c_g(t) \\ c_a(t) \\ c_b(t) \end{pmatrix} = H(t)\begin{pmatrix} c_g(t) \\ c_a(t) \\ c_b(t) \end{pmatrix}, \tag{5.26}$$

where

$$H(t)=\begin{bmatrix} S_g-\frac{i}{2}\gamma_g & \tilde{\Omega}_{ga} & S_{gb}-\frac{i}{2}\gamma_{gb} \\ \tilde{\Omega}_{ag} & -\delta_1-\frac{i}{2}(\Gamma_a+\gamma_a) & \tilde{\Omega}_{ab} \\ S_{bg}-\frac{i}{2}\gamma_{bg} & \tilde{\Omega}_{ba} & -\delta_1-\delta_2-\frac{i}{2}(\Gamma_b+\gamma_b) \end{bmatrix} \tag{5.27}$$

with $\delta_1=\omega_1-(E_a^{(0)}+S_a-E_g-S_g)$, $\delta_2=\omega_2-(E_b^{(0)}+S_b-E_a^{(0)}-S_a)$ being the detunings, $E_a^{(0)}$, $E_b^{(0)}$ and Γ_a, Γ_b the resonance energy and width of the autoionizing states. S_g, S_a, S_b, S_{gb} and γ_g, γ_a, γ_b, γ_{gb} the laser-induced shifts and widths, which is caused by the coupling of each resonance to all states other than the other resonance and is the same as the AC stark shift discussed in the previous section. The generalized complex Rabi frequencies $\tilde{\Omega}_{ga}$ and $\tilde{\Omega}_{ab}$ are defined as:

$$\tilde{\Omega}_{ga}=\Omega_{ga}(1-\frac{i}{q_a})=\frac{1}{2}E_1(t)D_{ga}^{(z)}(1-\frac{i}{q_a}) \tag{5.28}$$

and

$$\tilde{\Omega}_{ab}=\Omega_{ab}(1-\frac{i}{q_{ab}})=\frac{1}{2}E_2(t)D_{ab}^{(z)}(1-\frac{i}{q_{ab}}) \tag{5.29}$$

with D_z being the dipole moment along the polarization direction *z* and q_a, q_{ab} the Fano line shape parameter for the transition $|g\rangle\rightarrow|a\rangle$ and its generalization for the transition $|a\rangle\rightarrow|b\rangle$. Following Ref. 142, the coupled equations for the time-dependent amplitudes $c_a(t)$ and $c_b(t)$ were solved. The XUV and NIR laser pulse durations and intensities were chosen to be the same as in the experiment, and the energies, widths, and *q* parameters of the autoionizing states were taken from the literature ($q_a=-0.2$, $q_b=2.43$) [137, 155]. The dipole matrix elements $\langle g|z|a\rangle$ and $\langle a|z|b\rangle$ were calculated to be 0.027 and 1.54 a.u., respectively, using single particle wavefunctions calculated with an effective Coulomb potential [158]. The single-atom dipole radiation spectrum is given by:

$$\tilde{D}(\omega)=\left|\int_{-\infty}^{\infty}dtd(t)e^{i\omega t}\right|^2, \tag{5.30}$$

where $d(t)$ is the dipole matrix element:

$$d(t)=\langle\psi(t)|z|\psi(t)\rangle. \tag{5.31}$$

The simulated delay-dependent spectra are shown in Fig. 5-16 (a) and (b) for NIR laser intensities of 5×10^{11} and 1×10^{12} W/cm^2, respectively. The features observed in the experiment, including the asymmetric splitting, broadening, and weakening of the Fano lineshape, are reproduced very well by the model.

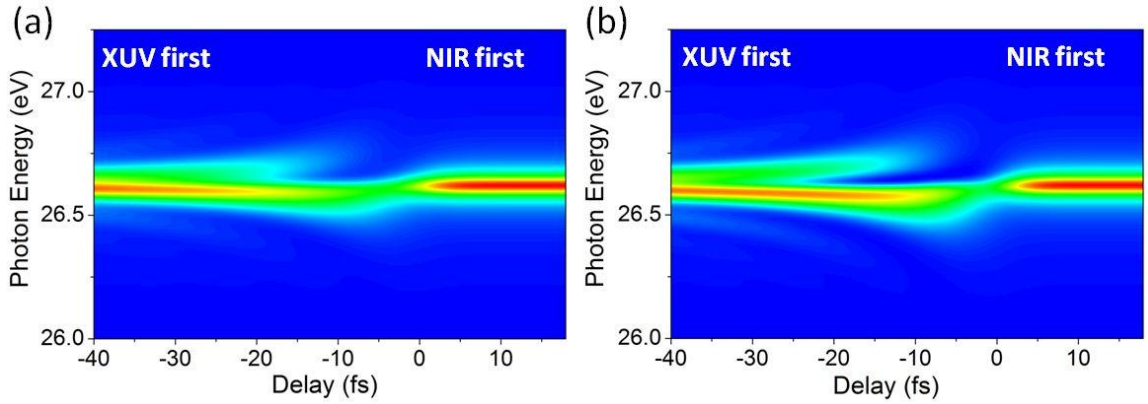

Figure 5-16 Simulated dipole radiation spectrum of laser-induced coupling of the $3s3p^6 4p$ and $3s3p^6 4d$ autoionizing states. The XUV laser had a pulse duration of 140 as and intensity of 10^{10} W/cm^2. The NIR laser had a pulse duration of 8 fs and intensity of (a) 5×10^{11} W/cm^2 and (b) 10^{12} W/cm^2. Simulations courtesy of Chang-hua Zhang, Feng He, and Uwe Thumm.

When the delay between the XUV pulse and NIR pulse was scanned in our experiment, the temporal overlap between the NIR pulse and the autoionization process which was triggered by a single attosecond pulse was also changed continuously. By changing the delay or NIR laser intensity, the q, E_r, and Γ parameters which characterize the autoionization process were controlled with attosecond precision. Further control could be afforded by tuning the NIR laser central frequency with respect to the resonance. Synchrotron pulse durations are still comparable or even longer than the lifetimes of most autoionizing states, and cannot be used as a trigger to control the autoionization process.

In conclusion, autoionization of argon with attosecond transient absorption spectroscopy was demonstrated for the first time. The capability of synchronizing an intense 8 fs NIR pulse and a 130 as XUV pulse on an argon gas target allows us to control the autoionization process with a lifetime of less than 10 fs. Several new features in autoionization are discovered. It was found that the NIR laser field causes changes to the resonance peak position, shape, and a reduction in the XUV transmission, and that these features depend strongly on the laser intensity.

The shifting, splitting, and broadening of the Fano resonance peak in the laser field are attributed to the coupling, both resonant and non-resonant, of the bound and continuum states by the NIR laser. Coupling between such short-lived highly-excited states has never before been studied in time-resolved experiments, as it requires laser pulses much shorter than the autoionization lifetime. Therefore, control of the autoionization process in argon clearly demonstrates that isolated attosecond pulses are crucial tools for studying electron correlation dynamics.

Such an experiment opens a new door for studying the electron correlation in the temporal domain. There are still several more tests that need to be done to fully understand our current experimental results. The first thing is to change the polarization of NIR pulse. In the current experiment, the XUV and NIR have the same polarization, it would be interesting to see the results of orthogonal polarization and compare it with theoretical simulations. The next thing is to use a pump pulse with different wavelength to dress argon atom. Since our current model attributes the shift of $3s3p^6 4p$ state to the resonant coupling between the neighboring states, it can be verified by detuning the frequency of NIR pump pulse, such as the long pass filtering or SHG of NIR pulse. To establish the full understanding of the physical picture of such phenomena, it would be easier to go to a simpler system, such as helium. It is expected that the full simulation of electron behavior in He under the strong laser field could be compared directly with the experimental results in the near future.

CHAPTER 6 - Final remarks

In this thesis I mainly discussed the control of few-cycle femtosecond pulses, generation of single attosecond pulses, and study of real time electron dynamics with such state of the art laser tools.

The first half of my thesis reported the generation of 5 fs few-cycle pulses from an adaptive phase modulator. The MIIPS method was used to characterize and compress the pulses. The CE phase has been stabilized, and the relation between the CE phase stability and power stability has been studied. By using our novel DOG approach, single attosecond pulses were directly produced from 8 fs driving laser fields, and attosecond streaking method is applied to characterize such pulse. Finally the few-cycle pulses were combined with single attosecond pulse to perform a pump-probe experiment with attosecond precision. We observed the change of the resonance profile, and the peak position of Fano resonance in Ar while the delay between the attosecond pulse and NIR pulse was scanned. The experiment demonstrated that the electron correlation in argon autoionizing state was controlled for the first time.

This is just the beginning of tracking and controlling the electron dynamics in atoms and molecules. The potential of our current laser tools hasn't been fully explored. For future experiments, the pulse shaping technique can be used to control the atom and molecules, while the single attosecond pulse can be used to track the electron dynamics. As the technology becomes mature, and our scientific understanding gets deeper, the dream of controlling and tracking electron dynamics will become reality.

References

1. J. J. Thomson, Philosophical Magazine **44**, 293 (1897).
2. B. H. Bransden and C. J. Joachain, Physics of atoms and molecules (Pearson Education, Second edition, 2004).
3. F. Krausz, M. Ivanov, Rev. Mod. Phys. **81**, 163 (2009).
4. M. Ferray, A. L'Huillier, X. F. Li, L. A. Lompré, G. Mainfray and C. Manus, J. Phys. B: At. Mol. Opt. Phys. **21**, L31(1988).
5. A. McPherson, G. Gibson, H. Jara, U. Johann, T. S. Luk, I. McIntyre, K. Boyer and C. K. Rhodes, J. Opt. Soc. Am. B **4**, 595 (1987).
6. P. A. Franken, A. E. Hill, C. W. Peters, and G. Weinreich, Phys. Rev. Lett. **15**, 118 (1961)
7. P. B. Corkum, Phys. Rev. Lett. **71**, 1993 (1993).
8. K. J. Schafer, B. Yang, L. DiMauro and K. C. Kulander , Phys. Rev. Lett. **70**, 1599 (1993).
9. M. Lewenstein, Ph. Balcou, M. Yu. Ivanov, Anne L'Huillier and P. B. Corkum, Phys. Rev. A **49**, 2117(1994).
10. L. V. Keldysh, Sov. Phys. JETP **20**, 1307 (1965).
11. M. V. Ammosov, N. B. Delone, and V. P. Krainov, Sov. Phys.-JETP , **64**, 1191 (1986).
12. G. L. Yudin, and M. Y. Ivanov, Phys. Rev. A, **64**, 013409 (2001).
13. P. M. Paul, E. S. Toma, P. Breger, G. Mullot, F. Augé, Ph. Balcou, H. G. Muller, and P. Agostini, Science **292**, 1689 (2001).
14. M. Hentschel, R. Kienberger, Ch. Spielmann, G. A. Reider, N. Milosevic, T. Brabec, P. Corkum, U. Heinzmann, M. Drescher, and F. Krausz, Nature **414**, 509 (2001).
15. T. Brabec and F. Krausz, Rev. Mod. Phys. **72**, 545 (2000).
16. E. Goulielmakis, M. Schultze, M. Hofstetter, V. S. Yakovlev, J. Gagnon, M. Uiberacker, A. L. Aquila, E. M. Gullikson, D. T. Attwood, R. Kienberger, F. Krausz and U. Kleineberg, Science **320**, 1614 (2008).
17. G. Sansone, E. Benedetti, F. Calegari, C. Vozzi, L. Avaldi, R. Flammini, L. Poletto, P. Villoresi, C. Altucci, R. Velotta, S. Stagira, S. De Silvestri, and M. Nisoli, Science, **314**, 443 (2006).
18. P. B. Corkum and F. Krausz, Nature Physics **3**, 381 (2007).

19. M. Drescher, M. Hentschel, R. Kienberger, M. Uiberacker, V. Yakovlev, A. Scrinzi, Th. Westerwalbesloh, U. Kleineberg, U. Heinzmann and F. Krausz, Nature **419**, 803 (2002).
20. M. Uiberacker, Th. Uphues, M. Schultze, A. J. Verhoef, V. Yakovlev, M. F. Kling, J. Rauschenberger, N. M. Kabachnik, H. Schröder, M. Lezius, K. L. Kompa, H. G. Muller, M. J. J. Vrakking, S. Hendel, U. Kleineberg, U. Heinzmann, M. Drescher, and F. Krausz, Nature **446**, 627 (2007).
21. M. F. Kling, Ch. Siedschlag, A. J. Verehoef, J. I. Khan, M. Schultze, Th. Uphues, Y. Ni, M. Uiberacker, M. Drescher, F. Krausz and M. J. J. Vrakking, Science **312**, 246 (2006).
22. S. Backus, C. G. Durfee III, M. M. Murnane, and H. C. Kapteyn, Rev. Sci. Instru. **69**, 1207 (1998).
23. D. Strickland, and G. Mourou, Opt. Commun. **56**, 219 (1985).
24. D. E. Spence, P. N. Kean, and W. Sibbett, Opt. Lett. **16**, 42 (1991).
25. R. Ell, U. Morgner, F. X. Kärtner, J. G. Fujimoto, E. P. Ippen, V. Scheuer, G. Angelow, T. Tschudi, M. J. Lederer, A. Boiko and B. Luther-Davies, Opt. Lett. **26**, 373 (2001).
26. E. B. Treacy, IEEE J. Quantum Electron. **5**, 454 (1969).
27. O. E. Martinez, IEEE J. Quantum Electron. **23**, 59 (1987).
28. M. Hentschel, Z. Cheng, F. Krausz, and Ch. Spielmann, Appl. Phys. B **70**, S161,(2000).
29. S. Backus, C. G. Durfee III, G. Mourou, H. C. Kapteyn and M. M. Murnane, Opt. Lett. **22**, 1256, (1997).
30. K. Wynne, G. D. Reid, and R. M. Hochstrasser, Opt. Lett. **19**, 895, (1994).
31. B. Shan, C. Wang, Z. Chang, U. S. Patent No. 7050474, (2006).
32. S. Gilbertson, Y. Wu, S. D. Khan, M. Chini, K. Zhao, X. Feng and Z. Chang, Phys. Rev. A **81**, 043810 (2010).
33. M. Nisoli, S. De Silvestri and O. Svelto, Appl. Phys. Lett. **68**, 2793 (1996).
34. A. L. Cavalieri, E. Goulielmakis, B. Horvath, W. Helml, M. Schultze, M. Fieβ, V. Pervak, L. Veisz, V. S. Yakovlev, M. Uiberacker, A. Apolonski, F. Krausz and R. Kienberger, New J. Phys. **9**, 242 (2007).
35. R. Szipöcs, K. Ferencz, C. Spielmann and F. Krausz, Opt. Lett. **19**, 201 (1994).
36. S. Ghimire, B. Shan, C. Wang and Z. Chang, Laser Phys. **15**, 838 (2005).
37. H. Mashiko, C. M. Nakamura, C. Li, E. Moom, H. Wang, J. Tackett and Z. Chang, Appl. Phys. Lett. **90**, 161114 (2007).

38. C. Vozzi, M. Nisoli, G. Sansone, S. Stagira, S. De Silvestri, Appl. Phys. B, **80**, 285 (2005).
39. R. Trebino, K. W. Delong, D. N. Fittinghoff, J. N. Sweetser, M. A. Krumbügel, B. A. Richman, and D. J. Kane, Rev. Sci. Instrum. **68**, 3277 (1997)
40. G. G. Paulus, F. Grasbon, H. Walther, P. Villoresi, M. Nisoli, S. Stagira, E. Priori, and S. De Silvestri, Nature (London) **414**, 182 (2001).
41. A. Baltuška, Th. Udem, M. Uiberacker, M. Hentschel, E. Goulielmakis, Ch. Gohle, R. Holzwarth, V. S. Yakovlev, A. Scrinzi, T. W. Hänsch, and F. Krausz, Nature (London) **421**, 611 (2003).
42. L. Xu, Ch. Spielmann, A. Poppe, T. Brabec, F. Krausz, and T.W. Hänsch, Opt. Lett. **21**, 2008 (1996).
43. www.femtolasers.com\
44. H. R. Telle, G. Steinmeyer, A. E. Dunlop, J. Stenger, D. H. Sutter, and U. Keller, Appl. Phys. B: Lasers Opt. **69**, 327 (1999).
45. D. J. Jones, S. A. Diddams, J. K. Ranka, A. Stentz, R. S. Windeler, J. L. Hall, and S. T. Cundiff, Science **288**, 635 (2000).
46. J. K. Ranka, R. S. Windeler, and A. J. Stentz, Opt. Lett. **25**, 25 (2000).
47. H. M. Crespo, J. R. Birge, M. Y. Sander, E. L. Falcão-Filho, A. Benedick, and F. X. Kärtner, J. Opt. Sco. Am. B **25**, B147 (2008).
48. T. Fuji, A. Apolonski, and F. Krausz, Opt. Lett. **29**, 632 (2004).
49. E. Moon, C. Li, Z. Duan, J. Tackett, K. L. Corwin, B. R. Washburn and Z. Chang, Opt. Express, **14**, 9758 (2006).
50. T. Yu, K. Hong, H. Choi, J. Sung, I. Choi, D. Ko, J. Lee, J. Kim, D. Kim, and C. Nam, Opt. Express **15**, 8203 (2007).
51. R. EII, J. R. Birge, M. Araghchini, and F. X. Kärtner, Opt. Express, **14**, 5829 (2006).
52. C. Yun, S. Chen, H. Wang, M. Chini, and Z. Chang, Appl. Opt. **48**, 5127 (2009).
53. M. E. Thomas, S. K. Andersson, R. M. Sova, and R. I. Joseph, Infrared Phys. Technol. **39** 235 (1998).
54. M. Kakehata, H. Takada, Y. Kobayashi, K. Torizuka, Y. Fujihira, T. Homma, and H. Takahashi, Opt. Lett. **26**, 1436 (2001).
55. Z. Chang, Appl. Opt. **45**, 8350 (2006).
56. C. Li, E. Moon, and Z. Chang, Opt. Lett. **31**, 3113 (2006).

57. E. Moon, H. Wang, S. Gilbertson, H. Mashiko, M. Chini, and Z. Chang, Laser & Photonics Reviews **4**, 160 (2009).
58. S. Chen, M. Chini, H. Wang, C. Yun, H. Mashiko, Y. Wu and Z. Chang, Appl. Opt. **48**, 5692 (2009)
59. C. Li, E. Moon, H. Mashiko, C. M. Nakamura, P. Ranitovic, C. M. Maharjan, C. L. Cocke, Z. Chang and G. G. Paulus, Opt. Express, **14**, 11468, (2006)
60. C. Li, E. Moon, H. Wang, H. Mashiko, C. M. Nakamura, J. Tackett, Z. Chang, Opt. Lett. **32**, 796 (2007).
61. A. Baltuška, M. Uiberacker, E. Goulielmakis, R. Kienberger, V. S. Yakovlev, T. Udem, T. W. Hänsch, F. Krausz, IEEE J. Sel. Top. Quantum Electron. **9**, 972 (2003).
62. A. L. Gaeta, Phys. Rev. Lett. **84**, 3582 (2000).
63. M. Bellini, and T. W. Hänsch, Opt. Lett. **25**, 1049 (2000).
64. FEMTOPOWER compact Pro. @www.femtolasers.com.
65. T. Oksenhendler, F. Legrand, M. Perdrix, O. Gobert, D. Kaplan, Appl. Phys. B **79**, 933 (2004).
66. F. P. Strohkendl, D. J. Files, and L. R. Dalton, J. Opt. Soc. Am. B **11**, 742 (1994).
67. H. Wang, C. Li, J. Tackett, H. Mashiko, C. M. Nakamura, E. Moon, and Z. Chang, Appl. Phys. B **89**, 275 (2007).
68. T. Wittmann, B. Horvath, W. Helm, M. G. Schätzel, X. Gu, A. L. Cavalieri, G. G. Paulus, and R. Kienberger, Nature Physics, **19**, 357, (2009).
69. A. Ishizawa, and H. Nakano, Jpn. J. Appl. Phys. **44**, 6039 (2005).
70. T. M. Fortier, J. Ye, S. T. Cundiff and R. S. Windeler, Opt. Lett. **27**, 445 (2002).
71. C. Li, E. Moon, H. Mashiko, H. Wang, C. M. Nakamura, J. Tackett, and Z. Chang, Appl. Opt. **48**, 1303 (2009).
72. H. Wang, M. Chini, E. Moon, H. Mashiko, C. Li and Z. Chang, Opt. Express **17**, 12082 (2009)
73. R. W. Boyd, Nonlinear Optics (Academic Press, Third edition, 2008).
74. E. Hecht, Optics (Addison Wesley, Forth edition, 2001).
75. H. J. Lehmeier, W. Leupacher and A. Penzkofer, Opt. Commun. **56**, 67 (1985).
76. R. Klingbeil, V. G. Kaveeshwar, and R. P. Hurst, Phys. Rev. A **4**, 1760 (1971).
77. G. Steinmeyer, Appl. Opt. **45**, 1484 (2006).

78. B. Schenkel, J. Biegert, U. Keller, C. Vozzi, M. Nisoli, G. Sansone, S. Stagire, S. De Silvestri, and O. Svelto, Opt. Lett. **28**, 1987 (2003).
79. M. Yamashita, K. Yamane, and R. Morita, IEEE J. Sel. Top. Quantum Electron. **12**, 213 (2006).
80. M. Schultze, E. Goulielmakis, M. Uiberacker, M. Hofstetter, J. Kim, D. Kim, F. Krausz, and U. Kleineberg, New J. Phys. **9**, 243 (2007).
81. R. N. Zare, Science, **279**, 1875 (1998)
82. D. Meshulach, and Y. Silberberg, Nature, **369**, 239 (1998)
83. Z. Chang, A. Rundquist, H. Wang, I. Christov, H. C. Kapteyn, and M. M. Murnane, Phys. Rev. A **58**, R30 (1998).
84. D. G. Lee, J. H. Kim, K. H. Hong, and C. H. Nam, Phys. Rev. Lett. **87**, 423902 (2001).
85. R. Bartels, S. Backus, E. Zeek, L. Misoguti, G. Vdovin, I. P. Christov, M. M. Murnane and H. C. Kapteyn, Nature (London) **406**, 164 (2000)
86. C. Winterfeldt, C. Spielmann, and G. Gerber, Rev. Mod. Phys. **80**, 117 (2008).
87. H. Wang, Y. Wu, C. Li, H. Mashiko, S. Gilbertson, and Z. Chang, Opt. Express, **16**, 14448 (2008)
88. K. Yamane, T. Kito, R. Morita, and M. Yamashita, Opt. Express **12**, 2762 (2004).
89. F. L. Légaré, J. M. Fraser, D. M. Villeneuve, and P. B. Corkum, App. Phys. B **74** [Suppl.], S279 (2002).
90. B. Xu, Y. Coello, V. V. Lozovoy, D. A. Harris, and M. Dantus, Opt. Express **14**, 10939 (2006).
91. B. Xu, J. M. Gunn, J. M. Dela Cruz, V. V. Lozovoy, and M. Dantus, J. Opt. Soc. Am. B **23**, 750 (2006).
92. K. Yamane, T. Kito, R. Morita, and M. Yamashita, in CLEO conference, Lasers and Electro-Optics, 1045 (2004).
93. A. Baltuška, M. S. Pshenichnikov, and D. A. Wiersma, IEEE J. Quantum Electron. **35**, 459 (1999).
94. S. Akturk, C. D'Amico, and A. Mysyrowicz, J. Opt. Soc. Am. B, **25**, A63, (2008)
95. H. Mashiko, S. Gilbertson, C. Li, S. D. Khan, M. M. Shakya, E. Moon, and Z. Chang, Phys. Rev. Lett. **100**, 103906 (2008).

96. M. B. Gaarde, J. L. Tate and K. J. Schafer, J. Phys. B: At. Mol. Opt. Phys. **41**, 132001 (2008).
97. H. Wang, M. Chini, Y. Wu, E. Moon, H. Mashiko and Z. Chang, Appl. Phys. B, **98**, 291 (2009)
98. F. W. Helbing, G. Steinmeyer, J. Stenger, H. R. Telle, U. Keller, Appl. Phys. B **74**, S35 (2002)
99. M. Kakehata, Y. Fujihira, H. Takada, Y. Kobayashi, K. Torizuka, T. Homma, H. Takahashi, Appl. Phys. B **74**, S43 (2002)
100. M. Kakehata, H. Takada, Y. Kobayashi, K. Torizuka, J. Photochem. Photobiol. A **182**, 220 (2006)
101. S. Bohman, A. Suda, T. Kanai, S. Yamaguchi, and K. Midorikawa, Opt. Lett. **35**, 1887, (2010)
102. C. F. Dutin, A. Dubrouil, S. Petit, E. Mével, E. Constant, and D. Descamps, Opt. Lett. **35**, 253, (2010)
103. M. Yamashita, H. Sone, R. Morita, and H. Shigekawa, IEEE J. Quantum Electron. **34**, 2145 (1998).
104. T. Tanigawa, Y. Sakakibara, S. Fang, T. Sekikawa, and M. Yamashita, Opt. Lett. **34**, 1696, (2009)
105. J. Zhu, T. Tanigawa, T. Chen, S. Fang, K. Yamane, T. Sekikawa, and M. Yamashita, Appl. Opt. **49**, 350 (2010)
106. K. Yamane, Z. Zhang, K. Oka, R. Morita, and M. Yamashita, Opt. Lett. **28**, 2258, (2003)
107. B. J. Sussman, R. Lausten, and A. Stolow, Phys. Rev. A, **77**, 043416 (2008)
108. J. J. Carrera and S. Chu, Phys. Rev. A, **75**, 033807 (2007)
109. P. Corkum, N. Burnett, and M. Ivnov, Opt. Lett. **19**, 1870 (1994)
110. B. Shan, S. Ghimire and Z. Chang, J. Mod. Opt. **52**, 277 (2005).
111. S. Gilbertson, H. Mashiko, C. Li, S. D. Khan, M. M. Shakya, E. Moon and Z. Chang, Appl. Phys. Lett. **92**, 071109 (2008)
112. S. Gilbertson, H. Mashiko, C. Li, E. Moon, and Z. Chang, Appl. Phys. Lett. **93**, 111105 (2008)
113. X. Feng, S. Gilbertson, H. Mashiko, H. Wang, S. D. Khan, M. Chini, Y. Wu, K. Zhao and Z. Chang, Phys. Rev. Lett. **103**, 183901 (2009)

114. J. Mauritsson, P. Johnsson, E. Gustafsson, A. L'Huillier, K. J. Schafer, and M. B. Gaarde, Phys. Rev. Lett. **97**, 013001 (2006).

115. Y. Oishi, M. Kaku, A. Suda, F. Kannari, and K. Midorikawa, Opt. Express, **14**, 7230 (2006).

116. Z. Chang, Phys. Rev. A, **70**, 043802 (2004)

117. K. S. Budil, P. Salières, A. L'Huillier, T. Ditmire and M. D. Perry, Phys. Rev. A, 48, R3437 (1993)

118. B. Shan, S. Ghimire, and Z. Chang, Phys. Rev. A, **69**, 021404 (R) (2004)

119. J. Itatani, F. Quéré, G. L. Yudin, M. Y. Ivanov, F. Krausz, and P. B. Corkum, Phys. Rev. Lett. **88,** 173903 (2002)

120. M. Kitzler, N. Milosevic, A. Scrinzi, F. Krausz, and T. Brabec, Phys. Rev. Lett. **88**, 173904 (2002)

121. D. J. Kane, J. Opt. Soc. Am. B **25**, A120 (2008)

122. Y. Mairesse and F. Quéré, Phys. Rev. A **71**, 011401 (2005)

123. H. Wang, M. Chini, S. D Khan, S. Chen, S. Gilbertson, X. Feng, H. Mashiko and Z. Chang, J. Phys. B: At. Mol. Opt. Phys., **42**, 134007 (2009)

124. H. Mashiko, S. Gilbertson, C. Li, E. Moon and Z. Chang, Phys Rev. A **77**, 063423 (2008)

125. P. Lee and G. L. Weissler , J. Opt. Soc. Am. **42**, 214 (1952)

126. D. N. Fittinghoff, K. W. DeLong, R. Trebino and C. L. Ladera, J. Opt. Soc. Am. B **12**, 1955 (1995)

127. R. Kienberger, E. Goulielmakis, M. Uiberacker, A. Baltuška, V. Yakovlev, F. Bammer, A. Scrinzi, Th. Westerwalbesloh, U. Kleineberg, U. Heinzmann, M. Drescher, and F. Krausz, Nature (London) **427**, 817 (2004)

128. G. G. Paulus, F. Crasbon, A. Dreischuh, and H. Walther , Phys. Rev. Let. **84**, 3791 (2000)

129. D. J. Kane, and R. Trebino, IEEE J. Quantum Electron. **29**, 571 (1993)

130. S. Gilbertson, X. Feng, S. Khan, M. Chini, H. Wang, H. Mashiko and Z. Chang, Opt. Lett. **34**, 2390 (2009)

131. J. Mauritsson, P. Johnsson, E. Gustafsson, A. L'Huillier, K. J. Schafer, and M. B. Gaarde Phys. Rev. Lett. **97**, 013001 (2006)

132. J. Mauritsson, P. Jonhsson, E. Mansten, M. Swoboda, T. Ruchon, A. L'Huillier, and K. J. Schafer, Phys. Rev. Lett. **100**, 073003 (2008)
133. D. J. Kennedy and S. T. Manson, Phys. Rev. A **5**, 227 (1972)
134. M. Chini, S. Gilbertson, S. D. Khan, and Z. Chang, Opt. Express **18**, 13006 (2010)
135. A. H. Zewail, J. Phys. Chem. A **104**, 5660 (2000)
136. U. Fano, Phys. Rev. **124**, 1866 (1961)
137. R. P. Madden, D. L. Ederer, and K. Codling, Phys. Rev. **177**, 136 (1969)
138. X. J. Liu, L. F. Zhu, Z. S. Yuan, W. B. Li, H. D. Cheng, Y. P. Huang, Z. P. Zhong, K. Z. Xu and J. M. Li, Phys. Rev. Lett. **91**, 193203 (2003)
139. J. Faist, F. Capasso, C. Sirtori, K. W. West, and L. N. Pfeiffer, Nature(London) **390**, 589 (1997)
140. V. Madhaven, W. Chen, T. Jamneala, M. F. Crommie, and N. S. Wingreen, Science **280**, 567 (1998)
141. P. Lambropoulos and P. Zoller, Phys. Rev. A **24**, 379 (1981)
142. S. I. Themelis, P. Lambropoulos, and M. Meyer, J. Phys. B **37**, 4281 (2004)
143. M. Wickenhauser, J. Burgdörfer, F. Krausz, and M. Drescher, Phys. Rev. Lett. **94**, 023002 (2005)
144. X. M. Tong and C. D. Lin, Phys. Rev. A, **71**, 033406 (2005)
145. Z. X. Zhao and C. D. Lin, Phys. Rev. A, **71**, 060702(R) (2005)
146. S. Gilbertson, X. Feng, S. D. Khan. M. Chini, H. Wang, and Z. Chang, CLEO Baltimore (2009)
147. L. Young, D. A. Arms, E. M. Dufresne, R. W. Dunford, D. L. Ederer, C. Höhr, E. P. Kanter, B. Krässig, E. C. Landahl, E. R. Peterson, J. Rudati, R. Santra, and S. H. Southworth, Phys. Rev. Lett. **97**, 083601 (2006)
148. Z. H. Loh, M. Khalil, R. E. Correa, R. Santra, C. Buth, and S. R. Leone, Phys. Rev. Lett. **98**, 143601 (2007)
149. H. P. Kelly and R. L. Simons, Phys. Rev. Lett. **30**, 529 (1973)
150. M. Chini, H. Mashiko, H. Wang, S. Chen, C. Yun, S. Scott, S. Gilbertson, and Z. Chang, Opt. Express **17**, 21459 (2009)
151. D. A. Mossessian, P. A. Heimann, E. Gullikson, R. K. Kaza, J. Chini, and J. Akre, Nucl. Instr. and Meth. in Phys. Res. A **347**, 244 (1994)

152. B. Shan, A. Cavalieri, Z. Chang, Appl. Phys. B, **74**, S23 (2002)
153. N. B. Delone, V. P. Kraĭnov, Physics-Uspekhi, **42**, 669 (1999)
154. H. Bachau, P. Lambropoulos, R. Shakeshaft, Phys. Rev. A, **34**, 4785 (1986)
155. J. W. McConkey and J. A. Preston, J. Phys. B **6**, L138 (1973)
156. Z. H. Loh, C. H. Greene, and S. R. Leone, Chem. Phys. **350**, 7 (2008)
157. S. H. Autler and C. H. Townes, Phys. Rev. **100**, 703 (1955)
158. X. M. Tong and C. D. Lin, J. Phys. B **38**, 2593 (2005)

Publications

1. He Wang, Michael Chini, Shouyuan Chen, Yan Cheng, Yi Wu, Feng He, Chang-Hua Zhang, Uwe Thumm and Zenghu Chang, "Attosecond Time-resolved autoionization of argon", submitted to Phys. Rev. Lett.
2. Steve Gilbertson, Michael Chini, Ximao Feng, Sabih Khan, Yi Wu, He Wang and Zenghu Chang, "Observation and control of electron dynamics in helium with isolated attosecond pulses", submitted to Phys. Rev. Lett.
3. Shouyuan Chen, Michael Chini, He Wang, Chenxia Yun, Hiroki Mashiko, Yi Wu and Zenghu Chang, "Carrier-envelope phase stabilization and control of 6 mJ, 30 fs laser pulses from a regenerative amplifier", *Appl. Opt*., **48**, 5692 (2009)
4. Michael Chini, Hiroki Mashiko, He Wang, Shouyuan Chen, Chenxia Yun, Shane Sctt, Steve Gilbertson and Zenghu Chang, "Delay control in attosecond pump-probe experiments", *Opt. Express,* **17**, 21459 (2009)
5. Ximao Feng, Steve Gilbertson, Hiroki Mashiko, He Wang, Sabih D. Khan, Michael Chini, and Zenghu Chang, "Generation of isolated attosecond pulses with 20 femtosecond lasers", *Phys. Rev. Lett.,* **103**, 183901 (2009)
6. Hiroki Mashiko, Steve Gilbertson, Ximao Feng, Chenxia Yun, Sabih D. Khan, He Wang, Michael Chini, Shouyuan Chen and Zenghu Chang, "XUV supercontinua supporting pulse durations of sub-one atomic unit of time", *Opt. Lett*., **34**, 3337 (2009)
7. Chenxia Yun, Shouyuan Chen, He Wang, Michael Chini, and Zenghu Chang, "Temperature feedback control for long-term carrier-envelope phase locking", *Appl. Opt*., **48**, 5127 (2009)
8. He Wang, Michael Chini, Yi Wu, Eric Moon, Hiroki Mashiko and Zenghu Chang, "Carrier-envelope phase stabilization of 5 fs, 0.5 mJ pulses from adaptive phase modulators", *Appl. Phys. B*, **98**, 291 (2009)
9. Steve Gilbertson, Ximao Feng, Sabih Khan, Michael Chini, He Wang, Hiroki Mashiko and Zenghu Chang, "Direct measurement of an electric field in femtosecond Bessel-Gaussian beams", *Opt. Lett*.,**34**, 2390 (2009)

10. He Wang, Michael Chini, Sabih D Khan, Shouyuan Chen, Steve Gilbertson, Ximao Feng, Hiroki Mashiko and Zenghu Chang, "Practical issues of retrieving isolated attosecond pulses", *J. Phys. B: At. Mol. Opt. Phys.*, **42**, 134007 (2009)
11. Michael Chini, He Wang, Sabih D Khan, Shouyuan Chen, Zenghu Chang, "Retrieval of satellite pulses of single isolated attosecond pulses", *Appl. Phys. Lett*., **96**, 161112, (2009)
12. Chengquan Li, Eric Moon, Hiroki Mashiko, He Wang, Christopher M. Nakamura, Jason Tackett, and Zenghu Chang, "Mechanism of phase-energy coupling in *f*-to-*2f* interferometry", *Appl. Opt.,* **48**, 1303 (2009)
13. Eric Moon, He Wang, Steve Gilbertson, Hiroki Mashiko, and Zenghu Chang, "Advances in carrier-envelope phase stabilization of grating-based chirped-pulse amplifier", *Laser & Photonics Reviews*, **4**, 160 (2009)
14. He Wang, Michael Chini, Eric Moon, Hiroki Mashiko, Chengquan Li and Zenghu Chang, "Coupling between energy and phase in hollow-core fiber based *f*-to-2*f* interferometers", *Opt. Express*, **17**, 12082 (2009)
15. Chengquan Li, Eric Moon, Hiroki Mashiko, He Wang, Christopher M. Nakamura, Jason Tackett and Zenghu Chang, "Mechanism of phase-energy coupling in *f*-to-2*f* interferometery", *Applied Optics*, **48**, 1303 (2009)
16. He Wang, Yi Wu, Chengquan Li, Hiroki Mashiko, Steve Gilbertson, and Zenghu Chang, "Generation of 0.5 mJ, few-cycle pulses by an adaptive phase modulator", *Opt. Express*, **16**, 14448 (2008)
17. Chengquan Li, Hiroki Mashiko, He Wang, Eric Moon, Steve Gilbertson and Zenghu Chang. "Carrier-envelope phase stabilization by controlling compressor grating separation," *Appl. Phys. Lett.* **92**,191114 (2008)
18. He Wang, Chengquan Li, Jason Tackett, Hiroki Mashiko, Christopher M. Nakamura, Eric Moon and Zenghu Chang, "Power locking of high-repetition-rate chirped pulse amplifiers", *Appl. Phys. B*, **89**, 275, (2007)
19. Chengquan Li, Eric Moon, He Wang, Hiroki Mashiko, Christopher M. Nakamura, Jason Tackett, and Zenghu Chang, "Determining the Phase-Energy Coupling Coefficient in Carrier-envelope Phase Measurements," *Opt. Lett*. **32**, 796 (2007).

20. Hiroki Mashiko, Christopher M. Nakamura, Chengquan Li, Eric Moon, He Wang, Jason Tackett, and Zenghu Chang, "Carrier-envelope phase stabilized 5.6 fs, 1.2 mJ pulses," *Appl. Phys. Lett.* **90**,161114 (2007).

Book chapters

Ximao Feng, Steve Gilbertson, Hiroki Mashiko, He Wang, Sabih D. Khan, Michael Chini, Yi Wu, and Zenghu Chang, "Single Isolated Attosecond Pulses Generation with Double Optical Gating", (invited) book chapter in ***Progress in Ultrafast Intense Laser Science***, Volume VI, Koru Yamanouchi, Andre Bandrauk, Gustav Gerber (Eds), Springer, in press (2009).

Conference talks and posters:

1. He Wang, Michael Chini, Shouyuan Chen, and Zenghu Chang, "Attosecond XUV transient absorption spectroscopy" 37th International Conference on Vacuum Ultraviolet and X-ray Physics, Vancouver, Canada, July 2010
2. He Wang, Michael Chini, Eric Moon, Hiroki Mashiko and Zenghu Chang, "Coupling between energy and carrier-envelope phase in hollow-core fiber based f-to-2f interferometers", Second International Conference on Attosecond Physics, Manhattan, KS, T24 (July-Aug., 2009)
3. He Wang, Michael Chini, Sabih D. Khan, and Zenghu Chang, "Practical issues of retrieving isolated attosecond pulses", Second International Conference on Attosecond Physics, Manhattan, KS, S17 (July-Aug., 2009)
4. He Wang, Yi Wu, Michael Chini, Hiroki Mashiko, and Zenghu Chang, "Generation of CE phase stabilized 5 fs, 0.5 mJ pulses from adaptive phase modulator", Second International Conference on Attosecond Physics, Manhattan, KS, S21 (July-Aug., 2009)
5. He Wang, Yi Wu, Hiroki Mashiko, Chengquan Li, Steve Gilberston and Zenghu Chang, "Generation of 5.1 fs, 0.5 mJ CE phase stabilized pulses with an adaptive phase modulator", Annual meeting of the Conference on Lasers and Electro-Optics Optics (CLEO), Baltimore, MD, JFA1 (June, 2009)

6. He Wang, Sabih Khan, Michael Chini, Shouyuan Chen, and Zenghu Chang, "Effect of streaking laser intensity on the characterization of isolated attosecond pulses", Annual meeting of the Division of Atomic, Molecular, and Optical Physics of the American Physical Society (DAMOP), Charletteville, VA, S5.00007 (May, 2009)
7. He Wang, Chengquan Li, Jason Tackett, Hiroki Mashiko, Christopher M. Nakamura, Eric Moon, and Zenghu Chang, "Laser power locking for improvement of carrier-envelope phase stability", Annual meeting of the Conference on Lasers and Electro-Optics Optics (CLEO), San Jose, CA, JWA69 (June, 2008)

Patent

Zenghu Chang, He Wang, and Yi Wu, "Phase modulator system for generating millijoule level few cycle laser pulses", filed.

Zenghu Chang, Chenxia Yun, Shouyuan Chen, He Wang, and Michael Chini, "Temperature feedback control for long-term carrier envelope phase locking", filed

Appendix A - Classical picture of recollison model and ADK formula

A.1 Classical picture of recollison model

The semiclassical treatment and time dependent Schrödinger equation (TDSE) method of simulating HHG is beyond the scope of this thesis. Instead, a classical simulation is present to facilitate the understanding of essential physics in the HHG process, such as the HHG cutoff, trajectory issue, and attosecond chirp. In this one-dimension model the electron is assumed to start the motion from origin x_0=0 with initial velocity of v_0=0 in a linear laser field, and the electron motion is governed by the electric field of laser. Mathematically such motion can be expressed as:

$$a(t) = \ddot{x}(t) = \frac{e\xi_{laser}}{m}\cos(\omega t), \tag{A.1}$$

$$v(t) = \dot{x}(t) = \frac{e\xi_{laser}}{m\omega}\sin(\omega t) + v_0, \tag{A.2}$$

$$x(t) = -\frac{e\xi_{laser}}{m\omega^2}\cos(\omega t) + v_0 t + x_0. \tag{A.3}$$

When the electron is born at the time $t = t_0$ during the cycle through tunneling ionization, considering the initial condition $v(t_0) = 0$, Eq. (A.2) leads to the electron drift velocity:

$$v_0 = -\frac{e\xi_{laser}}{m\omega}\sin(\omega t_0). \tag{A.4}$$

Hence the velocity of the electron at any later time can be written as:

$$v(t) = \frac{e\xi_{laser}}{m\omega}[\sin(\omega t) - \sin(\omega t_0)]. \tag{A.5}$$

Also considering the initial condition $x(t_0) = 0$, Eq. (A.3) yields:

$$x_0 = \frac{e\xi_{laser}}{m\omega^2}\cos(\omega t_0) - v_0 t_0. \tag{A.6}$$

Hence the electron position at any time t can be written as

$$x(t) = \frac{e\xi_{laser}}{m\omega^2}[\cos(\omega t_0) - \cos(\omega t)] + \frac{e\xi_{laser}}{m\omega}(t_0 - t)\sin(\omega t_0). \tag{A.7}$$

Now we are in a position to evaluate the kinetic energy when the electron is driven back to the ion by the field, for which we can impose the boundary conditions for re-collision time $t_r > t_0$ and $x(t_r) = 0$, it immediately follows that:

$$\cos(\omega t_0) + \omega t_0 \sin(\omega t_0) = \cos(\omega t_r) + \omega t_r \sin(\omega t_0), \tag{A.8}$$

where t_0 and t_r are the birth time and recombination time respectively. We can simplify equation by assigning $\phi_0 = \omega t_0$ and $\phi_r = \omega t_r$ respectively, which gives $\cos\phi_0 + \phi_0 \sin\phi_0 = \cos\phi_r + \phi_r \sin\phi_0$ and was shown in Fig. A.1.

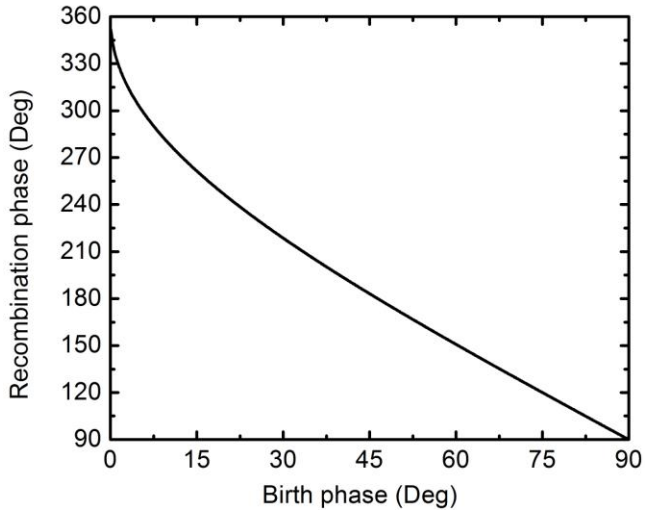

Figure A.1 Birth phase and recombination phase of electron in laser filed.

The kinetic energy of the returning electron thus becomes:

$$KE = \frac{1}{2} v(t_r)^2 = 2U_p(\sin\phi_r - \sin\phi_0)^2, \tag{A.9}$$

where U_p is the ponderomotive potential. The result is plot in Fig. A.2, and it can be seen that the maximum kinentic energy of $3.17U_p$ is accumulated when the electron was born at the phase of 18 degree, which predicts the cutoff of HHG as $\hbar\omega_{cutoff} = 3.17U_p + I_p$. Below the cutoff energy, there are contributions from the two trajectories. According to the time interval between birth and recombination, they are termed as long and short trajectory respectively.

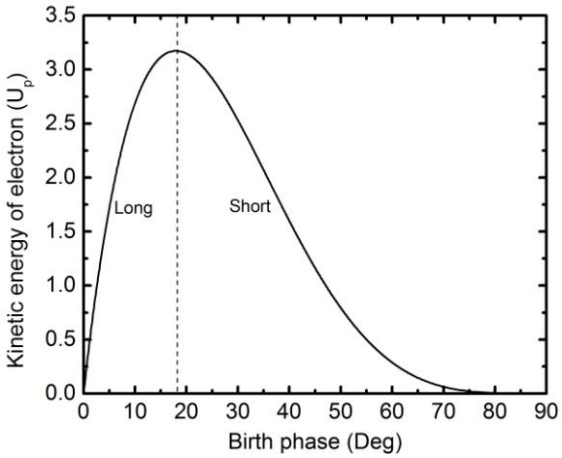

Figure A.2 Plot of birth time and final kinetic energy. When the electron was born at 18 degree, the kinetic energy of free electron reach the cutoff 3.17 Up. Below the cutoff, two trajectories lead to the same final energy.

For XUV attosecond pulse emitted from each trajectory, due to the different recombination time of electrons, they are naturally chirped as show in Fig. A.3.

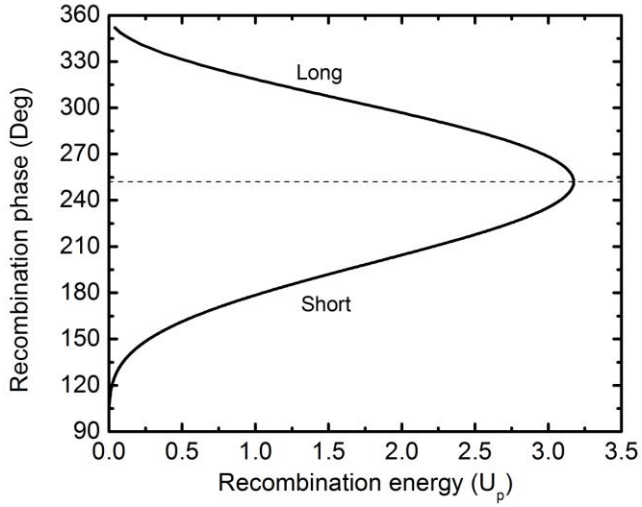

Figure A.3 Recombination phase for electrons with different kinentic energy.

A.2 ADK formula

The ADK formula is given by:

$$W = \omega_P \left| C_{n^* l^*} \right|^2 G_{lm} \left(\frac{4\omega_P}{\omega_T}\right)^{2n^* - m - 1} \exp[-4\omega_P / (3\omega_T)], \qquad \text{(A.10)}$$

where

$$\omega_P = I_P \big/ \hbar \,, \quad \omega_T = e\xi_0 \big/ \sqrt{2mI_P} \,, \quad n^* = (I_P^H \big/ I_P)^{1/2} \,,$$

$$\left|C_{n^*l^*}\right|^2 = 2^{2^{n^*}} [n^* \Gamma(n^* + l^* + 1)\Gamma(n^* - l^*)]^{-1} \,,$$

$$G_{lm} = (2l+1)(l+|m|)!(2^{-|m|})/[|m|!-(l-|m|)!] \,.$$

In those equations above, I_p is the ionization potential of the atom of interest, I^H_p is the ionization potential of atomic hydrogen, l and m are the orbital angular momentum and magnetic quantum numbers, respectively. ξ is the electric field amplitude and Γ is Euler's gamma function. The effective quantum number l^* is given by $l^*=0$ for $l<<n$ and $l^*=n^*-1$ otherwise. The probability of ionization during the time interval dt is

$$P(t) = \int_{-\infty}^{t} W[\xi(t)]dt \,. \qquad \text{(A.11)}$$

Appendix B - 4f system geometry and components

Our 4*f* system is designed for the wavelength range between 500 nm and 1000 nm for P polarization of the hollow-core fiber spectrum, the 235 *l/mm* silver coated grating from Newport is used and its efficiency is shown in Fig. B.1:

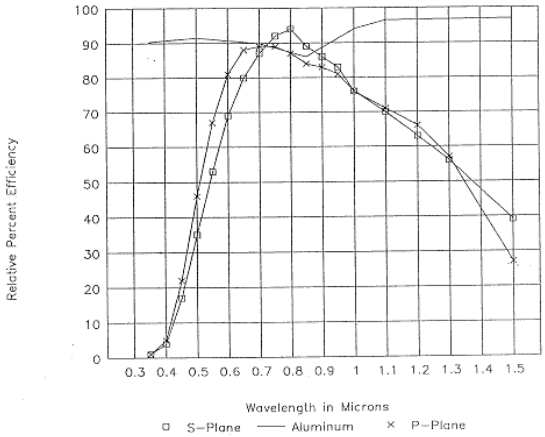

Figure B.1 Newport grating efficiency curves.

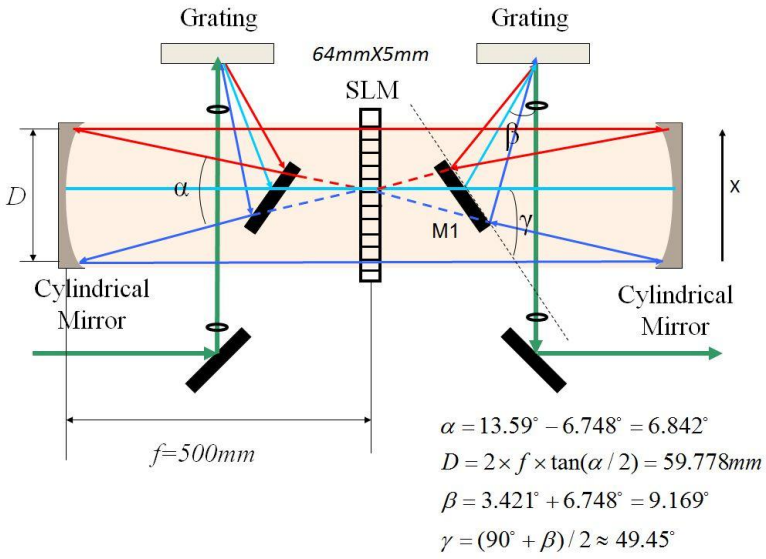

Figure B.2 Geometry of 4f system.

Under the normal incidence, the diffraction angle for 500 nm, and 1000 nm can be calculated as:

$$\sin\theta_{500} = \lambda / a = 500nm/(10^6/235nm) = 0.1175 \Rightarrow \theta_{500} = 6.748^\circ$$

$$\sin\theta_{1000} = \lambda / a = 1000nm/(10^6/235nm) = 0.235 \Rightarrow \theta_{1000} = 13.59^\circ$$

As shown in Fig. B.2, when *f*=500 mm mirror is used, the spatial separation between 500 nm and 1000 nm is 60 mm, which matches the dimension of our 640 pixel SLM (64 mm X 9 mm). As the calculation shown, to guarantee the on axis incidence of the diffraction beam on cylindrical mirror and minimize the aberration during the collimation, the first mirror M1 need to be put around 50 degree.

In our setup, we used liquid crystal based spatial light modulator. Fig. B.3 shows the structure of the liquid crystal, each pixel is 100 μm long, including 97 μm active area and 3 μm gap between neighboring pixels. The inner wall of glass plates are coated with transparent ITO materials, and liquid crystal is sandwiched between them. As shown in Fig. B.4, the liquid crystal molecule is like birefringent crystal. When the voltage is applied, its optical axis starts to reorient and introduce the voltage dependence of phase retardation.

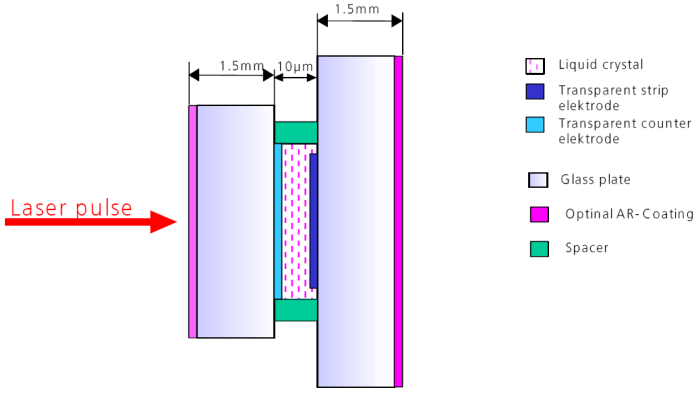

Figure B.3 Structure of liquid crystal.

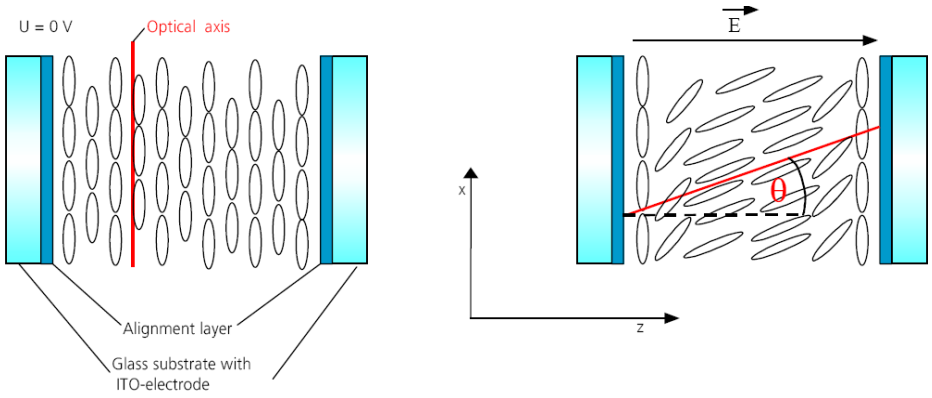

Figure B.4 Operating principle of liquid crystal.

One very important consideration of SLM is its damage threshold. According to the company specifications, the damage threshold of liquid crystal SLM can be as high as

$4.5GW/cm^2$ or $1100\mu J/cm^2$ when it was tested by 790 nm, 1.85 KHz, 250 fs laser pulse. For our application of compressing 1 mJ few cycle pulses, if the spherical mirrors were used to collimate the diffracted beam, the vertical focal spot is around 25 μm, assuming the other dimension of 64 mm, the fluence pass through the liquid crystal is:

$$J = \frac{E}{S} = \frac{1mJ}{25\mu m \times 64mm} = 62.5mJ/cm^2,$$

which is about 50 times higher than the damage threshold of the liquid crystal even though the stretched the pulse may longer than 250 fs. Instead the cylindrical mirror were used, which gives the peak fluence of :

$$J = \frac{E}{S} = \frac{1mJ}{1cm \times 64mm} = 156\mu J/cm^2$$

Since this value is seven times smaller than the specified damage threshold, the liquid crystal is able to run under normal condition.

Appendix C - 4*f* system alignment procedure and wavelength calibration

Procedures for setting up 4*f* system by 532 nm green laser

1. Make input beam normal incidence on grating surface G1

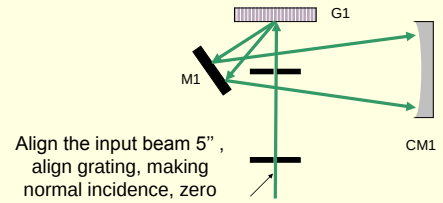

Align the input beam 5" , align grating, making normal incidence, zero order diffraction goes back in the same path.

2. Determine the position of right side cavity mirror

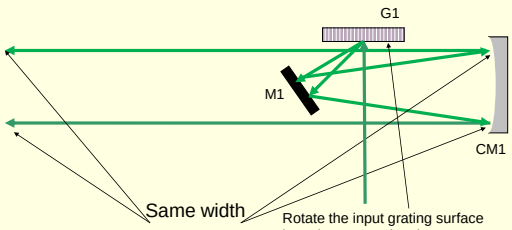

Rotate the input grating surface in a plane normal to the incidence beam to make first order and second order diffraction same height after collimation of cylindrical mirror

3. Cavity alignment

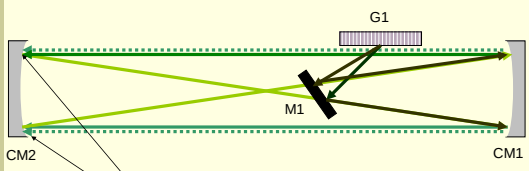

Make the green laser three trips inside cavity, and let the spots of first trip and third trip overlap

4. Make 1st order and 2nd order spots overlap on the output grating

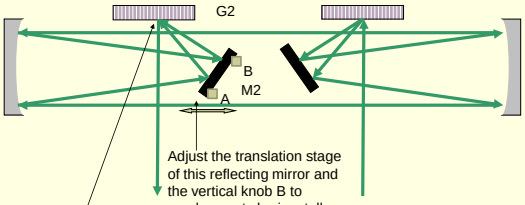

Spots overlap

Adjust the translation stage of this reflecting mirror and the vertical knob B to overlap spots horizontally and vertically on grating surface. Fine tune knob A to optimize the fringes in order to see the whole beam blinking

5. Make 1 order and 2 order spots overlap on the output grating

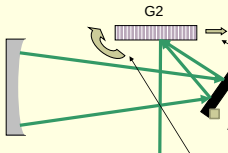

Rotate the second grating surface G2 in a plane normal to the output beam to overlap far field spots vertically.

Rotate grating G2 a little bit in the plane parallel to the optical table to overlap spots horizontally.

Make spots overlap, and whole beam is blinking

1. Make normal incidence on the first grating G1, and zero order reflection should overlap with the incoming beam. Adjust M1 to about 45 degree (according to the calculation of on axis focusing condition)

2. Translate CM1, make sure the distance between G1 surface to CM1 is f by checking the parallelity of the first order and second order diffraction of green laser beam at far field.

3. Translate CM2, let light travel forward and backward in the cavity, with same separation when they are on both surfaces of cylindrical mirror.

4. Tilt down CM2, and deliver light through M2 to G2. Try to make two spot overlap on G2 at height of 5 inch by translating M2 and adjust the knobs A and B.

5. Rotate the G2 in two orthogonal planes to overlap the first order and second order diffraction in the far field. One criteria for good alignment is that the wave front of first order and second order diffraction parallel to each other and the whole wave front interfere in the same way. If you put a paper and look at the output beam profile, by introducing optical path vibration inside the $4f$ system, the whole spot blink at the same time.

Appendix D - Choosing MIIPS parameters α and γ

In the frequency domain, a laser pulse can be described as $E(\omega)=|E(\omega)|e^{j\varphi(\omega)}$. In the MIIPS setup, the spectral phase $\varphi(\omega)$ after the 4*f* system is the sum of the phase of the input pulses, $\phi(\omega)$, the scanning phase introduced by the liquid crystal, $\Phi(\omega)=\alpha\cos(\gamma\omega-\delta)$, and the correction phase also added by the SLM,

$$\varphi(\omega)=\phi(\omega)-\sum_m \phi_m(\omega)+\alpha\cos(\gamma\omega-\delta). \quad (1)$$

m is the iteration number. Here we explain how the parameters α and γ were chosen for compressing pulses from hollow-core fibers.

When the laser beam after the 4*f* system is incident on a second harmonic generation crystal, the SH signal intensity $S^{(2)}$ at the frequency 2ω can be written as

$$S^{(2)}(2\omega)\propto\left|\int|E(\omega+\Omega)||E(\omega-\Omega)\exp\{j[\varphi(\omega+\Omega)+\varphi(\omega-\Omega)]\}d\Omega\right|^2. \quad (2)$$

The sum of the spectral phases can be expressed as a Taylor expansion

$$\varphi(\omega+\Omega)+\varphi(\omega-\Omega)=2\varphi(\omega)+\varphi''(\omega)\Omega^2+\ldots+\frac{2}{(2n)!}\varphi^{2n'}(\omega)\Omega^{2n}. \quad (3)$$

If the high order terms (n>1) can be neglected, the SH signal reaches a local maximum $S^{(2)}(2\omega)\propto\left|\int|E(\omega+\Omega)||E(\omega-\Omega)d\Omega\right|^2$ at 2ω when $\varphi''(\omega)=\phi''(\omega)-\sum_m\phi_m''(\omega)+\alpha\gamma^2\cos(\gamma\omega-\delta)$ is equal to zero. After *m* times of iteration, if $\phi''(\omega)-\sum_m\phi_m''(\omega)=0$ then the SH signal peak distribution in the 2ω-δ map satisfies $\cos(\gamma\omega-\delta)=0$, i.e., $2\omega=(2n+1)\pi/\gamma+2\delta/\gamma$, n=1, 2…, which are straight, parallel, equal spaced lines as shown in Fig. 3(b). When such a MIIPS pattern appears, we can determine $\phi(\omega)$ from $\sum_m\phi_m(\omega)$, which is the principle that MIIPS is based on.

For MIIPS to work well, the high order (n>1) terms in (3) must be smaller than the second order. This condition can be satisfied by properly choosing the γ value, which can be illustrated by considering the last iteration. For the last iteration, $\phi''(\omega)-\sum_m\phi_m''(\omega)=0$, and therefore $\varphi''(\omega)=\alpha\gamma^2\cos(\gamma\omega-\delta)$. Replacing Ω by the bandwidth of the laser spectrum $\Delta\omega$ in

(3), the ratio of the higher order even terms (for n>1) to the second order term can be expressed as

$$\frac{\frac{1}{(2n)!}\alpha\gamma^{2n}\left|\cos(\gamma\omega+\delta)\right|\Delta\omega^{2n}}{\frac{1}{2}\alpha\gamma^{2}\left|\cos(\gamma\omega+\delta)\right|\Delta\omega^{2}}=\frac{2}{(2n)!}\gamma^{2n-2}\Delta\omega^{2n-2}\approx\frac{2}{(2n)!}\left(\frac{\gamma}{\tau_p}\right)^{2n-2} \quad , \tag{4}$$

where τ_p is the transform limited pulse duration. If we choose $\gamma\approx\tau_p$, then the contribution of high order terms can be neglected in (2).

In our experiment, γ =7 *fs*, which was close to the transform limited pulse duration of ~5 *fs*. Considering the largest high order phase term, the ratio of fourth order term to second order terms is about 15%, which is the much less than one. By scanning δ, $\Phi(\omega,\delta)$ covers the range from $-\alpha\gamma^2$ to $\alpha\gamma^2$. We choose $\alpha=5$, so that $\alpha\gamma^2\sim250\,fs^2$. By adding the pre-compensated GDD $\phi_0''(\omega)=500\ fs^2$ before the first iteration, this number is close to the GDD of the white-light pulse, $\phi''(\omega)\approx700$ fs^2, estimated by taking into account the self-phase modulation in the hollow-core fiber, dispersions of 8 m of air, 3 mm of glass in the SLM and the 1 mm compensation plate in the FROG. The requirement $\alpha\gamma^2+\phi''_0(\omega)\approx\phi''(\omega)$ is necessary for realizing $\varphi''(\omega)=\phi''(\omega)-\sum_m\phi_m''(\omega)+\Phi''(\omega)=0$ for all frequencies and for all iterations.

Appendix E - Simulated MIIPS trace and MIIPS program

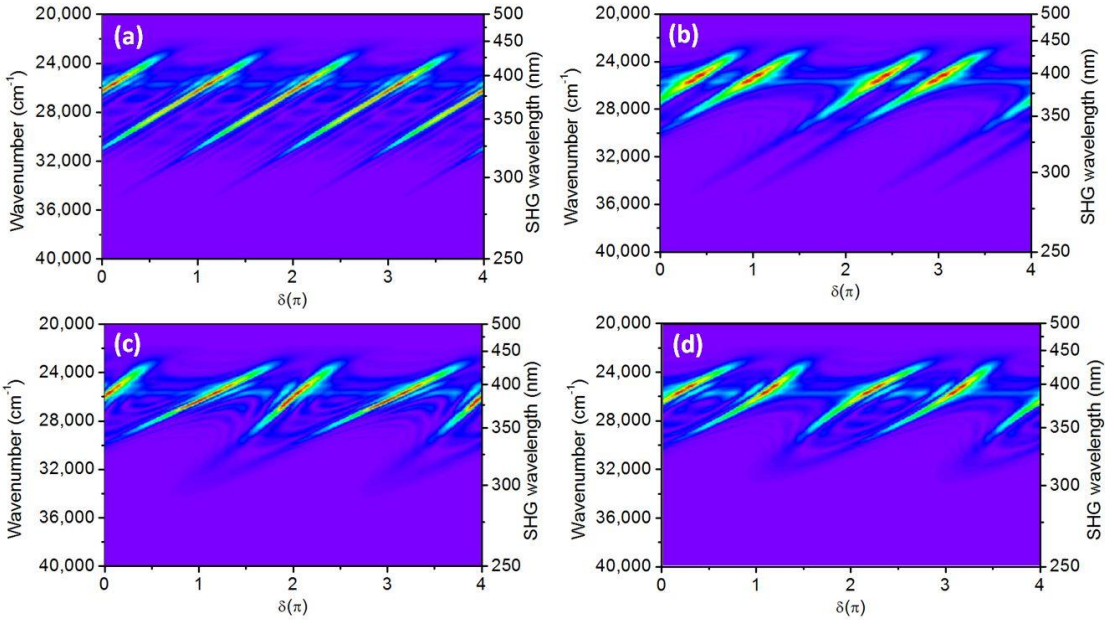

Figure E.1 Simulated MIIPS trace.

In the simulation above, the hollow core fiber spectrum was used, and the phase matching of SHG is assumed to be perfect. $\alpha = 5$, $\gamma = 7\,fs$ Fig. E.1(a) is the MIIPS trace for transformed limited pulse, the SHG peaks are parallel to each other and equal spacing. Fig. E.1(b) is the MIIPS trace for $GDD = 300\,fs^2$ pulse, the SHG peaks are still parallel but no longer equal spacing. Fig. E.1(c) is the MIIPS trace for for $TOD = 300\,fs^3$ pulse, the SHG peaks are straight lines but on longer parallel to each other. Fig. E.1(d) is the MIIPS trace for for $FOD = 300\,fs^3$ pulse, the SHG peaks are no longer straight lines and they form curves.

Fig. E.2 shows the front panel of the MIIPS trace simulation program and the Fig. E.3 shows the block diagram of that program, the input spectrum first are interpolated from wavelength domain to frequency domain, together with the input chirps and MIIPS phase, the SHG spectrum are simulated by convolving the fundamental spectrum. Finally all the SHG spectrum are added together to form the MIIPS trace.

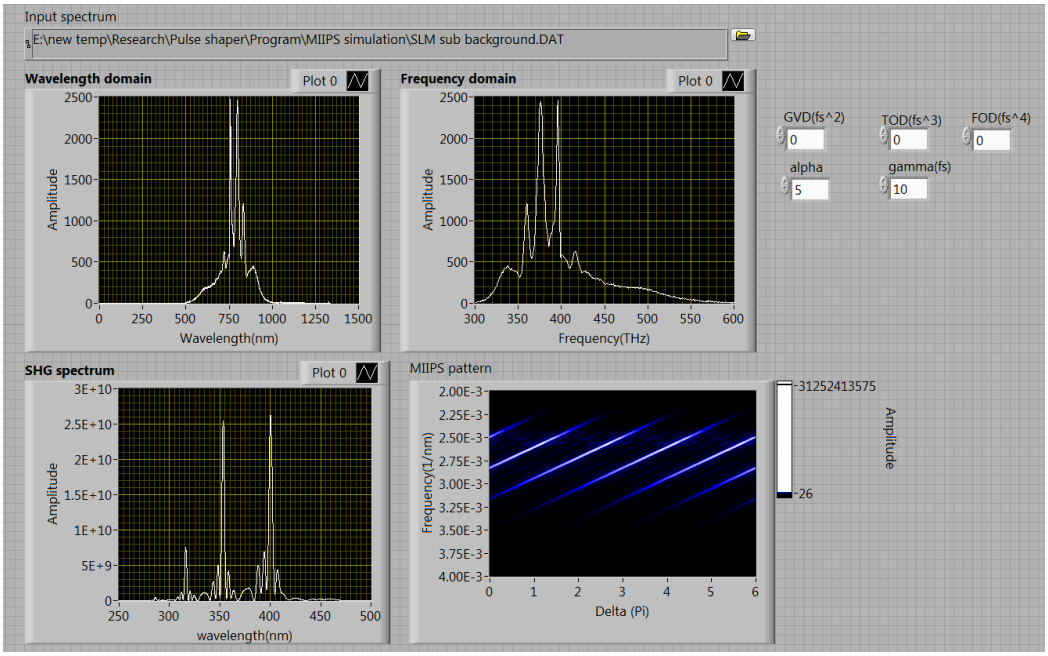

Figure E.2 Front pannel of MIIPS trace simulation program.

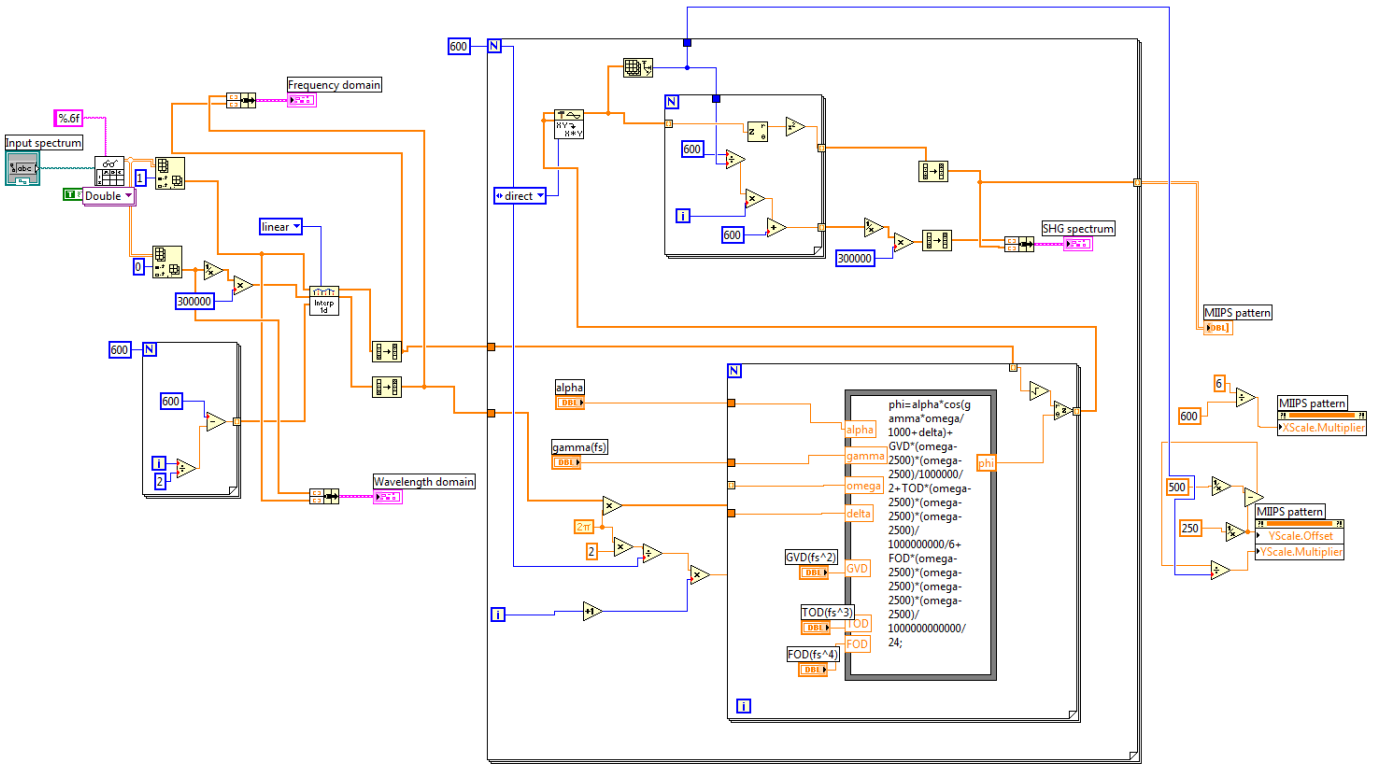

Figure E.3 Block diagram of MIIPS trace simulation program.

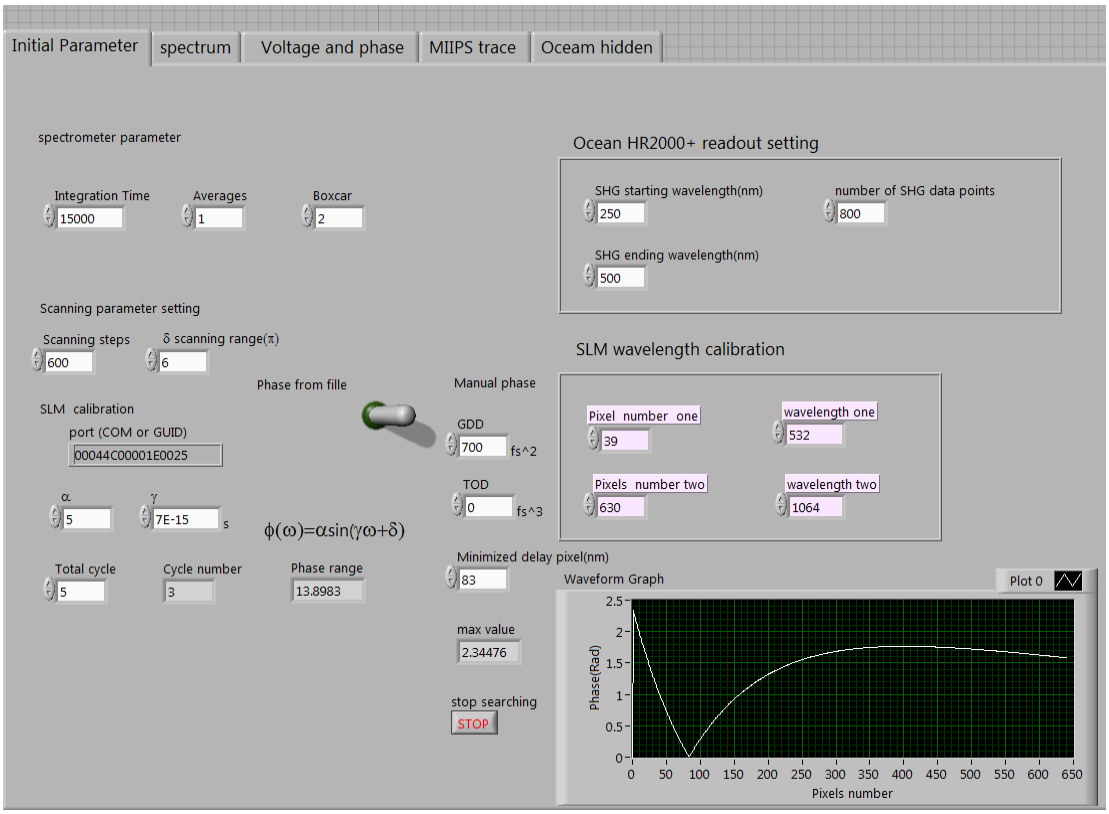

Figure E.4 MIIPS pulse compression program-input parameters.

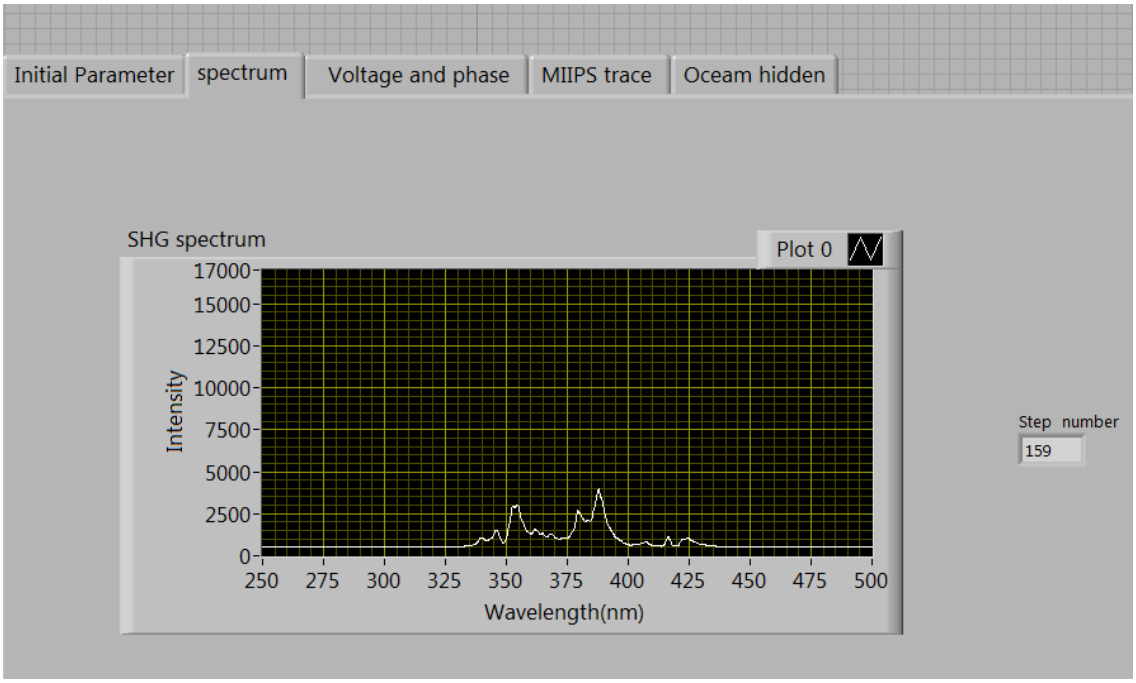

Figure E.5 MIIPS pulse compression program-SHG spectrum.

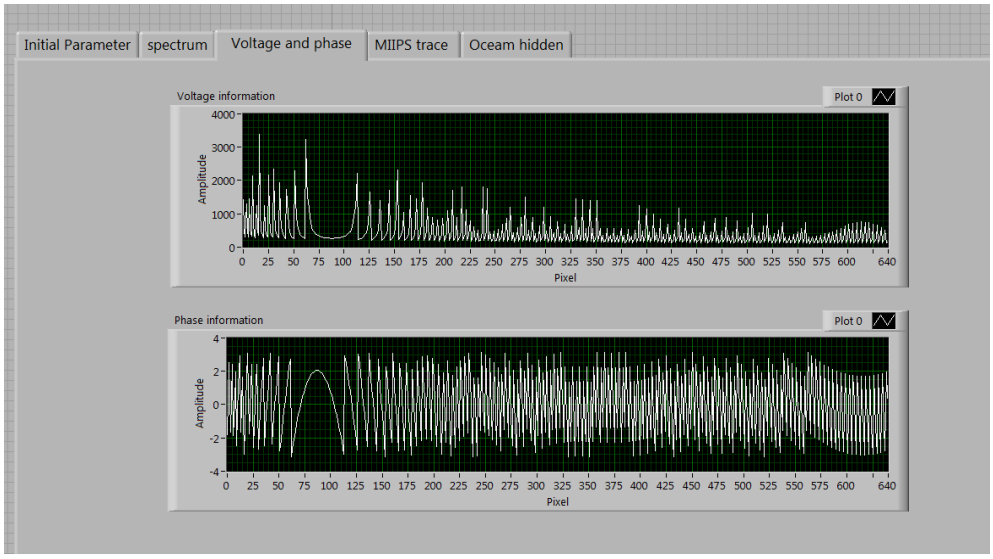

Figure E.6 MIIPS pulse compression program-wrapped phase and voltage.

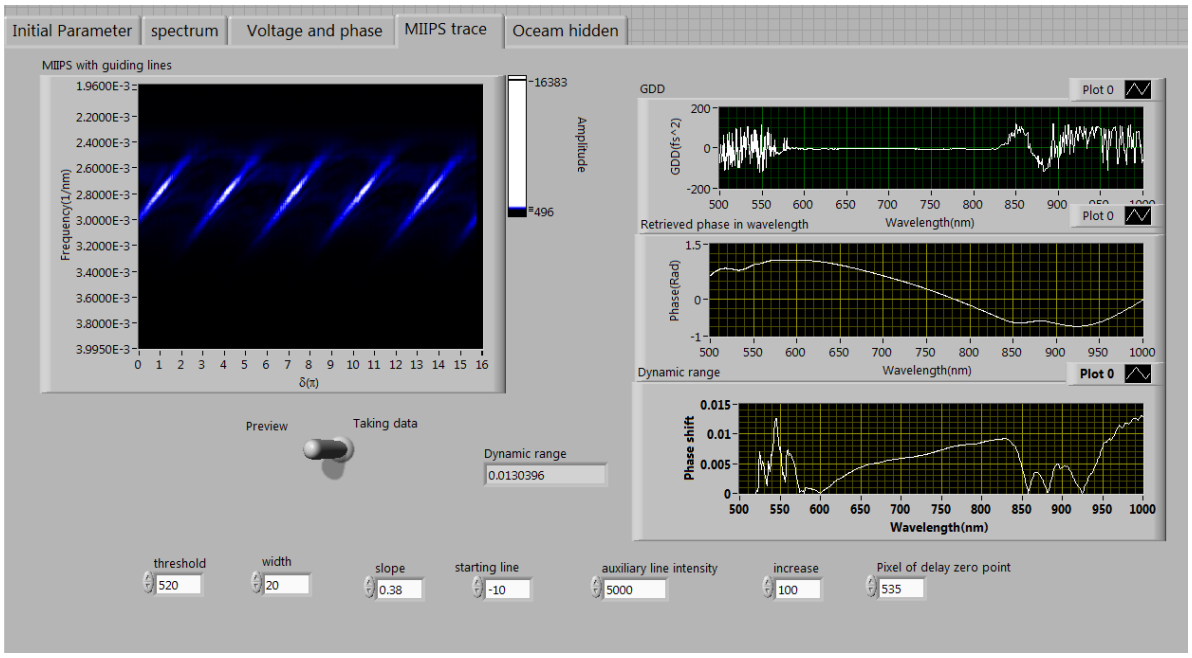

Figure E.7 MIIPS pulse compression program-MIIPS trace measurement.

Fig. E.4, Fig. E.5, Fig. E.6 and Fig. E.7 show the front panels of the MIIPS phase retrieval program. In Tab one, the spectrometer integration time and the number of sampling points, the SLM wavelength calibration and MIIPS parameters α, γ, step size of δ need to be set as inputs. In order to start with proper MIIPS trace to do iterations, the pre-compensation of the chirp need to be added. When the pre-compensated chirp was applied, a linear component is added and need to be adjusted to minimize the load on the each pixel.

Tab two shows the generated SHG spectrum measured for each spectral phase pattern. Tab three is the wrapped voltage and phase applied on liquid crystal. Tab four shows the measured MIIPS trace. It has preview mode and data acquisition mode, usually in the experiment, the MIIPS trace was first taken in the preview mode, under such mode, guiding line will be drawn on the MIIPS trace to define the area of peak search. Once the SHG peak was found for each wavelength, the GDD for each frequency can be calculated and the phase correction can be obtained by integrating twice.

Appendix F - PCGPA algorithm

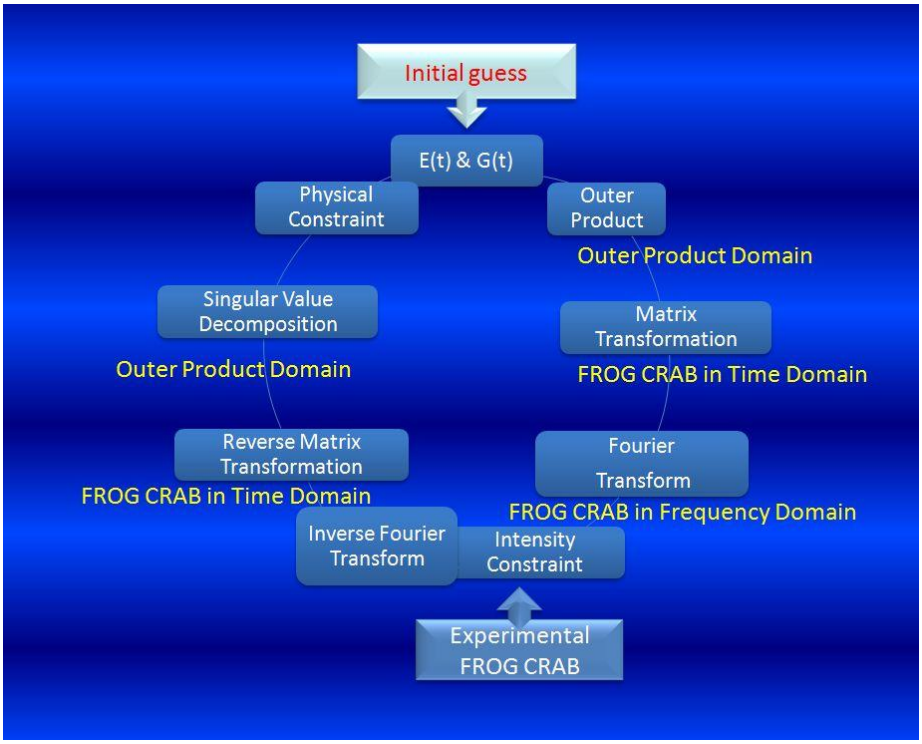

Figure F.1 Flow diagram PCGPA algorithm.

Principle component generalized projection algorithm (PCGPA) is a blind algorithm. It is based the mathematical theorem that the 2D phase retrieval has a unique solution. As shown in Fig. F.1 the program starts by assuming the initial guess for E(t) and G(t) in the temporal domain, after calculation of outer product and Fourier transform it into 2D spectrogram with delay and frequency axis, the amplitude of each matrix elements are replaced by the experimental data, and their original phase are kept. After transforming the 2D spectrogram back from frequency domain into time domain, singular value decomposition (SVD) or power method is used to generate the next guess of E(t), G(t). It is a closed loop algorithm, after several times of iteration, it converges to E(t), and G(t).

Fig. F.2 shows the front panel of the PCGPA. Before the run of this program, the raw streaking data from experiment need be interpolated into a square matrix(NXN, N has to be the power of 2)

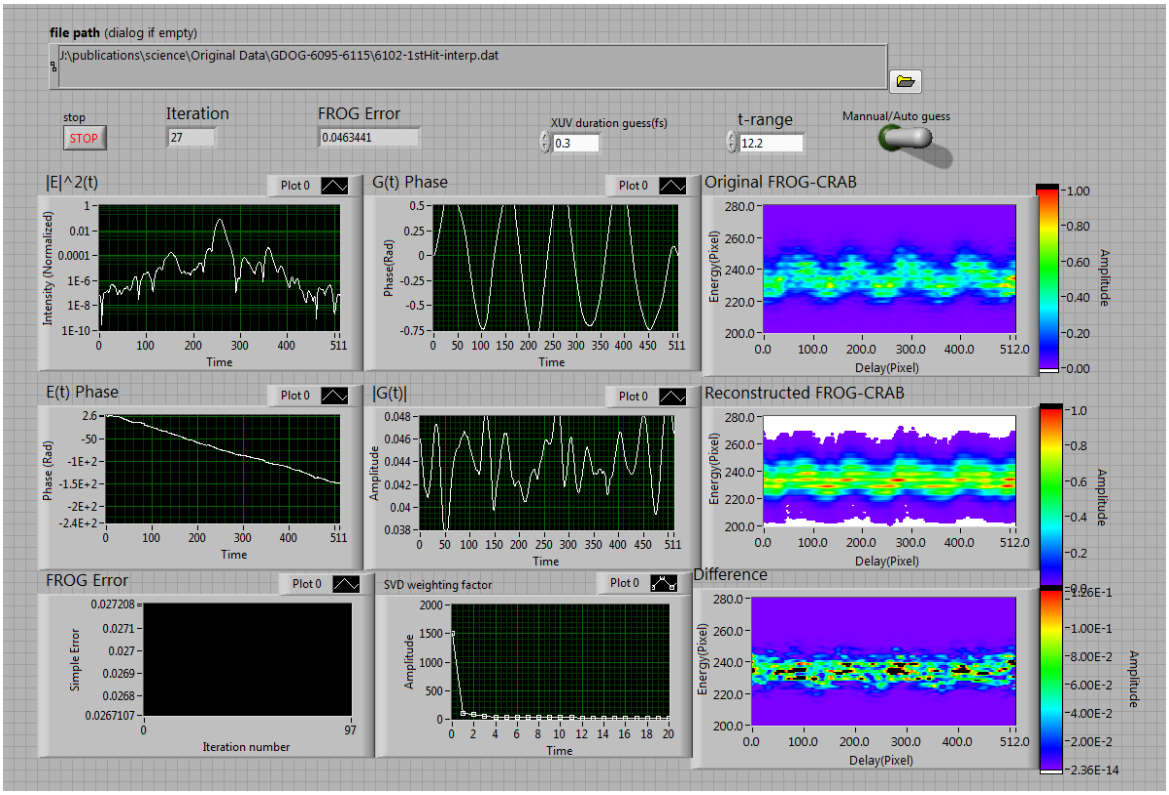

Figure F.2 Front panel of PCGPA program.

Appendix G - MCP phosphor detector spatial resolution estimation

Multi-channel plate amplify the signal (Electron, X-ray, ion and high energy particles) by accelerate the secondary electron along the channel as shown in Fig. G.1:

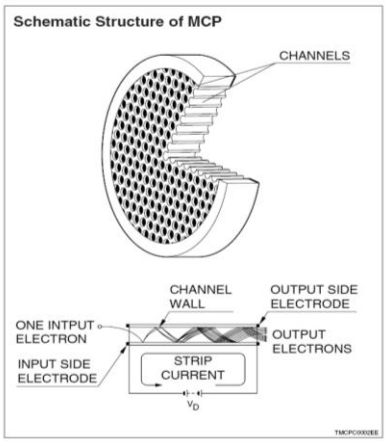

Figure G.1 MCP structure.

Typical the channel size is 12~25 μm, and the channel pitch (channel separation) is 15~32 μm. The later number limits the spatial resolution of single stage MCP as shown in Fig. G.2.

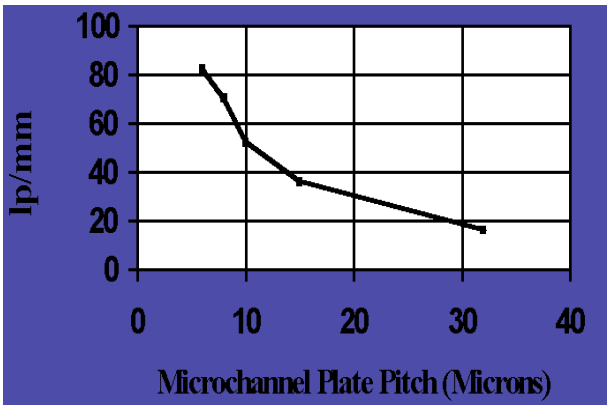

Figure G.2 MCP spatial resolution under different pitch sizes.

The spatial resolution is defined in the unit of line pairs per mm. For 25 μm channel size (32 μm pitch size) MCP used in our experiment, the single stage MCP has spatial resolution of about 30 μm. Since we used two stage MCP (Chevron configuration, typical gain of 10^6), due to the bias angle (8 degree) between two stages as shown in Fig. G.3, the combined resolution of MCP stack could be around 50~100 μm.

Figure G.3 Bias angle in Chevron MCP stack.

The next factor influencing the spatial resolution is MCP phosphor spacing as shown in Fig. G.4. In our setup the spacing between the back surfaces of MCP to the front surface of phosphor is around 1 mm, and their voltage difference is around 2000 V. Since, the electrons have transverse velocity V_x (corresponding to the energy of 20 eV) right after the MCP, the spatial spread Δx at the phosphor is about 100 μm after the acceleration of the electric field.

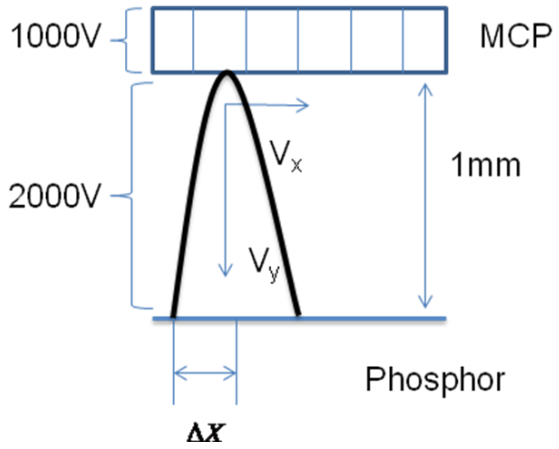

Figure G.4 Electron spread after the amplification of MCP.

Phosphor screen is made of fine particles and usually has better spatial resolution than the factors discussed above. Therefore the overall spatial resolution of the MCP phosphor detection system is about 100 μm.

Appendix H - Copyright approval from the publisher

To: Permissions/IOPP@IOPP,
Cc:
Bcc:
Subject: Fw: copyright question
From: Jill Membrey/IOPP - Wednesday 07/07/2010 10:44

From: "Wang, He" <wanghe@phys.ksu.edu>
To: <isabelle.auffret-babak@iop.org>
Cc: <info@ioppubusa.com>
Date: 06/07/2010 18:09
Subject: copyright question

Dear Isabelle:

My name is He Wang. Right now I am writing my Ph. D thesis, in my thesis I want to include the figures of the paper already published in the Journal of Physics B, could you tell me what the exact policy or procedure I need to follow if I want to quote those figures. The paper I want to use is listed below:

Total of 14 figures

1. He Wang, Michael Chini, Sabih D Khan, Shouyuan Chen, Steve Gilbertson, Ximao Feng, Hiroki Mashiko and Zenghu Chang, "Practical issues of retrieving isolated attosecond pulses", *J. Phys. B: At. Mol. Opt. Phys.*, **42**, 134007, (2009)

Thanks for your help.
Regards
He Wang
Graduate Research Assistant
Department of Physics
Kansas State University

PERMISSION TO REPRODUCE AS REQUESTED
IS GIVEN PROVIDED THAT:

~~(a) the consent of the author(s) is obtained~~
(b) the source of the material including author/editor, title, date and publisher is acknowledged.

IOP Publishing Ltd
Dirac House
Temple Back
BRISTOL
BS1 6BE

9/7/2010 Date

Rights & Permissions

License Number	2465521184264
License date	Jul 10, 2010
Licensed content publisher	Springer
Licensed content publication	Applied Physics B
Licensed content title	Power locking of high-repetition-rate chirped pulse amplifiers
Licensed content author	He Wang
Licensed content date	Jan 1, 2007
Volume number	89
Issue number	2
Type of Use	Thesis/Dissertation
Portion	Figures
Author of this Springer article	Yes and you are the sole author of the new work
Order reference number	
Title of your thesis / dissertation	FROM FEW-CYCLE FEMTOSECOND PULSE TO SINGLE ATTOSECOND PULSE-CONTROL AND TRACK ELECTRON DYNAMICS WITH ATTOSECOND PRECISION
Expected completion date	Aug 2010
Estimated size(pages)	180
Total	0.00 USD

License Number	2465520917936
License date	Jul 10, 2010
Licensed content publisher	Springer
Licensed content publication	Applied Physics B
Licensed content title	Carrier–envelope phase stabilization of 5-fs, 0.5-mJ pulses from adaptive phase modulator
Licensed content author	H. Wang
Licensed content date	Jan 1, 2009
Volume number	98
Issue number	2
Type of Use	Thesis/Dissertation
Portion	Figures
Author of this Springer article	Yes and you are the sole author of the new work
Order reference number	
Title of your thesis / dissertation	FROM FEW-CYCLE FEMTOSECOND PULSE TO SINGLE ATTOSECOND PULSE-CONTROL AND TRACK ELECTRON DYNAMICS WITH ATTOSECOND PRECISION
Expected completion date	Aug 2010
Estimated size(pages)	180
Total	0.00 USD

Dear He Wang:

The Optical Society of America considers this requested use of its copyrighted materials to be allowed under the OSA Author Agreement submitted by the requester on acceptance for publication of his/her manuscript. It is requested that a complete citation of the original material be included in any publication.

MS. DELOIS MILLNER July 8, 2010
Authorized Agent

The Optical Society

2010 Massachusetts Ave., NW
Washington, DC 20036 USA
Direct:+1.202.416.1920 Fax: +1.202.416.6129
Email: dmilln@osa.org
http://www.osa.org